Delft University of Technology

Document Version
Final published version

Citation (APA)
Ai, X. (2026). *Structural Cohesive Element for the Modelling of Composites Delamination*. [Dissertation (TU Delft), Delft University of Technology]. https://doi.org/10.4233/uuid:5e9a48ef-8e21-4e25-bc8d-40c6c2e12082

Important note
To cite this publication, please use the final published version (if applicable).
Please check the document version above.

Copyright
In case the licence states “Dutch Copyright Act (Article 25fa)”, this publication was made available Green Open Access via the TU Delft Institutional Repository pursuant to Dutch Copyright Act (Article 25fa, the Taverne amendment). This provision does not affect copyright ownership.
Unless copyright is transferred by contract or statute, it remains with the copyright holder.

Sharing and reuse
Other than for strictly personal use, it is not permitted to download, forward or distribute the text or part of it, without the consent of the author(s) and/or copyright holder(s), unless the work is under an open content license such as Creative Commons.

Takedown policy
Please contact us and provide details if you believe this document breaches copyrights.
We will remove access to the work immediately and investigate your claim.

This work is downloaded from Delft University of Technology.

STRUCTURAL COHESIVE ELEMENT FOR THE MODELLING OF COMPOSITES DELAMINATION

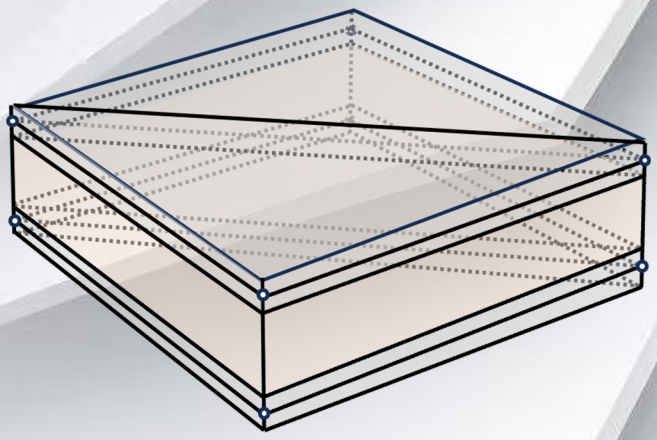

Xiaopeng Ai

艾霄鹏

Structural Cohesive Element for the Modelling of Composites Delamination

STRUCTURAL COHESIVE ELEMENT FOR THE MODELLING OF COMPOSITES DELAMINATION

Dissertation

for the purpose of obtaining the degree of doctor
at Delft University of Technology
by the authority of the Rector Magnificus,
Prof. dr. ir. H. Bijl,
chair of the Board for Doctorates
to be defended publicly on
Wednesday 9 December 2026 at 10:00 am

by

Xiaopeng AI

This dissertation has been approved by the promotors.

Composition of the doctoral committee:

Rector Magnificus,	Chairperson
Prof. dr. C. Kassapoglou,	Delft University of Technology, promotor
Prof. dr. B. Chen,	Soochow University, promotor
Independent members:	
Prof. dr. ir. L.J. Sluys,	Delft University of Technology, Netherlands
Univ.Prof.Dr.techn C. Schuecker,	Montanuniversitaet Leoben, Austria
Dr. R. Higuchi,	University of Tokyo, Japan
Dr. ir. J.J.C. Remmers,	Eindhoven University of Technology, Netherlands
Dr. ir. F.P. van der Meer,	Delft University of Technology, Netherlands
Reserve member:	
Dr. D. Zarouchas,	Delft University of Technology, Netherlands

Keywords: Composite laminates; Delamination; Cohesive zone model; Cohesive element; Structural element; Free-edge effect; Interlaminar stresses; Penalty stiffness

Printed by: Proefschrift

Copyright © 2026 by Xiaopeng Ai

ISBN 978-94-6518-527-9

An electronic version of this dissertation is available at
http://repository.tudelft.nl/.

To my beloved wife, my parents,
and everyone who has supported me throughout this journey.

CONTENTS

Summary xi

Samenvatting xiii

Nomenclature xv

List of Figures xix

List of Tables xxiii

1 Introduction 1
- 1.1 Composite laminate and delamination . . . 2
- 1.2 Cohesive zone modelling . . . 2
- 1.3 Cohesive zone limitation and solutions . . . 3
- 1.4 Structural cohesive element and associated challenges . . . 4
- 1.5 Interlaminar stress in Kirchhoff–Love shell element and free edge effect . . . 6
- 1.6 Research goal and scope . . . 7
- 1.7 Thesis outline . . . 8
- References . . . 9

2 Structural cohesive element for the modelling of delamination 13
- 2.1 Introduction . . . 14
- 2.2 Method . . . 15
  - 2.2.1 Overall illustration . . . 15
  - 2.2.2 Cubic plate element . . . 15
  - 2.2.3 Formation of shell element . . . 21
  - 2.2.4 Structural CE between two plies . . . 22
- 2.3 Results . . . 28
  - 2.3.1 Unidirectional laminate benchmarks: DCB, ENF, and MMB . . . 29
  - 2.3.2 Unidirectional laminate benchmarks: Reinforced DCB . . . 33
  - 2.3.3 Multi-directional laminate benchmark: SLB . . . 36
- 2.4 Summary and conclusions . . . 40
- References . . . 41

3 A new approach for through-thickness stress recovery in composite Laminates 45
- 3.1 Introduction . . . 46
- 3.2 Method . . . 48
  - 3.2.1 3D stress calculation in cohesive elements . . . 48
  - 3.2.2 Interpolation method of stress distribution . . . 49
  - 3.2.3 Penalty stiffness of cohesive elements . . . 49

3.3 Numerical examples . . . 52
3.3.1 Uniform axial extension model . . . 52
3.3.2 Postprocessing technique for stress distribution along the width of laminates . . . 53
3.3.3 Results for cross-ply laminates $[0°/90°]_s$ . . . 54
3.3.4 Results for angle-ply laminates $[+\theta/-\theta]_s$ . . . 61
3.3.5 Results for quasi-isotropic laminates $[+45°/0°/-45°/90°]_s$ . . . 62
3.3.6 Results for laminates with general lay-ups . . . 65
3.4 Summary and conclusions . . . 69
References . . . 70

4 Accurate simulation of delamination with a resin-rich layer-dependent penalty stiffness 75
4.1 Introduction . . . 76
4.2 Method . . . 77
4.2.1 Cubic structural element . . . 77
4.2.2 Penalty stiffness based on the resin-rich layer . . . 78
4.2.3 Derivation of the normal and shear penalty stiffnesses . . . 79
4.3 Validation . . . 86
4.3.1 Mode I delamination benchmark: Double Cantilever Beam (DCB) . . . 87
4.3.2 Mode II delamination benchmark: End-Notched Flexure (ENF) . . . 93
4.3.3 Mixed-mode delamination benchmark: Mixed-Mode Bending (MMB) 98
4.3.4 Three-dimensional delamination benchmark: Reinforced Double Cantilever Beam (R-DCB) . . . 99
4.4 Summary and conclusions . . . 110
References . . . 111

5 Conclusion and recommendations 115
5.1 MAIN CONCLUSIONS . . . 116
5.1.1 A higher-order structural cohesive formulation for efficient delamination modelling . . . 116
5.1.2 A physically based cohesive penalty stiffness for three-dimensional stress recovery . . . 117
5.1.3 Extension of the physically based penalty stiffness to equivalent single-layer models . . . 117
5.2 RECOMMENDATIONS FOR FUTURE WORK . . . 118
References . . . 122

Appendices 123
A $\mathbf{H}$ matrix . . . 123
B $\mathbf{B}$ matrix . . . 125
C Closed-Form solutions of the DCB, MMB and ENF load displacement relationships . . . 131
C.1 DCB test . . . 131
C.2 ENF test . . . 131
C.3 MMB test . . . 131

D Analytical solution of SLB benchmark . . . 132
E TUBA3 element extension . . . 137
E.1 TUBA3 plate element . . . 137
E.2 General framework . . . 137
E.3 Degrees of freedom and shape functions . . . 140
E.4 Green-Lagrange strain . . . 141
E.5 $\mathbb{C}$ matrix . . . 142
E.6 Second Piola-Kirchhoff stress . . . 143
E.7 B matrix . . . 143
E.8 $\mathbf{K}_{\mathrm{mat}}$ matrix . . . 145
E.9 Internal force vector $\mathbf{f}_{\mathrm{int}}$ . . . 145
E.10 $\mathbf{K}_{\mathrm{geo}}$ matrix . . . 147
F TUBA3 shell element verification . . . 149
F.1 Membrane element verification . . . 149
F.2 Plate element verification . . . 150
G TUBA3 shape functions . . . 155

Acknowledgements **157**

Curriculum Vitæ **159**

List of Publications **161**

SUMMARY

FIBER-reinforced composite laminates have been widely used in the aerospace industry for their high specific stiffness and strength. They have attracted attention from researchers in aerospace engineering, particularly in both experimental and numerical studies. Being able to predict the progressive failure of composites under different loading conditions accurately can greatly save the cost of the design by replacing physical experiments with accurate simulations, i.e., virtual testing. However, the numerical modelling of composites still lags behind the industrial application of this material. This is because the damage mechanisms of composite laminates are too complex to simulate. It significantly increases the computational time when all detailed damage mechanisms are considered. Therefore, it is crucial to develop a computationally efficient numerical method that can accurately simulate the failure of composite laminates.

Delamination is one of the most significant damage mechanisms in composite laminates. A widely used method, known as cohesive zone modeling (CZM), suffers from the cohesive zone limitation. It requires a very fine mesh within the cohesive zone length, which limits the computational efficiency. The objective of this thesis is to overcome this by developing a triangular structural element for the simulation of delamination in composite laminates by combining higher-order Kirchhoff–Love shell elements with compatible cohesive elements. By overcoming the cohesive zone limitation, the proposed method enables the use of coarser meshes and significantly reduces the computational cost. Based on this structural element, a physically based formulation of the cohesive penalty stiffness is developed.

The research presented in this thesis started with the development of a triangular cubic Kirchhoff–Love shell element. In this element, the transverse displacement field is approximated using a third-order polynomial, while the in-plane displacement components are interpolated linearly. This shell element is an extension of the cubic plate element. The extension was carried out in two aspects. First, the formulation was extended from isotropic materials to anisotropic composite materials. Second, the plate element was extended to a shell element to simulate delamination under complex loading conditions. The triangular shape is chosen because it would allow the flexibility of modelling shells of arbitrary geometry. Based on the cubic shell element, a compatible structural cohesive element was developed. The structural element was validated against Mode I, Mode II, mixed-mode, and fully three-dimensional benchmark problems. The single-leg bending model was also investigated to verify its accuracy and efficiency for arbitrary laminate stacking sequences. The results were compared with analytical solutions and three-dimensional solid elements to verify the accuracy of the method. A quantitative comparison of CPU time was conducted to demonstrate the computational efficiency of the proposed method.

Secondly, to develop a physically motivated penalty stiffness formulation that enables the recovery of out-of-plane stresses in the structural element, a physically based formulation for the cohesive penalty stiffness was derived from the material properties and thick-

ness of the resin-rich layer. This formulation satisfies the kinematic assumptions of Kirchhoff–Love shell theory. A parameter sensitivity analysis was conducted to evaluate the robustness of the proposed method. The proposed formulation was validated using cross-ply, angle-ply, quasi-isotropic, and general laminate configurations. The distribution of the out-of-plane stresses across the width and through the thickness of the laminate was obtained by linear interpolation. The results were compared with analytical solutions and three-dimensional solid-element models.

Finally, based on the proposed physically motivated penalty stiffness formulation, an equivalent single-layer formulation was introduced using assumed deformation fields under DCB and ENF loading conditions. The through-thickness distributions of the out-of-plane normal and shear stresses were derived from boundary conditions for pure Mode I and Mode II loading based on beam theory. By extending the layer-wise penalty stiffness mentioned earlier, an accurate penalty stiffness formulation was derived by combining the laminate stress distribution, material properties, and the thickness of the resin-rich layer. This method was evaluated using the Mode I, Mode II, mixed-mode, and fully three-dimensional benchmark problems, and the results were compared with those previously obtained. This method was also validated by predicting the traction distribution at the crack tip. The convergence and accuracy of the method were verified by comparing the results with those obtained using the previously developed structural cohesive element and three-dimensional solid-element models.

In conclusion, the thesis has proposed and developed an efficient and accurate method for damage modelling of composite laminates based on the structural element. The proposed method is applicable to the simulation of complex thin-walled composite laminate structures and offers the potential to reduce the computational cost of large-scale models.

SAMENVATTING

VEZELVERSTERKTE composietlaminaten worden vanwege hun hoge specifieke stijfheid en sterkte veel toegepast in de luchtvaartindustrie. Hierdoor hebben zij veel aandacht gekregen binnen de luchtvaarttechniek, zowel in experimenteel als in numeriek onderzoek. Het nauwkeurig kunnen voorspellen van progressieve schade onder verschillende belastingscondities kan de ontwerpkosten aanzienlijk verlagen doordat fysieke experimenten gedeeltelijk kunnen worden vervangen door betrouwbare numerieke simulaties, ook wel virtual testing genoemd.

Ondanks de brede industriële toepassing blijft de numerieke modellering van composietlaminaten achter bij de technologische ontwikkeling van deze materialen. De voornaamste oorzaak is de complexiteit van de verschillende schadeprocessen die in composieten optreden. Het gelijktijdig modelleren van alle relevante schadeprocessen leidt tot een aanzienlijke toename van de rekentijd. Daarom is de ontwikkeling van een computationeel efficiënte numerieke methode die het schadegedrag van composietlaminaten nauwkeurig kan voorspellen van groot belang.

Delaminatie is een van de belangrijkste schadevormen in composietlaminaten. Een veelgebruikte benadering voor de modellering hiervan is de cohesive zone method (CZM). Deze methode wordt echter beperkt door de vereiste cohesieve zonelengte, waardoor een zeer fijn meshes noodzakelijk is en de rekenefficiëntie afneemt. Het doel van dit proefschrift is daarom de ontwikkeling van een driehoekig structureel element voor de simulatie van delaminatie in composietlaminaten door Kirchhoff–Love-schilelementen van hogere orde te combineren met compatibele cohesieve elementen. Door de beperking van de cohesieve zonelengte te overwinnen, maakt de voorgestelde methode het gebruik van grovere meshes mogelijk, waardoor de rekentijd aanzienlijk wordt verminderd. Daarnaast wordt, op basis van dit structurele element, een fysisch onderbouwde formulering voor de cohesieve penalty-stijfheid ontwikkeld.

Het onderzoek dat in dit proefschrift wordt gepresenteerd, begon met de ontwikkeling van een driehoekig kubisch Kirchhoff–Love-schilelement. In dit element wordt het transversale verplaatsingsveld benaderd met behulp van een polynoom van de derde orde, terwijl de in-vlakverplaatsingscomponenten lineair worden geïnterpoleerd. Dit schilelement vormt een uitbreiding van het kubische plaatelement. Deze uitbreiding is op twee aspecten uitgevoerd. Ten eerste is de formulering uitgebreid van isotrope materialen naar anisotrope composietmaterialen. Ten tweede is het plaatelement uitgebreid tot een schilelement om delaminatie onder complexe belastingsomstandigheden te kunnen simuleren. Er is gekozen voor een driehoekige elementvorm, omdat deze de flexibiliteit biedt om schillen met willekeurige geometrieën te modelleren.

Op basis van het kubische schilelement is vervolgens een compatibel structureel cohesief element ontwikkeld. Dit structurele element is gevalideerd aan de hand van benchmarkproblemen voor Mode I, Mode II, gemengde modusbelasting (mixed-mode) en volledig driedimensionale belastingsgevallen. Daarnaast is het single-leg-bending-model onder-

zocht om de nauwkeurigheid en efficiëntie van de methode voor willekeurige laminaatstapelingen te verifiëren. De resultaten zijn vergeleken met analytische oplossingen en driedimensionale solidelementen om de nauwkeurigheid van de methode vast te stellen. Tevens is een kwantitatieve vergelijking van de CPU-rekentijd uitgevoerd om de computationele efficiëntie van de voorgestelde methode aan te tonen.

Ten tweede is, met als doel een fysisch onderbouwde formulering voor de penaltystijfheid te ontwikkelen waarmee de uit-de-vlakspanningen in het structurele element kunnen worden gereconstrueerd, een fysisch gebaseerde formulering voor de cohesieve penaltystijfheid afgeleid uit de materiaaleigenschappen en de dikte van de harsrijke tussenlaag. Deze formulering voldoet aan de kinematische aannames van de Kirchhoff–Loveschilstheorie. Er is een gevoeligheidsanalyse uitgevoerd om de robuustheid van de voorgestelde methode te evalueren. De voorgestelde formulering is gevalideerd voor cross-ply-, angle-ply-, quasi-isotrope en algemene laminaatconfiguraties. De verdeling van de uit-de-vlakspanningen over de breedte en door de dikte van het laminaat is verkregen door middel van lineaire interpolatie. De resultaten zijn vergeleken met analytische oplossingen en modellen met driedimensionale solidelementen.

Ten slotte is, op basis van de voorgestelde fysisch onderbouwde formulering voor de penaltystijfheid, een equivalente enkellaagsformulering geïntroduceerd, waarbij gebruik is gemaakt van aangenomen vervormingsvelden onder DCB- en ENF-belastingsomstandigheden. De verdelingen van de uit-de-vlaknormaalspanningen en -schuifspanningen door de dikte zijn afgeleid uit de randvoorwaarden voor zuivere Mode I- en Mode II-belasting, op basis van de balkentheorie. Door de eerder beschreven laaggewijze penaltystijfheid uit te breiden, is een nauwkeurige formulering voor de penaltystijfheid afgeleid, waarbij de spanningsverdeling in het laminaat, de materiaaleigenschappen en de dikte van de harsrijke tussenlaag zijn gecombineerd. Deze methode is geëvalueerd aan de hand van benchmarkproblemen voor Mode I, Mode II, gemengde modusbelasting en volledig driedimensionale belastingsgevallen. De resultaten zijn vergeleken met de eerder verkregen resultaten. Daarnaast is de methode gevalideerd door de tractieverdeling aan de scheurtip te voorspellen. De convergentie en nauwkeurigheid van de methode zijn geverifieerd door de resultaten te vergelijken met die van het eerder ontwikkelde structurele cohesieve element en modellen met driedimensionale solidelementen.

Concluderend heeft dit proefschrift een efficiënte en nauwkeurige methode voor de modellering van schade in composietlaminaten op basis van structurele elementen voorgesteld en ontwikkeld. De voorgestelde methode is geschikt voor het simuleren van complexe dunwandige composietlaminaatconstructies en biedt mogelijkheden om de computationele kosten van grootschalige modellen te verlagen.

NOMENCLATURE

Latin characters

a_0	pre-crack length
a_1, a_2, a_3, a_4	unknown coefficients of the stress distribution
A	area of a membrane element
b	specimen width
$\mathbf{B}$	matrix connecting the vector $\mathbf{Q}$ and the vector α
$\mathbf{B}_{\text{mem}}$	strain–displacement matrix of a membrane element
$\mathbf{D}_{\text{mem}}$	constitutive tensor of a membrane element
$E_{(ij)}$	elastic modulus($i = 1, 2, 3$ $j = 1, 2, 3$)
E_{rr}	elastic modulus of the resin-rich layer
$\mathbf{f}_{\text{ext}}$	vector of the external force
$\mathbf{f}_{\text{int}}$	vector of the internal force
$\mathbf{f}_{\text{res}}$	vector of the residual force
G_{I}, G_{II}	Mode I, Mode II energy release rates
G_{Ic}, G_{IIc}	Mode I, Mode II critical energy release rates
G_{rr}	shear modulus of the resin-rich layer
G_{T}	total energy release rate
h	thickness of the laminate
h_{bot}	thickness of the bottom arm of the specimen
h_{rr}	thickness of the resin-rich layer
h_{top}	thickness of the top arm of the specimen
$\mathbf{H}$	matrix which contributes to the stiffness matrix of the plate element
$\mathbf{K}$	stiffness matrix of a finite element
K	penalty stiffness

K^{Turon}	penalty stiffness proposed by Turon et al.
K_n	normal penalty stiffness
K_n^{Ai}	normal penalty stiffness proposed by Ai et al.
K_s	shear penalty stiffness
K_s^{Ai}	shear penalty stiffness proposed by Ai et al.
K_s^{Bazilevs}	shear penalty stiffness proposed by Bazilevs et al.
l_{ij}	length of the side ij, $ij = 12, 23, 13$
L	specimen length
M_n	normal bending moment
$n_{\text{top}}, n_{\text{bot}}$	the number of plies in the top and bottom arms of the specimen
n_{total}	the total number of plies
$\mathbf{N}_w$	shape function related to the out-of-plane displacement
$\mathbf{N}_{\theta_x}, \mathbf{N}_{\theta_y}$	shape function related to the rotations around x and y, respectively
$p^*(x, y)$	prescribed distributed pressure load on the element
$\mathbf{q}$	vector of nodal degree of freedoms of a finite element
$\mathbf{Q}$	vector of generalized forces
R_N	concentrated force at the element vertex
t	thickness of a element
$\mathbf{T}$	matrix contributes the stiffness matrix of the plate element
u_i, v_i	displacements along x and y axes for node i
$\overline{\mathbf{U}}$	vector of nodal degree of freedoms of the membrane element
U	internal work
U_0	strain energy density
V_n	Kirchhoff shear force
w	displacement field in the element
$\overline{w}$	displacement on the boundary of the element
$\overline{\mathbf{W}}$	vector of nodal degree of freedoms of the plate element
W	external work

Greek characters

α	vector of coefficients that contributes to the out-of-plane displacement field
γ	angle between the normal n and the local axis x
$\Delta_{\mathrm{I}}, \Delta_x, \Delta_y$	opening displacement of Mode I and two shear openings along x and y axial
ε_z	out-of-plane normal strain
ε_{xz}	transverse shear strain
ν_{rr}	Poisson's ratio of the resin-rich layer
π	modified potential energy
σ_z	out-of-plane normal stress
σ_z^{max}	maximum out-of-plane normal stress
σ_z^{top}	out-of-plane normal stress in the top arm of the specimen
σ_z^{bot}	out-of-plane normal stress in the bottom arm of the specimen
τ_{xz}	transverse shear stress
τ_{xz}^{max}	maximum transverse shear stress
τ_{xz}^{top}	transverse shear stress in the top arm of the specimen
τ_{xz}^{bot}	transverse shear stress in the bottom arm of the specimen

Sub/superscripts

$\bullet_{\mathrm{bot}}$	related to the bot surface of a cohesive element
$\bullet_{\mathrm{CE}}$	related to cohesive elements
$\bullet_{\mathrm{mem}}$	related to membrane elements
$\bullet_n$	related to the normal direction
$\bullet_{\mathrm{plate}}$	related to plate elements
$\bullet_{\mathrm{shell}}$	related to shell elements
$\bullet_s$	related to the shear direction
$\bullet_x, \bullet_y$	related to the global x, y directions, respectively
$\bullet_z$	related to the global z-direction
$\bullet_{xz}$	related to the global xz-plane

$\bullet^{\mathrm{DCB}}$	related to the DCB specimen
$\bullet^{\mathrm{ENF}}$	related to the ENF specimen
$\bullet^{\mathrm{MMB}}$	related to the MMB specimen
$\bullet^{\mathrm{Mode\ I}}$	related to pure Mode I loading
$\bullet^{\mathrm{Mode\ II}}$	related to pure Mode II loading
$\bullet^{\mathrm{Unreinforced}}$	related to the unreinforced region of the R-DCB specimen
$\bullet^{\mathrm{Reinforced}}$	related to the reinforced region of the R-DCB specimen
$\bullet^{\mathrm{Undamaged}}$	related to the undamaged region of the R-DCB specimen

Abbreviations

CE	Cohesive Element
CZL	Cohesive Zone Length
CZM	Cohesive Zone Model
DCB	Double Cantilever Beam
DoF	Degrees of Freedom
ENF	End-Notched-Flexure
FE	Finite Element
FNM	Floating Node Method
FOSD	First Order Shear Deformation
FRP	Fiber-Reinforced Polymer
IG	InteGration points
LHS	Left-Hand Side
MMB	Mixed-Mode Bending
R-DCB	Reinforced Double Cantilever Beam
SLB	Single-Leg Bending
TL	Total Lagrangian
UAE	Uniform Axial Extension
VCCT	Virtual Crack Closure Technique

LIST OF FIGURES

1.1 Two types of cohesive law . . . 3
1.2 Development of the numerical cohesive zone [22] . . . 3
1.3 Configuration of the CE implemented by Russo [26] . . . 5
1.4 Geometrical comparison between conventional CE and structural CE . . . 5
1.5 Kinematic continuity is achieved when the displacements at the interface are equal in both plies . . . 6
1.6 (a) Uniaxial extension (b) Boundary stress (c) Normal interlaminar stress distributions (d) Shear interlaminar stress distributions . . . 7

2.1 Coordinate system and DoFs for the triangular cubic plate element [5] . . . 15
2.2 Sign conventions for shear force and bending moment resultants . . . 17
2.3 Mode I opening . . . 23
2.4 Mode II opening . . . 23
2.5 DCB, ENF, and MMB test specimens . . . 29
2.6 Results of the DCB, ENF, and MMB tests, showing the sensitivities of the conventional solid CE and the proposed structural CE on different mesh densities . . . 31
2.7 Load-displacement curves of the DCB model with different integration points on two different meshes . . . 33
2.8 Geometry of the R-DCB specimen (units in mm) [19] . . . 34
2.9 Boundary conditions and loading of the finite element model; U_3=7.5 mm . . . 34
2.10 Load-displacement curves of the reinforced DCB with different mesh sizes from simulation results . . . 35
2.11 Comparison of numerical and experimental results of the force-displacement curves [19] . . . 36
2.12 Comparison of numerical and experimental results of the delamination front position . . . 37
2.13 SLB specimen [12] . . . 38
2.14 Layer-wise model for SLB . . . 39
2.15 Load-displacement predictions of the SLB . . . 39

3.1 Triangular cubic structural element . . . 48
3.2 Coordinate system and DoFs for the triangular cubic plate element . . . 49
3.3 Interpolation method of the structural elements along thickness . . . 49
3.4 State of simple shear in the cohesive model . . . 50
3.5 State of tensile with resin-rich layer . . . 51
3.6 State of simple shear with resin-rich layer . . . 52
3.7 Geometry of the uniform axial extension laminate model . . . 53

3.8 Interpolation method of the structural elements along the width 53
3.9 Interlaminar normal stress σ_z at the mid-plane 55
3.10 Interlaminar normal stress σ_z at the interface between 0° and 90° 56
3.11 Interlaminar shear stress τ_{yz} at the interface between 0° and 90° 56
3.12 Distributions of interlaminar normal and shear stresses with different resin-rich layer thickness 57
3.13 Distributions of interlaminar normal and shear stresses with different elastic moduli 59
3.14 Distributions of interlaminar normal and shear stresses with different Poisson's ratios 60
3.15 Mesh sizes of solid-element model 60
3.16 Interlaminar stress distributions at the interface between 0° and 90° 61
3.17 Results comparison for the distributions of interlaminar normal and shear stresses 62
3.18 Interlaminar shear stress τ_{xz} at the $+\theta/-\theta$ interface $(z = h_0)$ 63
3.19 Quasi-isotropic laminate geometry 63
3.20 Interlaminar stress distributions through the thickness near the free edge $(y = 0.998b)$ in $[45/0/-45/90]_s$ laminate under axial extension 64
3.21 Through-thickness distributions of interlaminar stresses in the $[0^\circ/+55^\circ/+35^\circ/-35^\circ]_s$ laminate $(y = 0.998b)$ under axial extension 65
3.22 Interlaminar stress distributions at the interface between 35° and -35° . . . 66
3.23 Through-thickness distributions of interlaminar stresses in the $[0^\circ/+30^\circ/-45^\circ/+45^\circ]_s$ laminate $(y = 0.998b)$ under axial extension 67
3.24 Interlaminar stress distributions along the width direction at the interface between the -45° and 45° plies of $[0^\circ/+30^\circ/-45^\circ/+45^\circ]_s$ laminate 68
3.25 Interlaminar normal stress σ_z at the mid-plane 68
3.26 Displacement through the thickness 69

4.1 Triangular cubic structural element [8] 77
4.2 Penalty stiffness based on resin-rich layer [19] 78
4.3 Stress distributions in the laminate under pure Mode I loading 83
4.4 Stress distributions in the laminate under pure Mode II loading 86
4.5 Double cantilever beam (DCB) specimen [25] 87
4.6 Through-thickness distribution of out-of-plane normal stress in the 24-ply DCB specimen 88
4.7 Comparison of the load-displacement curves obtained from the DCB simulations using the conventional and proposed penalty stiffness formulations at different mesh densities 90
4.8 Definition of the integration interval for the normalized L_2 error calculation . 91
4.9 Normalized L_2 error of the DCB benchmark versus mesh size for different penalty stiffness formulations 92
4.10 Distribution of traction ahead of crack tip 92
4.11 Procedure for extracting the traction distribution from cohesive elements . . . 93

4.12 Comparison of normal traction distributions in the cohesive zone of the DCB specimen for different mesh sizes using the conventional and proposed penalty stiffness formulations . . . 93
4.13 Comparison of the predicted normal traction distributions ahead of the crack tip 94
4.14 End-notched flexure (ENF) specimen [25] . . . 94
4.15 Through-thickness distribution of transverse shear stress in the 24-ply ENF specimen . . . 96
4.16 Comparison of the load-displacement curves obtained from the ENF simulations using the conventional, Bazilevs', and proposed penalty stiffness formulations at different mesh densities . . . 97
4.17 Mixed-mode bending (MMB) specimen [25] . . . 98
4.18 Comparison of the load-displacement curves obtained from the MMB simulations using the conventional and proposed penalty stiffness formulations at different mesh densities . . . 99
4.19 Normalized L_2 error of the MMB benchmark versus mesh size for different penalty stiffness formulations . . . 100
4.20 Geometry of the R-DCB specimen (units in mm) [29] . . . 100
4.21 Boundary conditions and loading of the finite element model; U_3=7.5 mm . . . 101
4.22 Different regions of the R-DCB specimen . . . 102
4.23 Through-thickness distribution of out-of-plane normal stress in the 16-ply unreinforced region of the R-DCB specimen . . . 102
4.24 Through-thickness distribution of out-of-plane normal stress in the 16-ply reinforced region of the R-DCB specimen . . . 104
4.25 Finite element model of the undamaged region in the R-DCB specimen . . . 105
4.26 Through-thickness distribution of out-of-plane normal stress in the 8-ply undamaged region of the R-DCB specimen . . . 105
4.27 Through-thickness distribution of transverse shear stress in the 8-ply undamaged region of the R-DCB specimen . . . 106
4.28 Comparison of the load-displacement curves obtained from the R-DCB simulations using the conventional and proposed penalty stiffness formulations at different mesh densities . . . 107
4.29 Comparison of numerical and experimental results of the load-displacement curves [29] . . . 108
4.30 Comparison of numerical and experimental [29] delamination front positions 109

5.1 Transverse shear stress prediction along the thickness direction . . . 120
5.2 Integration points along the thickness direction . . . 120
5.3 Integration points along the thickness direction . . . 121
D.1 Analytical solution of SLB model . . . 132
D.2 Beam model of SLB specimen ($a < L$) . . . 133
D.3 Beam model of SLB specimen ($a \geq L$) . . . 136
E.4 Bell triangle (TUBA3) [1] . . . 137
E.5 Area coordinates of a point in the generic triangle . . . 140
F.6 Patch test of the membrane element . . . 150
F.7 Patch test results . . . 150

F.8 Simply supported plate with center load model 151
F.9 Coarse and fine finite element meshes for the simply supported plate 152
F.10 Boundary conditions of the simply supported plate 152
F.11 Cantilever plate model 153
F.12 Finite element meshes for the cantilever plate 154
F.13 Boundary condition of the cantilever plate 154
F.14 Results for the cantilever plate 155

List of Tables

2.1 Geometric parameters for unidirectional benchmarks . . . 29
2.2 Material properties for DCB [13] . . . 30
2.3 Material properties for ENF and MMB [13] . . . 30
2.4 Comparison of CPU time (unit: second) . . . 32
2.5 Lamina properties of the R-DCB model [20] . . . 34
2.6 Interlaminar properties of the R-DCB model [20] . . . 35
2.7 Geometric parameters for the SLB specimen . . . 38
2.8 C12K/R6376 material properties for SLB specimen [13] . . . 38

3.1 Geometric parameters for the 4-layer laminate model . . . 54
3.2 Material properties of cross-ply laminate [32] . . . 54
3.3 Penalty stiffness obtained by resin-rich layer . . . 54
3.4 Normal and shear penalty stiffness values for different resin-rich layer thicknesses . . . 57
3.5 Normal and shear penalty stiffness values for different resin-rich layer elastic moduli . . . 58
3.6 Normal and shear penalty stiffness values for different resin-rich layer Poisson's ratios . . . 58
3.7 Material properties of angle-ply laminate [36] . . . 61
3.8 Geometric parameters of the quasi-isotropic laminate benchmark model . . . 64
3.9 Material properties of the quasi-isotropic laminate [42] . . . 64
3.10 Comparison of CPU time per increment (unit: second) . . . 69

4.1 Material properties for the DCB specimen [25] . . . 87
4.2 Out-of-plane normal stress ratios at the interface layers of the top arm in the 24-ply DCB specimen . . . 88
4.3 Material parameters of the resin-rich layer in the DCB specimen . . . 89
4.4 Material properties of the ENF and MMB specimens [25] . . . 95
4.5 Material parameters of 8552 epoxy resin . . . 95
4.6 Transverse shear stress ratios at the interface layers of the top arm in the 24-ply ENF specimen . . . 95
4.7 Material properties for the R-DCB specimen[31] . . . 101
4.8 Material parameters of Araldite 2015 . . . 101
4.9 Out-of-plane normal stress ratios at the interface layers of the top arm in the 16-ply unreinforced region . . . 102
4.10 Out-of-plane normal stress ratios at the interface layers of the top arm in the 16-ply reinforced region . . . 103

4.11 Out-of-plane normal stress ratios at the interface layers of the 8-ply undamaged region . . . 106
4.12 Transverse shear stress ratios at the interface layers of the 8-ply undamaged region . . . 106

F.1 Parameters of the simply supported plate . . . 151
F.2 Center deflection of the simply supported isotropic plate subjected to a concentrated center load . . . 153
F.3 Parameters of the cantilever plate . . . 154

1

INTRODUCTION

1

1.1. COMPOSITE LAMINATE AND DELAMINATION

FIBER-reinforced composites are nowadays popular in aerospace structures [1, 2]. Reliable prediction of structural strength and damage tolerance is an indispensable aspect in the design of composite aircraft structures [3]. An accurate numerical simulation for predicting the progressive failure of composite materials under various loading conditions can reduce design costs by replacing physical experiments. However, significant challenges remain in the numerical modelling of composite failure. On the one hand, the damage mechanisms of composites are complex to model, including intralaminar damage and interlaminar delamination. On the other hand, detailed three-dimensional simulations are computationally expensive, especially for large-scale engineering applications. Among these failure mechanisms, delamination is one mode of composite failure that occurs in the layers of the composite laminate. Therefore, accurate and efficient prediction of delamination is important for the reliable design of aerospace composite structures.

1.2. COHESIVE ZONE MODELLING

THE cohesive element (CE) is a widely used finite element method to model delamination. CE is developed based on the Cohesive Zone Model proposed by Dugdale and Barenblatt [4, 5]. A fracture process zone, generally called the cohesive zone, exists along the interface, ahead of the stress-free crack tip. A traction-separation relationship, namely the cohesive law, describes how the interfacial stresses and damage evolve with respect to the interfacial openings. Standard CEs are usually developed for use between two solid elements to model their debonding under static or fatigue loads [6–15].

In finite element implementation, cohesive zone models are classified into intrinsic and extrinsic types, shown in Figure 1.1. In the intrinsic model, CEs are embedded in the initial mesh between continuum elements to model their debonding. Intrinsic CEs firstly undergo an elastic loading phase, up to the critical stress state for damage onset, before going through the softening phase of the cohesive law. In the extrinsic model, CEs are inserted/activated in the mesh on the fly when the stress state in the continuum has reached damage onset. Hence, extrinsic CEs only go through the softening phase of the cohesive law. Comprehensive comparisons of the two approaches have been performed for dynamic fracture problems [16–18]. Intrinsic CEs are easy to implement and parallelize, but suffer from the artificial compliance problems in crack-tip speed and elastic wave propagation [18]. High penalty stiffness is needed to reduce the artificial compliance problems, but this would lead to ill-conditioning of the stiffness matrix for implicit analysis and stringent stability requirements for explicit analysis. Extrinsic CEs do not add artificial compliance before fracture. However, their implementation would require advanced data structures and frequent updates of the mesh [19], making implementation and parallelization more difficult. Discontinuous-Galerkin [20] and Augmented Lagrangian [21] approaches have been developed to mitigate the artificial compliance problems of the intrinsic CEs without requiring mesh updates of the extrinsic CEs. However, they still suffer from the mesh dependency problems due to the restriction that the cohesive fracture can only propagate along existing mesh boundaries. In this work, we focus on quasi-static analysis of delamination in composites. Hence, the artificial compliance issues in dynamic fracture are neglected, and the intrinsic model is assumed for the CEs hereafter.

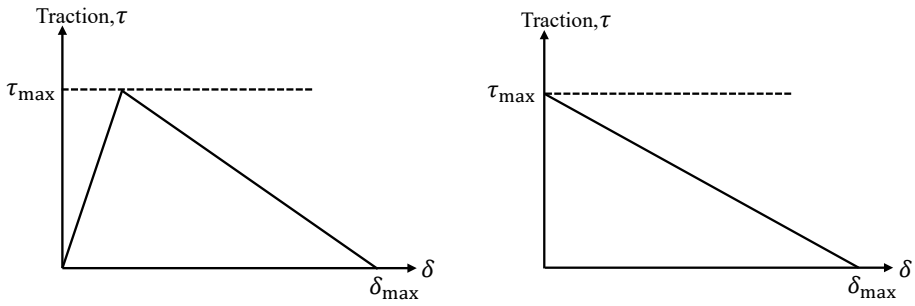

(a) Intrinsic CZM (b) Extrinsic CZM

Figure 1.1: Two types of cohesive law

1.3. COHESIVE ZONE LIMITATION AND SOLUTIONS

WHILE being a popular and versatile tool to model delamination, standard CEs suffer from a well-known limit on the mesh density – the element size must be much smaller than the Cohesive Zone Length (CZL), shown in Figure 1.2, to accurately predict delamination. As the name indicates, the cohesive zone length is defined as the length of the cohesive zone, which is a region where CEs experience an irreversible deformation. This parameter is necessary for all simulations employing cohesive zone modeling (CZM)-based methods.

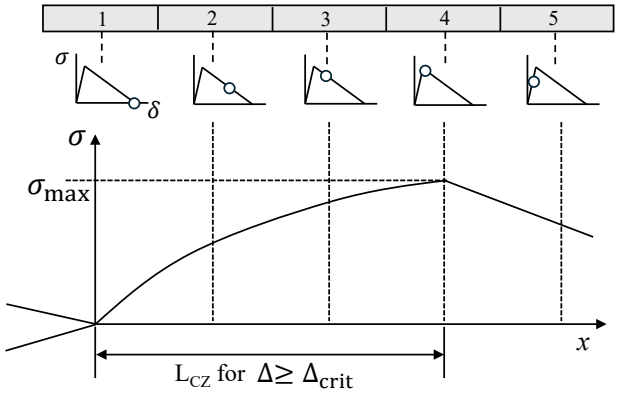

Figure 1.2: Development of the numerical cohesive zone [22]

According to the previous analysis [6, 7], high-stress gradients could be produced within the cohesive zone during delamination in composites. A very fine CE mesh must be used there to sufficiently capture the stress gradients such that the internal virtual work of the CEs can be accurately integrated. So far, there is no fixed rule on how fine the mesh should

be in the literature. In some research [8–10], the authors have demonstrated that a minimum of two to three CEs is required within the cohesive zone, as illustrated in Figure 1.2. With coarser meshes, simulations would significantly over-predict the peak load [11]. In a typical mode I delamination test of a unidirectional composite coupon, i.e., the Double Cantilever Beam (DCB) test, the CZL is less than 1 mm. Therefore, the CE size needs to be smaller than approximately 0.5 mm to ensure sufficient mesh number in the cohesive zone. Such a fine mesh increases the number of elements and the computational cost.

The problem of cohesive zone limit on the mesh has drawn the attention of many researchers in the past. Turon et al. [11] adopted an engineering method to solve the problem by reducing the material strength to numerically extend the CZL. While shown to be promising in the Mode I DCB case, in cases such as the pure mode II End-Notched-Flexure (ENF) test, decreasing the cohesive strength can cause excessive under-prediction of the overall strength [22, 23]. Yang [24] and Do [25]'s research work demonstrated that larger CE sizes can be achieved by placing enough integration points in the cohesive zone. Their method could predict the peak load correctly for CE sizes up to 1.43 times the estimated CZL. However, its first-order shape function limits the effectiveness of this method in further expanding CE beyond the scale of the cohesive zone [26]. Guiamatsia et al. [27–29] used the beam on elastic foundation solution as an enrichment function and tested it in mixed-mode delamination. However, the enrichment method could lead to inaccuracies in interpolation for elements larger than 3 mm [28]. Another enrichment approach with the piecewise linear shape functions was proposed by Samimi [30–32]. However, the over-prediction problem of peak load under large CE has not been solved. Van der Meer et al. [33] used the level set method with an energy-based criterion to propagate delamination without the cohesive zone limit. However, this method is limited to the case of a single delamination. Lu et al. [34] proposed an adaptive version of the Floating Node Method (FNM) [35] to adaptively refine the CEs in the cohesive zone. However, this method is currently implemented for 2D problems. Alvarez et al. [36] used quadratic CEs between quadratic solid elements and used a higher number of integration points, which increased the grid size to be comparable to CZL but not beyond [26]. Mukhopadhyay and Bhatia [37] developed an hp refinement strategy to simulate the delamination between two solid elements. However, it is only implemented in 2D in their work. Daniel [38] developed an ERR-Cohesive method to simulate delamination with large elements by estimating the energy release rate by means of the virtual crack closure technique (VCCT). However, this method is only presented in 2D, and the VCCT approach relies on the existence of an initial crack and the assumption of self-similar crack propagation.

1.4. STRUCTURAL COHESIVE ELEMENT AND ASSOCIATED CHALLENGES

INSPIRED by the earlier works in the literature, Russo and Chen [26] developed a so-called structural CE, shown in Figure 1.3, which conforms to Kirchhoff-Love structural elements for the neighbouring plies. Their work was done in 2D. The Euler-Bernoulli beam elements were used to model the plies. The structural CE, sharing its nodes with the beam elements, was developed to model the delamination. An adaptive integration scheme was used to place more integration points in CEs containing the cohesive zone.

Their results showed that the structural CE could overcome the cohesive zone limit on mesh density, allowing the element size to be ten times larger than that of the standard linear CEs. Motivated by Russo and Chen's work, Tosti Balducci and Chen [39] extended the structural CE to the three-dimensional DCB problem by developing a structural CE compatible with the TUBA3 plate elements [40]. Their results showed that the TUBA3-based structural formulation of CE could overcome the cohesive zone limit.

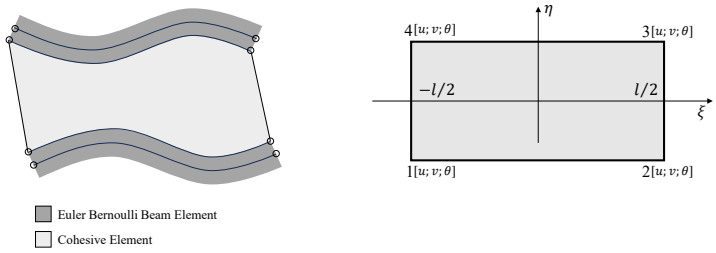

Figure 1.3: Configuration of the CE implemented by Russo [26]

A fundamental challenge in developing cohesive elements connecting structural elements arises from the fact that their kinematics differ from those of conventional solid cohesive elements. In conventional solid cohesive element formulations (shown in Figure 1.4a), the cohesive element nodes are located directly on the two opposing surfaces of the adjacent bulk elements. Consequently, the relative displacement between the corresponding upper and lower nodes directly represents the opening and sliding displacement of the cohesive interface. In contrast, when a cohesive element is introduced between structural elements (shown in Figure 1.4b), such as shell elements, its nodes do not lie on the actual surfaces of the adjacent structural elements. Therefore, the relative displacement between the cohesive-element nodes does not directly correspond to the physical displacement jump across the cohesive interface.

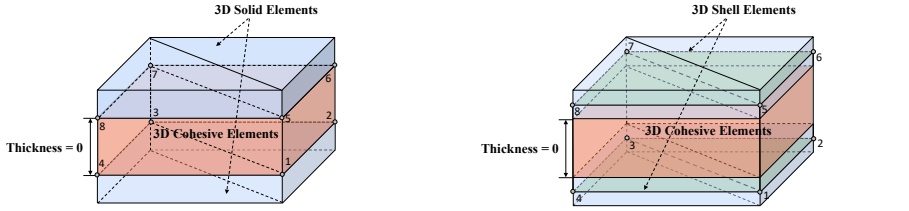

(a) Conventional CE between solids: interface thickness = distance between node 4 and node 8

(b) Structural CE between shells: interface thickness $\neq$ distance between node 4 and node 8

Figure 1.4: Geometrical comparison between conventional CE and structural CE

Although structural elements offer significant advantages for simulating thin-walled structures, there is a non-negligible thickness of the cohesive element between them. In contrast, when solid elements are used, the corresponding cohesive elements assume zero-thickness interfaces. If the penalty stiffness in the cohesive law is assigned the same value

as that used for solid elements, it will lead to an overestimation of the apparent structural stiffness. The overestimation is due to not accounting for the actual thickness and stiffness of the resin-rich layer. This overestimation affects the opening displacement and may artificially delay the onset of damage. Previous studies [41] employed Mindlin–Reissner plate theory combined with First-Order Shear Deformation (FOSD) theory to ensure continuity of degrees of freedom at the interface, as shown in Figure 1.5. This consistent kinematic framework allows the continued use of previously established penalty stiffness values.

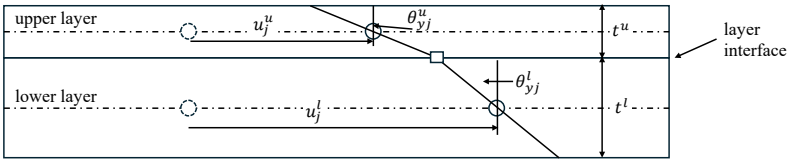

Figure 1.5: Kinematic continuity is achieved when the displacements at the interface are equal in both plies

However, for Kirchhoff–Love shell elements, which inherently neglect transverse shear deformation, the accurate determination of values for penalty stiffness becomes critical and impacts the accuracy of the simulation results.

1.5. INTERLAMINAR STRESS IN KIRCHHOFF–LOVE SHELL ELEMENT AND FREE EDGE EFFECT

ANOTHER challenge associated with Kirchhoff–Love shell elements is calculating the out-of-layer stress distributions. Since Kirchhoff–Love theory neglects the deformation in the thickness direction, the stress components can not be directly derived from the shell element's degrees of freedom. As a result, the important information for predicting out-of-plane failure analysis and damage progression is missing. Although intralaminar stresses have a relatively weak influence on out-of-plane delamination, expanding the damage simulation of composites to a wider range of loading conditions will inevitably involve intralaminar damage mechanisms, such as matrix cracking and fiber damage. In the corresponding damage criteria, out-of-plane stresses can not be neglected and will play a critical role in damage initiation and evolution predictions. Therefore, there is a need to develop a method that can accurately evaluate the interlaminar stress distribution within Kirchhoff–Love shell element models.

The free-edge effect refers to the presence of significant, and potentially singular, localized three-dimensional stress fields near the interfaces between dissimilar laminate layers [42–45]. This singularity leads to a significant increase in interlaminar tensile and shear stresses in the free edge region, making it prone to crack initiation and propagation at the interlaminar interface, thereby causing delamination. Traditional shell elements struggle to accurately capture the complex three-dimensional stress state near free edges, often underestimating interlayer stress peaks, leading to inaccurate damage prediction. Therefore, the free edge effect becomes a crucial validation for high-precision stress distribution in higher-order structural models.

A classical free-edge effect benchmark problem was proposed by Pagano [42]. The

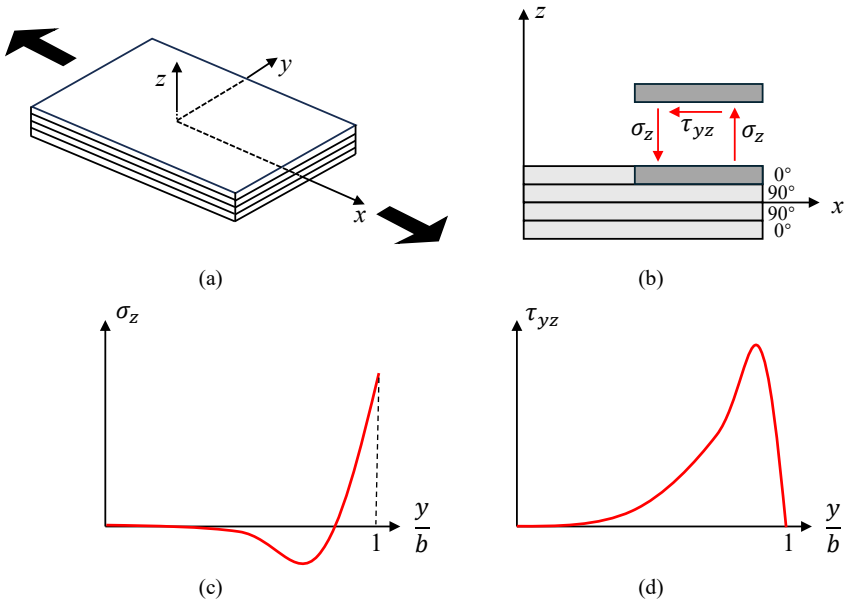

Figure 1.6: (a) Uniaxial extension (b) Boundary stress (c) Normal interlaminar stress distributions (d) Shear interlaminar stress distributions

model consists of a symmetric laminated composite plate with a stacking sequence of $[0/90]_s$, as shown in Figure 1.6, which is well known for exhibiting high interlaminar stresses near the free edge. The coordinate system (x, y, z) is defined as shown in the figure, with the origin located at the laminate mid-surface in the plane. The x-axis is along the length of the model, the y-axis is along the width of the model, and the z-axis is through-the-thickness direction of the model. The analysis of this case using classical laminate theory can only predict a stress state comprising the in-plane stresses. The interlaminar shear stresses σ_{xz} and σ_{yz}, as well as the interlaminar normal stress σ_z, can not be obtained from the classical laminate theory. The typical distributions of σ_z and σ_{xz} in the interface between the $0°$ and $90°$-layer are given in the lower part of Figure 1.6.

1.6. RESEARCH GOAL AND SCOPE

DUE to the problem of cohesive zone limitation, a large number of cohesive elements are used to accurately overcome the limitation, thus affecting computational efficiency. To address this issue, we aim to establish a composite delamination model that simultaneously meets the following requirements:

- It does not suffer from the cohesive zone limit on mesh density;
- It works in 3D space;
- It does not require artificial reduction of strengths;

- It does not require a pre-crack and the self-similar propagation assumption; and
- It can model delamination along multiple interfaces.

Based on the proposed structural-element model, a physically based formulation for the cohesive penalty stiffness is developed to enable accurate recovery of the three-dimensional stress field. The formulation derives the penalty stiffness directly from the material properties and thickness of the resin-rich layer rather than from the equivalent laminate thickness. As a result, the interlaminar stress components can be accurately recovered. The new structural-element-based three-dimensional model simultaneously meets the following requirements:

- It provides a physically based formulation for the penalty stiffness of structural cohesive elements;
- It retains the key advantage of the proposed formulation by eliminating the cohesive-zone mesh-density limitation in delamination analysis;
- It can accurately and efficiently recover the three-dimensional stress field in an arbitrary multi-ply composite laminate.

To extend the above penalty stiffness formulation from the layer-wise (LW) approach [46] to the equivalent single-layer (ESL) method [47], a new formulation is required. Unlike the LW approach, which models each layer individually using separate displacement fields to capture layer-wise deformation and interlaminar effects, the ESL method treats the multilayer composite model as an equivalent single layer with a unified displacement field, which reduces the number of degrees of freedom and computational cost [46]. The proposed formulation should provide an accurate penalty stiffness while satisfying the following requirements:

- It accounts for the through-thickness distributions of out-of-plane normal and transverse shear stresses;
- It incorporates the material properties and thickness of the resin-rich layer into the penalty stiffness formulation;
- It improves the mesh convergence and prediction accuracy of structural cohesive element models.

In conclusion, the overall objective of this thesis is to extend the structural cohesive element formulation to Kirchhoff–Love shell-element models and incorporate it with a physically based cohesive penalty stiffness formulation for efficient and accurate composite damage modelling.

1.7. THESIS OUTLINE

THIS thesis is organized to systematically achieve the research goals outlined in Section 1.6. The remainder of this thesis is organized as follows.

In Chapter 2, a new triangular shell element based on the Kirchhoff-Love hypothesis is developed to model interlaminar delamination. The proposed method is verified and validated against classical benchmark problems involving delamination in both unidirectional and multidirectional laminates. In addition, the geometric nonlinear extensions of the TUBA3 element and its limitations are also discussed in this chapter.

In Chapter 3, an accurate penalty stiffness is derived based on resin-rich layers of the composite material to enable accurate prediction of the out-of-plane stress distribution. The performance of this method is demonstrated through a series of uniaxial extension benchmark problems involving both cross-ply and angle-ply composite laminates.

In Chapter 4, the resin-rich layer-based penalty stiffness formulation extends from a layer-wise method to an equivalent single-layer method. The proposed method is validated and compared against the benchmark problems introduced in Chapter 2 using the mode-dependent cohesive law. Furthermore, the stress distribution at the crack tip in the DCB model is also analyzed.

Finally, Chapter 5 summarizes the main conclusions of the thesis and provides some suggestions for future work.

REFERENCES

1. Krueger, R. A summary of benchmark examples to assess the performance of quasi-static delamination propagation prediction capabilities in finite element codes. *Journal of Composite Materials* **49,** 3297–3316 (2015).
2. Kaddour, A., Hinton, M. J., Smith, P. A. & Li, S. Mechanical properties and details of composite laminates for the test cases used in the third world-wide failure exercise. *Journal of composite materials* **47,** 2427–2442 (2013).
4. Barenblatt, G. I. The mathematical theory of equilibrium cracks in brittle fracture. *Advances in applied mechanics* **7,** 55–129 (1962).
5. Dugdale, D. S. Yielding of steel sheets containing slits. *Journal of the Mechanics and Physics of Solids* **8,** 100–104 (1960).
6. Qiu, Y., Crisfield, M. A. & Alfano, G. An interface element formulation for the simulation of delamination with buckling. *Engineering Fracture Mechanics* **68,** 1755–1776 (2001).
7. Yang, Q. & Cox, B. Cohesive models for damage evolution in laminated composites. *International Journal of Fracture* **133,** 107–137 (2005).
8. Camanho, P. P. & Dávila, C. G. Mixed-mode decohesion finite elements for the simulation of delamination in composite materials. *NASA Technical Reports* **211737** (2002).
9. Moës, N. & Belytschko, T. Extended finite element method for cohesive crack growth. *Engineering fracture mechanics* **69,** 813–833 (2002).
10. Xu, X.-P. & Needleman, A. Void nucleation by inclusion debonding in a crystal matrix. *Modelling and Simulation in Materials Science and engineering* **1,** 111 (1993).
11. Turon, A., Davila, C. G., Camanho, P. P. & Costa, J. An engineering solution for mesh size effects in the simulation of delamination using cohesive zone models. *Engineering fracture mechanics* **74,** 1665–1682 (2007).

12. Pirondi, A., Giuliese, G., Moroni, F., Bernasconi, A. & Jamil, A. Comparative study of cohesive zone and virtual crack closure techniques for three-dimensional fatigue debonding. *The Journal of Adhesion* **90,** 457–481 (2014).
13. Chen, J., Crisfield, M., Kinloch, A., Busso, E. P., Matthews, F. L. & Qiu, Y. Predicting progressive delamination of composite material specimens via interface elements. *Mechanics of composite materials and structures* **6,** 301–317 (1999).
14. Rafiee, R. & Sotoudeh, S. A hysteresis cohesive approach for predicting mixed-mode delamination onset of composite laminates under cyclic loading: Part I, model development. *Composite Structures* **277,** 114667 (2021).
15. Rafiee, R. & Sotoudeh, S. A hysteresis cohesive approach for predicting mixed-mode delamination onset of composite laminates under cyclic loading: Part II, numerical and experimental analyses. *Composite Structures* **277,** 114668 (2021).
16. Falk, M. L., Needleman, A. & Rice, J. R. A critical evaluation of cohesive zone models of dynamic fracture. *Le Journal de Physique IV* **11,** Pr5–43 (2001).
17. Kubair, D. V. & Geubelle, P. H. Comparative analysis of extrinsic and intrinsic cohesive models of dynamic fracture. *International Journal of Solids and Structures* **40,** 3853–3868 (2003).
19. Pandolfi, A. & Ortiz, M. An efficient adaptive procedure for three-dimensional fragmentation simulations. *Engineering with computers* **18,** 148–159 (2002).
20. Mergheim, J., Kuhl, E. & Steinmann, P. A hybrid discontinuous Galerkin/interface method for the computational modelling of failure. *Communications in numerical methods in engineering* **20,** 511–519 (2004).
21. Lorentz, E. A mixed interface finite element for cohesive zone models. *Computer methods in applied mechanics and engineering* **198,** 302–317 (2008).
22. Harper, P. W. & Hallett, S. R. Cohesive zone length in numerical simulations of composite delamination. *Engineering Fracture Mechanics* **75,** 4774–4792 (2008).
23. Lu, X., Ridha, M., Chen, B., Tan, V. & Tay, T. On cohesive element parameters and delamination modelling. *Engineering Fracture Mechanics* **206,** 278–296 (2019).
24. Yang, Q., Fang, X., Shi, J. & Lua, J. An improved cohesive element for shell delamination analyses. *International journal for numerical methods in engineering* **83,** 611–641 (2010).
25. Do, B., Liu, W., Yang, Q. & Su, X. Improved cohesive stress integration schemes for cohesive zone elements. *Engineering Fracture Mechanics* **107,** 14–28 (2013).
26. Russo, R. & Chen, B. Overcoming the cohesive zone limit in composites delamination: modeling with slender structural elements and higher-order adaptive integration. *International Journal for Numerical Methods in Engineering* **121,** 5511–5545 (2020).
27. Guiamatsia, I., Ankersen, J., Davies, G. & Iannucci, L. Decohesion finite element with enriched basis functions for delamination. *Composites Science and Technology* **69,** 2616–2624 (2009).
28. Guiamatsia, I., Davies, G., Ankersen, J. & Iannucci, L. A framework for cohesive element enrichment. *Composite structures* **92,** 454–459 (2010).

29. Guiamatsia, I., Ankersen, J. & Iannucci, L. A study of mixed-mode composite delamination using enriched interface elements. *The Aeronautical Journal* **117,** 959–967 (2013).

30. Samimi, M., Van Dommelen, J. & Geers, M. An enriched cohesive zone model for delamination in brittle interfaces. *International journal for numerical methods in engineering* **80,** 609–630 (2009).

31. Samimi, M., Van Dommelen, J. & Geers, M. A self-adaptive finite element approach for simulation of mixed-mode delamination using cohesive zone models. *Engineering Fracture Mechanics* **78,** 2202–2219 (2011).

32. Samimi, M., Van Dommelen, J. & Geers, M. A three-dimensional self-adaptive cohesive zone model for interfacial delamination. *Computer Methods in Applied Mechanics and Engineering* **200,** 3540–3553 (2011).

33. Van der Meer, F., Moës, N. & Sluys, L. J. A level set model for delamination–Modeling crack growth without cohesive zone or stress singularity. *Engineering Fracture Mechanics* **79,** 191–212 (2012).

34. Lu, X., Chen, B.-Y., Tan, V. B. & Tay, T.-E. Adaptive floating node method for modelling cohesive fracture of composite materials. *Engineering Fracture Mechanics* **194,** 240–261 (2018).

35. Chen, B., Pinho, S., De Carvalho, N., Baiz, P. & Tay, T. A floating node method for the modelling of discontinuities in composites. *Engineering Fracture Mechanics* **127,** 104–134 (2014).

36. Álvarez, D., Blackman, B., Guild, F. & Kinloch, A. Mode I fracture in adhesively-bonded joints: A mesh-size independent modelling approach using cohesive elements. *Engineering Fracture Mechanics* **115,** 73–95 (2014).

37. Mukhopadhyay, S. & Bhatia, S. Accurate coarse mesh simulation of delamination in composites using a novel hp-adaptive cohesive element. *Journal of Composite Materials* **57,** 2201–2218 (2023).

38. Daniel, P. M., Främby, J., Fagerström, M. & Maimí, P. An efficient ERR-Cohesive method for the modelling of delamination propagation with large elements. *Composites Part A: Applied Science and Manufacturing* **167,** 107423 (2023).

39. Tosti Balducci, G. & Chen, B. Overcoming the cohesive zone limit in the modelling of composites delamination with TUBA cohesive elements. *arXiv preprint arXiv:2403.09895* (2024).

40. Bell, K. A refined triangular plate bending finite element. *International journal for numerical methods in engineering* **1,** 101–122 (1969).

41. Dávila, C. G., Camanho, P. P. & Turon, A. Effective simulation of delamination in aeronautical structures using shells and cohesive elements. *Journal of Aircraft* **45,** 663–672 (2008).

42. Pagano, N. Stress fields in composite laminates. *International Journal of Solids and Structures* **14,** 385–400 (1978).

43. Pipes, R. B. & Pagano, N. Interlaminar stresses in composite laminates under uniform axial extension. *Journal of composite materials* **4,** 538–548 (1970).

44. Kassapoglou, C. & Lagace, P. An efficient method for the calculation of interlaminar stresses in composite materials (1986).

45. Kassapoglou, C. & Lagace, P. A. Closed form solutions for the interlaminar stress field in angle-ply and cross-ply laminates. *Journal of Composite materials* **21,** 292–308 (1987).

46. Reddy, J. An evaluation of equivalent-single-layer and layerwise theories of composite laminates. *Composite structures* **25,** 21–35 (1993).

47. Abrate, S. & Di Sciuva, M. Equivalent single layer theories for composite and sandwich structures: A review. *Composite Structures* **179,** 482–494 (2017).

2

STRUCTURAL COHESIVE ELEMENT FOR THE MODELLING OF DELAMINATION

Delamination is a critical mode of failure that occurs between plies in a composite laminate. The cohesive element, developed based on the cohesive zone model, is widely used for modeling delamination. However, standard cohesive elements suffer from a well-known limit on the mesh density—the element size must be much smaller than the cohesive zone size. This work extends the line of research on structural *cohesive elements onto 3D mixed-mode problems. A new triangular Kirchhoff-Love shell element is developed for orthotropic materials to model the plies. A new* structural *cohesive element, conforming to the shell elements of the plies, is developed to model the interface delamination. The proposed method is verified and validated on the classical benchmark problems of Mode I, Mode II, and mixed-mode delamination of unidirectional laminates, a recent unidirectional benchmark problem with curved delamination front, as well as the single-leg bending problem of a multi-directional laminate, significantly increasing the range and complexity of applicable problems as compared to the previous works. All the results show that the element size in the proposed models can be ten times larger than that in the standard cohesive element models, with more than 90% reduction in CPU time, while retaining prediction accuracy. This would then allow more effective and efficient modeling of delamination in composites without worrying about the cohesive zone limit on the mesh density.*

Parts of this chapter have been published in X. Ai, B. Chen, C. Kassapoglou, Structural cohesive element for the modelling of delamination in composite laminates without the cohesive zone limit, Engineering Fracture Mechanics (2025) 111586.

2.1. INTRODUCTION

As discussed in Chapter 1, higher-order structural elements can overcome the cohesive zone limitation. Based on the earlier works [1, 2], the aim of this chapter is to develop a triangular Kirchhoff-Love shell element without curvature DoFs to model the composite plies, then formulate the conforming structural CE to be used between the plies to model their delamination. Although previous researchers [3, 4] have used shell elements and the corresponding CEs to simulate delamination, their focus was mainly on the use of shell elements per se and did not solve the problem of cohesive zone limitations on mesh density. The shell element in this work is based on a simple triangle Kirchhoff-Love plate element, the cubic displacement element proposed by Allman [5]. There are only three DoFs at each node, one for out-of-plane displacement and two for rotations. These DoFs are commonly used by engineers and are much easier to handle than the curvature ones when setting boundary conditions. Therefore, this article will extend this triangle plate element for the modeling of composite plies and develop the corresponding structural CE for the interfaces. If such a structural CE could overcome the cohesive zone limit on its mesh density, then it would achieve all the requirements listed above. Although this paper addresses objectives similar to those of previous studies [1, 2], it offers significant advantages over the preceding two works in the following aspects:

(1) The previous methods did not modify the underlying isotropic beam or previous cubic plate element for the plies, limiting the scope of the modelling to isotropic beam or plate bending problems. In contrast, this study firstly enriches the baseline cubic plate element to include in-plane degrees of freedom, thereby extending the plate element to a shell element. It then extends the supported material model from being isotropic to being suitable for composites. These developments are essential for the modelling of generic deformations of composite shell structures.

(2) The previous methods are applicable to 2D mixed-mode [1] or 3D mode-I [2] problems. This study extends the structural CE method to be applicable for 3D mixed-mode problems, thereby enabling the modelling of more general and more complex problems beyond the plane-strain delamination problems of the standard test coupons;

(3) The baseline plate element employed in this study features a reduced number of degrees of freedom compared to the TUBA3 element in the previous 3D work [2]. As a result, the implementation of the method is simpler and the application of boundary conditions more direct than in the case of the TUBA3 elements. These advantages will make simulations more efficient when dealing with large-scale and complex models with complex boundary conditions.

(4) Furthermore, this study verifies the method on fully 3D problems with complex stacking sequences and crack fronts. This is a significant improvement over the earlier work in terms of the complexity and scope of the verification.

It should be noted that the TUBA3 plate element has been extended by the author to account for geometric nonlinearity, and additional membrane degrees of freedom have been incorporated to formulate an enhanced shell element. Detailed derivations and implementation procedures are provided in Appendix E to this chapter.

2.2. METHOD

2.2.1. OVERALL ILLUSTRATION

THE overall idea of the proposed modelling approach is to represent the composite plies by Kirchhoff–Love shell elements and the interfaces by structural CEs. Figure 1.4 shows the geometrical comparison between the conventional modelling approach with solid elements and the proposed structural approach with shells. Looking at the structural CE, the difference from the conventional CE is that the nodes of the CE are placed at the mid-plane of the two shell elements, which are not the actual surfaces of the cohesive interface. Hence, the opening of the actual interface does not equate to the distance between the upper nodes and lower ones of the structural CE. This opening shall be calculated using the shell kinematics to be detailed in later subsections. The rest of this section will firstly present the cubic plate element formulation by Allman [5] and its adaptation for flat composite shells, then move on to derive the structural CE formulation.

2.2.2. CUBIC PLATE ELEMENT

GEOMETRIC DEFINITIONS OF THE PLATE ELEMENT

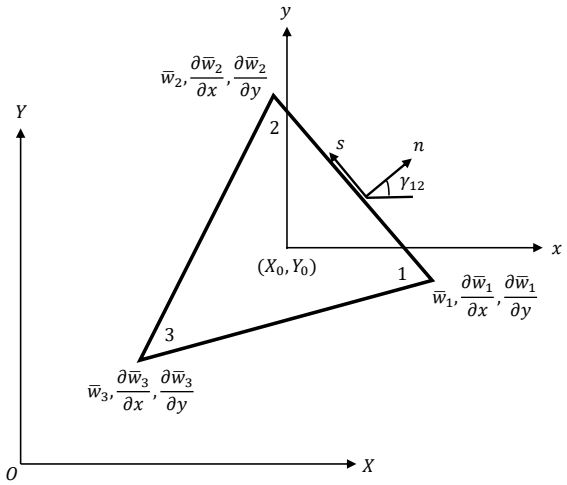

Figure 2.1: Coordinate system and DoFs for the triangular cubic plate element [5]

THE plate part of the shell element in this work is based on the triangular cubic plate element developed by Allman [5], as shown in Figure 2.1. A local coordinate system is used in this element, with origin at the centroid of the triangular element. The local axes are represented by lowercase letters, x and y, to distinguish them from the global ones, X and Y. The area of this triangular element is A. s is the anti-clockwise coordinate along the element boundary. n is the exterior normal. The angle between the normal n and the local axis x is γ. The out-of-plane displacement defined over the domain is $w(x, y)$. An independent out-of-plane boundary displacement, $\overline{w}(s)$, and its compatible normal deriva-

tive, $\partial\overline{w}/\partial n(s)$, are assumed along the boundary ∂A. The DoFs at each node include the displacement $\overline{w}$ and two rotations $\partial\overline{w}/\partial x$, $\partial\overline{w}/\partial y$.

The cubic plate element in Allman's work only considered the case of isotropic material [5]. This work extends the cubic plate element using the classical laminate theory, such that symmetric composite laminates can also be modelled by this plate element. The original cubic element formulation will be presented in detail, with adaptations for composites specified along the way.

MODIFIED POTENTIAL ENERGY FOR THE PLATE ELEMENT

The minimum potential energy principle is used to derive the finite element formulation of the triangular plate element. The potential energy used is referred to as the modified potential energy in Allman's work [5]: [5]:

$$\pi = \iint_A U_0 \mathrm{d}x\mathrm{d}y + \sum_{N=1}^{3} R_N(\overline{w}_N - w_N) + \int_{\partial A} V_n(\overline{w} - w)\,\mathrm{d}s$$
$$- \int_{\partial A} M_n(\frac{\partial\overline{w}}{\partial n} - \frac{\partial w}{\partial n})\mathrm{d}s - \iint_A p^* w \mathrm{d}x\mathrm{d}y - \sum_{N=1}^{3} R_N^* \overline{w}_N$$
$$- \int_{\partial A} V_n^* \overline{w}\mathrm{d}s + \int_{\partial A} M_n^* \frac{\partial\overline{w}}{\partial n}\,\mathrm{d}s \tag{2.1}$$

where U_0 is the strain energy density. M_n is the normal bending moment resultant and V_n is the Kirchhoff shear force distribution on the element boundary, respectively. $R_{N\,(N=1,2,3)}$ are the concentrated forces at the element vertices. In addition, R_N^*, V_n^*, and M_n^* are the values of prescribed concentrated force, Kirchhoff shear force, and normal bending moment resultant, respectively. $p^*(x, y)$ denotes the prescribed distributed pressure load on the element. This potential energy essentially uses R_N, V_n, and M_n as Lagrange multipliers to enforce the compatibility between the two fields w and $\overline{w}$ and their normal derivatives along the boundary. The variational principle based on this modified potential energy satisfies the equilibrium equations, the boundary conditions, and the compatibility requirement between w and $\overline{w}$ [5].

The expression of U_0 for composites will be different from that for isotropic materials in Allman's work [5]. The classical laminate theory can be used to describe the constitutive relationship of a composite laminate under Kirchhoff-Love kinematic assumptions. For the case of a symmetric laminate (the smallest of which would be a single composite ply) considered in this work, there would be no membrane-bending coupling. Therefore, the expressions of the moments are:

$$M_x = -D_{11}\frac{\partial^2 w}{\partial x^2} - D_{12}\frac{\partial^2 w}{\partial y^2} - 2D_{16}\frac{\partial^2 w}{\partial x \partial y}$$
$$M_y = -D_{12}\frac{\partial^2 w}{\partial x^2} - D_{22}\frac{\partial^2 w}{\partial y^2} - 2D_{26}\frac{\partial^2 w}{\partial x \partial y}$$
$$M_{xy} = -D_{16}\frac{\partial^2 w}{\partial x^2} - D_{26}\frac{\partial^2 w}{\partial y^2} - 2D_{66}\frac{\partial^2 w}{\partial x \partial y} \tag{2.2}$$

Using the above moment-curvature relations (Equation 2.2), the strain energy density U_0 can be written as:

$$U_0 = \frac{1}{2}\left[D_{11}\left(\frac{\partial^2 w}{\partial x^2}\right)^2 + D_{22}\left(\frac{\partial^2 w}{\partial y^2}\right)^2 + 2D_{12}\frac{\partial^2 w}{\partial x^2}\frac{\partial^2 w}{\partial y^2} + 4D_{16}\frac{\partial^2 w}{\partial x^2}\frac{\partial^2 w}{\partial x \partial y} + 4D_{26}\frac{\partial^2 w}{\partial y^2}\frac{\partial^2 w}{\partial x \partial y} + 4D_{66}\left(\frac{\partial^2 w}{\partial x \partial y}\right)^2\right] \tag{2.3}$$

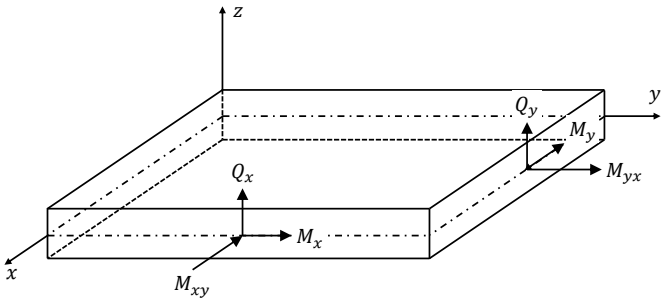

Figure 2.2: Sign conventions for shear force and bending moment resultants

The sign conventions for the shear force and bending moment resultants are shown in Figure 2.2. For the triangular plate element, the normal bending moment resultant M_n, Kirchhoff shear force distribution V_n and concentrated forces $R_{N\,(N=1,2,3)}$ can be expressed as [5]:

$$M_n = M_x \cos^2\gamma + M_y \sin^2\gamma + M_{xy}\sin 2\gamma \tag{2.4}$$

$$V_n = Q_n + \frac{\partial M_{ns}}{\partial s} \tag{2.5}$$

$$R_N = [M_{ns}]_{s^-}^{s^+} \tag{2.6}$$

where

$$M_{ns} = \frac{1}{2}(M_y - M_x)\sin 2\gamma + M_{xy}\cos 2\gamma \tag{2.7}$$

$$Q_n = \frac{\partial M_n}{\partial n} + \frac{\partial M_{ns}}{\partial s} \tag{2.8}$$

In this element, linear variation of the normal bending moment resultant and constant Kirchhoff shear force distribution are assumed along the edges:

$$M_n = M_n^{12}(1-\xi) + M_n^{21}\xi \tag{2.9}$$

$$V_n = V_n^{12} \tag{2.10}$$

where M_n^{12} and M_n^{21} are the normal bending moment resultant values at node 1 and node 2 of side 1-2 respectively. The coefficient ξ in Equation 2.9 is defined as $\xi = s/l_{12}$. V_n^{12} is the value of the Kirchhoff shear force distribution along the side 1-2. The cyclic permutation of superscripts 1, 2, and 3 in Equations 2.9 and 2.10 produces the shear force distribution and moment resultant on the other two sides (side 2-3 and side 3-1) of the triangular element.

The terms in brackets in Equation 2.6 represent the difference in bending moment resultant values at the element vertices. Therefore, the expressions of $R_{N\,(N=1,2,3)}$ are:

$$\begin{aligned} R_1 &= M_{ns}^{12} - M_{ns}^{13} \\ R_2 &= M_{ns}^{23} - M_{ns}^{21} \\ R_3 &= M_{ns}^{31} - M_{ns}^{32} \end{aligned} \tag{2.11}$$

Finally, the directional derivatives in equations 2.8 are given by:

$$\begin{aligned} \frac{\partial}{\partial s} &= -\sin\gamma \frac{\partial}{\partial x} + \cos\gamma \frac{\partial}{\partial y} \\ \frac{\partial}{\partial n} &= \cos\gamma \frac{\partial}{\partial x} + \sin\gamma \frac{\partial}{\partial y} \end{aligned} \tag{2.12}$$

FINITE ELEMENT APPROXIMATION AND THE DISCRETIZED EQUILIBRIUM EQUATION

For finite element implementation, the potential energy π should be discretized. In this element, the internal out-of-plane displacement field $w(x, y)$ is approximated by a cubic polynomial:

$$\begin{aligned} w(x,y) = A_1 + A_2\,x + A_3\,y + \alpha_1\,x^2 + \alpha_2\,xy + \alpha_3\,y^2 \\ +\alpha_4\,x^3 + \alpha_5\,x^2y + \alpha_6\,xy^2 + \alpha_7\,y^3 \end{aligned} \tag{2.13}$$

The three coefficients A_1, A_2, and A_3 represent the rigid body motion and do not affect the value of the strain energy density.

With the above choice of w, applying Green's theorem [6] to transform the strain energy integral to a boundary integral gives:

$$2\iint_A U_0\,\mathrm{d}x\mathrm{d}y = \sum_{N=1}^{3} R_N w_N + \int_{\partial A} V_n w\,\mathrm{d}s - \int_{\partial A} M_n \frac{\partial w}{\partial n}\,\mathrm{d}s \tag{2.14}$$

In this work, we assume that there is no distributed pressure load $p^*(x, y)$. Then, the modified potential energy (Equation 2.1) can be rewritten more simply as:

$$\begin{aligned} \pi = -\iint_A U_0\,\mathrm{d}x\mathrm{d}y + \sum_{N=1}^{3} R_N \overline{w}_N + \int_{\partial A} V_n \overline{w}\,\mathrm{d}s - \int_{\partial A} M_n \frac{\partial \overline{w}}{\partial n}\,\mathrm{d}s \\ - \sum_{N=1}^{3} R_N^* \overline{w}_N - \int_{\partial A} V_n^* \overline{w}\,\mathrm{d}s + \int_{\partial A} M_n^* \frac{\partial \overline{w}}{\partial n}\,\mathrm{d}s \end{aligned} \tag{2.15}$$

Substituting Equation 2.13 into Equation 2.3, the strain energy can be rewritten as:

$$\iint_A U_0 \,\mathrm{d}x\mathrm{d}y = \frac{1}{2}\boldsymbol{\alpha}^{\mathrm{T}}\,\mathbf{H}\,\boldsymbol{\alpha} \tag{2.16}$$

where the vector $\boldsymbol{\alpha}$ is:

$$\boldsymbol{\alpha} = \{\alpha_1,\, \alpha_2,\, \alpha_3,\, \alpha_4,\, \alpha_5,\, \alpha_6,\, \alpha_7\}^{\mathrm{T}} \tag{2.17}$$

The matrix $\mathbf{H}$ is more complicated to derive for symmetric composite laminates than for isotropic materials considered in Reference [5]. Its detailed derivation is presented in Appendix A.

After the strain energy, the 2nd, 3rd and 4th terms in Equation 2.15 denote the work of the so-called generalized forces:

$$\sum_{N=1}^{3} R_N \overline{w}_N + \int_{\partial A} V_n \overline{w}\,\mathrm{d}s - \int_{\partial A} M_n \frac{\partial \overline{w}}{\partial n}\,\mathrm{d}s = \mathbf{Q}^{\mathrm{T}}\mathbf{q} \tag{2.18}$$

where $\mathbf{Q}$ is the vector of the twelve generalized forces:

$$\mathbf{Q} = \{R_1, R_2, R_3, V_n^{12}, V_n^{23}, V_n^{31}, M_n^{12}, M_n^{21}, M_n^{23}, M_n^{32}, M_n^{31}, M_n^{13}\}^{\mathrm{T}} \tag{2.19}$$

Substituting Equations 2.9 and 2.10 into Equation 2.18, the generalized displacements corresponding to the generalized forces in Equation 2.19 compose the vector $\mathbf{q}$:

$$\begin{aligned}\mathbf{q} = \Bigg\{ & \overline{w}_1,\, \overline{w}_2,\, \overline{w}_3,\, l_{12}\int_0^1 \overline{w}\,\mathrm{d}\xi,\, l_{23}\int_0^1 \overline{w}\,\mathrm{d}\xi,\, l_{31}\int_0^1 \overline{w}\,\mathrm{d}\xi, \\ & -l_{12}\int_0^1 \frac{\partial \overline{w}}{\partial n}(1-\xi)\,\mathrm{d}\xi,\, -l_{12}\int_0^1 \frac{\partial \overline{w}}{\partial n}\xi\,\mathrm{d}\xi,\, -l_{23}\int_0^1 \frac{\partial \overline{w}}{\partial n}(1-\xi)\,\mathrm{d}\xi, \\ & -l_{23}\int_0^1 \frac{\partial \overline{w}}{\partial n}\xi\,\mathrm{d}\xi,\, -l_{31}\int_0^1 \frac{\partial \overline{w}}{\partial n}(1-\xi)\,\mathrm{d}\xi,\, -l_{31}\int_0^1 \frac{\partial \overline{w}}{\partial n}\xi\,\mathrm{d}\xi \Bigg\}^{\mathrm{T}}\end{aligned} \tag{2.20}$$

A matrix $\mathbf{B}$ can be constructed to connect the vector $\mathbf{Q}$ and the vector $\boldsymbol{\alpha}$:

$$\mathbf{Q} = \mathbf{B}^{\mathrm{T}}\boldsymbol{\alpha} \tag{2.21}$$

With the moment-curvature relationship for composites in Equation 2.2 and the expression of w in Equation 2.13, the matrix $\mathbf{B}$ has been derived for composites in this work. The details are shown in Appendix B.

A matrix $\mathbf{T}$ can be defined to represent the relationship between the nodal DoFs $\overline{\mathbf{W}}$ and the vector $\mathbf{q}$:

$$\mathbf{q} = \mathbf{T}\overline{\mathbf{W}} \tag{2.22}$$

where $\overline{\mathbf{W}}$ is the vector of the nodal DoFs defined by

$$\overline{\mathbf{W}} = \left\{ \overline{w}_1, \frac{\partial \overline{w}_1}{\partial x}, \frac{\partial \overline{w}_1}{\partial y}, \overline{w}_2, \frac{\partial \overline{w}_2}{\partial x}, \frac{\partial \overline{w}_3}{\partial y}, \overline{w}_3, \frac{\partial \overline{w}_3}{\partial x}, \frac{\partial \overline{w}_3}{\partial y} \right\}^{\mathrm{T}} \tag{2.23}$$

With the assumptions of cubic line function for $\overline{w}$ and linear variation for $\partial\overline{w}/\partial n$ along each edge of the element, the $\mathbf{T}$ matrix can be derived as [5]:

$$\begin{bmatrix}
1 & 0 & 0 & 0 & 0 & 0 & 0 & 0 & 0 \\
0 & 0 & 0 & 1 & 0 & 0 & 0 & 0 & 0 \\
0 & 0 & 0 & 0 & 0 & 0 & 1 & 0 & 0 \\
\frac{l_{12}}{2} & -\frac{l_{12}^2}{12}\sin\gamma_{12} & \frac{l_{12}^2}{12}\cos\gamma_{12} & \frac{l_{12}}{2} & \frac{l_{12}^2}{12}\sin\gamma_{12} & -\frac{l_{12}^2}{12}\cos\gamma_{12} & 0 & 0 & 0 \\
0 & 0 & 0 & \frac{l_{23}}{2} & -\frac{l_{23}^2}{12}\sin\gamma_{23} & \frac{l_{23}^2}{12}\cos\gamma_{23} & \frac{l_{23}}{2} & \frac{l_{23}^2}{12}\sin\gamma_{23} & -\frac{l_{23}^2}{12}\cos\gamma_{23} \\
\frac{l_{31}}{2} & \frac{l_{31}^2}{12}\sin\gamma_{31} & -\frac{l_{31}^2}{12}\cos\gamma_{31} & 0 & 0 & 0 & \frac{l_{31}}{2} & -\frac{l_{31}^2}{12}\sin\gamma_{31} & \frac{l_{31}^2}{12}\cos\gamma_{31} \\
0 & -\frac{l_{12}}{3}\cos\gamma_{12} & -\frac{l_{12}}{3}\sin\gamma_{12} & 0 & -\frac{l_{12}}{6}\cos\gamma_{12} & -\frac{l_{12}}{6}\sin\gamma_{12} & 0 & 0 & 0 \\
0 & -\frac{l_{12}}{6}\cos\gamma_{12} & -\frac{l_{12}}{6}\sin\gamma_{12} & 0 & -\frac{l_{12}}{3}\cos\gamma_{12} & -\frac{l_{12}}{3}\sin\gamma_{12} & 0 & 0 & 0 \\
0 & 0 & 0 & 0 & -\frac{l_{23}}{3}\cos\gamma_{23} & -\frac{l_{23}}{3}\sin\gamma_{23} & 0 & -\frac{l_{23}}{6}\cos\gamma_{23} & -\frac{l_{23}}{6}\sin\gamma_{23} \\
0 & 0 & 0 & 0 & -\frac{l_{23}}{6}\cos\gamma_{23} & -\frac{l_{23}}{6}\sin\gamma_{23} & 0 & -\frac{l_{23}}{3}\cos\gamma_{23} & -\frac{l_{23}}{3}\sin\gamma_{23} \\
0 & -\frac{l_{31}}{6}\cos\gamma_{31} & -\frac{l_{31}}{6}\sin\gamma_{31} & 0 & 0 & 0 & 0 & -\frac{l_{31}}{3}\cos\gamma_{31} & -\frac{l_{31}}{3}\sin\gamma_{31} \\
0 & -\frac{l_{31}}{3}\cos\gamma_{31} & -\frac{l_{31}}{3}\sin\gamma_{31} & 0 & 0 & 0 & 0 & -\frac{l_{31}}{6}\cos\gamma_{31} & -\frac{l_{31}}{6}\sin\gamma_{31}
\end{bmatrix} \tag{2.24}$$

STIFFNESS MATRIX AND FORCE VECTORS OF CUBIC PLATE ELEMENT

Substituting Equations 2.16, 2.21 and 2.22 into Equation 2.15, the total modified potential energy represented by the finite element method under prescribed boundary loads is:

$$\pi = -\frac{1}{2}\boldsymbol{\alpha}^{\mathrm{T}}\mathbf{H}\boldsymbol{\alpha} + \boldsymbol{\alpha}^{\mathrm{T}}(\mathbf{BT})\overline{\mathbf{W}} - \mathbf{Q}^{*\mathrm{T}}\mathbf{T}\overline{\mathbf{W}} \tag{2.25}$$

where the vector $\mathbf{Q}^*$, whose components are obtained by replacing the generalized forces in vector $\mathbf{Q}$ with the corresponding prescribed quantities, denotes all the external forces:

$$\begin{aligned}\mathbf{Q}^* = \{&R_1^*, R_2^*, R_3^*, V_n^{*12}, V_n^{*23}, V_n^{*31}, \\ &M_n^{*12}, M_n^{*21}, M_n^{*23}, M_n^{*32}, M_n^{*31}, M_n^{*13}\}^{\mathrm{T}}\end{aligned} \tag{2.26}$$

Thus, the internal work U and the external work W of the potential energy can be expressed as:

$$U = -\frac{1}{2}\boldsymbol{\alpha}^{\mathrm{T}}\mathbf{H}\boldsymbol{\alpha} + \boldsymbol{\alpha}^{\mathrm{T}}(\mathbf{BT})\overline{\mathbf{W}} \tag{2.27}$$

$$W = \mathbf{Q}^{*\mathrm{T}}\mathbf{T}\overline{\mathbf{W}} \tag{2.28}$$

Based on Equation 2.25, the minimum total potential energy principle gives:

$$\delta\pi = \delta\boldsymbol{\alpha}^{\mathrm{T}}[(\mathbf{BT})\overline{\mathbf{W}} - \mathbf{H}\boldsymbol{\alpha}] + \delta\overline{\mathbf{W}}^{\mathrm{T}}[(\mathbf{BT})^{\mathrm{T}}\boldsymbol{\alpha} - \mathbf{T}^{\mathrm{T}}\mathbf{Q}^*] = 0 \tag{2.29}$$

Setting the coefficient of the arbitrary variation $\delta\boldsymbol{\alpha}^{\mathrm{T}}$ to zero gives:

$$\boldsymbol{\alpha} = \mathbf{H}^{-1}(\mathbf{BT})\overline{\mathbf{W}} \tag{2.30}$$

Performing the variation of U as expressed in 2.27 with $\boldsymbol{\alpha}$ substituted by Equation 2.30, we arrive at δU for the element as:

$$\delta U = \delta\overline{\mathbf{W}}^{\mathrm{T}}(\mathbf{BT})^{\mathrm{T}}\mathbf{H}^{-1}(\mathbf{BT})\overline{\mathbf{W}} = \delta\overline{\mathbf{W}}^{\mathrm{T}}\mathbf{f}_{\mathrm{int}} \tag{2.31}$$

where $\mathbf{f}_{\mathrm{int}}$ is the internal force vector of the plate element:

$$\mathbf{f}_{\mathrm{int}} = (\mathbf{BT})^{\mathrm{T}}\mathbf{H}^{-1}(\mathbf{BT})\,\overline{\mathbf{W}} = \mathbf{K}_{\mathrm{plate}}\,\overline{\mathbf{W}} \tag{2.32}$$

and $\mathbf{K}_{\mathrm{plate}}$ is the stiffness matrix of the plate element:

$$\mathbf{K}_{\mathrm{plate}} = (\mathbf{BT})^{\mathrm{T}}\mathbf{H}^{-1}(\mathbf{BT}) \tag{2.33}$$

The variation of the external work W gives the external force vector of the element in the absence of distributed pressure load:

$$\delta W = \delta\overline{\mathbf{W}}\,\mathbf{T}^{\mathrm{T}}\mathbf{Q}^{*} = \delta\overline{\mathbf{W}}\,\mathbf{f}_{\mathrm{ext}}, \quad \Rightarrow \quad \mathbf{f}_{\mathrm{ext}} = \mathbf{T}^{\mathrm{T}}\mathbf{Q}^{*} \tag{2.34}$$

2.2.3. FORMATION OF SHELL ELEMENT

To form a flat shell element that considers membrane deformation and bending, we superimpose a linear membrane element on top of the plate element developed in the previous section. The displacement fields u, v are defined in terms of area coordinates L_1, L_2, L_3:

$$u = u_1L_1 + u_2L_2 + u_3L_3 \tag{2.35}$$

$$v = v_1L_1 + v_2L_2 + v_3L_3 \tag{2.36}$$

where u_i and v_i represent the displacements along x and y for node i, respectively. The DoFs vector of the membrane element $\overline{\mathbf{U}}$ is:

$$\overline{\mathbf{U}} = \{u_1,\, v_1,\, u_2,\, v_2,\, u_3,\, v_3\}^{\mathrm{T}} \tag{2.37}$$

The stiffness matrix of the triangular membrane element is given by the expression:

$$\mathbf{K}_{\mathrm{mem}} = \iint_{\Delta} \mathbf{B}_{\mathrm{mem}}^{\mathrm{T}}\,\mathbf{D}_{\mathrm{mem}}\,\mathbf{B}_{\mathrm{mem}}\,t\,\mathrm{d}x\,\mathrm{d}y \tag{2.38}$$

where t is the thickness of the membrane element and $\mathbf{B}_{\mathrm{mem}}$ matrix in Equation 2.38 is

$$\mathbf{B}_{\mathrm{mem}} = \frac{1}{2A}\begin{bmatrix} b_1 & 0 & b_2 & 0 & b_3 & 0 \\ 0 & c_1 & 0 & c_2 & 0 & c_3 \\ c_1 & b_1 & c_2 & b_2 & c_3 & b_3 \end{bmatrix} \tag{2.39}$$

A is the area of the membrane element and:

$$b_1 = y_2 - y_3, \quad b_2 = y_3 - y_1, \quad b_3 = y_1 - y_2 \tag{2.40}$$

$$c_1 = x_3 - x_2, \quad c_2 = x_1 - x_3, \quad c_3 = x_2 - x_1 \tag{2.41}$$

The $\mathbf{D}^{\text{mem}}$ matrix in Equation 2.38 is:

$$\mathbf{D}_{\text{mem}} = \begin{bmatrix} \frac{E_1}{1-\nu_{12}\nu_{21}} & \frac{\nu_{12}E_2}{1-\nu_{12}\nu_{21}} & 0 \\ & \frac{E_2}{1-\nu_{12}\nu_{21}} & 0 \\ \text{symmetric} & & G_{12} \end{bmatrix} \tag{2.42}$$

From Equations 2.33 and 2.38, we have obtained the stiffness matrices of the plate and membrane elements, respectively. They are assembled to form the stiffness matrix of the shell element:

$$\mathbf{K}_{\text{shell}} = \begin{bmatrix} \mathbf{K}_{\text{mem}} & 0 \\ 0 & \mathbf{K}_{\text{plate}} \end{bmatrix} \tag{2.43}$$

The corresponding DoF vector of the shell element is simply:

$$\begin{aligned} \mathbf{q}_{\text{shell}} &= \left\{ \overline{\mathbf{U}}, \overline{\mathbf{W}} \right\} \\ &= \left\{ u_1, v_1, u_2, v_2, u_3, v_3, w_1, \frac{\partial \overline{w}_1}{\partial x}, \frac{\partial \overline{w}_1}{\partial y}, \overline{w}_2, \frac{\partial \overline{w}_2}{\partial x}, \frac{\partial \overline{w}_3}{\partial y}, \overline{w}_3, \frac{\partial \overline{w}_3}{\partial x}, \frac{\partial \overline{w}_3}{\partial y} \right\}^{\text{T}} \end{aligned} \tag{2.44}$$

The contribution of the shell element to the overall force residual of the finite element system equation is $\mathbf{f}_{\text{ext}} - \mathbf{f}_{\text{int}}$. When the applied loads are nodal forces, $\mathbf{f}_{\text{ext}}$ does not need to be calculated explicitly in the element subroutine as the nodal forces can be directly entered in the global external force vector of the system. In this case, the residual contribution of this element can be expressed as:

$$\mathbf{f}_{\text{res}} = -\mathbf{f}_{\text{int}} = -\mathbf{K}_{\text{shell}}\, \mathbf{q}_{\text{shell}} \tag{2.45}$$

2.2.4. STRUCTURAL CE BETWEEN TWO PLIES

DOFS AND OPENING VECTOR

THE structural CEs must be compatible with the top and bottom shell elements kinematically. Thus, they need to share the same DoFs and displacement interpolations along the interface. The DoF vector of the CE can be defined as:

$$\mathbf{q}_{\text{CE}} = \left[\overline{\mathbf{U}}_{\text{bot}}^{\text{T}}, \overline{\mathbf{W}}_{\text{bot}}^{\text{T}}, \overline{\mathbf{U}}_{\text{top}}^{\text{T}}, \overline{\mathbf{W}}_{\text{top}}^{\text{T}} \right]^{\text{T}} \tag{2.46}$$

where $\overline{\mathbf{U}}_{\text{bot/top}}, \overline{\mathbf{W}}_{\text{bot/top}}$ are the membrane and plate DoFs of the bottom/top ply, respectively.

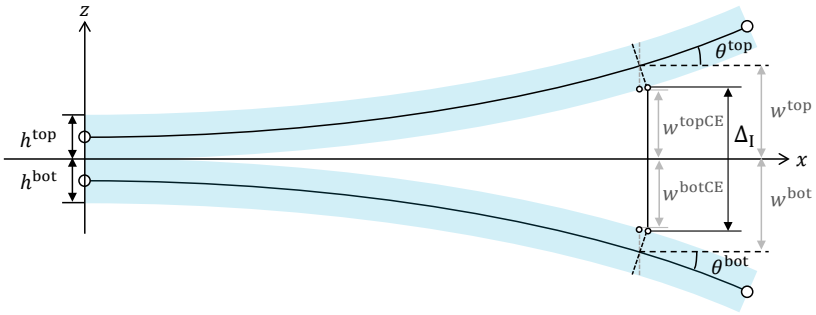

Figure 2.3: Mode I opening

The Mode I opening displacement of the CE can be expressed as

$$\Delta_{\mathrm{I}} = w^{\mathrm{topCE}} - w^{\mathrm{botCE}} \tag{2.47}$$

where w^{topCE} and w^{botCE} are the vertical displacements of the top and bottom CE surfaces, respectively. From Figure 2.3, using classical plate theory, we have:

$$w^{\mathrm{topCE}} = w^{\mathrm{top}} + \frac{h^{\mathrm{top}}}{2}(1 - \cos\theta^{\mathrm{top}}) \tag{2.48}$$

$$w^{\mathrm{botCE}} = w^{\mathrm{bot}} - \frac{h^{\mathrm{bot}}}{2}(1 - \cos\theta^{\mathrm{bot}}) \tag{2.49}$$

h^{top} and h^{bot} are the thickness of top and bottom plies, respectively. w^{top} and w^{bot} are the vertical displacements of the neutral planes of top and bottom plies, respectively. In this work, only geometrical linearity is considered. Thus, the rotations are small such that $1 - \cos\theta \approx 0$. The mode I opening is then simply the relative displacement between the mid-planes of the plies:

$$\Delta_{\mathrm{I}} = w^{\mathrm{top}} - w^{\mathrm{bot}} \tag{2.50}$$

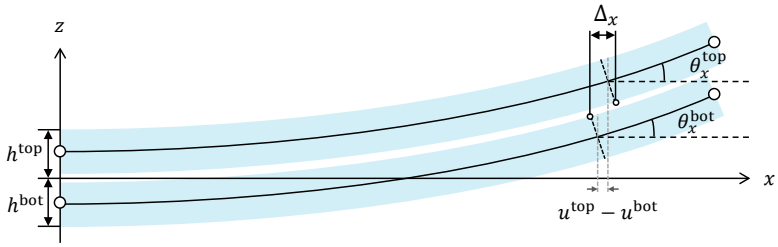

Figure 2.4: Mode II opening

The Mode II opening of the CE shown in Figure 2.4 can be expressed as:

$$\Delta_x = u^{\text{topCE}} - u^{\text{botCE}} \tag{2.51}$$

where u^{topCE} and u^{botCE} are the displacements along the x-axis of the top and bottom CE surfaces, respectively. Considering the rotations of the shells' neutral planes and the offsets of shell surfaces from the neutral planes, they can be written as:

$$u^{\text{topCE}} = u^{\text{top}} + \frac{h^{\text{top}}}{2} \sin\theta_x^{\text{top}} \tag{2.52}$$

$$u^{\text{botCE}} = u^{\text{bot}} - \frac{h^{\text{bot}}}{2} \sin\theta_x^{\text{bot}} \tag{2.53}$$

where u^{top}, u^{bot} are the displacement u of the neutral planes of the top and bottom shells, respectively. For a small rotation θ in geometrically linear problems, $\sin\theta \approx \theta$. Then, the shear opening along x is:

$$\Delta_x = u^{\text{top}} - u^{\text{bot}} + \frac{h^{\text{top}}}{2}\theta_x^{\text{top}} + \frac{h^{\text{bot}}}{2}\theta_x^{\text{bot}} \tag{2.54}$$

The shear opening along y is found from analogous kinematics in the yz-plane. Hence:

$$\Delta_y = v^{\text{top}} - v^{\text{bot}} + \frac{h^{\text{top}}}{2}\theta_y^{\text{top}} + \frac{h^{\text{bot}}}{2}\theta_y^{\text{bot}} \tag{2.55}$$

The central task of CE formulation is to find the matrix, $\mathbf{B}_{\text{CE}}$, that relates the opening vector to its nodal DoFs:

$$\boldsymbol{\Delta} = [\Delta_{\text{I}}, \Delta_x, \Delta_y]^{\text{T}} = \mathbf{B}_{\text{CE}}\, \mathbf{q}_{\text{CE}} \tag{2.56}$$

Examining the expressions of $\Delta_{\text{I}}, \Delta_{\text{II}}, \Delta_{\text{III}}$ in Equations 2.50, 2.54, and 2.55, we can see that the $\mathbf{B}_{\text{CE}}$ matrix shall be composed of sub-matrices that relate the following terms to the nodal DoFs in $\mathbf{q}_{\text{CE}}$:

$$w^{\text{top}},\ w^{\text{bot}},\ u^{\text{top}},\ u^{\text{bot}},\ v^{\text{top}},\ v^{\text{bot}},\ \theta_x^{\text{top}},\ \theta_x^{\text{bot}},\ \theta_y^{\text{top}},\ \theta_y^{\text{bot}} \tag{2.57}$$

In Equation 2.35, the in-plane displacements u and v are already expressed in the nodal membrane DoFs. However, the out-of-plane displacements w and the rotations θ in the above list remain to be explicitly expressed in terms of nodal DoFs in $\mathbf{q}_{\text{CE}}$.

SHAPE FUNCTIONS OF w

The displacement w shall be expressed in terms of plate DoFs $\overline{\mathbf{W}}$ in this section. Referring back to Equation 2.13, the displacement w is defined in the local Cartesian coordinates (x and y) by the coefficients A_i and the vector $\boldsymbol{\alpha}$. The expression of w is then divided into two parts. The first part only contains A_i, and the second part only contains α_j:

$$w = w_A + w_\alpha \tag{2.58}$$

where

$$w_A = A_1 + A_2\,x + A_3\,y \tag{2.59}$$

$$w_\alpha = \alpha_1\,x^2 + \alpha_2\,xy + \alpha_3\,y^2 + \alpha_4\,x^3 + \alpha_5\,x^2y + \alpha_6\,xy^2 + \alpha_7\,y^3 \tag{2.60}$$

w_A can be rewritten as:

$$w_A = \mathbf{S}^{\mathrm{T}}\,\mathbf{A}, \quad \mathbf{S} = [1,\,x,\,y]^{\mathrm{T}},\ \mathbf{A} = [A_1,\,A_2,\,A_3]^{\mathrm{T}} \tag{2.61}$$

Similarly, w_α can be rewritten as:

$$w_\alpha = \mathbf{R}^{\mathrm{T}}\,\boldsymbol{\alpha}, \quad \mathbf{R} = [x^2,\,xy,\,y^2,\,x^3,\,x^2y,\,xy^2,\,y^3]^{\mathrm{T}} \tag{2.62}$$

Let us firstly look at w_α. Based on Equation 2.30, $\boldsymbol{\alpha}$ and $\overline{\mathbf{W}}$ can be related by multiplying the three matrices $\mathbf{H}$, $\mathbf{B}$ and $\mathbf{T}$ in section 2.2.2. Here, for simplicity, we replace the product of these three matrices with matrix $\mathbf{C}$:

$$\mathbf{C} = \mathbf{H}^{-1}(\mathbf{B}\mathbf{T}) \tag{2.63}$$

Thus, the vector $\boldsymbol{\alpha}$ can be rewritten as:

$$\boldsymbol{\alpha} = \mathbf{C}\overline{\mathbf{W}} \tag{2.64}$$

Substituting Equation 2.64 in to 2.62, we can obtain the expression of w_α in terms of $\overline{\mathbf{W}}$:

$$w_\alpha = \mathbf{R}^{\mathrm{T}}\mathbf{C}\overline{\mathbf{W}} \tag{2.65}$$

Next, we move on to express w_A in terms of $\overline{\mathbf{W}}$. From equations 2.58, 2.61 and 2.65, we have:

$$w_A = \mathbf{S}^{\mathrm{T}}\,\mathbf{A} = w - \mathbf{R}^{\mathrm{T}}\mathbf{C}\overline{\mathbf{W}} \tag{2.66}$$

Evaluating w_A at the three nodes, we can obtain:

$$w_A(x_i, y_i) = \mathbf{S}^{\mathrm{T}}(x_i, y_i)\,\mathbf{A} = \overline{w}_i - \mathbf{R}^{\mathrm{T}}(x_i, y_i)\,\mathbf{C}\overline{\mathbf{W}}, \quad i = 1, 2, 3 \tag{2.67}$$

which give us the following matrix equation:

$$\underbrace{\begin{bmatrix} 1 & x_1 & y_1 \\ 1 & x_2 & y_2 \\ 1 & x_3 & y_3 \end{bmatrix}}_{\mathbf{M}_A}\mathbf{A} = \begin{bmatrix} \overline{w}_1 \\ \overline{w}_2 \\ \overline{w}_3 \end{bmatrix} - \underbrace{\begin{bmatrix} x_1^2 & x_1y_1 & y_1^2 & x_1^3 & x_1^2y_1 & x_1y_1^2 & y_1^3 \\ x_2^2 & x_2y_2 & y_2^2 & x_2^3 & x_2^2y_2 & x_2y_2^2 & y_2^3 \\ x_3^2 & x_3y_3 & y_3^2 & x_3^3 & x_3^2 3_2 & x_3y_3^2 & y_3^3 \end{bmatrix}}_{\mathbf{M}_\alpha}\mathbf{C}\overline{\mathbf{W}} \tag{2.68}$$

Since

$$\begin{bmatrix} \overline{w}_1 \\ \overline{w}_2 \\ \overline{w}_3 \end{bmatrix} = \underbrace{\begin{bmatrix} 1 & 0 & 0 & 0 & 0 & 0 & 0 & 0 & 0 \\ 0 & 0 & 0 & 1 & 0 & 0 & 0 & 0 & 0 \\ 0 & 0 & 0 & 0 & 0 & 0 & 1 & 0 & 0 \end{bmatrix}}_{\mathbf{B}_A}\overline{\mathbf{W}} \tag{2.69}$$

we can obtain $\mathbf{A}$ as:

$$\mathbf{A} = \mathbf{M}_A^{-1} \left(\mathbf{B}_A - \mathbf{M}_\alpha \, \mathbf{C}\right) \overline{\mathbf{W}} \tag{2.70}$$

Using Equation 2.61, we obtain:

$$w_A = \mathbf{S}^{\mathrm{T}} \mathbf{M}_A^{-1} \left(\mathbf{B}_A - \mathbf{M}_\alpha \, \mathbf{C}\right) \overline{\mathbf{W}} \tag{2.71}$$

Combining with Equation 2.65, we obtain the expression of w:

$$w = \mathbf{S}^{\mathrm{T}} \mathbf{M}_A^{-1} \left(\mathbf{B}_A - \mathbf{M}_\alpha \, \mathbf{C}\right) \overline{\mathbf{W}} + \mathbf{R}^{\mathrm{T}} \mathbf{C} \overline{\mathbf{W}} = \mathbf{N}_w \, \overline{\mathbf{W}} \tag{2.72}$$

where the matrix $\mathbf{N}_w$ (1×9) can be extracted as:

$$\mathbf{N}_w = \mathbf{S}^{\mathrm{T}} \mathbf{M}_A^{-1} (\mathbf{B}_A - \mathbf{M}_\alpha \mathbf{C}) + \mathbf{R}^{\mathrm{T}} \mathbf{C} \tag{2.73}$$

SHAPE FUNCTIONS OF θ

Using the cubic polynomial expression of w from Equation 2.13, θ_x can be expressed as:

$$\theta_x = \frac{\partial w}{\partial x} = A_2 + 2\alpha_1 x + \alpha_2 y + 3\alpha_4 x^2 + 2\alpha_5 xy + \alpha_6 y^2 \tag{2.74}$$

Similarly to the case of w, the expression of the above rotations can also be divided into two parts, one containing the A coefficients only and another the α coefficients only:

$$\theta_x = A_2 + \theta_{x\alpha} \tag{2.75}$$

Since A_2 is part of the vector $\mathbf{A}$ which has been expressed in Equation 2.70, we have:

$$A_2 = \mathbf{B}_x \mathbf{A} = \mathbf{B}_x \mathbf{M}_A^{-1} (\mathbf{B}_A - \mathbf{M}_\alpha \mathbf{C}) \overline{\mathbf{W}} \tag{2.76}$$

where $\mathbf{B}_x$ is a Boolean matrix:

$$\mathbf{B}_x = \begin{bmatrix} 0 & 1 & 0 \end{bmatrix} \tag{2.77}$$

The expression $\theta_{x\alpha}$ can be written as:

$$\theta_{x\alpha} = \mathbf{R}_x^{\mathrm{T}} \boldsymbol{\alpha} = \mathbf{R}_x^{\mathrm{T}} \mathbf{C} \overline{\mathbf{W}} \tag{2.78}$$

where Equation 2.64 is used to express $\boldsymbol{\alpha}$ and $\mathbf{R}_x$ is also a vector of local coordinates:

$$\mathbf{R}_x = \begin{bmatrix} 2x & y & 0 & 3x^2 & 2xy & y^2 & 0 \end{bmatrix}^{\mathrm{T}} \tag{2.79}$$

Substituting the expressions above into Equation 2.74, the expression of θ_x is

$$\theta_x = \mathbf{B}_x \mathbf{M}_A^{-1} (\mathbf{B}_A - \mathbf{M}_\alpha \mathbf{C}) \overline{\mathbf{W}} + \mathbf{R}_x^{\mathrm{T}} \mathbf{C} \overline{\mathbf{W}} \tag{2.80}$$

The shape function $\mathbf{N}_x$ of rotation θ_x is therefore:

$$\mathbf{N}_x = \mathbf{B}_x \mathbf{M}_A^{-1} (\mathbf{B}_A - \mathbf{M}_\alpha \mathbf{C}) + \mathbf{R}_x^{\mathrm{T}} \mathbf{C} \tag{2.81}$$

The derivation of shape function $\mathbf{N}_y$ for rotation θ_y is very similar to that for θ_x and is omitted here for brevity.

$\mathbf{B}_{\mathrm{CE}}$ MATRIX

Once we have determined the shape functions, the next step is to assemble the $\mathbf{B}_{\mathrm{CE}}$ matrix that relates the DoFs vector $\mathbf{q}_{\mathrm{CE}}$ to the opening vector $\boldsymbol{\Delta}$ (c.f. Equation 2.56). Substituting the shape functions in Equations 2.73 and 2.81 to express the w and θ terms in Equations 2.50, 2.54, and 2.55, the expression of $\mathbf{B}_{\mathrm{CE}}$ can be obtained as the following:

$$\mathbf{B}_{\mathrm{CE}} = \begin{bmatrix} 0 & 0 & 0 & 0 & 0 & 0 & -\mathbf{N}_w & 0 & 0 & 0 & 0 & 0 & 0 & \mathbf{N}_w \\ -L_1 & 0 & -L_2 & 0 & -L_3 & 0 & \frac{h^{\mathrm{bot}}}{2}\mathbf{N}_x & L_1 & 0 & L_2 & 0 & L_3 & 0 & \frac{h^{\mathrm{top}}}{2}\mathbf{N}_x \\ 0 & -L_1 & 0 & -L_2 & 0 & -L_3 & \frac{h^{\mathrm{bot}}}{2}\mathbf{N}_y & 0 & L_1 & 0 & L_2 & 0 & L_3 & \frac{h^{\mathrm{top}}}{2}\mathbf{N}_y \end{bmatrix} \tag{2.82}$$

$\mathbf{D}_{\mathrm{CE}}$ MATRIX

The relationship between traction $\boldsymbol{\tau}$ and opening vector $\boldsymbol{\Delta}$ is expressed through the constitutive matrix $\mathbf{D}_{\mathrm{CE}}$:

$$\boldsymbol{\tau} = \mathbf{D}_{\mathrm{CE}}\,\boldsymbol{\Delta}, \quad \mathbf{D}_{\mathrm{CE}} = \begin{bmatrix} (1-d_{\mathrm{I}})K & 0 & 0 \\ 0 & (1-d)K & 0 \\ 0 & 0 & (1-d)K \end{bmatrix} \tag{2.83}$$

where K and d are the penalty stiffness and the damage variable of the CE, respectively. The damage variable d in this work is updated by the bi-linear cohesive law proposed by Turon et al. [7, 8]. The damage variable d_{I} under Mode I loading is distinguished from d to avoid interpenetration of the top and bottom surfaces under compression:

$$d_{\mathrm{I}} = \begin{cases} d, & \Delta_{\mathrm{I}} \geq 0 \\ 0, & \Delta_{\mathrm{I}} < 0 \end{cases} \tag{2.84}$$

The penalty stiffness K is set as:

$$K = \alpha \frac{E_3}{t} \tag{2.85}$$

where E_3 is the out-of-plane laminate Young's modulus, t is the thickness of the laminate and α is a constant: not to be confused with the matrix $\boldsymbol{\alpha}$ used in Equation 2.64, here set to be 50 [9].

STIFFNESS MATRIX AND RESIDUAL VECTOR

In this work, the secant stiffness matrix is used as the stiffness matrix of the CE:

$$\mathbf{K}_{\mathrm{CE}} = \int_{\Gamma} \mathbf{B}_{\mathrm{CE}}^{\mathrm{T}}\,\mathbf{D}_{\mathrm{CE}}\,\mathbf{B}_{\mathrm{CE}}\,\mathrm{d}\,\Gamma \tag{2.86}$$

where Γ represents the domain of the interface. The integral in Equation 2.86 is hard to calculate analytically. Thus, the Gaussian integration scheme is applied to obtain the stiffness

matrix numerically. Earlier works have shown that using a higher number of quadrature points improves the accuracy and smoothness of the load-displacement solutions of delamination simulations [1, 2, 10]. Therefore, thirteen quadrature points are used in this work for the integration of the structural CE, with their coordinates and weights taken from the work of Cowper [11].

Assuming that no external distributed loads are applied to the cohesive interfaces, only the internal force vector of the CE contributes to the overall residual vector of the system. The residual vector contribution from this CE can then be written as:

$$\mathbf{f}_{\text{res}} = -\mathbf{f}_{\text{int}} = -\mathbf{K}_{\text{CE}}\,\mathbf{q}_{\text{CE}} \tag{2.87}$$

Note that although the cohesive element developed in this paper appears to have finite thickness between its nodes, the actual integration domain is in fact the zero-thickness interface between the plies. The finite thickness of the cohesive element is entirely due to the fact that the nodes of the cohesive element, shared with the top and bottom ply elements, are positioned on the midplanes of the plies. Through kinematic derivations, the displacements at the upper and lower surfaces of the interface are obtained. The separation vector is then calculated as the difference between them. Subsequently, the corresponding tractions and damage variables are calculated using the penalty stiffness and the cohesive law. Thus, the cohesive behavior at the zero-thickness interface can be achieved even though the cohesive element has finite thickness between its nodes. In the situation where the physical thickness of the interface, i.e., the resin-rich region between two plies, is a matter of importance, different considerations may apply. If the membrane stiffness of the resin-rich region cannot be neglected, then solid elements would be needed to model this region. In general, however, the membrane stiffness of the resin-rich region is negligible; hence a cohesive law can still be assumed to represent the out-of-plane behavior of the interface. We have developed an approach that relates the finite thickness of the resin-rich region to material properties and the penalty stiffness of the traction separation law. This is the subject of a future communication.

2.3. RESULTS

THE structural elements Section 2.2 have been implemented in the Abaqus user-defined element subroutines. The structural CE model was first verified on the three classical benchmarks, namely the double cantilever beam (DCB), the end-notched flexure (ENF), and the mixed-mode bending (MMB) problems. As the above benchmarks only pertain to unidirectional laminates, a multi-directional laminate problem, namely the single-leg bending (SLB) problem [12, 13], was simulated to demonstrate the 3D capacity of the model. All simulations of the structural CE model were performed in implicit analysis using the Quasi-Newton solver without damping or viscosity. The reference solutions on these problems were obtained with analytical equations and Abaqus standard FE simulations using 8-node linear solid elements (C3D8I element in Abaqus) for the plies and 8-node linear CEs for the interfaces. The linear CEs were implemented as user-defined elements following the formulation in [14], with the cohesive law from Turon et al. [7, 8]. The problem descriptions and modelling details will be presented in this section, followed by comparisons of load-displacement curves and computational time.

2.3.1. UNIDIRECTIONAL LAMINATE BENCHMARKS: DCB, ENF, AND MMB

DESCRIPTION OF THE UNIDIRECTIONAL LAMINATE TESTS

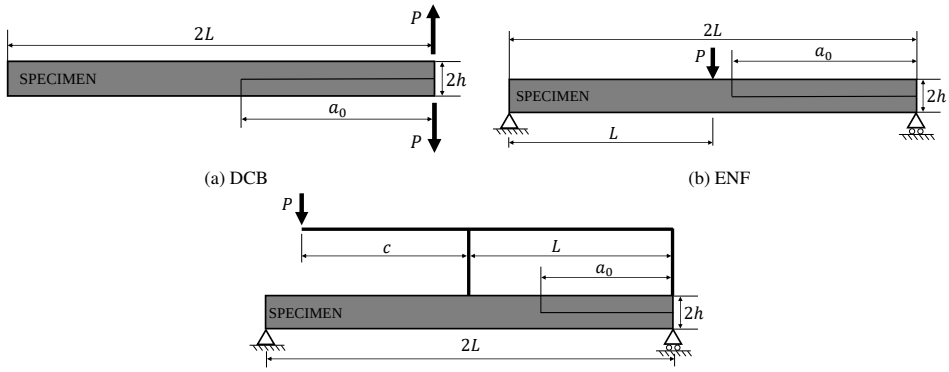

Figure 2.5: DCB, ENF, and MMB test specimens

THE unidirectional laminate benchmarks are drawn from the work by Krueger [13], except that the pre-crack length of the ENF model is increased to 35 mm in this work to avoid the snapback in the load-displacement response. The geometric parameters and boundary conditions are shown in Figure 2.5 and Table 2.1. The detailed material properties are shown in Table 2.2 and 2.3. The mixed mode ratio of the SLB specimen is approximately 40% mode II (G_{II} / G_{T}=0.4) and the MMB specimen is 0.5 (G_{II} / G_{T}=0.5).

Table 2.1: Geometric parameters for unidirectional benchmarks

Param. (mm) / Model	$2L$	a_0	h	b (width)	c
DCB	150.0	30.5	1.50	25.0	-
ENF	101.6	35.0	2.25	25.4	-
MMB	100.8	25.4	2.25	25.4	41.3

DESCRIPTION OF THE MODEL

Since the plies of the benchmarks in this section are all 0°, the symmetric lay-up conditions in Equation 2.2 are met. Therefore, the structural model could simply use one layer of shell elements on each side of the delamination, with one layer of structural CEs in between. The Abaqus solid models are built according to the work of Krueger [13], except that CEs, instead of VCCT, are used to model delamination.

LOAD-DISPLACEMENT CURVES

The load-displacement curves obtained from the simulations are shown in Figure 2.6. The designations “-solid" and “-structural" denote the results of the traditional solid element

Table 2.2: Material properties for DCB [13]

T300/1076 Unidirectional graphite/epoxy prepreg		
E_{11}= 139.4 GPa	E_{22}= 10.16 GPa	E_{33} = 10.16 GPa
ν_{12} = 0.30	ν_{13} = 0.30	ν_{23} = 0.436
G_{12} = 4.6 GPa	G_{13} = 4.6 GPa	G_{23} = 3.54 GPa
Fracture toughness data		
$G_{\mathrm{Ic}} = 0.170\,\mathrm{kJ/m^2}$	$G_{\mathrm{IIc}} = 0.494\,\mathrm{kJ/m^2}$	$\eta = 1.62$
Interfacial strength data [8, 15]		
$\tau_{\mathrm{Ic}} = 30\,\mathrm{MPa}$	$\tau_{\mathrm{IIc}} = 60\,\mathrm{MPa}$	

Table 2.3: Material properties for ENF and MMB [13]

IM7/8552 Unidirectional graphite/epoxy prepreg		
E_{11}= 161 GPa	E_{22}= 11.38 GPa	E_{33} = 11.38 GPa
ν_{12} = 0.32	ν_{13} = 0.32	ν_{23} = 0.45
G_{12} = 5.2 GPa	G_{13} = 5.2 GPa	G_{23} = 3.9 GPa
Fracture toughness data		
$G_{\mathrm{Ic}} = 0.212\,\mathrm{kJ/m^2}$	$G_{\mathrm{IIc}} = 0.774\,\mathrm{kJ/m^2}$	$\eta = 2.1$
Interfacial strength data [8, 15]		
$\tau_{\mathrm{Ic}} = 30\,\mathrm{MPa}$	$\tau_{\mathrm{IIc}} = 60\,\mathrm{MPa}$	

model and those of the proposed structural CE model, respectively. The results on meshes of different element sizes are plotted together with the analytical solutions [16–18].

The DCB results in Figure 2.6 indicated that the standard model with solid elements requires that the element size should not exceed 0.5 mm. When the element sizes are greater than or equal to 1 mm, the simulation results differ greatly from the analytical solution. The error on peak load exceeds 30%, and the post-peak curve also stays way above the analytical one. With the proposed structural model, the results on 2-mm mesh remain in close agreement with the analytical solution, with a less than 3% error on the peak load. The post-peak curve also closely follows the analytical curve. The slight over-prediction of the stiffness is expected as a result of neglecting transverse shear in the Kirchhoff-Love shell elements. The analytical solution based on the corrected beam theory, however, includes such a transverse shear effect [16]. Even on a 5-mm mesh, the structural model can predict the peak load fairly well despite the post-peak oscillations right above the analytical curve. Such oscillations are due to the larger spacing between the integration points on coarser meshes.

In the ENF case, the solid element model on 1-mm mesh could capture the peak load correctly, thanks to the larger cohesive zone in Mode II delamination than in Mode I. However, the result on 2.5-mm mesh already shows a clear drift towards over-prediction. As

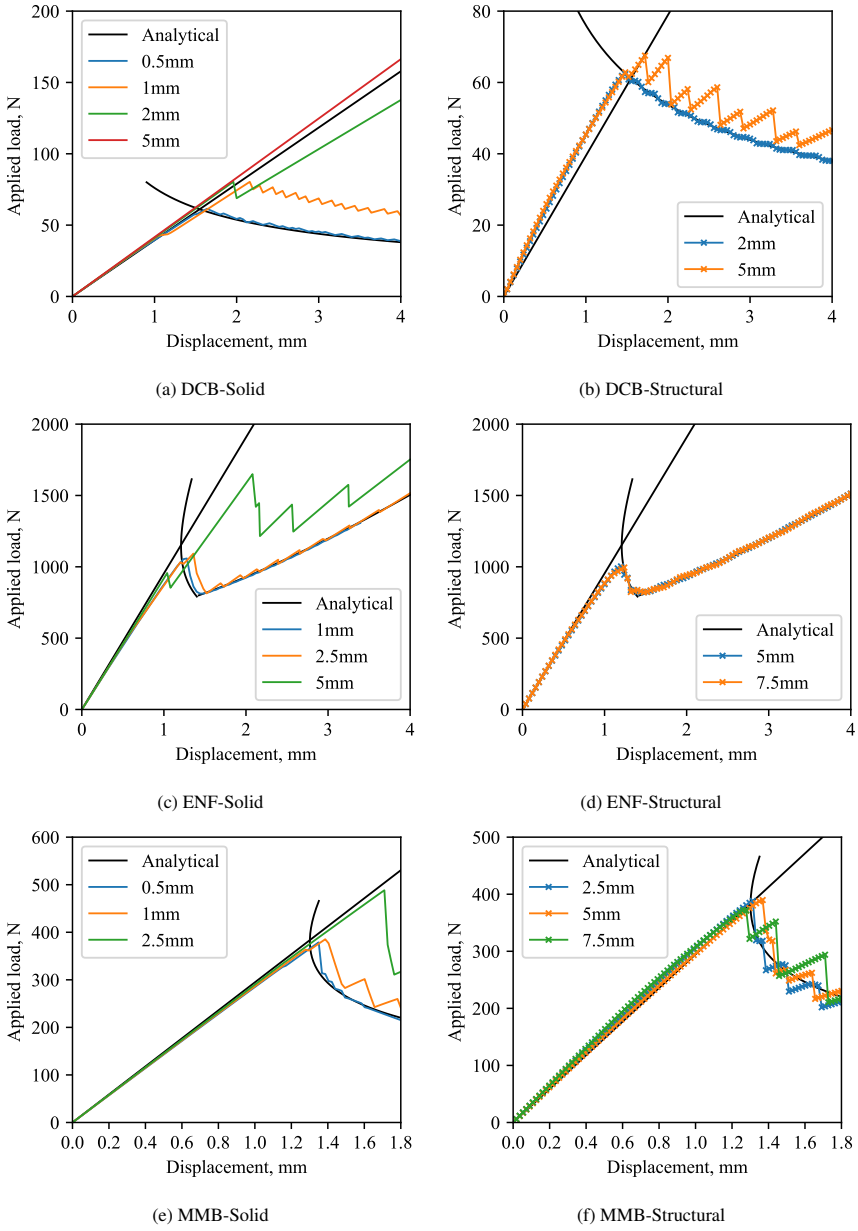

(a) DCB-Solid

(b) DCB-Structural

(c) ENF-Solid

(d) ENF-Structural

(e) MMB-Solid

(f) MMB-Structural

Figure 2.6: Results of the DCB, ENF, and MMB tests, showing the sensitivities of the conventional solid CE and the proposed structural CE on different mesh densities

the element size increases to 5 mm, the peak load and post-peak response again become severely over-predicted. Correspondingly, if the structural model is used on the 5-mm mesh,

the predicted curve remains close to the analytical solution throughout the loading history. Even the 7.5-mm structural model manages to capture the load-displacement response very accurately. The slight under-prediction of the peak load is expected, as the analytical curve is based on Linear Elastic Fracture Mechanics, which ignores the presence of material softening (i.e. the cohesive zone) at the crack tip.

In the MMB case, very similar trends can be observed. The solid model on the 2.5-mm mesh cannot capture the correct load-displacement response, while the structural model's predictions on the 2.5-mm and 5-mm meshes oscillate closely around the analytical curve. Even the 7.5-mm structural model predicts the peak load correctly, albeit with bigger oscillations during the load drop section due to the coarser distribution of integration points in larger elements.

COMPUTATIONAL PERFORMANCES

Table 2.4: Comparison of CPU time (unit: second)

	DCB	ENF	MMB
Solid model (mesh size)	5311.8 (0.5mm)	4239.7 (1mm)	5560.7 (0.5mm)
Structural model (mesh size)	197.15 (5mm) 836.76 (2mm)	285.33 (7.5mm) 736.41 (5mm)	370.02 (7.5mm) 474.79 (5mm)
Reduction by structural	96.3% 84.2%	93.3% 82.6%	93.3% 91.5%

By allowing larger elements to be used, the proposed structural model is able to reduce the computational time of the delamination simulations considerably. The results of the structural model are compared against those of the solid element model. The comparison of CPU time is reported in Table 2.4. It can be seen that the structural model can reduce the computational time in all three problems by more than 90%, while retaining accurate predictions of the peak loads and the overall load-drop curves.

STUDIES ON INTEGRATION POINTS

In this section, the influence of the number of integration points in one element on the simulation results is discussed, using the error of the load-displacement curves with respect to the analytical solutions. The earlier work in 2D [1] showed the largest influence of integration points in the DCB model. Therefore, only DCB is studied here. The load-displacement curves with different integration points are reported in Figure 2.7. The use of 52 integration points in the element domain is achieved through subdomain integration as detailed in Tosti Balducci and Chen [2].

From Figure 2.7a, on the 5-mm mesh, it is clear that as we increase the number of integration points, the predicted curves become closer to the analytical one, consistent with earlier results [1, 2]. It is also clear that even with just 3 integration points, the prediction does not exhibit the same overshoot of peak load as seen in the solid-element model in Figure 2.6a. This indicates that it is the higher-order continuity in the kinematics of the

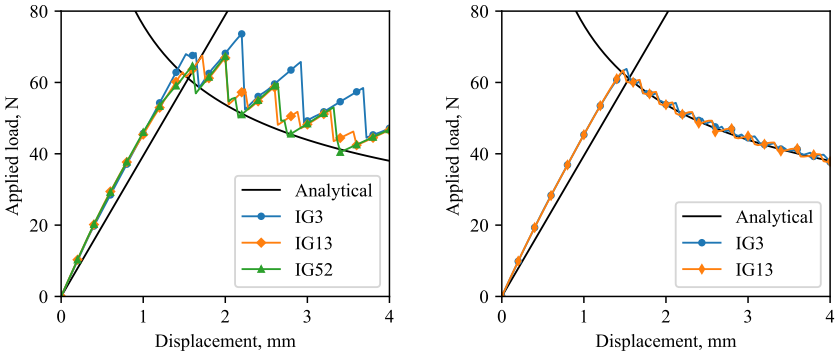

(a) Results on 5-mm mesh

(b) Results on 2-mm mesh

Figure 2.7: Load-displacement curves of the DCB model with different integration points on two different meshes

structural elements that brings down this overshoot and hence enables the use of larger elements. From Figure 2.7b, on the 2-mm mesh, the number of integration points does not seem to show any effect. In summary, having more integration points increases the prediction accuracy on coarse meshes, but has little effect once the mesh is sufficiently refined. This suggests a trade-off between using more integration points and using finer meshes. As the element size determines the size of the system matrix, while the operations at integration points are local to each element and can be parallelized, it would be more efficient to use more integration points on a coarser mesh.

2.3.2. UNIDIRECTIONAL LAMINATE BENCHMARKS: REINFORCED DCB

ALTHOUGH the earlier benchmarks are modelled in 3D, they can actually be modelled in 2D [1] as the delamination front does not vary significantly across the width of the specimens. To verify the capacity of the proposed elements in modelling delamination in 3D, the Reinforced DCB (R-DCB) problem is studied in this section.

DESCRIPTION OF THE REINFORCED DCB

The R-DCB experiment was proposed by Carreras et al. [19]. The main part of the R-DCB specimen is a standard DCB specimen made of 16 unidirectional plies at 0°. Two reinforcement parts, made of 8 plies of the same material at 0°, are attached on the top and bottom of the DCB specimen. The elastic properties of the ply material are shown in Table 2.5. The pre-crack is 35 mm long on the opposite side of the reinforcement. The geometry of the R-DCB specimen is shown in Figure 2.8.

The R-DCB problem is modelled with the proposed structural elements. Symmetry is used to reduce the size of the model. The boundary conditions of the model are shown in Figure 2.9. The right side of the model is fixed and a displacement loading is applied on the left side. The two arms of the DCB and the two reinforcement parts are each modelled with one layer of cubic shell elements. Their interfaces are each modelled with one layer of structural CEs. The properties for the structural CEs are shown in Table 2.6.

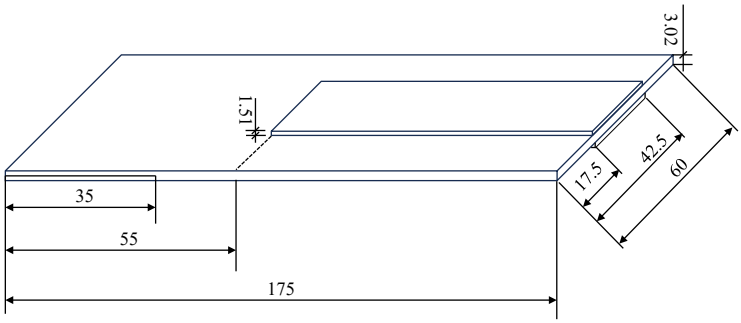

Figure 2.8: Geometry of the R-DCB specimen (units in mm) [19]

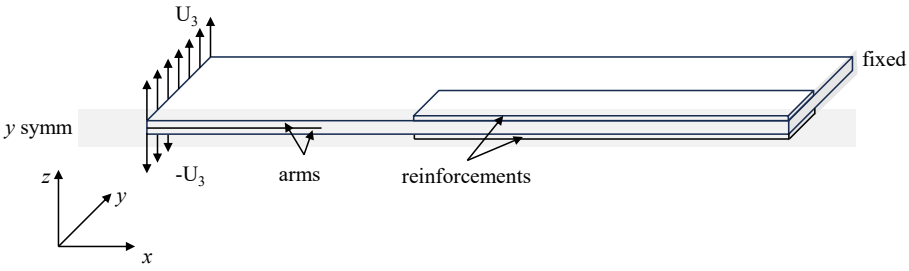

Figure 2.9: Boundary conditions and loading of the finite element model; U_3=7.5 mm

Table 2.5: Lamina properties of the R-DCB model [20]

Property	Value	Units
E_{11}	154	GPa
$E_{22} = E_{33}$	8.5	GPa
$G_{12} = G_{13}$	4.2	GPa
G_{23}	3.04	GPa
$\mu_{12} = \mu_{13}$	0.35	-
μ_{23}	0.4	-

RESULTS AND COMPARISONS

Similarly to the previous section, different mesh sizes are used for mesh convergence analysis. The predicted load-displacement curves on different mesh sizes are shown in Figure 2.10. We can see that the three curves agree well with each other. The 5-mm curve is not as smooth as the other two, consistent with the DCB results in Figure 2.6b. The

Table 2.6: Interlaminar properties of the R-DCB model [20]

Property	Value	Units
K: Penalty stiffness	10^5	$\mathrm{N/mm^3}$
G_{Ic}	0.305	N/mm
G_{IIc}	2.77	N/mm
η	2.05	-
τ_{Ic}	32.6	MPa
τ_{IIc}	98	MPa

most obvious difference is that the 5-mm curve slightly over-predicts the second peak load and the corresponding opening displacement. The 2-mm and 1-mm curves fall on top of each other, indicating that the mesh has converged. The 2-mm curve is used for subsequent comparison with experimental data.

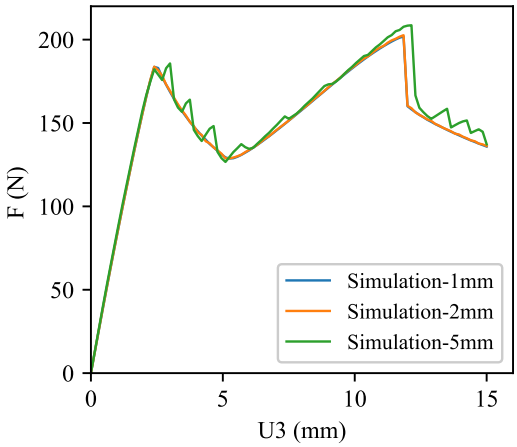

Figure 2.10: Load-displacement curves of the reinforced DCB with different mesh sizes from simulation results

In Figure 2.11, it can be seen that the predicted load-displacement curve agrees reasonably well with the experimental data from 4 specimens. However, there are three obvious differences. Firstly, the initial stiffness is greater than the experimental one. This could be due to the fact that the loading grips and test machine increase compliance, which is not included in the model. Looking closely at the initial part of the experimental load-displacement curves, we can see that there is a slight increase in stiffness at around 0.5 mm displacement. This indicates the presence of some initial machine compliance, which is not taken into account in the simulation. Secondly, for the second peak load that denotes the onset of delamination in the reinforced region, the numerical prediction is greater than the experimental result by 15%. This could be due to the lack of transverse shear compliance

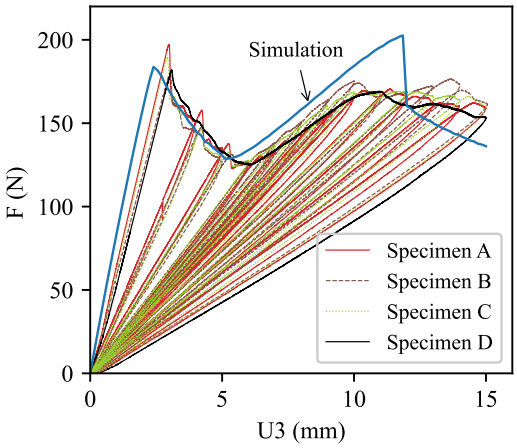

Figure 2.11: Comparison of numerical and experimental results of the force-displacement curves [19]

in the model, particularly in the reinforced region. This leads to a stiffer response in the model than in the experiments when the reinforced region is loaded. This stiffer reinforcement slows down the delamination propagation when it first encounters the reinforcement, leading to slower damage creation. Third, the numerical curve after the second peak falls sharply and below the experimental curves. This indicates that the fracture toughness value used by the structural CEs may have underestimated the fracture energy for the crack propagation in the reinforced region, which may include crack toughening mechanisms such as fibre bridging due to the curved delamination front.

In Figure 2.12, the positions of the crack fronts of the test specimens and numerical models are plotted at multiple opening displacements. It can be observed that the delamination front shapes of the numerical results are consistent with the experimental results: the delamination front is a straight line before it goes into the reinforced part. When it extends to the reinforced region, the shape changes from a straight line to a curve. However, the delamination propagates faster in the numerical results than in the experiments, except at 10-mm displacement, when the delamination propagation in the middle is clearly hindered by the stiff reinforcement. However, once delamination initiates in the reinforced region, it again propagates faster in the simulation than in the experiment, as shown by the curves at 12-mm and 15-mm displacements. The reason for the faster numerical propagation could be that the stiffness in the simulation is higher than that in the experiments due to the lack of initial machine compliance and the lack of transverse shear compliance in the model. Therefore, in the simulation, a smaller displacement loading on the arms would be needed than in the experiments to open the cohesive crack tip to reach its delamination onset. This also means that for the same amount of displacement loading, the simulation would predict the delamination front to propagate further than in the experiments.

2.3.3. MULTI-DIRECTIONAL LAMINATE BENCHMARK: SLB

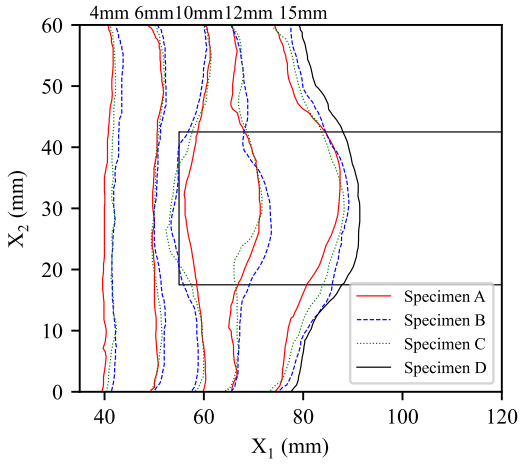

(a) Experiment results [19]

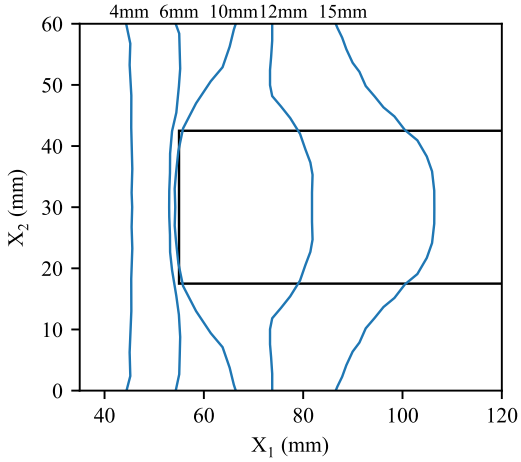

(b) Numerical results

Figure 2.12: Comparison of numerical and experimental results of the delamination front position

DESCRIPTION OF THE SLB TEST

THE SLB specimen is shown in Figure 2.13, with its geometrical parameters specified in Table 2.7. Unlike in the previous benchmarks, the ply angles here are no longer all $0°$. The material of the SLB model is C12K/R6376 and its properties are shown in Table 2.8. Unfortunately, the value of τ_{IIc} cannot be found in the literature. However, the value of τ_{IIc} can be estimated from τ_{Ic} in Equation 2.88, which is derived from the equations in Reference [8] with the same penalty stiffness of mode I and mode II. Hence, the value of τ_{IIc} here is estimated to be 58 MPa.

$$\tau_{\mathrm{IIc}} = \tau_{\mathrm{Ic}} \sqrt{\frac{G_{\mathrm{IIc}}}{G_{\mathrm{Ic}}}} \tag{2.88}$$

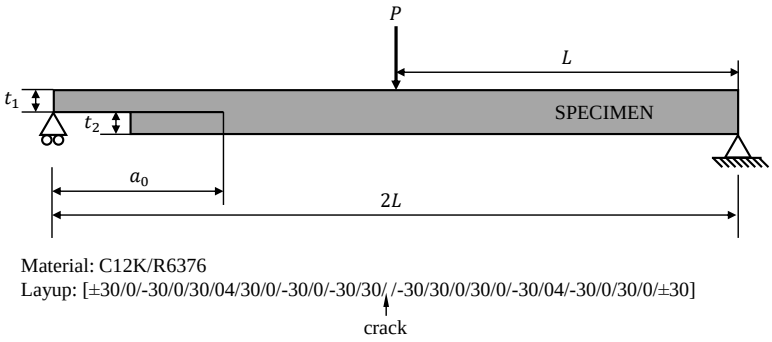

Figure 2.13: SLB specimen [12]

Table 2.7: Geometric parameters for the SLB specimen

Parameter	$2L$	a_0	t_1	t_2	b (width)
value (mm)	177.8	60	2	2	25.4

Table 2.8: C12K/R6376 material properties for SLB specimen [13]

C12K/R6376 Unidirectional graphite/epoxy prepreg		
E_{11}= 146.9 GPa	E_{22}= 10.6 GPa	E_{33} = 10.6 GPa
ν_{12} = 0.33	ν_{13} = 0.33	ν_{23} = 0.33
G_{12} = 5.45 GPa	G_{13} = 5.45 GPa	G_{23} = 3.99 GPa
Fracture toughness data		
$G_{\mathrm{Ic}} = 0.34\,\mathrm{kJ/m^2}$	$G_{\mathrm{IIc}} = 1.286\,\mathrm{kJ/m^2}$	$\eta = 3.39$
Interfacial strength data		
$\tau_{\mathrm{Ic}} = 25\,\mathrm{MPa}$ [21]	$\tau_{\mathrm{IIc}} = 58\,\mathrm{MPa}$*	

* Estimated [15]

DESCRIPTION OF THE MODEL

Since the SLB specimen is a multi-directional laminate and its lay-up is not symmetric, we can no longer model the entire laminate with a single layer of shell elements on each side

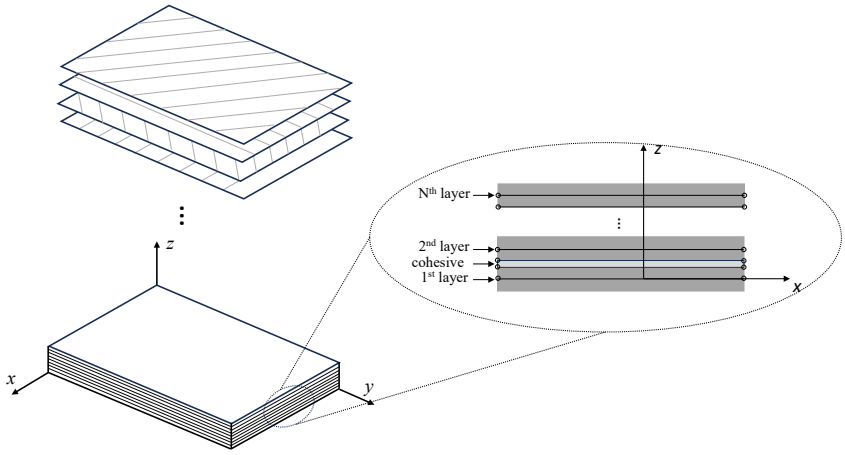

Figure 2.14: Layer-wise model for SLB

of the delamination, as done in the unidirectional models. Therefore, the SLB model uses one layer of shell elements for each ply and one layer of structural CEs between every two plies (c.f., Figure 2.14).

LOAD-DISPLACEMENT CURVES

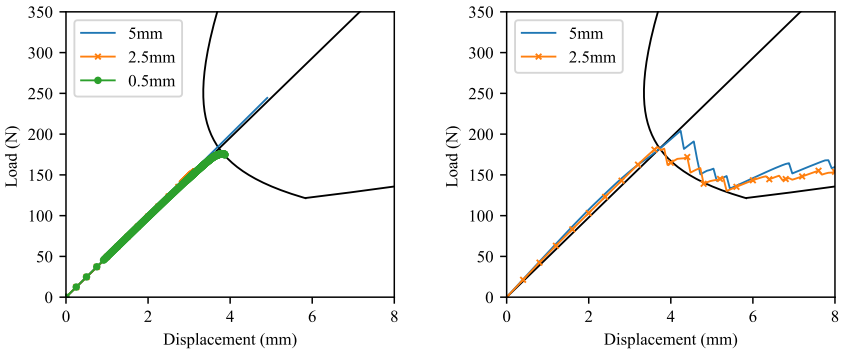

(a) SLB-Solid

(b) SLB-Structural

Figure 2.15: Load-displacement predictions of the SLB

In Figure 2.15, the load-displacement curves are reported for the solid and structural models. Both are compared with the analytical solution derived in Appendix D. All the load-displacement predictions by the solid model could not reach numerical convergence within the allowable settings on solver iterations. As a result, the load-decreasing section of the curve could not be obtained. From the left figure, it can be seen that only the 0.5-

mm solid model can capture the correct peak load. For the 2.5-mm solid model, the peak load is much lower than the analytical solution due to premature divergence of the analysis. However, the peak load of the model on the 5-mm mesh is much larger than the analytical solution, in line with the solid model's performance in the unidirectional benchmarks. The right figure shows that all the structural models can obtain converged solutions throughout the full loading history. Overall speaking, the predicted curves of the structural models follow the analytical solution well. On the 2.5-mm mesh, the error of peak load is 2%, the same level of accuracy as that of the unidirectional structural model. On the 5-mm mesh, the predicted peak load is larger by 12.5%. However, the post-peak part of the curve quickly converges to that of the 2.5-mm mesh result. It should be noted that the initial stiffness of the structural models is 5% larger than that of the analytical solution. The reason is that the compliance C obtained by Equation D.87 is calculated by simplifying the SLB model into a 2D beam model (c.f., Figure D.1), where the neutral axis is assumed to be aligned with the centerline of the uncracked region for simplicity. However, the actual neutral axis of the SLB model should be slightly above the assumed one, as only the top part of the cracked region would be under bending. This discrepancy would cause the analytical stiffness to be slightly lower than that in the actual situation. Another discrepancy to note is that when the crack length a is longer than L, the load increases again with increasing displacement (c.f., Appendix D, curve DFE). For this part, the predicted curves of the structural models are above the analytical curve. This discrepancy is expected. As the crack length a increases with delamination propagation, the mixed-mode ratio B is found to also increase, particularly when $a > L$ [22], which causes the critical energy release rate G_c to increase as well. However, the analytical solution in Appendix D assumes a fixed mixed-ratio, which underestimates G_c for $a > L$, hence resulting in the analytical curve being below the numerical ones. The analytical curve could be corrected should an analytical expression of G_c in terms of a become available.

In addition, it needs to be emphasized that the difficulty of convergence of the solid model leads to a significant increase in computational time. Due to this reason, artificial viscosity would be needed to continue the simulation through the convergence difficulties. However, this would introduce a fitting parameter, which generally requires trial and error to properly set its value. This suggests that the proposed structural model not only allows coarser meshes with faster computations but also ensures better numerical stability than the solid element model.

2.4. SUMMARY AND CONCLUSIONS

THIS work aims to establish a state-of-the-art numerical method to simulate the delamination of composite laminates aimed at overcoming the cohesive zone limit on mesh density. The Kirchhoff-Love triangular cubic plate element from Allman [5] has been extended for the modelling of symmetric laminate shells. A structural CE, conforming with the shell element, has been developed to model delamination between the shells. The combination of the Kirchhoff-Love shell element and the structural CE is shown to be a powerful new method that overcomes the cohesive zone limit and models delamination with high accuracy and efficiency under different loading conditions. This capability is expected to make a strong impact in the composites modeling community, as the cohesive zone limit has been a long-lasting and well-known problem for delamination modeling.

This method has also been validated on the DCB, ENF, MMB, and SLB problems. The results show excellent agreement with the analytical solutions. By comparing the results with those from the solid element model, the structural model has shown the following advantages: 1) it can accurately predict the load-displacement curves with significantly coarser meshes than the solid element model, allowing 5-mm elements to be used instead of the 0.5-mm elements in the latter; 2) its computational speed is much faster than that of the solid element model, achieving more than 90% reduction in CPU time; and 3) it has better numerical stability than the solid element model, reaching convergence without needing artificial viscosity for stabilization. In addition, the method has been applied on the R-DCB problem where the delamination front is highly curved. Its predictions on the load-displacement curve and delamination fronts are in very good agreement with the experimental data.

Next work includes the incorporation of intralaminar damage in the structural model. Since Kirchhoff-Love thin shell elements are used to model the plies, the transverse strains are ignored. This will impact the prediction of intralaminar damage in the model because an accurate three-dimensional damage criterion would require out-of-plane stresses and/or strains as inputs. Since the layer-by-layer modelling method used in this work employs CEs between every two plies, the required out-of-plane stresses can be obtained by extracting the tractions of the CEs and interpolating them between the layers [1]. This method will be shown in Chapter 3. However, the current formulation does not account for the nonlinear coupling between in-plane and out-of-plane deformations arising from large displacements and rotations. Its applicability to problems involving large deflections, buckling, and post-buckling behaviour is limited. Extending the proposed formulation to geometrically nonlinear problems will be considered in future work. This is the subject of ongoing work in the group.

REFERENCES

1. Russo, R. & Chen, B. Overcoming the cohesive zone limit in composites delamination: modeling with slender structural elements and higher-order adaptive integration. *International Journal for Numerical Methods in Engineering* **121,** 5511–5545 (2020).
2. Tosti Balducci, G. & Chen, B. Overcoming the cohesive zone limit in the modelling of composites delamination with TUBA cohesive elements. *arXiv preprint arXiv:2403.09895* (2024).
3. Dávila, C. G., Camanho, P. M. P. R. d. C. & Turon Travesa, A. Cohesive elements for shells. © *NASA TP Technical Reports, 2007, núm. 214869* (2007).
4. Bazilevs, Y., Pigazzini, M., Ellison, A. & Kim, H. A new multi-layer approach for progressive damage simulation in composite laminates based on isogeometric analysis and Kirchhoff–Love shells. Part I: basic theory and modeling of delamination and transverse shear. *Computational Mechanics* **62,** 563–585 (2018).
5. Allman, D. A simple cubic displacement element for plate bending. *International Journal for Numerical Methods in Engineering* **10,** 263–281 (1976).
6. Przemieniecki, J. S. *Theory of matrix structural analysis* (Courier Corporation, 1985).

7. Turon, A., Camanho, P. P., Costa, J. & Dávila, C. A damage model for the simulation of delamination in advanced composites under variable-mode loading. *Mechanics of materials* **38,** 1072–1089 (2006).
8. Turon, A., Camanho, P., Costa, J. & Renart, J. Accurate simulation of delamination growth under mixed-mode loading using cohesive elements: Definition of interlaminar strengths and elastic stiffness. *Composite structures* **92,** 1857–1864 (2010).
9. Turon, A., Davila, C. G., Camanho, P. P. & Costa, J. An engineering solution for mesh size effects in the simulation of delamination using cohesive zone models. *Engineering fracture mechanics* **74,** 1665–1682 (2007).
10. Álvarez, D., Blackman, B., Guild, F. & Kinloch, A. Mode I fracture in adhesively-bonded joints: A mesh-size independent modelling approach using cohesive elements. *Engineering Fracture Mechanics* **115,** 73–95 (2014).
11. Cowper, G. Gaussian quadrature formulas for triangles. *International Journal for Numerical Methods in Engineering* **7,** 405–408 (1973).
12. Davidson, B., Krüger, R. & König, M. Three-dimensional analysis of center-delaminated unidirectional and multidirectional single-leg bending specimens. *Composites Science and Technology* **54,** 385–394 (1995).
13. Krueger, R. A summary of benchmark examples to assess the performance of quasi-static delamination propagation prediction capabilities in finite element codes. *Journal of Composite Materials* **49,** 3297–3316 (2015).
14. Camanho, P. P. & Dávila, C. G. Mixed-mode decohesion finite elements for the simulation of delamination in composite materials. *NASA Technical Reports* **211737** (2002).
15. Lu, X., Ridha, M., Chen, B., Tan, V. & Tay, T. On cohesive element parameters and delamination modelling. *Engineering Fracture Mechanics* **206,** 278–296 (2019).
16. Williams, J. The fracture mechanics of delamination tests. *The Journal of strain analysis for engineering design* **24,** 207–214 (1989).
17. *ASTM D5528/D5528M-21: Standard Test Method for Mode I Interlaminar Fracture Toughness of Unidirectional Fiber-Reinforced Polymer Matrix Composites* ASTM International (West Conshohocken, PA, 2021).
18. *ASTM D6671/D6671M-22, Standard test method for mixed mode I/mode II interlaminar fracture toughness of unidirectional fiber reinforced polymer matrix composites* (ASTM-International, West Conshohocken, PA, 2022).
19. Carreras, L., Renart, J., Turon, A., Costa, J., Bak, B. L. V., Lindgaard, E., de la Escalera, F. M. & Essa, Y. A benchmark test for validating 3D simulation methods for delamination growth under quasi-static and fatigue loading. *Composite Structures* **210,** 932–941 (2019).
20. Carreras, L., Turon, A., Bak, B. L., Lindgaard, E., Renart, J., de la Escalera, F. M. & Essa, Y. A simulation method for fatigue-driven delamination in layered structures involving non-negligible fracture process zones and arbitrarily shaped crack fronts. *Composites Part A: Applied Science and Manufacturing* **122,** 107–119 (2019).

21. Bruyneel, M., Delsemme, J.-P., Jetteur, P. & Germain, F. Modeling inter-laminar failure in composite structures: illustration on an industrial case study. *Applied Composite Materials* **16,** 149–162 (2009).

22. Krueger, R., Deobald, L. & Gu, H. A benchmark example for delamination growth predictions based on the Single Leg Bending specimen under fatigue loading. *Advanced Modeling and Simulation in Engineering Sciences* **7,** 1–25 (2020).

3

A NEW APPROACH FOR THROUGH-THICKNESS STRESS RECOVERY IN COMPOSITE LAMINATES

Thin shell elements based on the Kirchhoff-Love hypothesis account for only three stress components: the in-plane normal stresses (σ_x and σ_y) and the in-plane shear stress (τ_{xy}). The out-of-plane stress components required by conventional three-dimensional (3D) damage criteria are unavailable. As a result, damage initiation in composite laminates cannot be accurately predicted. This paper presents a method for capturing free-edge effects in multilayer structural elements with arbitrary composite lay-ups based on the Kirchhoff–Love hypothesis. The proposed formulation employs structural cohesive elements to model composite laminates and utilizes an accurate penalty stiffness derived from the resin-rich layers of the laminate. By accurately characterizing the interfacial mechanical response, out-of-plane stress components can be recovered in the uniform axial extension model.

Part of this chapter has been submitted for publication in X. Ai, C. Kassapoglou, B. Chen, A new approach for the determination of through- thickness and free-edge stresses in composite laminates based on structural elements, 2026. DOI: https://doi.org/10.48550/arXiv.2607.27559

3.1. INTRODUCTION

FIBER-reinforced composites are popular choices for lightweight structures in aerospace [1, 2]. The prediction of strength and damage tolerance is an indispensable aspect in the design of composite aircraft structures [3]. The shell element is widely used in the simulation of thin-walled composite structures due to its efficiency [4, 5]. However, since the traditional thin-shell element can only obtain in-plane stress, important information needed for out-of-plane failure analysis and damage prediction is missing.

Extensive research has been devoted to the recovery of out-of-plane stresses in shell elements. Most existing methods are based on the Mindlin–Reissner shell theory, in which the through-thickness shear deformation is considered [6–8]. The out-of-plane normal stress is then obtained through the stress recovery method [9, 10]. However, these methods primarily focus on in-plane failure mechanisms, such as matrix cracking and fiber failure, while neglecting interlaminar delamination. For delamination analysis, cohesive elements (CEs) are widely used as the interface element based on the cohesive zone model (CZM) [11, 12]. However, when Mindlin–Reissner shell elements are used, compatible cohesive elements still face the bottleneck of the mesh-density limitation imposed by the cohesive zone model. To ensure prediction accuracy, the element size must be several times smaller than the cohesive zone [13, 14]. In previous studies, the authors overcame the limitation of conventional cohesive zone modeling by developing high-order shell elements and compatible cohesive elements. The proposed formulation was validated through delamination simulations of a series of benchmark problems [15]. However, the shell element employed in the proposed formulation is based on the Kirchhoff-Love hypothesis. Existing approaches for recovering out-of-plane stresses developed for Mindlin–Reissner shell elements are not applicable. A dedicated approach is therefore required to recover the out-of-plane stress field within the Kirchhoff–Love shell element.

Främby et al. [16, 17] proposed a stress recovery method based on the Kirchhoff–Love hypothesis. The method recovers the out-of-plane stresses from the in-plane stress field of shell elements. It accurately predicts the through-thickness stress distribution in thin-shell structures. However, because it does not incorporate cohesive elements, it cannot simulate delamination initiation and propagation. Leong et al. [10] adopted this method by incorporating cohesive elements for damage analysis. His approach only recovered out-of-plane normal stress, while the out-of-plane shear stresses were obtained from the Mindlin–Reissner plate theory. In addition, the shell elements adopted in Främby's method are not high-order shell elements. When combined with cohesive elements, the mesh-density limitation imposed by the cohesive zone model still remains. By applying the stress recovery method to the proposed cubic structural element, all out-of-plane stress components can be recovered within a unified framework. However, the implementation requires transferring the stresses from the adjacent shell elements to the cohesive element, which substantially increases the complexity of the user element (UEL) subroutine implementation. In a different approach, Russo and Chen [13] employed the cohesive tractions as the out-of-plane stresses. However, this method was developed only for two-dimensional models and may produce excessive compressive stresses ahead of the cohesive zone.

Inspired by these studies, the present work directly employs the cohesive tractions obtained from three-dimensional cohesive elements to recover the out-of-plane stress components. One important parameter of the proposed method is the penalty stiffness of the

cohesive element. Turon et al. [18] proposed a penalty stiffness based on the laminate elastic modulus and thickness. However, the formulation is predicated on the assumption that the cohesive element has zero thickness. In practice, the shell-based cohesive element located between the two shell elements possesses a finite effective thickness, which equals one-half of the sum of the thicknesses of the adjacent shell elements [19, 20]. Therefore, the penalty stiffness predicted by Turon's formulation is significantly higher than the actual stiffness of structural cohesive elements. The calculated stress distribution overestimates the true stress levels. This discrepancy motivates the development of a more physically representative penalty stiffness formulation. Polla et al. [21] proposed a method for evaluating the penalty stiffness of cohesive elements inserted between shell elements. However, the cohesive element thickness is defined as the sum of the thicknesses of the upper and lower shell elements, rather than one-half of the sum. Bazilevs et al. [22] proposed an alternative penalty stiffness formulation based on the shell thickness. In this formulation, the cohesive element thickness is defined as one-half of the sum of the thicknesses of the adjacent shell elements. However, this formulation considers only the shear penalty stiffness and does not account for the dependence of the normal penalty stiffness on the shell thickness. Both methods assume that the shell undergoes simple through-thickness shear deformation under transverse shear loading. This assumption is inconsistent with the Kirchhoff–Love shell theory, in which the shell normal remains straight and perpendicular to the mid-plane during deformation. Both studies focused on improving delamination simulations, whereas the recovery of a complete three-dimensional stress field was not considered. Magisano et al. [23] proposed a hierarchical Kirchhoff–Love shell model with a warping model by introducing a soft layer between two stiff layers. With an appropriate warping model, the formulation accurately reproduces the response predicted by three-dimensional solid models. However, it is limited to the prediction of displacements, stability, in-plane stresses in the stiff layers, and transverse shear deformation in the soft interlayer. Predictions of out-of-plane stresses were not presented.

In this chapter, a new penalty stiffness formulation for recovering out-of-plane stresses in layer-wise classical shell models of composite laminates is presented. The proposed formulation expresses the penalty stiffness as a function of the mechanical properties and the thickness of the resin-rich regions between adjacent plies. The objective of this work is to extend the previously developed structural-element-based three-dimensional model for composite laminates while satisfying the following requirements:

1. It retains the key advantage of the previous formulation by eliminating the cohesive-zone mesh-density limitation in delamination analysis;

2. It can accurately and efficiently recover the three-dimensional stress field in an arbitrary multi-ply composite laminate.

The rest of the chapter is organized as follows: Section 3.2 presents the proposed method in detail. Section 3.3 demonstrates the performance of these elements on a series of uniaxial extension benchmarks for both cross-ply and angle-ply laminates. In the end, Section 3.4 concludes this work and discusses some potential future work.

3.2. METHOD

THE proposed formulation is based on the Kirchhoff–Love hypothesis and employs a layer-wise representation of composite laminates. Each ply is modeled using a cubic shell element, while adjacent plies are connected by structural cohesive elements, as shown in Figure 3.1. The detailed derivation of the cubic shell element and the compatible structural cohesive element formulations is presented in Ai et al. [15].

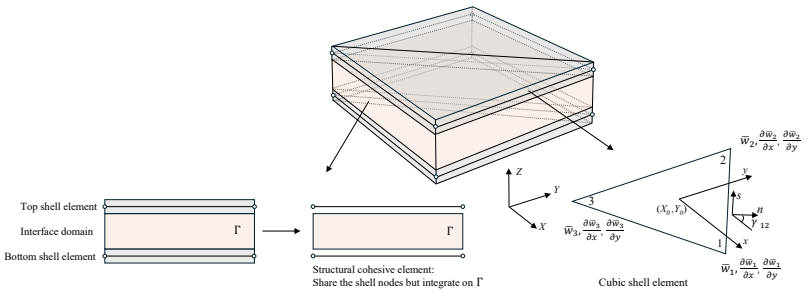

Figure 3.1: Triangular cubic structural element

3.2.1. 3D STRESS CALCULATION IN COHESIVE ELEMENTS

MOST 3D composite failure criteria, such as those proposed by Hashin [24], Puck [25], and Pinho [26, 27], require the complete stress state within each ply. However, cubic shell elements based on the Kirchhoff-Love hypothesis provide only the in-plane stress components. The out-of-plane stresses can be recovered from the tractions transmitted by the structural cohesive elements.

Based on the shell thickness and kinematic equations, it is possible to determine the displacements at the interfaces of two adjacent shell elements. Consider an infinitesimal element located adjacent to the interface of the upper shell element, as illustrated in Figure 3.2. Three stress components act on the surface in contact with the cohesive element, namely the out-of-plane normal stress (denoted as σ_z) and the two transverse shear stresses (denoted as τ_{xz} and τ_{zy}). By equilibrium, these stresses are equal in magnitude and opposite in direction to the corresponding cohesive tractions (τ_n, τ_s, and τ_t), respectively.

$$\sigma_z = -\tau_n \tag{3.1}$$

$$\tau_{zx} = -\tau_s \tag{3.2}$$

$$\tau_{zy} = -\tau_t \tag{3.3}$$

Therefore, the normal and shear tractions transmitted by the cohesive elements provide the out-of-plane components of the three-dimensional stress tensor.

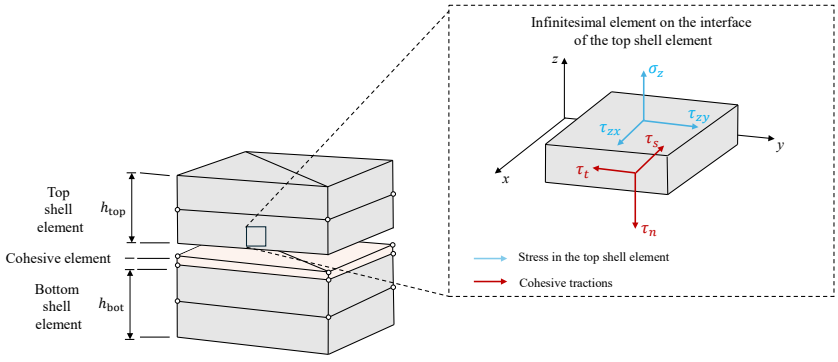

Figure 3.2: Coordinate system and DoFs for the triangular cubic plate element

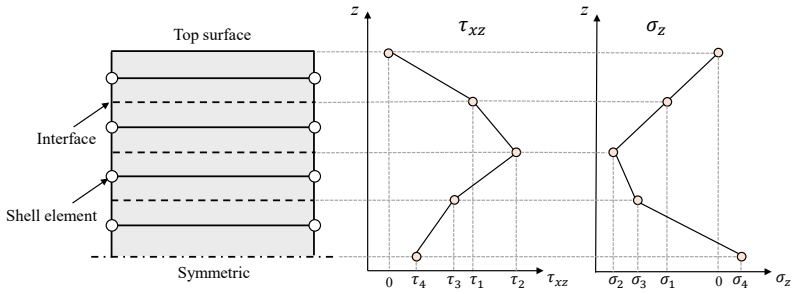

Figure 3.3: Interpolation method of the structural elements along thickness

3.2.2. INTERPOLATION METHOD OF STRESS DISTRIBUTION

THE cohesive tractions described in Section 3.2.1 are evaluated at the integration points of the cohesive elements. In this work, each cohesive element contains 13 integration points. Since the traction values are not directly available at the nodes, they are obtained by substituting the node coordinates into the shape function of the element. As each node is shared by multiple adjacent elements, the nodal traction is calculated by averaging the extrapolated values from all neighboring elements associated with this node. Following this procedure, the interfacial stresses at every ply interface can be determined. The through-thickness distributions of the out-of-plane normal and shear stresses are then derived by interpolation. For simplicity, a linear interpolation is adopted between adjacent cohesive interfaces, as shown in Figure 3.3. The implementation and validation of this interpolation procedure are presented in Section 3.3.

3.2.3. PENALTY STIFFNESS OF COHESIVE ELEMENTS

THE cohesive elements are characterized based on a proper traction separation law, which describes a constitutive relation linking the opening displacements and stresses

under the three fracture modes. In this work, a bilinear traction-separation law is adopted. The law is defined by three parameters: the interface strength, τ, the fracture toughness, G_c, and the penalty stiffness, K. The interface strength and fracture toughness are used for damage initiation and evolution, whereas the penalty stiffness determines the elastic response before damage initiation. Since the present study focuses on the recovery of the three-dimensional stress field, all cohesive elements are assumed to remain undamaged. Accordingly, the displacement, δ, is required to remain below the damage initiation displacement, Δ_0.

As reviewed in Section 3.1, Turon et al. [18] proposed an analytical formulation for determining the cohesive penalty stiffness. In their formulation, zero-thickness cohesive elements are inserted between adjacent three-dimensional solid elements. The penalty stiffness is derived as a function of the material parameters and a coefficient, α, which is defined from the experimental results:

$$K_n = \frac{\alpha E_3}{h} \tag{3.4}$$

$$K_s = K_t = \frac{\alpha G_{13}}{h} \tag{3.5}$$

where h is the thickness of the laminate and coefficient α typically assumes a value of 50 [18].

Subsequently, Bazilevs et al. [22] proposed a modified formulation for the penalty stiffness based on the Reissner-Mindlin theory. The formulation is derived by reproducing the deformation of solid elements under simple shear loading, as shown in Figure 3.4:

$$K_s = K_t = \frac{G_{13}}{h_{\text{top}}/2 + h_{\text{bot}}/2} \tag{3.6}$$

where h_{top} and h_{bot} correspond to the thicknesses of the top and bottom laminates, respectively. As discussed in Section 3.1, no corresponding formulation was proposed for the normal penalty stiffness. Furthermore, Equation 3.6 is derived under the assumption of simple shear deformation of the solid element and is therefore inconsistent with the kinematic assumptions of the Kirchhoff–Love shell theory. The formulations proposed in this work for the normal and shear penalty stiffnesses are presented in the following sections.

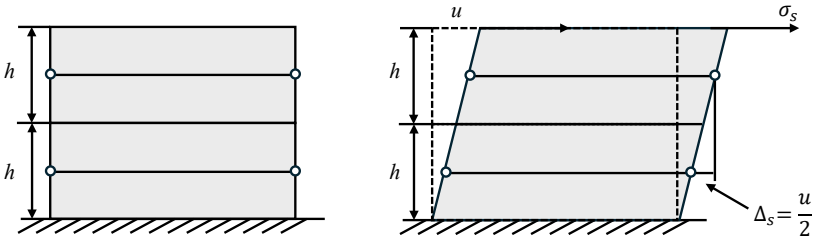

Figure 3.4: State of simple shear in the cohesive model

NORMAL PENALTY STIFFNESS K_n

Consider a structural element subjected to a uniform normal tensile traction acting on the top surface of the shell element, as illustrated in Figure 3.5. Assuming that the deformation is concentrated in the resin-rich layer, the out-of-plane normal stress can be expressed as:

$$\begin{aligned} \sigma_n &= E_3 \varepsilon_z \\ &= \frac{E_3 w}{2 h_{\text{rr}}} \end{aligned} \tag{3.7}$$

where w is the total normal displacement of shell elements, E_3 and h_{rr} are the out-of-plane elastic modulus and thickness of the resin-rich layer, respectively.

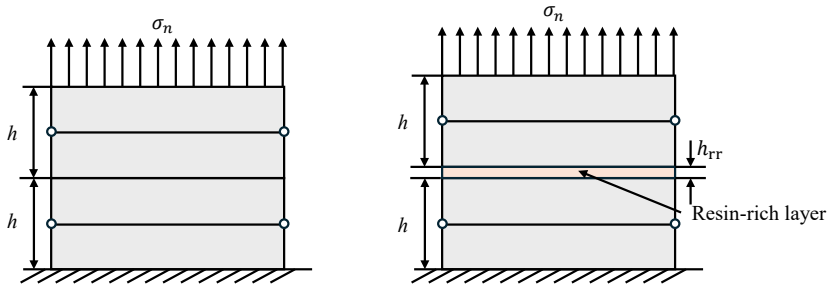

Figure 3.5: State of tensile with resin-rich layer

The cohesive normal jump displacement, Δ_n, is defined as the displacement difference between the nodes of the adjacent shell elements rather than the displacement at the shell surfaces. Since the displacement w represents the displacement between the shell surfaces, the normal jump displacement can be expressed as:

$$\Delta_n = \frac{w}{2} \tag{3.8}$$

Combining Equations 3.7 and 3.8, the normal penalty stiffness is obtained as:

$$\begin{aligned} K_n &= \frac{\sigma_n}{\Delta_n} \\ &= \frac{E_3}{h_{\text{rr}}} \end{aligned} \tag{3.9}$$

SHEAR PENALTY STIFFNESS, K_s AND K_t

To determine the shear penalty stiffnesses, K_s and K_t, a different kinematic assumption from those adopted in previous studies is employed. Consistent with the Kirchhoff-Love hypothesis, the shell normals remain perpendicular to the mid-plane throughout the deformation. Furthermore, the deformation produced by transverse shear loading is assumed to occur only within the resin-rich region, as illustrated in Figure 3.6. Assuming the resin-rich

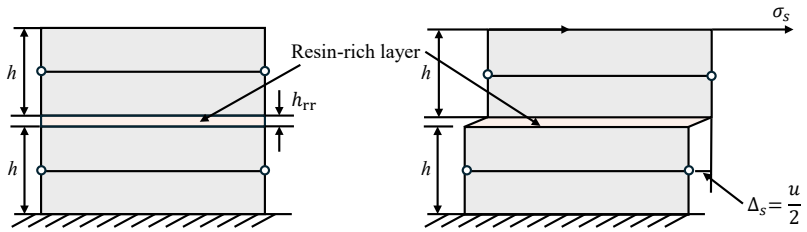

Figure 3.6: State of simple shear with resin-rich layer

layer material is isotropic, the transverse shear strain is uniform and can be expressed as:

$$\gamma = \frac{u}{2h_{rr}} \tag{3.10}$$

The corresponding transverse shear stress is given by:

$$\sigma_s = G\gamma = \frac{Gu}{2h_{rr}} \tag{3.11}$$

where G is the shear modulus of the resin-rich layer. Similar to the tensile case, the cohesive shear jump displacement Δ_s is:

$$\Delta_s = \frac{u}{2} \tag{3.12}$$

Combining the above relations, the shear penalty stiffness is obtained as

$$\begin{aligned} K_s &= \frac{\sigma_s}{\Delta_s} \\ &= \frac{G}{h_{rr}} \end{aligned} \tag{3.13}$$

3.3. NUMERICAL EXAMPLES

As discussed in Section 3.1, the high stress gradients near the free edge are commonly attributed to stress singularities. This section aims to verify the proposed formulation by recovering the three-dimensional stress field and evaluating its ability to predict free-edge stresses. To achieve these objectives, a uniform axial extension (UAE) model is adopted for verification. For cross-ply and angle-ply laminates, the predicted stress distributions are compared with analytical solutions and finite element results obtained using C3D8 solid elements in Abaqus. For general laminate lay-ups, the comparisons are performed only against the C3D8 solid-element model. The detailed results are presented in the following sections.

3.3.1. UNIFORM AXIAL EXTENSION MODEL

THE geometric configuration of the composite laminate is shown in Figure 3.7. The laminate has a total thickness of h, a width of $2b$, and a length of L. It consists of multiple

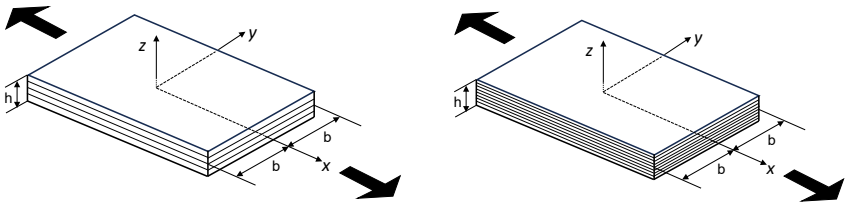

(a) 4-ply model (b) 8-ply model

Figure 3.7: Geometry of the uniform axial extension laminate model

plies, each with a thickness of h_0. For the four-ply laminates considered in Sections 3.3.3 and 3.3.4, the half-width is taken as $b = 4h_0$. For the eight-ply laminates, $b = 16h_0$. Each ply is modeled using a single layer of cubic shell elements, while adjacent plies are connected by cubic structural cohesive elements. The origin of the global coordinate system is located at the center of the laminate. The X-axis is along the length of the model, the Y-axis is along the width of the model, and the Z-axis is through-the-thickness direction of the model. A uniform displacement, u, is applied in the longitudinal direction. Rigid-body motion is prevented by imposing pin constraints at the center of the laminate.

3.3.2. POSTPROCESSING TECHNIQUE FOR STRESS DISTRIBUTION ALONG THE WIDTH OF LAMINATES

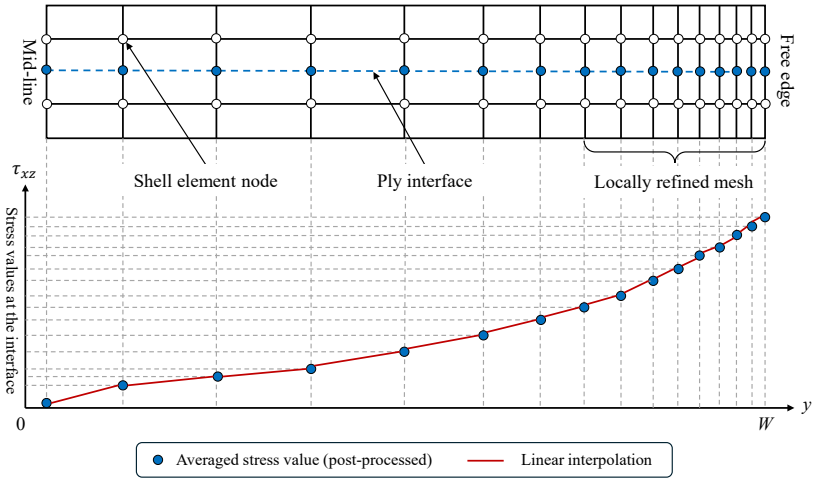

Figure 3.8: Interpolation method of the structural elements along the width

To obtain the stress distribution along the laminate width at a given ply interface, the mesh is locally refined near the free edge. The nodal stresses are then evaluated using the averaging procedure described in Section 3.2.2. The resulting nodal values are plotted

and connected by straight line segments to reconstruct the stress distribution. The post-processing procedure for the shear stress (τ_{xz}) distribution at the mid-plane is illustrated in Figure 3.8.

3.3.3. RESULTS FOR CROSS-PLY LAMINATES $[0°/90°]_s$

CROSS-ply $[0°/90°]_s$ laminate has been widely used as a benchmark for free-edge stress analysis [28, 29]. In the present study, it is adopted to evaluate the out-of-plane normal stress, σ_z, and transverse shear stress, τ_{yz}, at the $(0°/90°)$ interface and the laminate mid-plane. The geometry of the 4-ply laminate model is illustrated in Figure 3.7, and the corresponding geometric parameters are presented in Table 3.1. The material properties of the cross-ply laminate are summarized in Table 3.2.

Table 3.1: Geometric parameters for the 4-layer laminate model

Parameter	h_0	h	b (width)
value (mm)	0.125	0.5	1

The elastic modulus and Poisson's ratio of the resin-rich layer are taken from Burhan et al. [30], while the thickness of the resin-rich layer is taken from Grande et al. [31]. The corresponding penalty stiffnesses are calculated using Equations. 3.9 and 3.13. The resulting values are listed in Table 3.3. It should be noted that the exact properties of the resin-rich layer are unavailable for the laminates considered. Therefore, the values reported in Table 3.3 are approximate and are estimated from similar material. The influence of these parameters is investigated through a sensitivity analysis in the following section.

Table 3.2: Material properties of cross-ply laminate [32]

Material properties of $[0°/90°]_s$ laminate		
E_{11}= 137900 MPa	E_{22}= 14500 MPa	E_{33} = 14500 MPa
ν_{12} = 0.21	ν_{13} = 0.21	ν_{23} = 0.21
G_{12} = 5900 MPa	G_{13} = 5900 MPa	G_{23} = 5900 MPa

Table 3.3: Penalty stiffness obtained by resin-rich layer

E $(\mathrm{N/mm^2})$	ν	RRL thickness $(10^{-3}$inch)	RRL thickness (mm)	$\mathbf{K}_n$ $(\mathrm{N/mm^3})$	$\mathbf{K}_t$ $(\mathrm{N/mm^3})$	$\mathbf{K}_s$ $(\mathrm{N/mm^3})$
3000	0.3	0.9	0.02286	131233	50474	50474

NUMERICAL RESULTS OBTAINED BY THE PROPOSED PENALTY STIFFNESS

Figure 3.9 compares the interlaminar normal stress, σ_z, at the laminate mid-plane. The analytical solution is compared with the proposed structural-element model for a resin-rich

layer thickness of 0.9×10^{-3} inch. The black solid line represents the analytical solution reported by Pagano [32], while the orange solid line corresponds to the results obtained using the proposed structural elements. It can be found that the numerical results agree well with the analytical solution for $y/b < 0.5$. As y/b exceeds 0.5, a small deviation is observed. Specifically, the maximum stress at the free edge predicted by the proposed method is slightly lower than the analytical solution.

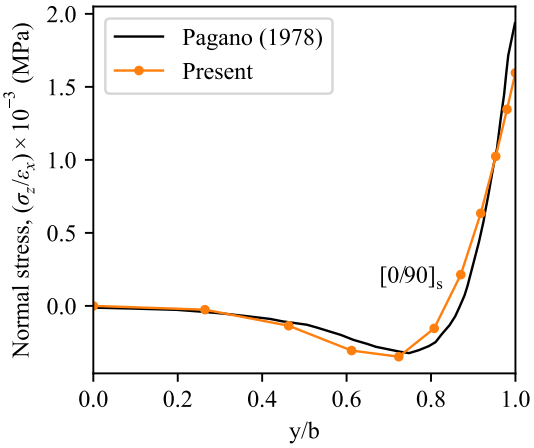

Figure 3.9: Interlaminar normal stress σ_z at the mid-plane

Figure 3.10 compares the numerical and analytical distributions of the interlaminar normal stress, σ_z, at the $(0°/90°)$ interface. The agreement is even better than that obtained at the laminate mid-plane. For $y/b < 0.9$, the numerical results are identical to the analytical solution. Unlike the mid-plane results, the maximum stress at the free edge is also accurately predicted, remaining very close to the analytical solution.

Finally, Figure 3.11 compares the interlaminar shear stress, τ_{yz}, at the $(0°/90°)$ interface. Overall, the numerical and analytical solutions are in good agreement. An obvious discrepancy is observed only at the free edge, where the numerical stress does not reduce to the zero value predicted by the analytical solution. This difference is attributed to the nodal interpolation procedure employed in the post-processing stage.

The above results demonstrate that, when the resin-rich layer properties listed in Table 3.3 are adopted, the predicted stress distributions are in good agreement with the analytical solutions. In practical applications, the material properties and thickness of the resin-rich layer are generally uncertain. As shown in Equations 3.9 and 3.13, the penalty stiffness is governed primarily by these two parameters. A sensitivity analysis is therefore conducted to evaluate their influence on the predicted stress distributions.

SENSITIVITY ANALYSIS: RESIN-RICH LAYER THICKNESS

Grande et al. [31] measured the average thickness of the resin-rich layer through quantitative analysis of polished cross-sectional micrographs. Three representative resin-rich layer thicknesses, 0.6×10^{-3}, 0.7×10^{-3}, and 0.9×10^{-3} inch, were reported. The corresponding

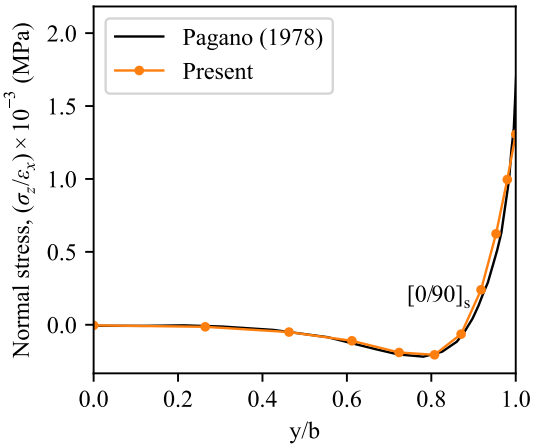

Figure 3.10: Interlaminar normal stress σ_z at the interface between $0°$ and $90°$

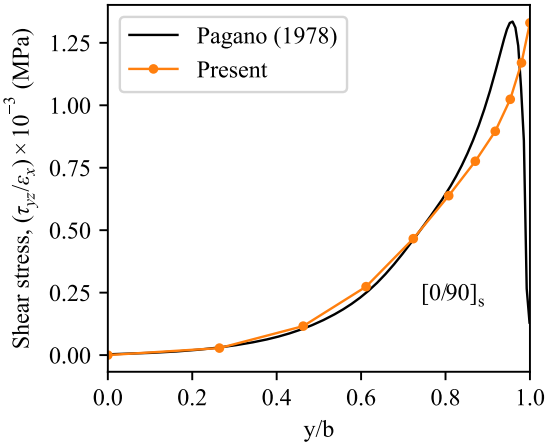

Figure 3.11: Interlaminar shear stress τ_{yz} at the interface between $0°$ and $90°$

penalty stiffnesses were calculated for each thickness using the proposed formulation, and the resulting values are summarized in Table 3.4.

The T-0.6 and T-0.7 models have the same geometry and boundary conditions as the T-0.9 model. To evaluate the influence of the resin-rich layer thickness, the predicted stress distributions are compared with the analytical solution and the results obtained from the T-0.9 model. The comparisons include the interlaminar normal stress, σ_z, at the laminate mid-plane and the $(0°/90°)$ interface, as well as the interlaminar shear stress, τ_{yz}, at the $(0°/90°)$ interface. The corresponding results are presented in Figure 3.12.

Only small differences are observed among the three models, and all predictions remain in close agreement with the analytical solution. This demonstrates that the proposed

Table 3.4: Normal and shear penalty stiffness values for different resin-rich layer thicknesses

Model name	RRL thickness (10^{-3}inch)	RRL thickness (mm)	$\mathbf{K}_n$ ($\mathrm{N/mm^3}$)	$\mathbf{K}_t$ ($\mathrm{N/mm^3}$)	$\mathbf{K}_s$ ($\mathrm{N/mm^3}$)
T-0.9	0.9	0.02286	131233	50474	50474
T-0.7	0.7	0.01778	168728	64895	64895
T-0.6	0.6	0.01524	196850	75711	75711

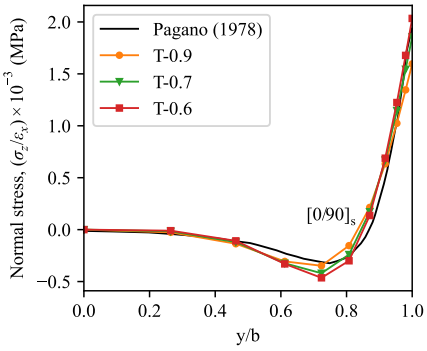

(a) σ_z at the central plane

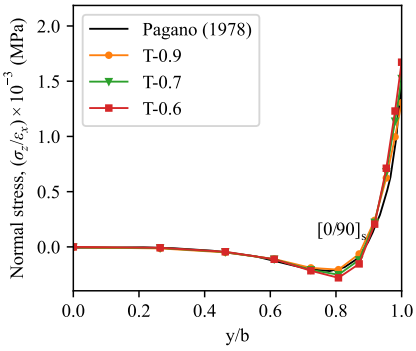

(b) σ_z at the interface between 0° and 90°

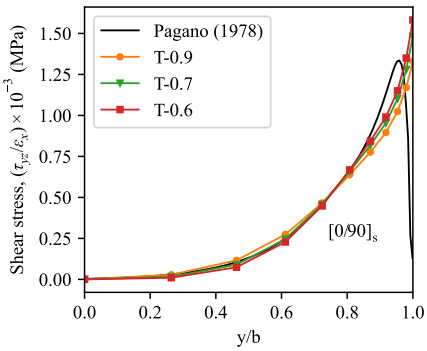

(c) τ_{yz} at the interface between 0° and 90°

Figure 3.12: Distributions of interlaminar normal and shear stresses with different resin-rich layer thickness

penalty stiffness formulation is insensitive to the variation in resin-rich layer (RRL) thickness within the range reported by Grande et al. [31]. In practical applications, once the material properties and thickness of the RRL are measured, the corresponding penalty stiffnesses can be determined directly from Equations 3.9 and 3.13. Based on these results, an RRL thickness of 0.9×10^{-3} inch is adopted in the subsequent validation studies.

SENSITIVITY ANALYSIS: ELASTIC MODULUS AND POISSON'S RATIO

In the study by Burhan et al. [30], the resin-rich layer was assumed to have an elastic modulus of $E = 3\,\text{GPa}$ and a Poisson's ratio of $\nu = 0.3$. In practice applications, the mechanical properties of the resin-rich layer vary with the epoxy resins employed [33–35]. Gupta et al. [34] reported an elastic modulus ranging from 2.7 to 4.1 GPa. Krueger and Minguet [33] reported $E = 4.67\,\text{GPa}$ and $\nu = 0.37$ for the 8552 epoxy resin in the IM7/8552 composite. Based on these data, this study adopts ranges of $3-5\,\text{GPa}$ for the resin-rich layer elastic modulus and $0.2-0.4$ for Poisson's ratio in the sensitivity analysis. The corresponding penalty stiffnesses are summarized in Tables 3.5 and 3.6, respectively.

Table 3.5: Normal and shear penalty stiffness values for different resin-rich layer elastic moduli

Model name	Elastic modulus (N/mm^2)	RRL thickness (10^{-3}inch)	$\mathbf{K}_n$ (N/mm^3)	$\mathbf{K}_t$ (N/mm^3)	$\mathbf{K}_s$ (N/mm^3)
E-3000	3000	0.9	131233	50474	50474
E-4000	4000	0.9	174978	67299	67299
E-5000	5000	0.9	218722	84124	84124

Table 3.6: Normal and shear penalty stiffness values for different resin-rich layer Poisson's ratios

Model name	Poisson's ratio	RRL thickness (10^{-3}inch)	$\mathbf{K}_n$ (N/mm^3)	$\mathbf{K}_t$ (N/mm^3)	$\mathbf{K}_s$ (N/mm^3)
Nu-0.3	0.3	0.9	131233	50474	50474
Nu-0.2	0.2	0.9	131233	54680	54680
Nu-0.4	0.4	0.9	131233	46869	46869

Figure 3.13 presents the interlaminar normal stress, σ_z, and the interlaminar shear stress, τ_{yz}, for different elastic moduli of the resin-rich layer. The stress distributions are evaluated at the laminate mid-plane and the $(0°/90°)$ interface over the range $0 \leq y/b \leq 1$. As shown in the figure, only small differences are observed among the different elastic modulus cases. Therefore, the influence of the elastic modulus is relatively small. All numerical results remain in good agreement with the analytical solution.

Figure 3.14 presents the interlaminar stress distributions obtained for different Poisson's ratios. Compared with Figure 3.13, the influence of Poisson's ratio is even smaller. No significant differences are observed among the different cases, either at the laminate mid-plane or at the $(0°/90°)$ interface. These results indicate that the influence of Poisson's ratio on the predicted stress distributions is negligible. This behavior can be attributed to the fact that Poisson's ratio affects only the shear modulus, while the normal penalty stiffness, K_n, remains unchanged. Therefore, the variation in the interlaminar normal stress (σ_z) is negligible. As for the shear penalty stiffness, the variations are also relatively small.

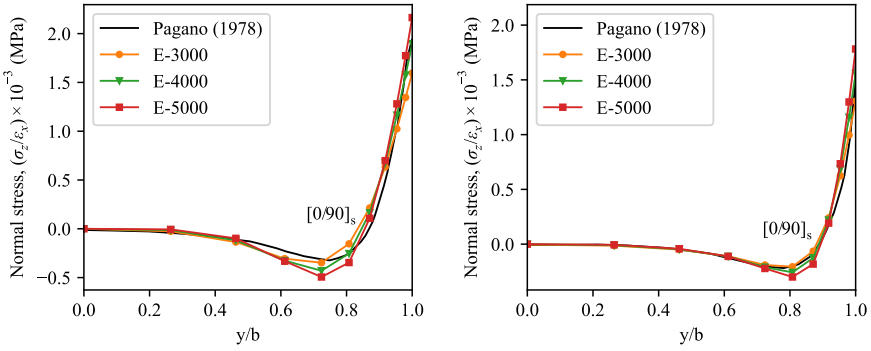

(a) σ_z at the central plane

(b) σ_z at the interface between 0° and 90°

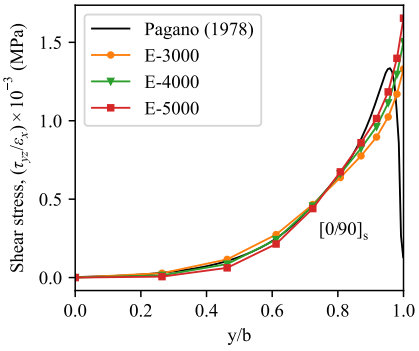

(c) τ_{yz} at the interface between 0° and 90°

Figure 3.13: Distributions of interlaminar normal and shear stresses with different elastic moduli

Therefore, the predicted shear stress, τ_{yz}, is insensitive to Poisson's ratio.

In summary, the predicted stress distributions exhibit only minor variations over the range of epoxy resin properties considered. The predicted stress distributions remain in close agreement with the analytical solution. For consistency with the previous validation cases, the resin-rich layer properties are taken as $E = 3000\,\text{MPa}$ and $\nu = 0.3$ in all subsequent analyses.

MESH CONVERGENCE ANALYSIS OF THE SOLID-ELEMENT MODEL

In this section, a mesh convergence study of the solid-element models is presented. The study has two objectives. The first is to compare the predictions of the solid-element model, the proposed structural-element model, and the available analytical solutions. This comparison provides a reference for assessing the accuracy of the solid-element model. The second is to establish a reliable benchmark for problems without analytical solutions. This is particularly important for predicting through-thickness stress distributions in complex laminate lay-ups, such as the general laminate configurations presented in Section 3.3.6. In these cases, the proposed formulation is validated through quantitative comparisons with high-fidelity solid-element simulations.

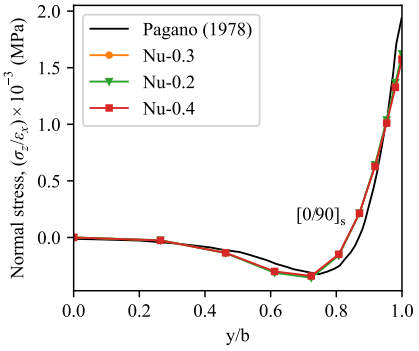

(a) σ_z at the mid-plane

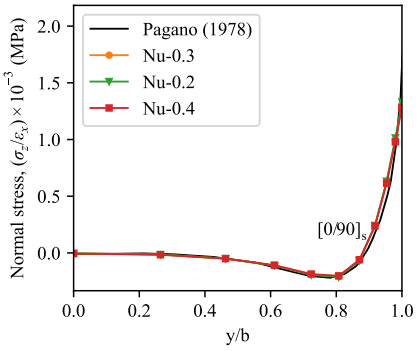

(b) σ_z at the interface between 0° and 90°

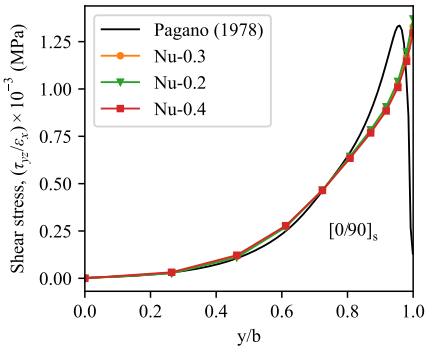

(c) τ_{yz} at the interface between 0° and 90°

Figure 3.14: Distributions of interlaminar normal and shear stresses with different Poisson's ratios

The mesh convergence study focuses only on mesh refinement in the through-thickness direction. The mesh density along the laminate width is identical to that used in the structural-element model. Three through-thickness mesh schemes are considered, as illustrated in Figure 3.15: (1) one solid element per ply (four elements through the thickness); (2) four solid elements per ply; and (3) eight solid elements per ply.

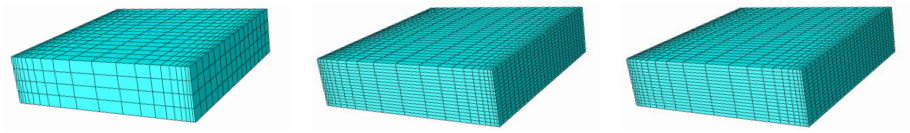

(a) Mesh size: 1 element per layer (b) Mesh size: 4 elements per layer (c) Mesh size: 8 elements per layer

Figure 3.15: Mesh sizes of solid-element model

Figure 3.16 presents the stress distributions at $(0^\circ/90^\circ)$ interface for different through-thickness mesh densities. The results show that employing only one solid element per ply does not provide sufficient accuracy. In contrast, refining the mesh to four or eight elements

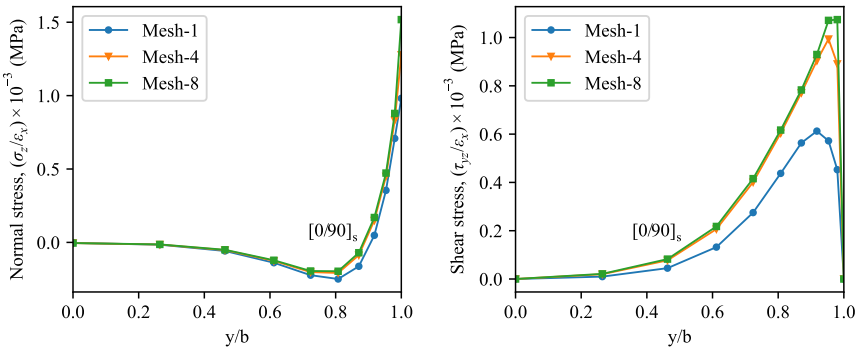

(a) Interlaminar normal stress σ_z

(b) Interlaminar shear stress τ_{yz}

Figure 3.16: Interlaminar stress distributions at the interface between 0° and 90°

per ply results in a clear improvement. This improvement is particularly evident for the interlaminar shear stress, τ_{yz}, shown in Figure 3.16b. Based on these results, all solid-element models used in this study employ eight elements per ply through the thickness to ensure accurate stress predictions.

COMPARISON WITH ANALYTICAL AND SOLID-ELEMENT SOLUTIONS

The previous validation results are summarized through direct comparisons of the analytical solutions, the proposed structural-element results, and the solid-element results. The results are presented in Figures 3.17a, 3.17b, and 3.17c. The comparisons show that both numerical models accurately reproduce the analytical stress distributions.

3.3.4. RESULTS FOR ANGLE-PLY LAMINATES $[+\theta/-\theta]_s$

IN this section, the stress distributions in the $[+\theta/-\theta]_s$ angle-ply laminate are investigated. The geometric dimensions and boundary conditions are identical to those of the cross-ply laminate presented in Section 3.3.3. However, different composite material properties are adopted. The corresponding material properties are listed in Table 3.7.

Table 3.7: Material properties of angle-ply laminate [36]

Material properties of $[+\theta/-\theta]_s$ laminate		
E_{11}= 13200 MPa	E_{22}= 10800 MPa	E_{33} = 10800 MPa
ν_{12} = 0.238	ν_{13} = 0.238	ν_{23} = 0.49
G_{12} = 5650 MPa	G_{13} = 5650 MPa	G_{23} = 3360 MPa

Unlike the cross-ply laminate, the interlaminar stresses τ_{yz} and σ_z in the $[+\theta/-\theta]_s$ laminate are negligible, as discussed in Subsection 3.3.3. In contrast, previous studies [37–40] have shown that the interlaminar shear stress, τ_{xz}, becomes significant near the free edge of the $[+45°/-45°]$ interface. Therefore, the stress distributions are normalized with

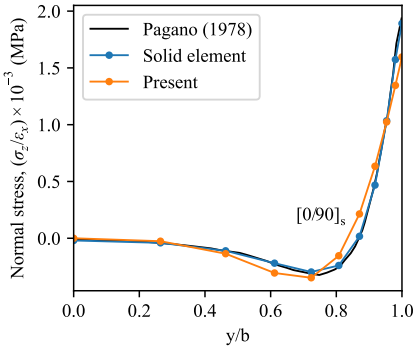

(a) σ_z at the central plane

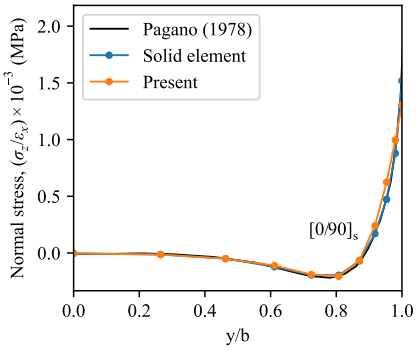

(b) σ_z at the interface between 0° and 90°

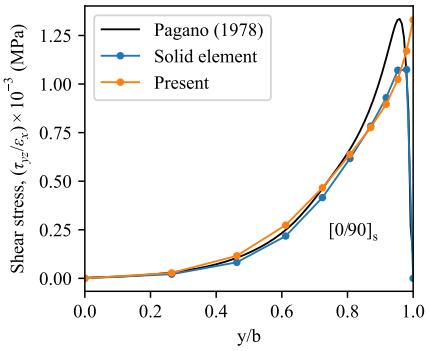

(c) τ_{yz} at the interface between 0° and 90°

Figure 3.17: Results comparison for the distributions of interlaminar normal and shear stresses

respect to the corresponding peak values for each lay-up angle. The normalized results are then compared with the analytical solution [36] and the finite element results reported by Herakovich [41]. The corresponding comparison results are presented in Figure 3.18.

Figure 3.18 shows that the normalized interlaminar shear stress, $\tau_{xz}/\max(\tau_{xz})$, predicted by the proposed method. The result is in excellent agreement with both the analytical solutions and the finite element results. Combined with the validation results for the cross-ply laminates, these results further confirm the accuracy of the proposed formulation. Therefore, the proposed method provides a computationally efficient alternative to solid-element models for predicting interlaminar stress distributions.

3.3.5. RESULTS FOR QUASI-ISOTROPIC LAMINATES $[+45^\circ/0^\circ/-45^\circ/90^\circ]_s$

IN Sections 3.3.3 and 3.3.4, the proposed method was validated using four-ply laminates with relatively simple stacking sequences. In this section, the method is further validated using the eight-ply quasi-isotropic laminate proposed by Reddy [42]. The predicted stress distributions are compared with the corresponding analytical solutions. It should be noted that the geometry of this model, shown in Figure 3.19, differs from that described in

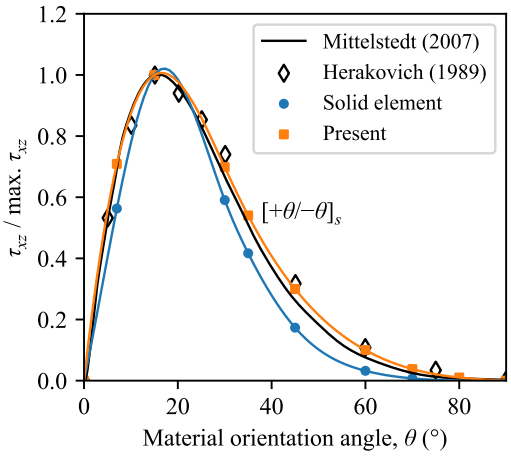

Figure 3.18: Interlaminar shear stress τ_{xz} at the $+\theta/-\theta$ interface ($z = h_0$)

Section 3.3.1. The specific geometric parameters are summarized below:

$$(45/0/-45/90)_s \text{ laminate} : h = 8h_0,\ b = 60h_0,\ a = 10b \tag{3.14}$$

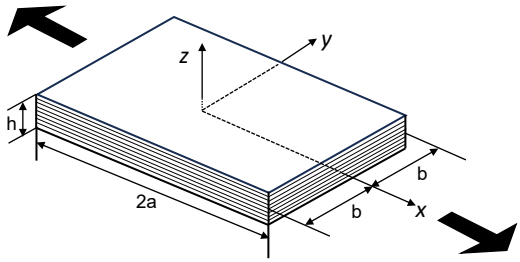

Figure 3.19: Quasi-isotropic laminate geometry

In the present study, the thickness of each ply is set to $h_0 = 0.125\,\text{mm}$. The remaining geometric dimensions of the laminate are determined from Equation 3.14, and the corresponding values are listed in Table 3.8. In addition, the material properties are summarized in Table 3.9. To achieve the tensile strain of $\varepsilon_x = 0.01$ adopted by Reddy [42], a tensile displacement of $0.75\,\text{mm}$ is applied at both ends of the laminate.

A comparison between the interlaminar stresses (σ_z and τ_{xz}) predicted by the proposed method and those obtained from Mittelstedt's analytical solution [36] is shown in Figure 3.20. The comparison is performed through the laminate thickness at the location ($x = -0.0115a, y = 0.998b$). As observed, the results obtained using the proposed numerical method are in good agreement with those predicted by Mittelstedt's layerwise analytical

Table 3.8: Geometric parameters of the quasi-isotropic laminate benchmark model

Parameter	h_0	h	b (width)	a (length)
value (mm)	0.125	1	7.5	75

Table 3.9: Material properties of the quasi-isotropic laminate [42]

Material properties of $[+45/0/-45/90]_s$ **laminate**		
E_{11}= 134448 MPa	E_{22}= 10204 MPa	E_{33} = 10204 MPa
ν_{12} = 0.3	ν_{13} = 0.3	ν_{23} = 0.3
G_{12} = 5516 MPa	G_{13} = 5516 MPa	G_{23} = 5516 MPa

method. The orange markers in Figure 3.20 represent the stress values at the ply interfaces. All interface stresses lie on or very close to the analytical solution. The orange solid line is obtained by applying the linear interpolation procedure described in Section 3.2.2. As shown in the right panel, the predicted distribution of the interlaminar shear stress (τ_{xz}) agrees well with the analytical solution. In contrast, small discrepancies are observed in the normal stress (σ_z). These discrepancies arise because the stress variation between several adjacent interfaces is non-monotonic and cannot be accurately captured by linear interpolation. Employing a higher-order interpolation scheme is expected to further improve the agreement with the analytical solution.

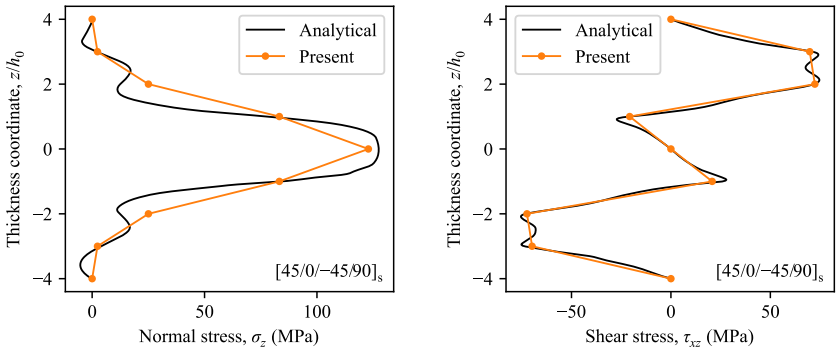

(a) Interlaminar normal stress σ_z

(b) Interlaminar shear stress τ_{xz}

Figure 3.20: Interlaminar stress distributions through the thickness near the free edge ($y = 0.998b$) in $[45/0/-45/90]_s$ laminate under axial extension

A limitation of the proposed method is observed at the $[0°/-45°]$ interface, where the predicted σ_z values are slightly higher than the analytical solution. This discrepancy is attributed to the use of a single shell element to represent each ply, without additional integration points through the thickness. Complex through-thickness stress variations cannot be

captured exactly. Nevertheless, the overall agreement with the analytical solution remains good. These results demonstrate the reliability of the proposed method. They also confirm its applicability to thick laminates containing four or more plies, which are commonly considered in free-edge stress analyses of composite laminates.

3.3.6. RESULTS FOR LAMINATES WITH GENERAL LAY-UPS

THE previous validation cases focused on laminate configurations with available analytical solutions. In practical engineering applications, composite laminates often employ complex or arbitrary stacking sequences for which no analytical solutions are available. Therefore, the proposed method is further validated using two arbitrary laminate lay-ups inspired by Andakhshideh and Tahani [43]. The two stacking sequences considered are: (a) $[0°/+55°/+35°/-35°]_s$ and (b) $[0°/+30°/-45°/+45°]_s$. Since both laminates contain eight plies, the same geometric dimensions, material properties, and loading conditions as those described in Section 3.3.5 are adopted.

$[0°/+55°/+35°/-35°]_s$ LAY-UP LAMINATE

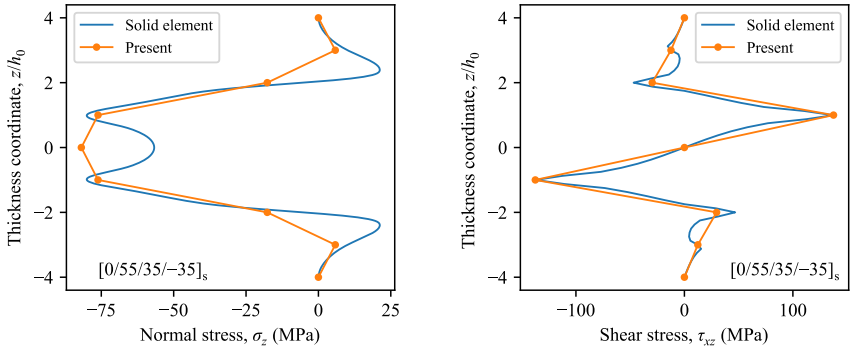

(a) Normal stress σ_z

(b) Shear stress τ_{xz}

Figure 3.21: Through-thickness distributions of interlaminar stresses in the $[0°/+55°/+35°/-35°]_s$ laminate ($y = 0.998b$) under axial extension

Figure 3.21 compares the through-thickness distributions of the interlaminar normal stress (σ_z) and the interlaminar shear stress (τ_{xz}) for the $[0/55/35/-35]_s$ laminate. The predicted σ_z distribution agrees closely with the solid-element solution. Only small discrepancies are observed in the mid-plane. Therefore, the stress distribution cannot be fully captured by the linear interpolation procedure. Figure 3.21b shows the corresponding interlaminar shear stress distribution. Excellent agreement is obtained throughout the laminate thickness, including at the ply interfaces represented by the orange markers. In conclusion, the proposed method provides predictions of the interlaminar stress distributions that are comparable in accuracy to those obtained using the solid-element model.

Following the through-thickness comparison shown in Figure 3.21, the interlaminar stress distributions along the laminate width are compared at the interface between the $35°$ and $-35°$ plies, as shown in Figure 3.22. The proposed method shows excellent agreement with the solid-element results over the laminate width. In particular, the free-edge

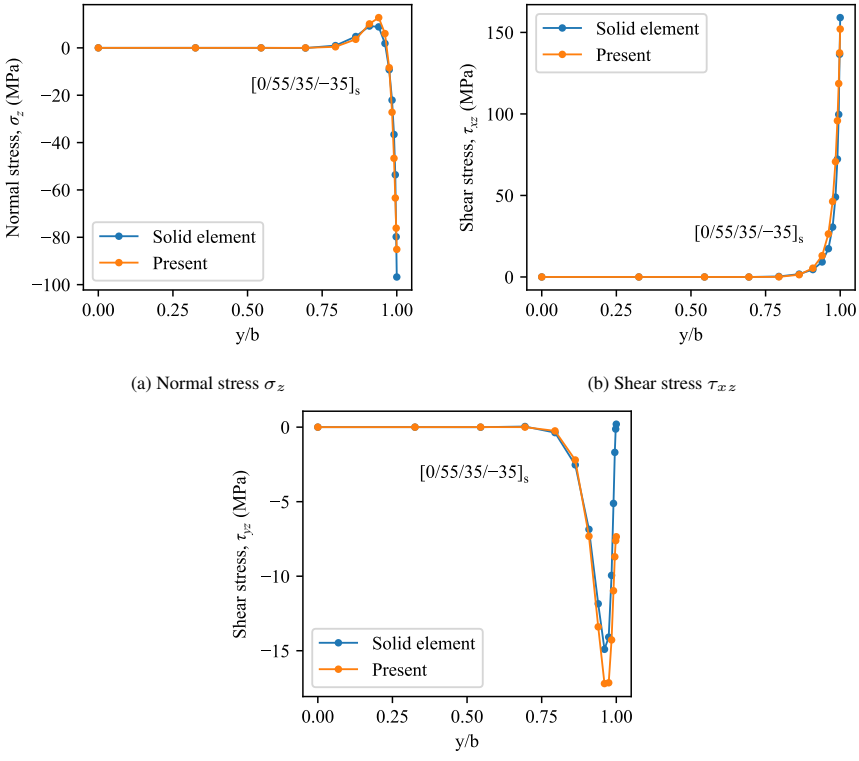

(a) Normal stress σ_z

(b) Shear stress τ_{xz}

(c) Shear stress τ_{yz}

Figure 3.22: Interlaminar stress distributions at the interface between $35°$ and $-35°$

stress singularity is accurately captured. A small discrepancy is observed in the predicted τ_{yz} distribution, although the overall trend remains consistent with the solid-element solution. This discrepancy is attributed to the interpolation procedure rather than the proposed formulation itself.

$[0°/+30°/-45°/+45°]_s$ LAY-UP LAMINATE

After validating the $[0/55/35/-35]_s$ laminate, the $[0/30/-45/45]_s$ laminate is considered to further assess the general applicability of the proposed method. Compared with the previous lay-up, this result shows even better agreement with the solid-element solution because the through-thickness stress distribution is nearly monotonic. The proposed method accurately reproduces the maximum and minimum stresses, as well as the intermediate stress variation. A small discrepancy is observed only for σ_z in the mid-plane, where the predicted values are slightly lower than those of the solid-element model. This difference is attributed to the finer through-thickness discretization of the solid-element model, which captures the local stress singularity more accurately.

Similarly, the interlaminar stress distributions along the laminate width for the $[0/30/-45/45]_s$ laminate are presented in Figure 3.24. The predicted normal stress σ_z follows the same

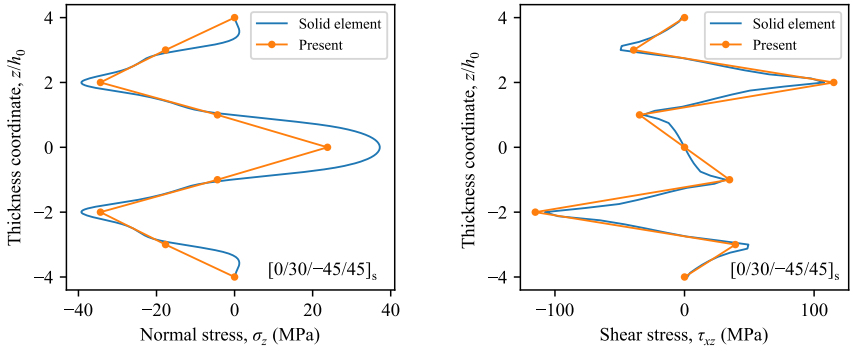

(a) Normal stress σ_z

(b) Shear stress τ_{xz}

Figure 3.23: Through-thickness distributions of interlaminar stresses in the $[0°/+30°/-45°/+45°]_s$ laminate ($y = 0.998b$) under axial extension

trend as the solid-element solution. It begins with a small compressive stress, reaches a tensile peak at approximately $y/b = 0.94$, and then decreases rapidly toward the free edge. The only difference is a slightly higher peak tensile stress predicted by the proposed method. This discrepancy is attributed to the relatively low magnitude of the normal stress in this ply. It makes the prediction more sensitive to numerical interpolation. The interlaminar shear stress distributions are shown in Figures 3.24b and 3.24c. The predicted shear stress τ_{xz} is in excellent agreement with the solid-element results. The proposed method accurately captures both the stress extrema and the free-edge stress singularity. For the remaining shear stress component (τ_{yz}), a small discrepancy is observed only at the free edge. This behavior is consistent with the interpolation-related limitation discussed previously.

NORMAL STRESS DISTRIBUTION AT THE LAMINATE MID-PLANE

As in the previous sections, the stress distribution along the laminate width is also evaluated at the mid-plane. The corresponding results are presented in Figure 3.25. Since the interlaminar shear stresses vanish throughout the mid-plane, only the normal stress (σ_z) is considered. As shown in the figure, the proposed method shows excellent agreement with the solid-element results. It accurately reproduces both the overall stress distribution and the corresponding peak values.

DISPLACEMENT DISTRIBUTION ALONG THE THICKNESS

Finally, the through-thickness displacement distribution is validated, as shown in Figure 3.26. Despite the highly nonlinear through-thickness displacement distribution, the proposed method accurately captures both the overall variation and the displacement values at the ply interfaces. Small discrepancies are observed only in regions where the displacement varies rapidly. These discrepancies are attributed to the linear interpolation procedure. These results further demonstrate the accuracy of the proposed method in recovering the through-thickness displacement field for laminates with general stacking sequences.

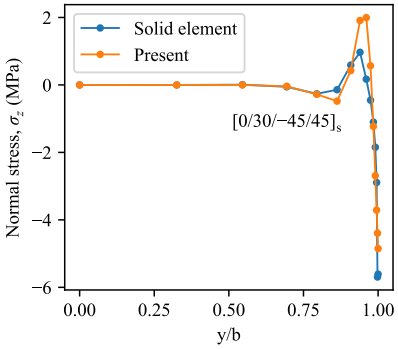

(a) Normal stress σ_z

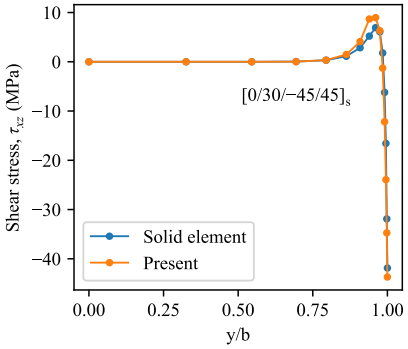

(b) Shear stress τ_{xz}

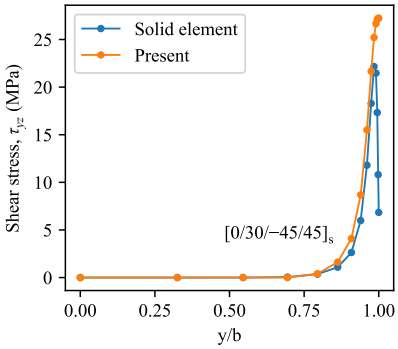

(c) Shear stress τ_{yz}

Figure 3.24: Interlaminar stress distributions along the width direction at the interface between the $-45°$ and $45°$ plies of $[0°/+30°/-45°/+45°]_s$ laminate

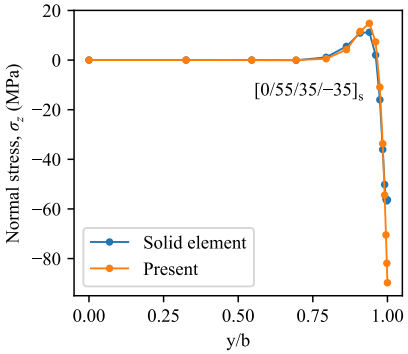

(a) $[0°/+55°/+35°/-35°]_s$ laminate

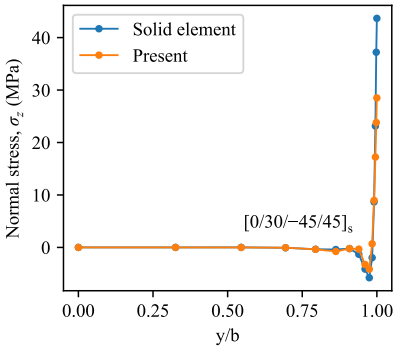

(b) $[0°/+30°/-45°/+45°]_s$ laminate

Figure 3.25: Interlaminar normal stress σ_z at the mid-plane

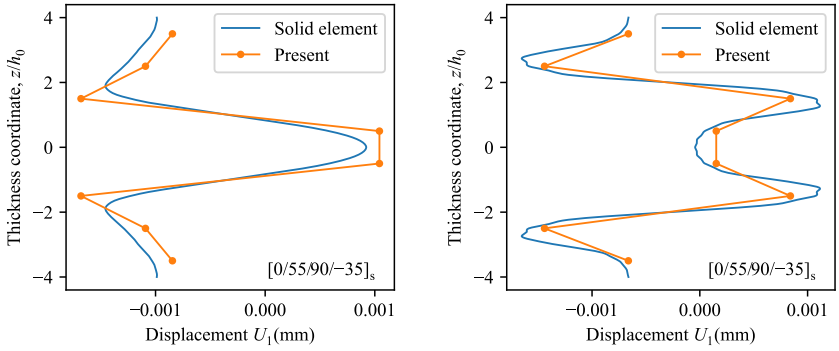

(a) $[0^\circ/+55^\circ/+35^\circ/-35^\circ]_s$ laminate (b) $[0^\circ/+30^\circ/-45^\circ/+45^\circ]_s$ laminate

Figure 3.26: Displacement through the thickness

COMPUTATIONAL PERFORMANCE

The proposed method employs shell elements, with each ply represented by a single element layer. Consequently, the computational cost is significantly lower than that of the corresponding solid-element model. The CPU times are compared in Table 3.10. The proposed method reduces the CPU time per increment by approximately 45% while maintaining accurate predictions of the interlaminar stress distributions.

Table 3.10: Comparison of CPU time per increment (unit: second)

General lay-up laminate	CPU time per increment
Solid model	9.52
Present model	5.21
Reduction by proposed method	45.3%

3.4. SUMMARY AND CONCLUSIONS

THIS work proposes a resin-rich layer based formulation for the cohesive penalty stiffness and demonstrates its application to the recovery of three-dimensional stress fields in shell-element models of composite laminates. The proposed penalty stiffness is derived from the material properties and thickness of the resin-rich layer. It enables accurate simulation of uniform axial extension and free-edge stresses using the structural cohesive elements proposed by Ai et al. [15]. The proposed formulation preserves the Kirchhoff–Love kinematic assumptions while providing a physically based definition of the cohesive penalty stiffness. The proposed method shows low sensitivity to variations in the properties of the resin-rich layer and is applicable to a wide range of composite laminates. It also provides a physically based foundation for the further development of structural cohesive element models.

The proposed method has been validated using cross-ply, angle-ply, quasi-isotropic, and general symmetric laminate configurations. Excellent agreement is obtained with both analytical solutions and solid-element models. Compared with solid-element models, the proposed method requires a much coarser through-thickness discretization while maintaining comparable accuracy in predicting interlaminar stress distributions. These results confirm the applicability of the proposed method to composite laminates with complex stacking sequences.

Finally, the proposed method improves previous work on Kirchhoff-Love ply and cohesive elements for composites modelling, where accurate out-of-plane stresses can now be obtained throughout the thickness of the laminate. It establishes a framework for simulating combined in-plane damage and delamination efficiently on coarse meshes in the future.

REFERENCES

1. Krueger, R. A summary of benchmark examples to assess the performance of quasi-static delamination propagation prediction capabilities in finite element codes. *Journal of Composite Materials* **49,** 3297–3316 (2015).
2. Kaddour, A., Hinton, M. J., Smith, P. A. & Li, S. Mechanical properties and details of composite laminates for the test cases used in the third world-wide failure exercise. *Journal of composite materials* **47,** 2427–2442 (2013).
3. Kassapoglou, C. *Design and analysis of composite structures: with applications to aerospace structures* (Wiley Online Library, 2010).
4. Carrera, E., Pagani, A. & Valvano, S. Shell elements with through-the-thickness variable kinematics for the analysis of laminated composite and sandwich structures. *Composites Part B: Engineering* **111,** 294–314 (2017).
5. Soltani, Z. & Kordkheili, S. A. H. Interlaminar stress analysis of composite shell structures using a geometrically nonlinear layer-wise shell finite element. *Composite Structures* **257,** 113074 (2021).
6. Reddy, J. An evaluation of equivalent-single-layer and layerwise theories of composite laminates. *Composite structures* **25,** 21–35 (1993).
7. Groh, R. & Weaver, P. M. A computationally efficient 2D model for inherently equilibrated 3D stress predictions in heterogeneous laminated plates. Part II: Model validation. *Composite Structures* **156,** 186–217 (2016).
8. Szekrenyes, A. Stress and fracture analysis in delaminated orthotropic composite plates using third-order shear deformation theory. *Applied Mathematical Modelling* **38,** 3897–3916 (2014).
9. Leong, K., Zhi, J., Lee, H., Tan, V. & Tay, T. Adaptive Multi-Fidelity (AMF) modelling of delamination migration under bending. *Composite Structures* **305,** 116549 (2023).
10. Leong, K., Zhi, J., Tan, V., Lee, H. & Tay, T. Adaptive Multi-Fidelity (AMF) modelling of damage in composites under Low-Velocity impact and compression after impact. *Composites Part A: Applied Science and Manufacturing* **178,** 107974 (2024).

11. Barenblatt, G. I. The mathematical theory of equilibrium cracks in brittle fracture. *Advances in applied mechanics* **7,** 55–129 (1962).

12. Dugdale, D. S. Yielding of steel sheets containing slits. *Journal of the Mechanics and Physics of Solids* **8,** 100–104 (1960).

13. Russo, R. & Chen, B. Overcoming the cohesive zone limit in composites delamination: modeling with slender structural elements and higher-order adaptive integration. *International Journal for Numerical Methods in Engineering* **121,** 5511–5545 (2020).

14. Balducci, G. T. & Chen, B. Overcoming the cohesive zone limit in the modelling of composites delamination with TUBA cohesive elements. *Composites Part A: Applied Science and Manufacturing* **185,** 108356 (2024).

15. Ai, X., Chen, B. & Kassapoglou, C. Structural cohesive element for the modelling of delamination in composite laminates without the cohesive zone limit. *Engineering Fracture Mechanics,* 111586 (2025).

16. Främby, J., Brouzoulis, J. & Fagerström, M. Assessment of two methods for the accurate prediction of transverse stress distributions in laminates. *Composite Structures* **140,** 602–611 (2016).

17. Främby, J., Fagerström, M. & Brouzoulis, J. Adaptive modelling of delamination initiation and propagation using an equivalent single-layer shell approach. *International Journal for Numerical Methods in Engineering* **112,** 882–908 (2017).

18. Turon, A., Davila, C. G., Camanho, P. P. & Costa, J. An engineering solution for mesh size effects in the simulation of delamination using cohesive zone models. *Engineering fracture mechanics* **74,** 1665–1682 (2007).

19. Dávila, C. G., Camanho, P. M. P. R. d. C. & Turon Travesa, A. Cohesive elements for shells. © *NASA TP Technical Reports, 2007, núm. 214869* (2007).

20. Dávila, C. G., Camanho, P. P. & Turon, A. Effective simulation of delamination in aeronautical structures using shells and cohesive elements. *Journal of Aircraft* **45,** 663–672 (2008).

21. Polla, A., Piana, P., Cestino, E., Frulla, G., *et al. Delamination and fracture modeling techniques for shell composite structures in LS-DYNA* in *Proc. 13th European LS-DYNA Conference 2021* (2021).

22. Bazilevs, Y., Pigazzini, M., Ellison, A. & Kim, H. A new multi-layer approach for progressive damage simulation in composite laminates based on isogeometric analysis and Kirchhoff–Love shells. Part I: basic theory and modeling of delamination and transverse shear. *Computational Mechanics* **62,** 563–585 (2018).

23. Magisano, D., Corrado, A., Leonetti, L., Kiendl, J. & Garcea, G. Large deformation Kirchhoff–Love shell hierarchically enriched with warping: Isogeometric formulation and modeling of alternating stiff/soft layups. *Computer Methods in Applied Mechanics and Engineering* **418,** 116556 (2024).

24. Hashi, Z. Failure criteria for unidirectional fiber composite. *Journal of Applied Mechanics* **47,** 3292334 (1980).

25. Puck, A. & Schürmann, H. in *Failure criteria in fibre-reinforced-polymer composites* 832–876 (Elsevier, 2004).

26. Pinho, S. T., Iannucci, L. & Robinson, P. Physically-based failure models and criteria for laminated fibre-reinforced composites with emphasis on fibre kinking: Part I: Development. *Composites Part A: Applied Science and Manufacturing* **37,** 63–73 (2006).

27. Chen, B., Tay, T., Baiz, P. & Pinho, S. Numerical analysis of size effects on open-hole tensile composite laminates. *Composites Part A: Applied Science and Manufacturing* **47,** 52–62 (2013).

28. Wang, A. & Crossman, F. W. Some new results on edge effect in symmetric composite laminates. *Journal of Composite Materials* **11,** 92–106 (1977).

29. Wang, J. T. & Dickson, J. N. Interlaminar stresses in symmetric composite laminates. *Journal of Composite Materials* **12,** 390–402 (1978).

30. Burhan, M., Scalici, T., Ullah, Z., Kazancı, Z. & Catalanotti, G. A three-dimensional Finite Fracture Mechanics model to predict free edge delamination in angle-ply laminates. *Engineering Fracture Mechanics* **306,** 110156 (2024).

31. Grande, D. H., Ilcewicz, L. B., Avery, W. B. & Bascom, W. D. *Effects of intra-and inter-laminar resin content on the mechanical properties of toughened composite materials* in *NASA. Langley Research Center, First NASA Advanced Composites Technology Conference, Part 2* (1991).

32. Pagano, N. Stress fields in composite laminates. *International Journal of Solids and Structures* **14,** 385–400 (1978).

33. Krueger, R. & Minguet, P. J. *Analysis of composite panel-stiffener debonding using a shell/3D modeling technique* tech. rep. (2006).

34. Gupta, M., Srivastava, R. & Bisaria, H. Potential of jute fibre reinforced polymer composites: A review. *Int. J. Fiber Text. Res* **5,** 30–38 (2015).

35. Li, Y.-F., Sio, W.-K. & Tsai, Y.-K. A compressive peak strength model for CFRP-confined thermal insulation materials under elevated temperature. *Materials* **13,** 26 (2019).

36. Mittelstedt, C. & Becker, W. The Pipes–Pagano-problem revisited: elastic fields in boundary layers of plane laminated specimens under combined thermomechanical load. *Composite structures* **80,** 373–395 (2007).

37. Pipes, R. B. & Pagano, N. Interlaminar stresses in composite laminates under uniform axial extension. *Journal of composite materials* **4,** 538–548 (1970).

38. Pipes, R. B. & Pagano, N. Interlaminar stresses in composite laminates—an approximate elasticity solution (1974).

39. Kassapoglou, C. & Lagace, P. An efficient method for the calculation of interlaminar stresses in composite materials (1986).

40. Kassapoglou, C. & Lagace, P. A. Closed form solutions for the interlaminar stress field in angle-ply and cross-ply laminates. *Journal of Composite materials* **21,** 292–308 (1987).

41. Herakovich, C. Free edge effects in laminated composites. *Failure in Comp* **4,** 205–219 (1989).

42. Reddy, J. *Mechanics of Laminated Composite Plates and Shells: Theory and Analysis* (CRC press, 2004).

43. Andakhshideh, A. & Tahani, M. Interlaminar stresses in general thick rectangular laminated plates under in-plane loads. *Composites Part B: Engineering* **47,** 58–69 (2013).

4

ACCURATE SIMULATION OF DELAMINATION WITH A RESIN-RICH LAYER-DEPENDENT PENALTY STIFFNESS

Thin shell models preserve many of the predictive capabilities of three-dimensional models while offering the computational efficiency required for engineering applications. However, shell-based cohesive elements tend to overestimate the compression ahead of the crack tip because of approximations in the penalty stiffness. In this study, the higher-order structural cohesive element previously developed by the authors is enhanced with a resin-rich layer-dependent penalty stiffness to improve both computational efficiency and predictive accuracy. The proposed formulation distinguishes between the normal and shear penalty stiffnesses. It extends the resin-rich layer-based penalty stiffness from the layer-wise to the equivalent single-layer framework. This extension is achieved using the through-thickness distributions of the out-of-plane normal and transverse shear stresses derived from the beam assumption. The proposed method is verified and validated against benchmark problems for Mode I, Mode II, mixed-mode, and reinforced DCB configurations. Compared with the conventional formulation, it exhibits significantly improved mesh convergence and provides more accurate predictions of the compression distribution ahead of the crack tip and the delamination propagation.

Part of this chapter has been submitted for publication in X. Ai, C. Kassapoglou, B. Chen, Accurate simulation of delamination with a resin-rich layer-dependent penalty stiffness based on structural cohesive elements, 2026. DOI: https://doi.org/10.48550/arXiv.2608.05881.

4.1. INTRODUCTION

FIBER-reinforced polymer (FRP) composites are widely used in aerospace structures [1]. The prediction of strength and damage tolerance is an indispensable aspect in the design of composite aircraft structures [2, 3]. Among the various failure mechanisms, delamination is one principal mode of composite failure that occurs between the layers in the composite laminate [4, 5]. Progressive failure prediction during delamination is essential because reliable numerical simulations can reduce the need for expensive physical experiments under different loading conditions. The cohesive element (CE) [6, 7], based on the cohesive zone model (CZM), is widely employed as an interface element to simulate delamination by capturing the fracture process zone ahead of the crack tip. However, the standard CE is subject to a well-known limitation related to mesh density: the element size must be smaller than the cohesive zone length (CZL) to ensure accurate prediction of delamination because of high-stress gradients at the crack tip.

Recently, a higher-order structural cohesive element method has been developed to model delamination of composite laminates based on the Kirchhoff-Love hypothesis [8]. This approach overcomes the cohesive zone limitation while significantly improving computational efficiency by replacing solid hexahedral elements with higher-order triangular shell elements. The primary objective of that study was to develop a higher-order structural cohesive element. Consequently, the formulation focused mainly on the strain-displacement matrix (B-matrix), whereas the constitutive matrix (D-matrix) received little attention. A conventional cohesive law proposed by Turon et al. [9, 10] was adopted as the constitutive model, in which the penalty stiffness is defined by the laminate thickness and its out-of-plane elastic modulus. Although this formulation has been widely adopted for both solid [11, 12] and shell elements [13–15], the penalty stiffness significantly influences the prediction of through-thickness stress distributions in Kirchhoff-Love shell models. Since these stresses play an important role in the initiation of in-plane failure, such as matrix cracking, the accurate prediction of these stresses is particularly important. Previous studies on two- and three-dimensional structural cohesive elements based on Kirchhoff–Love theory showed that the conventional penalty stiffness failed to accurately predict the normal traction distribution ahead of the crack tip [15, 16]. In particular, the compression was significantly overestimated, and mesh convergence could not be achieved. Several researchers have proposed alternative penalty stiffness formulations for thin-shell elements based on the laminate thickness and material properties. Polla et al. [17] proposed a method to evaluate both normal and shear penalty stiffness. In this formulation, the cohesive element thickness is defined as the sum of the thicknesses of the top and bottom shell elements. The formulation was evaluated against Turon's penalty stiffness in the DCB and ENF benchmarks, but no significant improvement was observed. The study reported only the load-displacement curves of the benchmark problems, without providing any analysis of the traction distribution. Bazilevs et al. [18] proposed a method for determining shear penalty stiffness by defining the thickness of the cohesive element as half the sum of the thicknesses of the adjacent shell elements. The formulation was validated on both the DCB and ENF benchmark models. However, the ENF results showed a significant underestimation of initial stiffness and the peak load compared with the analytical solution. Despite their different definitions of the cohesive element thickness, both Bazilevs' and Polla's formulations assume simple shear deformation of the plies under transverse shear loading.

We proposed a resin-rich-layer-based formulation that accurately predicts the through-thickness stress distribution in multilayer composite laminates in Chapter 3. The formulation has been successfully applied to higher-order structural elements, leading to a significant improvement in computational efficiency. The penalty stiffness obtained by this formulation only depends on the thickness and material properties of the resin-rich layer between adjacent plies. It requires layer-wise modeling of multi-layer composite laminates. This approach is acceptable for laminates with a relatively small number of plies. However, for laminates containing many plies with the same fiber orientation, the model becomes computationally inefficient. These plies are more efficiently represented as a single ply block using one shell element. Consequently, the formulation cannot be directly applied to equivalent single-layer models.

To overcome this limitation, the present study develops a new penalty stiffness formulation for structural cohesive elements used between shell elements representing multi-ply blocks. The proposed formulation preserves the accuracy of the resin-rich layer approach while being directly applicable to equivalent single-layer models. The structure of the paper is organised as follows. Section 4.2 presents the proposed penalty stiffness formulation. Section 4.3 validates the performance of the proposed formulation on a series of benchmarks on delamination. Section 4.4 summarizes the conclusions of this study and outlines potential directions for future research.

4.2. METHOD

4.2.1. CUBIC STRUCTURAL ELEMENT

In this work, all benchmark models are discretized by high-order triangular structural elements, which are implemented through user-defined element subroutines in Abaqus. Cubic shell elements represent the laminate plies, while the interfaces between the adjacent shell elements are represented by compatible cohesive elements, as illustrated in Figure 4.1. This element overcomes the cohesive zone limitation, while the use of triangular elements enhances geometric flexibility. The detailed kinematic description and stiffness matrix formulation of the element can be found in Reference [8] and Chapter 2.

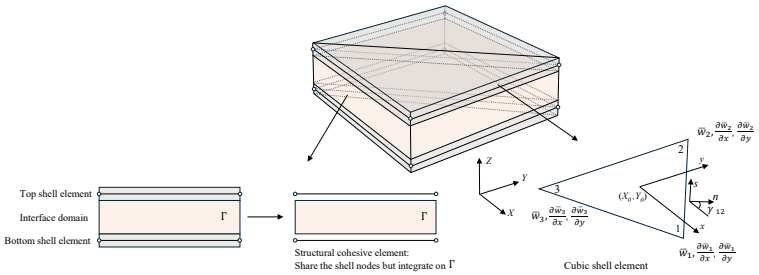

Figure 4.1: Triangular cubic structural element [8]

4.2.2. PENALTY STIFFNESS BASED ON THE RESIN-RICH LAYER

THE conventional penalty stiffness formulation for cohesive elements, mentioned in Section 4.1, is proposed by Turon et al. [10]:

$$K^{\text{Turon}} = \alpha \frac{E_3}{h} \tag{4.1}$$

where E_3 is the laminate out-of-plane elastic modulus and h is the laminate thickness. The parameter α is a scaling parameter which is typically chosen sufficiently large to prevent artificial separation before damage initiation. The excessively large penalty stiffness value may lead to numerical instability and convergence difficulties. When this formulation is applied to shell-based cohesive elements, the out-of-plane stress distribution through the thickness cannot be accurately predicted. To overcome this limitation, an accurate penalty stiffness was derived based on a resin-rich layer in our previous study [19]. The normal and shear penalty stiffnesses were derived separately under the pure tension and simple shear loading conditions, as shown in Figure 4.2:

$$K_n^{\text{Ai}} = \frac{E_{\text{rr}}}{h_{\text{rr}}} \tag{4.2}$$

$$K_s^{\text{Ai}} = \frac{G_{\text{rr}}}{h_{\text{rr}}} \tag{4.3}$$

where E_{rr} and G_{rr} are the elastic modulus and shear modulus of the resin-rich layer material, respectively, and h_{rr} is the thickness of the resin-rich layer at the ply interface of interest. This formulation provides a clear physical interpretation as the penalty stiffness directly corresponds to the transverse stiffness of the resin-rich layer. The formulation assumes that the interlaminar normal and shear stresses are transferred through the resin-rich layer, which are significantly more compliant than the adjacent composite plies. Although this method could in principle model laminates of arbitrary stacking sequences, it requires structural cohesive elements to be inserted between every pair of adjacent plies, regardless of whether the plies have the same fiber orientations.

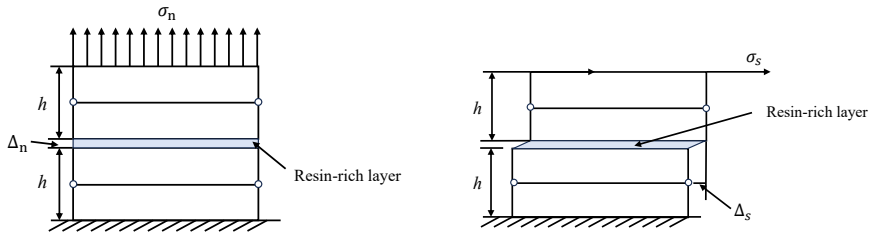

(a) Normal penalty stiffness (b) Shear penalty stiffness

Figure 4.2: Penalty stiffness based on resin-rich layer [19]

In many practical applications, such as the DCB benchmark [20, 21], adjacent plies with the same fiber orientation are homogenized into a single shell element using the equivalent single-layer approach. This method significantly reduces the number of finite elements and

thereby improves computational efficiency. When the equivalent single-layer approach is employed, the parameter h in Figure 4.2 no longer represents the thickness of an individual ply but that of the entire ply block. Therefore, the interface penalty stiffness should account for the transverse stiffness of all the resin-rich layers contained within the homogenized laminate. To achieve this objective, the through-thickness stress distribution is incorporated while preserving the original physical meaning of h_{rr}, thereby enabling the determination of an accurate penalty stiffness. The derivation of a physically reasonable through-thickness stress distribution is a key component of the proposed method. The derivations of the corresponding normal and shear penalty stiffnesses are presented in Section 4.2.3. Because the out-of-plane normal and transverse shear stress distributions exhibit distinct characteristics, separate normal and shear penalty stiffnesses are derived. Accordingly, the mode-dependent cohesive law proposed by Turon et al. [11] is adopted in the structural cohesive element formulation.

4.2.3. DERIVATION OF THE NORMAL AND SHEAR PENALTY STIFFNESSES

SINCE Kirchhoff-Love shell elements do not explicitly account for transverse stresses, it is necessary to determine the through-thickness stress distributions based on classical mechanics. To facilitate the derivation, the three-dimensional shell problem is reduced to a two-dimensional beam problem. Under the Kirchhoff-Love assumptions, the axial stress varies linearly through the thickness, whereas the transverse shear stress follows a quadratic distribution. For consistency with the laminate coordinate system adopted in this work, the transverse coordinate in the beam formulation is hereafter represented by z. Accordingly, the transverse shear stress is assumed to take the following form:

$$\tau_{xz} = f(x) * (a_1 z^2 + a_2 z + a_3) \tag{4.4}$$

where $f(x)$ describes the variation along x and a_1, a_2, and a_3 are unknown coefficients

The corresponding two-dimensional equilibrium equation is

$$\frac{\partial \tau_{xz}}{\partial x} + \frac{\partial \sigma_z}{\partial z} = 0 \tag{4.5}$$

According to Equation 4.5, a quadratic distribution of τ_{xz} leads to a cubic distribution of the out-of-plane normal stress σ_z, which can be expressed as

$$\sigma_z = f'(x) \left(\frac{a_1}{3} z^3 + \frac{a_2}{2} z^2 + a_3 z + a_4 \right) \tag{4.6}$$

where a_4 is an additional unknown coefficient.

The derivation of K_n begins with the through-thickness distribution of the out-of-plane normal stress. According to Hooke's law, the out-of-plane normal strain at the ith interface can be obtained:

$$\varepsilon_z(z_i) = \frac{\sigma_z(z_i)}{E_{\text{rr}}} \tag{4.7}$$

where z_i represents the coordinate of the ith interface layer. The $\sigma_z(z_i)$ and $\varepsilon_z(z_i)$ represent the out-of-plane normal stress and strain values at the ith interface layer. E_{rr} is the elastic modulus of the resin-rich layer.

For pure Mode I loading, i.e., the Double Cantilever Beam (DCB) model, the top and bottom arms are subjected to different boundary conditions. Consequently, the contributions of the two arms must be considered separately. The total opening displacement of the cohesive element can be expressed as the sum of the product of normal strains at each interface and the physical thickness of the resin-rich layer h_{rr}:

$$\begin{aligned}\Delta_{\text{I}}^{\text{total}} &= \sum_{i=1}^{n_{\text{top}}} \varepsilon_z(z_i)\, h_{\text{rr}} + \sum_{j=1}^{n_{\text{bot}}} \varepsilon_z(z_j)\, h_{\text{rr}} \\ &= \sum_{i=1}^{n_{\text{top}}} \frac{\sigma_z(z_i)}{E_{\text{rr}}}\, h_{\text{rr}} + \sum_{j=1}^{n_{\text{bot}}} \frac{\sigma_z(z_j)}{E_{\text{rr}}}\, h_{\text{rr}}\end{aligned} \tag{4.8}$$

where n_{top} and n_{bot} represent the number of plies in the top and bottom arms, respectively. The total number of plies n_{total} is:

$$n_{\text{total}} = n_{\text{top}} + n_{\text{bot}} \tag{4.9}$$

Based on the traction-separation law of the cohesive model, the maximum out-of-plane normal stress can be expressed as:

$$\sigma_z^{\max} = K_n\, \Delta_{\text{I}}^{\text{total}} \tag{4.10}$$

where $\sigma_z^{\max}$ is the maximum value of the out-of-plane normal stress distribution and K_n is the normal penalty stiffness.

Substituting Equations 4.7 and 4.8 into Equation 4.10 leads to the following expression for the normal penalty stiffness:

$$\begin{aligned}K_n &= \frac{\sigma_z^{\max}}{\displaystyle\sum_{i=1}^{n_{\text{top}}} \frac{\sigma_z(z_i)}{E_{\text{rr}}}\, h_{\text{rr}} + \sum_{j=1}^{n_{\text{bot}}} \frac{\sigma_z(z_j)}{E_{\text{rr}}}\, h_{\text{rr}}} \\ &= \frac{1}{\displaystyle\sum_{i=1}^{n_{\text{top}}} \frac{\sigma_z(z_i)}{\sigma_z^{\max}} \frac{h_{\text{rr}}}{E_{\text{rr}}} + \sum_{j=1}^{n_{\text{bot}}} \frac{\sigma_z(z_j)}{\sigma_z^{\max}} \frac{h_{\text{rr}}}{E_{\text{rr}}}}\end{aligned} \tag{4.11}$$

Since h_{rr} and E_{rr} are geometric and material properties of the resin-rich layer, the quantity $h_{\text{rr}}/E_{\text{rr}}$ is known. Therefore, determining K_{n} reduces to deriving the through-thickness distribution of the out-of-plane normal stress and, in particular, the stress ratios $\sigma_z(z_i)/\sigma_z^{\max}$ shown in Equation 4.11.

The DCB model considered in this work is symmetric about the mid-plane. Therefore, the out-of-plane normal stress reaches its maximum at the mid-plane and vanishes at the upper and lower free surfaces:

$$\sigma_z(0) = \sigma_z^{\max} \tag{4.12}$$

$$\sigma_z(\pm h) = 0 \tag{4.13}$$

where h is the thickness of each laminate arm.

Because the top and bottom arms of the DCB model are subjected to different boundary conditions, the out-of-plane normal stress distribution is derived separately for each arm. Accordingly, the cubic function given in Equation 4.6 is applied separately to the top and bottom arms. For the top arm, the unknown coefficient a_4 can be derived from the boundary condition in Equation 4.12:

$$a_4 = \sigma_z^{\max} \tag{4.14}$$

To simplify the derivation, the maximum out-of-plane normal stress is normalized to unity, i.e. $\sigma_z^{\max} = 1$. Accordingly, $a_4 = 1$. By applying the free-surface boundary condition in Equation 4.13, the following constraint on the unknown coefficients is obtained:

$$\frac{a_1}{3}h^3 + \frac{a_2}{2}h^2 + a_3 h + 1 = 0 \tag{4.15}$$

To determine the remaining unknown coefficients, the boundary conditions for the shear stress in the DCB model must also be considered. In contrast to the out-of-plane normal stress, the shear stress vanishes not only at the free surfaces but also at the mid-plane:

$$\tau_{xz}(0) = 0 \tag{4.16}$$

$$\tau_{xz}(\pm h) = 0 \tag{4.17}$$

Substituting the boundary conditions in Equations 4.16 and 4.17 into Equation 4.4, the following constraints on the unknown coefficients can be given as:

$$a_3 = 0 \tag{4.18}$$

$$a_1 h^2 + a_2 h = 0 \tag{4.19}$$

Since the shear stress distribution in the top arm is positive over the interval $0 < z < h$, the coefficient a_1 must be positive, i.e., $a_1 > 0$. Combining Equations 4.18 and 4.19 gives

$$a_1 = \frac{6}{h^3} \tag{4.20}$$

$$a_2 = -\frac{6}{h^2} \tag{4.21}$$

Substituting the obtained coefficients into Equations 4.4 and 4.6, the following expressions for the shear stress and out-of-plane normal stress in the top arm are given by:

$$\tau_{xz}^{\text{top}} \propto \frac{6}{h^3}z^2 - \frac{6}{h^2}z \tag{4.22}$$

$$\sigma_z^{\text{top}} \propto \frac{2}{h^3}z^3 - \frac{3}{h^2}z^2 + 1 \tag{4.23}$$

The stress distributions in the bottom arm can be derived using the same procedure. The unknown coefficients are determined by enforcing the boundary conditions given in Equations 4.12, 4.13, 4.16 and 4.17. In addition, the out-of-plane normal stress distribution is

required to remain symmetric about the laminate mid-plane. The corresponding coefficients are:

$$\text{DCB bottom arm:} \quad \begin{cases} a_1 = -\dfrac{6}{h^3} \\ a_2 = -\dfrac{6}{h^2} \\ a_3 = 0 \\ a_4 = 1 \end{cases} \tag{4.24}$$

Substituting these coefficients into Equations 4.4 and 4.6, the expressions for the shear stress and out-of-plane normal stress distributions in the bottom arm are given as follows:

$$\tau_{xz}^{\text{bot}} \propto -\frac{6}{h^3}z^2 - \frac{6}{h^2}z \tag{4.25}$$

$$\sigma_{z}^{\text{bot}} \propto -\frac{2}{h^3}z^3 - \frac{3}{h^2}z^2 + 1 \tag{4.26}$$

Combining Equations 4.22 and 4.25 gives the piecewise expression for the shear stress distribution under pure Mode I opening:

$$\tau_{xz}^{\text{Mode I}} \propto \begin{cases} \dfrac{6}{h^3}z^2 - \dfrac{6}{h^2}z, & h \geq z \geq 0 \\ -\dfrac{6}{h^3}z^2 - \dfrac{6}{h^2}z, & 0 > z \geq -h \end{cases} \tag{4.27}$$

Similarly, combining Equations 4.23 and 4.26 yields the following piecewise expression for the out-of-plane normal stress distribution:

$$\sigma_{z}^{\text{Mode I}} \propto \begin{cases} \dfrac{2}{h^3}z^3 - \dfrac{3}{h^2}z^2 + 1, & h \geq z \geq 0 \\ -\dfrac{2}{h^3}z^3 - \dfrac{3}{h^2}z^2 + 1, & 0 > z \geq -h \end{cases} \tag{4.28}$$

The through-thickness distributions of the shear stress and out-of-plane normal stress under pure Mode I loading are shown in Figure 4.3. In the figure, σ_z^i and τ_{xz}^i are the values of $\sigma_z^{\text{Mode I}}$ and $\tau_{xz}^{\text{Mode I}}$, respectively, at the ith interface layer. Once the through-thickness distribution of $\sigma_z^{\text{Mode I}}$ has been determined, the stress ratios $\sigma_z(z_i)/\sigma_z^{\max}$ in Equation 4.11 can be easily evaluated. Therefore, the normal penalty stiffness K_n can be calculated directly.

For the shear penalty stiffness, the derivation is based on the through-thickness distribution of transverse shear stress, τ_{xz}. According to Hooke's law, the corresponding shear strain at each interface can be obtained:

$$\varepsilon_{xz}(z_i) = \frac{\tau_{xz}(z_i)}{G_{\text{rr}}} \tag{4.29}$$

where $\tau_{xz}(z_i)$ and $\varepsilon_{xz}(z_i)$ represent the transverse shear stress and strain at the ith interface layer, respectively. In addition, G_{rr} is the shear modulus of the resin-rich layer.

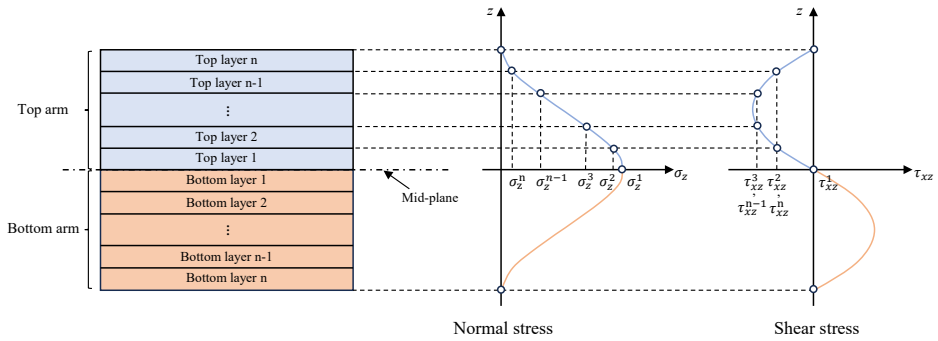

Figure 4.3: Stress distributions in the laminate under pure Mode I loading

4

For pure Mode II loading, i.e., the End-Notched Flexure (ENF) model, the top and bottom arms are also subjected to different boundary conditions. Consequently, the contributions of the two arms must be considered separately in the pure Mode I case. The total sliding displacement of the cohesive element can therefore be written as:

$$\begin{aligned}\Delta_{\mathrm{II}}^{\mathrm{total}} &= \sum_{i=1}^{n_{\mathrm{top}}} \varepsilon_{xz}(z_i)\, h_{\mathrm{rr}} + \sum_{j=1}^{n_{\mathrm{bot}}} \varepsilon_{xz}(z_j)\, h_{\mathrm{rr}} \\ &= \sum_{i=1}^{n_{\mathrm{top}}} \frac{\tau_{xz}(z_i)}{G_{\mathrm{rr}}}\, h_{\mathrm{rr}} + \sum_{j=1}^{n_{\mathrm{bot}}} \frac{\tau_{xz}(z_j)}{G_{\mathrm{rr}}}\, h_{\mathrm{rr}}\end{aligned} \tag{4.30}$$

According to the Mode II traction-separation law, the maximum transverse shear stress can be derived as follows:

$$\tau_{xz}^{\max} = K_s\, \Delta_{\mathrm{II}}^{\mathrm{total}} \tag{4.31}$$

where $\tau_{xz}^{\max}$ is the maximum transverse shear stress, and K_s is the shear penalty stiffness.

Substituting Equations 4.29 and 4.30 into Equation 4.31, the expression for the shear penalty stiffness is given by:

$$\begin{aligned}K_s &= \frac{\tau_{xz}^{\max}}{\displaystyle\sum_{i=1}^{n_{\mathrm{top}}} \frac{\tau_{xz}(z_i)}{G_{\mathrm{rr}}}\, h_{\mathrm{rr}} + \sum_{j=1}^{n_{\mathrm{bot}}} \frac{\tau_{xz}(z_j)}{G_{\mathrm{rr}}}\, h_{\mathrm{rr}}} \\ &= \frac{1}{\displaystyle\sum_{i=1}^{n_{\mathrm{top}}} \frac{\tau_{xz}(z_i)}{\tau_{xz}^{\max}} \frac{h_{\mathrm{rr}}}{G_{\mathrm{rr}}} + \sum_{j=1}^{n_{\mathrm{bot}}} \frac{\tau_{xz}(z_j)}{\tau_{xz}^{\max}} \frac{h_{\mathrm{rr}}}{G_{\mathrm{rr}}}}\end{aligned} \tag{4.32}$$

Since $h_{\mathrm{rr}}/G_{\mathrm{rr}}$ is a known constant for a given resin-rich layer, the determination of the shear penalty stiffness depends on the through-thickness shear stress ratios, $\tau_{xz}(z_i)/\tau_z^{\max}$, in Equation 4.32.

In the symmetric ENF model, the top and bottom arms contain the same number of plies. Consequently, the transverse shear stress reaches its maximum value at the mid-plane and vanishes at the upper and lower free surfaces:

$$\tau_{xz}(0) = \tau_{xz}^{\max} \tag{4.33}$$

$$\tau_{xz}(\pm h) = 0 \tag{4.34}$$

Although the top and bottom arms have the same laminate configuration, they are subjected to different loading conditions. Following the procedure adopted for the DCB model, the transverse shear stress distribution is derived separately for the top and bottom arms of the ENF model. Enforcing the boundary condition in Equation 4.33 into the quadratic expression for the shear in Equation 4.4 gives:

$$a_3 = \tau_{xz}^{\max} \tag{4.35}$$

Similarly, the maximum shear stress is normalized to unity. Applying the free-surface boundary condition at the upper surface of the top arm and substituting coefficient a_3 into Equation 4.4 yields the following relation between the remaining unknown coefficients:

$$a_1 h^2 + a_2 h + 1 = 0 \tag{4.36}$$

The remaining unknown coefficients, a_1 and a_2, are determined from the boundary conditions of the out-of-plane normal stress in the ENF model. Since the out-of-plane normal stress vanishes at both the mid-plane and the free surfaces, the out-of-plane normal stress satisfies:

$$\sigma_z(0) = 0 \tag{4.37}$$

$$\sigma_z(\pm h) = 0 \tag{4.38}$$

Applying the above boundary conditions to Equation 4.6 yields the coefficient a_4 and an additional relationship between the remaining unknown coefficients a_1 and a_2:

$$a_4 = 0 \tag{4.39}$$

$$\frac{a_1}{3} h^3 + \frac{a_2}{2} h^2 + h = 0 \tag{4.40}$$

Combining Equations 4.36 and 4.40, together with the requirement that the shear stress reaches its maximum value at the mid-plane, leads to a positive value of a_1. The coefficients a_1 and a_2 are given by:

$$a_1 = \frac{3}{h^2} \tag{4.41}$$

$$a_2 = -\frac{4}{h} \tag{4.42}$$

Substituting these coefficients into Equations 4.4 and 4.6 gives the following stress distributions in the top arm of the ENF model:

$$\tau_{xz}^{\text{top}} \propto \frac{3}{h^2}z^2 - \frac{4}{h}z + 1 \tag{4.43}$$

$$\sigma_{z}^{\text{top}} \propto \frac{1}{h^2}z^3 - \frac{2}{h}z^2 + z \tag{4.44}$$

Because the transverse shear stress distribution in the ENF model is symmetric about the mid-plane, the coefficients for the bottom arm can be obtained directly from those of the top arm. The coefficient a_1 remains unchanged, whereas a_2 has the same magnitude but the opposite sign. The coefficients a_3 and a_4, determined from the mid-plane boundary conditions, are identical for both arms. Accordingly, the coefficients for the bottom arm are:

$$\text{ENF bottom arm:} \quad \begin{cases} a_1 = \dfrac{3}{h^2} \\ a_2 = \dfrac{4}{h} \\ a_3 = 1 \\ a_4 = 0 \end{cases} \tag{4.45}$$

Accordingly, the corresponding stress distributions in the bottom arm can be expressed as:

$$\tau_{xz}^{\text{bot}} \propto \frac{3}{h^2}z^2 + \frac{4}{h}z + 1 \tag{4.46}$$

$$\sigma_{z}^{\text{bot}} \propto \frac{1}{h^2}z^3 + \frac{2}{h}z^2 + z \tag{4.47}$$

Combining Equations 4.43 and 4.46 gives the following piecewise expression for the transverse shear stress distribution under pure Mode II loading:

$$\tau_{xz}^{\text{Mode II}} \propto \begin{cases} \dfrac{3}{h^2}z^2 - \dfrac{4}{h}z + 1, & h \geq z \geq 0 \\ \dfrac{3}{h^2}z^2 + \dfrac{4}{h}z + 1, & 0 > z \geq -h \end{cases} \tag{4.48}$$

Similarly, combining Equations 4.44 and 4.47 yields the following expression for the out-of-plane normal stress distribution:

$$\sigma_{z}^{\text{Mode II}} \propto \begin{cases} \dfrac{1}{h^2}z^3 - \dfrac{2}{h}z^2 + z, & h \geq z \geq 0 \\ \dfrac{1}{h^2}z^3 + \dfrac{2}{h}z^2 + z, & 0 > z \geq -h \end{cases} \tag{4.49}$$

Similarly, combining Equations 4.44 and 4.47 yields the following expression for the out-of-plane normal stress distribution:

$$\sigma_z^{\text{Mode II}} \propto \begin{cases} \dfrac{1}{h^2}z^3 - \dfrac{2}{h}z^2 + z, & h \geq z \geq 0 \\ \dfrac{1}{h^2}z^3 + \dfrac{2}{h}z^2 + z, & 0 > z \geq -h \end{cases} \tag{4.50}$$

The through-thickness distributions of the transverse shear stress and out-of-plane normal stress under pure Mode II loading, as described by Equations 4.48 and 4.50, are shown in Figure 4.4. In the figure, σ_z^i and τ_{xz}^i are the values of $\sigma_z^{\text{Mode II}}$ and $\tau_{xz}^{\text{Mode II}}$, respectively, at the ith interface layer.

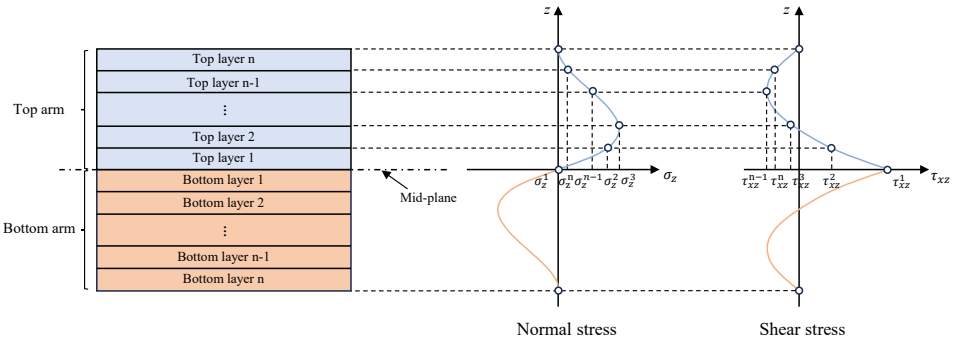

Figure 4.4: Stress distributions in the laminate under pure Mode II loading

The expression for the transverse shear stress directly provides the stress ratios $\tau_{xz}(z_i)/\tau_{xz}^{\max}$ shown in Equation 4.32. Substituting these ratios into Equation 4.32 yields the corresponding shear penalty stiffness.

4.3. VALIDATION

THE proposed penalty stiffness formulation is first validated against three classical delamination benchmarks: the Double Cantilever Beam (DCB), End-Notched Flexure (ENF), and Mixed-Mode Bending (MMB). The numerical predictions are systematically compared with analytical solutions [22–24] and finite element results using the conventional penalty stiffness. In addition, to highlight the advantages of the proposed method in compressive stress prediction, the traction distribution at the crack tip in the DCB model is examined and compared with the results reported in Reference [15].

In addition to the classical delamination benchmarks, the Reinforced Double Cantilever Beam (R-DCB) model is considered to further validate the proposed penalty stiffness for fully three-dimensional delamination problems. The predictions are compared with experimental data and numerical results obtained using the penalty stiffness proposed in the previous study [8]. This section first introduces the problem descriptions and modeling details, followed by comparisons of load-displacement curves and damage maps.

4.3.1. MODE I DELAMINATION BENCHMARK: DOUBLE CANTILEVER BEAM (DCB)

DESCRIPTION OF THE DCB SPECIMEN

THE DCB specimen, illustrated in Figure 4.5, is selected as the benchmark for Mode I delamination analysis because it exhibits pure Mode I fracture, with $(G_{II}/G_T) = 0$. The geometric parameters and boundary conditions are presented in Figure 4.5. The laminate is manufactured from T300/1076 composite material, and the corresponding material properties are summarized in Table 4.1.

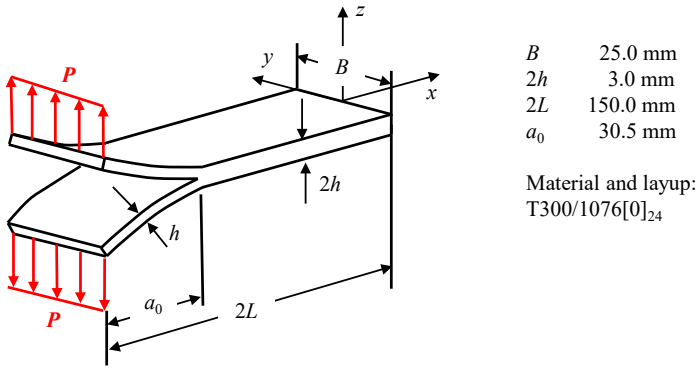

Figure 4.5: Double cantilever beam (DCB) specimen [25]

Table 4.1: Material properties for the DCB specimen [25]

T300/1076 Unidirectional graphite/epoxy prepreg		
E_{11}= 139.4 GPa	E_{22}= 10.16 GPa	E_{33} = 10.16 GPa
ν_{12} = 0.30	ν_{13} = 0.30	ν_{23} = 0.436
G_{12} = 4.6 GPa	G_{13} = 4.6 GPa	G_{23} = 3.54 GPa
Fracture toughness data		
$G_{Ic} = 0.170\,kJ/m^2$	$G_{IIc} = 0.494\,kJ/m^2$	$\eta = 1.62$
Interfacial strength data [11, 12]		
$\tau_{Ic} = 30\,MPa$	$\tau_{IIc} = 60\,MPa$	

All 24 plies in this benchmark have a fiber orientation of $0°$. Consequently, the laminate can be represented using one shell element layer for each arm and a single layer of structural cohesive elements located at the delamination interface. According to Equation 4.11, the normal penalty stiffness depends on the number of laminate plies. Since both the top and bottom arms contain 12 plies, the corresponding out-of-plane normal stress distribution through the thickness for the 24-ply DCB specimen is shown in Figure 4.6.

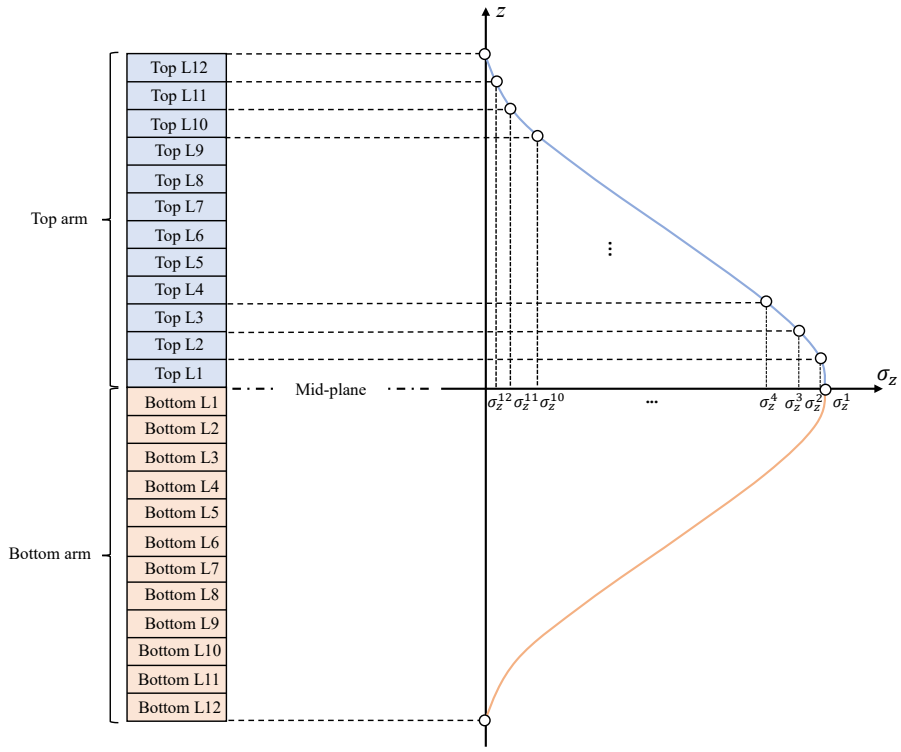

Figure 4.6: Through-thickness distribution of out-of-plane normal stress in the 24-ply DCB specimen

From the out-of-plane normal stress distribution in Figure 4.6 and Equation 4.28, the stress ratios $\sigma_z(z_i)/\sigma_z^{\max}$ for the interface layers can be readily evaluated. The corresponding values for the top arm are tabulated in Table 4.2.

Table 4.2: Out-of-plane normal stress ratios at the interface layers of the top arm in the 24-ply DCB specimen

$\frac{\sigma_z^1}{\sigma_z^{\max}}$	$\frac{\sigma_z^2}{\sigma_z^{\max}}$	$\frac{\sigma_z^3}{\sigma_z^{\max}}$	$\frac{\sigma_z^4}{\sigma_z^{\max}}$	$\frac{\sigma_z^5}{\sigma_z^{\max}}$	$\frac{\sigma_z^6}{\sigma_z^{\max}}$	$\frac{\sigma_z^7}{\sigma_z^{\max}}$	$\frac{\sigma_z^8}{\sigma_z^{\max}}$	$\frac{\sigma_z^9}{\sigma_z^{\max}}$	$\frac{\sigma_z^{10}}{\sigma_z^{\max}}$	$\frac{\sigma_z^{11}}{\sigma_z^{\max}}$	$\frac{\sigma_z^{12}}{\sigma_z^{\max}}$
1.00	0.98	0.93	0.84	0.74	0.62	0.50	0.38	0.26	0.16	0.07	0.02

where $n_{\text{top}}^{\text{DCB}}$ is the number of plies in the top arm of the DCB specimen.

Because the 24-ply DCB specimen is symmetric with respect to the mid-plane, the total sum of stress ratios in Equation 4.11 becomes:

$$\sum_{i=1}^{n_{\text{top}}^{\text{DCB}}} \frac{\sigma_z(z_i)}{\sigma_z^{\max}} + \sum_{j=1}^{n_{\text{bot}}^{\text{DCB}}} \frac{\sigma_z(z_j)}{\sigma_z^{\max}} = 2\sum_{i=1}^{12} \frac{\sigma_z(z_i)}{\sigma_z^{\max}}$$

$$= 2 \times 6.5 = 13 \tag{4.51}$$

where $n_{\text{bot}}^{\text{DCB}}$ is the number of plies in the bottom arm of the DCB specimen.

Because the elastic modulus $E_{\text{rr}}^{\text{DCB}}$ and Poisson's ratio $\nu_{\text{rr}}^{\text{DCB}}$ of the 1076 resin-rich layer are unavailable in the literature, approximate values are adopted from Crews et al. [26]. The DCB specimen considered in that study consisted of a 24-ply unidirectional graphite/epoxy laminate with a geometry similar to that investigated in this work. Accordingly, the reported material properties are expected to provide a reasonable approximation for the present DCB model and are listed in Table 4.3. The resin-rich layer thickness h_{rr} is obtained from Grande et al. [27], and the corresponding value is also given in Table 4.3.

Table 4.3: Material parameters of the resin-rich layer in the DCB specimen

$E_{\text{rr}}^{\text{DCB}}$ [26] (N/mm^2)	$G_{\text{rr}}^{\text{DCB}}$ [26] (N/mm^2)	$\nu_{\text{rr}}^{\text{DCB}}$ [26]	h_{rr} [27] (mm)
3400	1300	0.3	0.02286

Based on Equation 4.11, the normal penalty stiffness of the DCB specimen can be calculated as follows:

$$K_n^{\text{DCB}} = \frac{1}{\sum_{i=1}^{12} \frac{\sigma_z(z_i)}{\sigma_z^{\max}} \frac{h_{\text{rr}}}{E_{\text{rr}}^{\text{DCB}}} + \sum_{j=1}^{12} \frac{\sigma_z(z_j)}{\sigma_z^{\max}} \frac{h_{\text{rr}}}{E_{\text{rr}}^{\text{DCB}}}}$$

$$= \frac{1}{13 \times \frac{0.02286}{3400}} = 11441\,\text{N/mm}^3 \tag{4.52}$$

Because the DCB specimen represents a pure Mode I problem, the shear penalty stiffness has a negligible effect on the numerical predictions. Nearly identical results are obtained for different values of this parameter. Accordingly, the shear penalty stiffness is not considered further in this section.

LOAD-DISPLACEMENT CURVES

The load-displacement curves obtained from the numerical simulations are shown in Figure 4.7. The left panel corresponds to the conventional penalty stiffness, while the right panel corresponds to the proposed penalty stiffness. In both cases, the numerical results are compared with the analytical solution, represented by the black curve.

As shown in Figure 4.7a, the model using the conventional penalty stiffness fails to achieve mesh convergence when the element size exceeds 5 mm. In contrast, the proposed penalty stiffness maintains good convergence even with a 7.5 mm mesh size (Figure 4.7b). Comparing the results obtained with the 5 mm mesh in the two figures, the proposed normal penalty stiffness produces a load-displacement curve with smaller oscillations and better agreement with the analytical solution than the conventional penalty stiffness. It demonstrates that the proposed formulation significantly reduces the numerical error associated with coarser meshes. For finer meshes, such as the 2 mm mesh, both penalty stiffness formulations produce results that are in close agreement with the analytical solution, with no

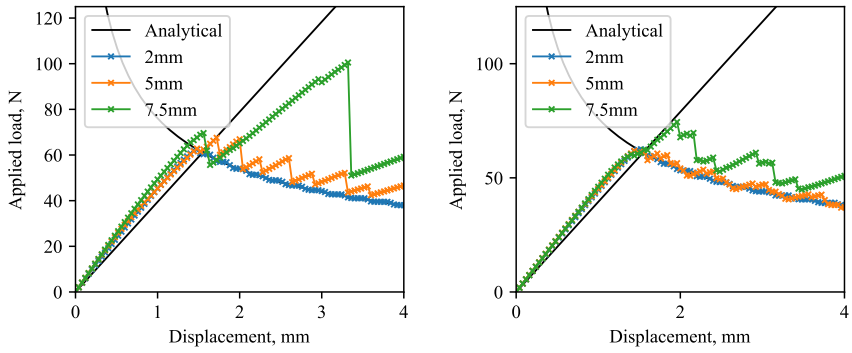

(a) Conventional penalty stiffness

(b) Proposed penalty stiffness

Figure 4.7: Comparison of the load-displacement curves obtained from the DCB simulations using the conventional and proposed penalty stiffness formulations at different mesh densities

significant differences observed. In summary, the proposed normal penalty stiffness significantly improves mesh convergence and allows accurate predictions with coarser meshes, thereby enhancing computational efficiency.

NORMALIZED L_2 ERROR ANALYSIS

To quantitatively evaluate the effects of the penalty stiffness and mesh convergence, the normalized L_2 error is adopted. It measures the discrepancy between the numerical load-displacement curve, denoted as $f^*(x)$, and the corresponding analytical solution $f(x)$. The normalized L_2 error is defined as follows:

$$e = \frac{\sqrt{\int_a^b (f^* - f)^2 \mathrm{d}x}}{\sqrt{\int_a^b f^2 \mathrm{d}x}} \tag{4.53}$$

Due to the fact that the numerical and analytical responses are in close agreement within the elastic region, and obvious differences arise only after the peak load, the lower integration limit a in Equation 4.53 is set to the displacement corresponding to the peak load (indicated by the black dot in Figure 4.8). The upper integration limit b is taken as the maximum displacement of the DCB simulation, i.e., 4 mm.

In this study, the trapezoidal rule is applied to numerically evaluate the integral in Equation 4.53. The integration interval is discretized according to the displacement points of the numerical load-displacement curves, and the integrand is assumed to vary linearly within each subinterval. The normalized L_2 error is then calculated by summing the areas of the trapezoids. The calculated errors are presented in Figure 4.9. From the figure, when the conventional penalty stiffness is adopted, the normalized L_2 error exceeds 50% for the 7.5 mm mesh, which is markedly larger than that obtained using the proposed normal penalty stiffness. As the mesh is progressively refined to 2 mm, the influence of the penalty stiffness reduces, and the errors predicted by the two formulations are approximately 0.8%.

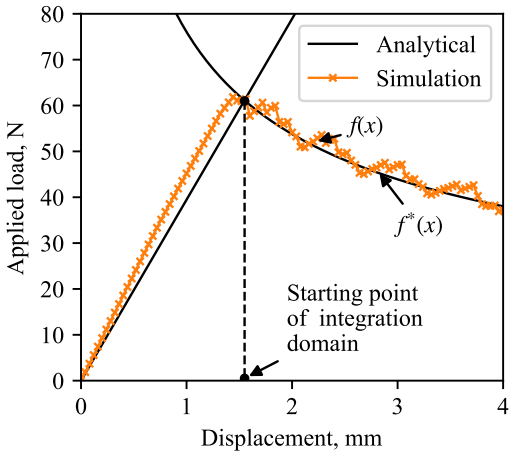

Figure 4.8: Definition of the integration interval for the normalized L_2 error calculation

NORMAL TRACTION DISTRIBUTION OF DCB CRACK TIP

Figure 4.10 presents the traction distribution ahead of the crack tip at the onset of delamination in the DCB specimen. As predicted by cohesive zone theory, the traction at the crack tip reduces to zero, where damage initiates. Subsequently, the traction increases in the direction of crack propagation until it reaches its maximum value. The distance between the crack tip and the location of the maximum traction is defined as the cohesive zone length (CZL). Beyond the maximum traction point, the traction decreases and becomes compressive. Then, the traction reaches a minimum value before eventually returning to zero.

In this section, the traction distribution in the DCB specimen is evaluated. The predicted results are compared with those obtained from the higher-order plate (TUBA3) model and a solid element model under a very refined mesh, as reported by Tosti Balducci et al. [15]. The traction extraction procedure and the corresponding comparison results are presented below.

First, the traction values are extracted from the integration points of the cohesive elements (CEs) and stored for post-processing. Then, these values are imported into ParaView and visualized according to their global coordinates, denoted as X and Y in Figure 4.11. The traction distribution is subsequently evaluated by interpolating along the specimen midline in the X-Y plane using the *Plot Over Line* filter. This procedure is shown in Figure 4.11 and enables a consistent evaluation of the traction distribution for finite element models with different mesh densities while minimizing the influence of free-edge effects.

Figure 4.12 compares the normal traction distributions ahead of the crack tip predicted by the DCB simulations. The left panel shows the results from the TUBA3 element with the conventional penalty stiffness at different mesh sizes, while the right panel shows the corresponding results from the cubic structural cohesive element with the proposed normal penalty stiffness.

As shown in Figure 4.12, both penalty stiffness formulations accurately capture the maximum traction, which is attributed to the identical peak traction of 30 MPa prescribed

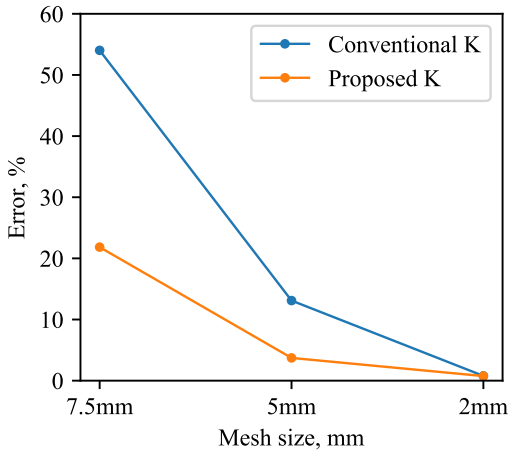

Figure 4.9: Normalized L_2 error of the DCB benchmark versus mesh size for different penalty stiffness formulations

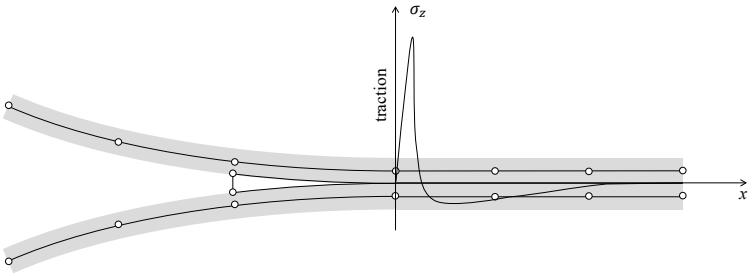

Figure 4.10: Distribution of traction ahead of crack tip

by the damage initiation criterion. A clear difference in mesh convergence is observed with respect to compression. For the conventional penalty stiffness, the predicted compression shows poor mesh convergence. Significant differences are observed between the 1 mm and 2 mm meshes, while the 5 mm mesh fails to converge and cannot reproduce the traction profile accurately. A similar lack of mesh convergence has also been reported for the two-dimensional DCB model based on higher-order beam elements [16]. In contrast, the proposed penalty stiffness exhibits excellent mesh convergence. The predicted traction distributions show significantly more stable predictions as the mesh is refined from 5 mm to 1 mm, demonstrating that accurate traction predictions can be achieved even with coarse meshes.

Figure 4.13 compares the traction distributions predicted by three numerical models. The black curve represents the 3D Abaqus cohesive contact model with a mesh size of 0.25 mm. The blue and orange curves correspond to the 1 mm TUBA3 model with the conventional penalty stiffness and the structural cohesive model with the proposed penalty

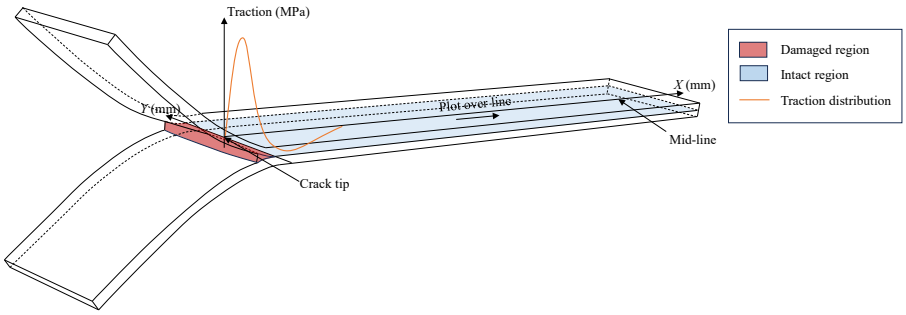

Figure 4.11: Procedure for extracting the traction distribution from cohesive elements

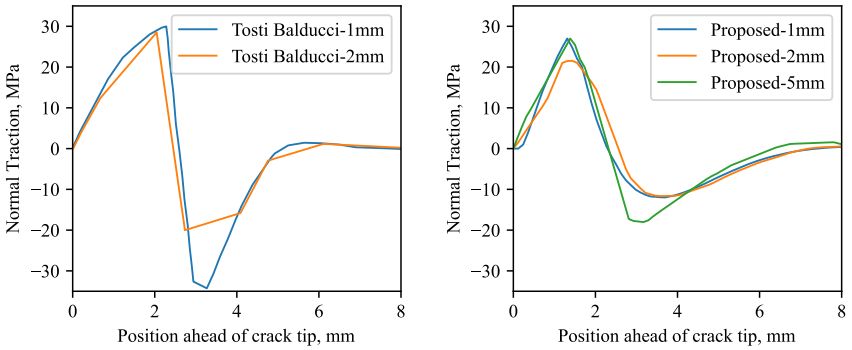

(a) Conventional penalty stiffness

(b) Proposed penalty stiffness

Figure 4.12: Comparison of normal traction distributions in the cohesive zone of the DCB specimen for different mesh sizes using the conventional and proposed penalty stiffness formulations

stiffness, respectively. The proposed penalty stiffness significantly reduces the predicted compression. The resulting compressive magnitude is approximately one-third of that predicted by the TUBA3 model. Nevertheless, it is still approximately two times greater than that predicted by the solid element model. This discrepancy is mainly attributed to the absence of transverse shear deformation in the structural ply element formulation. Further reducing the discrepancy with solid element models is beyond the scope of the present work and will be investigated in future research.

4.3.2. MODE II DELAMINATION BENCHMARK: END-NOTCHED FLEXURE (ENF)

DESCRIPTION OF THE ENF SPECIMEN

THE ENF specimen, shown in Figure 4.14, is selected as the Mode II delamination benchmark because it exhibits pure Mode II fracture ($G_{II}/G_T = 1$). The specimen geometry and boundary conditions are also illustrated in Figure 4.14. Unlike the DCB

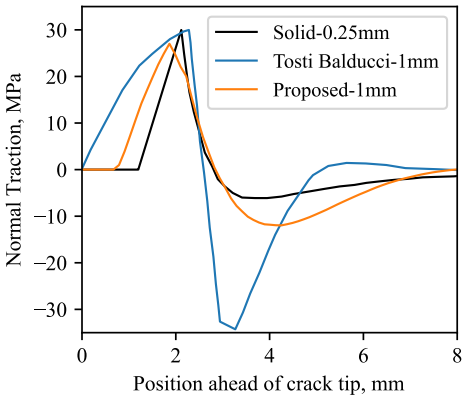

Figure 4.13: Comparison of the predicted normal traction distributions ahead of the crack tip

benchmark, the ENF specimen is fabricated from IM7/8552 composite laminate, whose material properties are listed in Table 4.4. The resin-rich layer is modelled using the 8552 epoxy material, whose material properties are taken from Krueger [28]. The corresponding parameters are summarized in Table 4.5.

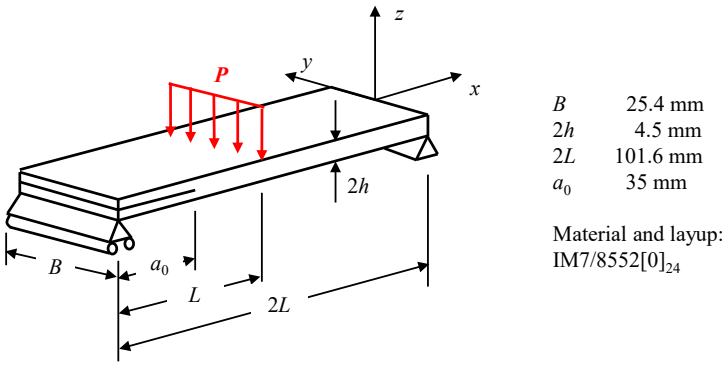

Figure 4.14: End-notched flexure (ENF) specimen [25]

Similar to the DCB model, the ENF model consists of a 24-ply laminate with a 0° layup throughout the specimen. According to Equation 4.32, the shear penalty stiffness is determined by taking into account the number of plies in each laminate arm. As the laminate is symmetric about the mid-plane, both the top and bottom arms contain 12 plies. The corresponding through-thickness transverse shear stress distribution is shown in Figure 4.15.

Based on the transverse shear stress distribution shown in Figure 4.15 and Equation 4.48, the stress ratio at each interface layer with respect to the maximum transverse shear stress is determined. The corresponding stress ratios for the interfaces in the top arm are summa-

Table 4.4: Material properties of the ENF and MMB specimens [25]

IM7/8552 Unidirectional graphite/epoxy prepreg		
E_{11}= 161 GPa	E_{22}= 11.38 GPa	E_{33} = 11.38 GPa
ν_{12} = 0.32	ν_{13} = 0.32	ν_{23} = 0.45
G_{12} = 5.2 GPa	G_{13} = 5.2 GPa	G_{23} = 3.9 GPa
Fracture toughness data		
$G_{\mathrm{Ic}} = 0.212\,\mathrm{kJ/m^2}$	$G_{\mathrm{IIc}} = 0.774\,\mathrm{kJ/m^2}$	$\eta = 2.1$
Interfacial strength data [11, 12]		
$\tau_{\mathrm{Ic}} = 30\,\mathrm{MPa}$	$\tau_{\mathrm{IIc}} = 60\,\mathrm{MPa}$	

Table 4.5: Material parameters of 8552 epoxy resin

$E_{\mathrm{rr}}^{\mathrm{ENF}}$ [28] $(\mathrm{N/mm^2})$	$G_{\mathrm{rr}}^{\mathrm{ENF}}$ [28] $(\mathrm{N/mm^2})$	$\nu_{\mathrm{rr}}^{\mathrm{ENF}}$ [28]	h_{rr} [27] (mm)
4700	1715	0.37	0.02286

rized in Table 4.6.

Table 4.6: Transverse shear stress ratios at the interface layers of the top arm in the 24-ply ENF specimen

$\frac{\tau_{xz}^1}{\tau_{xz}^{\max}}$	$\frac{\tau_{xz}^2}{\tau_{xz}^{\max}}$	$\frac{\tau_{xz}^3}{\tau_{xz}^{\max}}$	$\frac{\tau_{xz}^4}{\tau_{xz}^{\max}}$	$\frac{\tau_{xz}^5}{\tau_{xz}^{\max}}$	$\frac{\tau_{xz}^6}{\tau_{xz}^{\max}}$	$\frac{\tau_{xz}^7}{\tau_{xz}^{\max}}$	$\frac{\tau_{xz}^8}{\tau_{xz}^{\max}}$	$\frac{\tau_{xz}^9}{\tau_{xz}^{\max}}$	$\frac{\tau_{xz}^{10}}{\tau_{xz}^{\max}}$	$\frac{\tau_{xz}^{11}}{\tau_{xz}^{\max}}$	$\frac{\tau_{xz}^{12}}{\tau_{xz}^{\max}}$
1.0	0.69	0.42	0.19	0.00	-0.15	-0.25	-0.31	-0.33	-0.31	-0.25	-0.15

Therefore, the sum of the transverse shear stress ratios for the top arm is given by:

$$\sum_{i=1}^{n_{\mathrm{top}}^{\mathrm{ENF}}} \frac{\tau_{xz}(z_i)}{\tau_{xz}^{\max}} = \frac{\tau_{xz}^1 + \tau_{xz}^2 + \cdots + \tau_{xz}^{12}}{\tau_{xz}^{\max}} = 0.54 \tag{4.54}$$

where $n_{\mathrm{top}}^{\mathrm{ENF}}$ is the number of plies in the top arm of the ENF specimen.

Because the 24-ply ENF specimen is symmetric about the laminate mid-plane, the sum of the stress ratios in Equation 4.32 can be written as:

$$\sum_{i=1}^{n_{\mathrm{top}}^{\mathrm{ENF}}} \frac{\tau_{xz}(z_i)}{\tau_{xz}^{\max}} + \sum_{j=1}^{n_{\mathrm{bot}}^{\mathrm{ENF}}} \frac{\tau_{xz}(z_j)}{\tau_{xz}^{\max}} = 2\sum_{i=1}^{12} \frac{\tau_{xz}(z_i)}{\tau_{xz}^{\max}}$$
$$= 2 \times 0.54 = 1.08 \tag{4.55}$$

where $n_{\mathrm{bot}}^{\mathrm{ENF}}$ is the number of plies in the bottom arm of the ENF specimen.

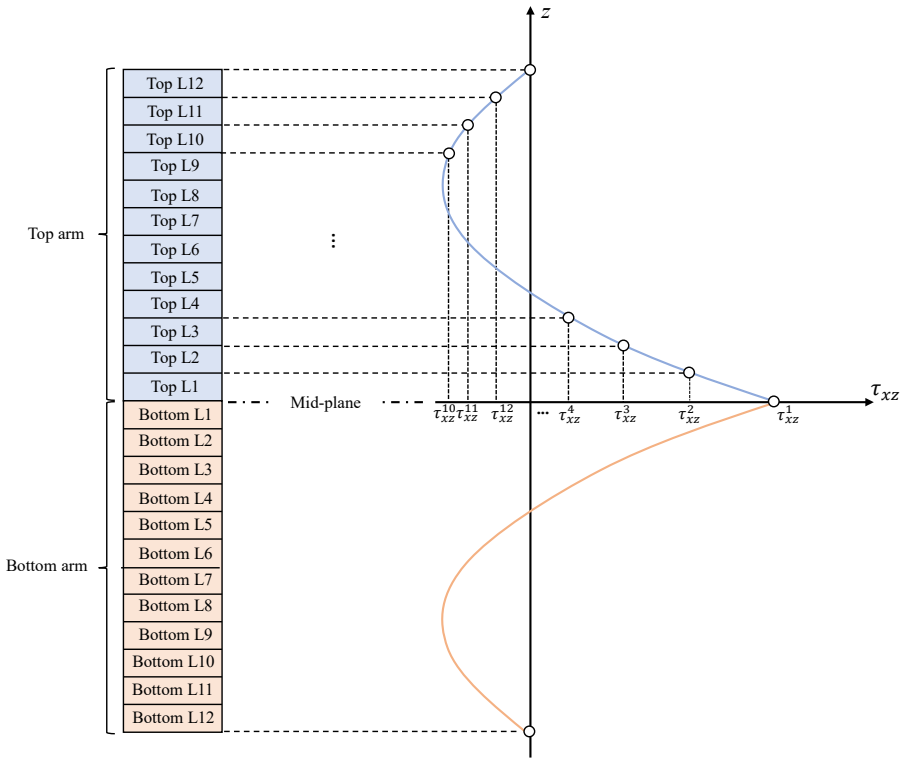

Figure 4.15: Through-thickness distribution of transverse shear stress in the 24-ply ENF specimen

According to Equation 4.32, the shear penalty stiffness of the ENF specimen can be calculated as:

$$K_s^{\text{ENF}} = \frac{1}{\sum_{i=1}^{12} \frac{\tau_{xz}(z_i)}{\tau_{xz}^{\max}} \frac{h_{\text{rr}}}{G_{\text{rr}}^{\text{ENF}}} + \sum_{j=1}^{12} \frac{\tau_{xz}(z_j)}{\tau_{xz}^{\max}} \frac{h_{\text{rr}}}{G_{\text{rr}}^{\text{ENF}}}}$$

$$= \frac{1}{1.08 \times \frac{0.02286}{1715}} = 69465\,\text{N/mm}^3 \tag{4.56}$$

LOAD-DISPLACEMENT CURVES

The load-displacement curves obtained from the ENF simulations are shown in Figure 4.16. The left panel presents the results obtained using the conventional penalty stiffness. The right panel compares the results obtained using the proposed shear penalty stiffness with those obtained using the formulation proposed by Bazilevs et al. [18]. The latter is represented by the green curve, and the corresponding expression for the Bazilevs shear penalty

stiffness is given below:

$$K_s^{\text{Bazilevs}} = \frac{G_{13}}{h_{\text{top}}/2 + h_{\text{bot}}/2} = \frac{5200}{2.25} = 2311\,\text{N/mm}^3 \tag{4.57}$$

where G_{13} is the transverse shear modulus of the composite laminate.

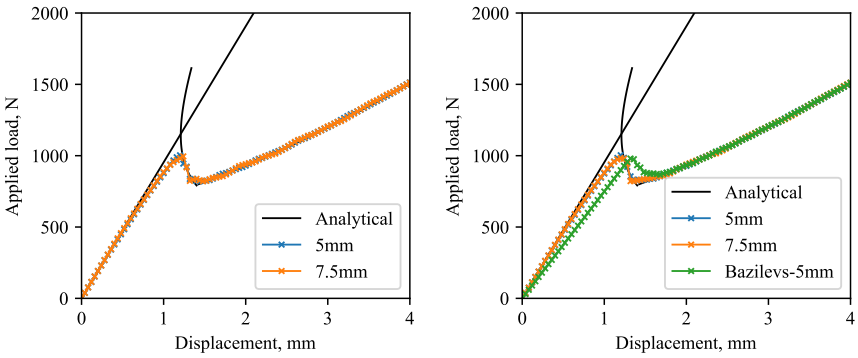

(a) Conventional penalty stiffness

(b) Proposed and Bazilevs' penalty stiffness

Figure 4.16: Comparison of the load-displacement curves obtained from the ENF simulations using the conventional, Bazilevs', and proposed penalty stiffness formulations at different mesh densities

Figure 4.16 compares the load–displacement curves obtained using the three shear penalty stiffness formulations. Both the conventional penalty stiffness and proposed shear penalty stiffness accurately capture the complete delamination process and exhibit excellent mesh convergence. Even with a coarse mesh size of 7.5 mm, the numerical predictions remain in close agreement with the analytical solution. In contrast, when Bazilevs's shear penalty stiffness is adopted, the initial stiffness is significantly underestimated. Although the predicted peak load is close to those obtained using the other two formulations, the corresponding displacement is noticeably larger than the analytical solution. This discrepancy is caused by the extremely low shear penalty stiffness defined in Equation 4.57, which makes the structural response excessively compliant and reduces the accuracy of the predicted delamination process. A similar response was also reported by Bazilevs et al. [18]. This result indicates that the improved performance of the present formulation is attributable to the proposed shear penalty stiffness rather than the shell element formulation

In summary, the proposed shear penalty stiffness does not provide a significant improvement over the conventional penalty stiffness. The difference between the proposed and conventional formulations is less pronounced than in the DCB model. Nevertheless, the proposed formulation produces more accurate predictions than other shear penalty stiffness formulations developed for shell elements.

4.3.3. MIXED-MODE DELAMINATION BENCHMARK: MIXED-MODE BENDING (MMB)

DESCRIPTION OF THE MMB SPECIMEN

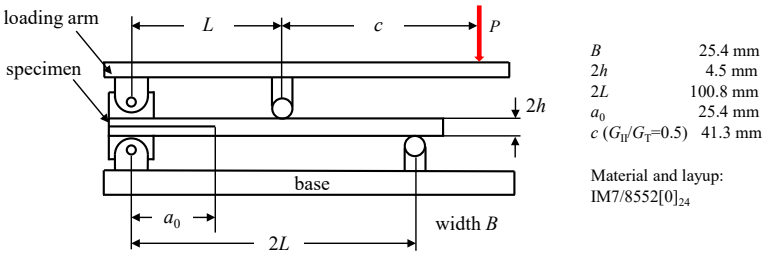

Figure 4.17: Mixed-mode bending (MMB) specimen [25]

THE MMB specimen, shown in Figure 4.17, is designed for a mixed-mode ratio of $G_{II}/G_T = 0.5$. The laminate layup, specimen geometry, and initial crack length, a_0 are also illustrated in the figure. The material properties are identical to those of the ENF model and are listed in Table 4.4. Because the laminate configuration and material properties are identical to those of the ENF model, the shear penalty stiffness is also identical and is given by Equation 4.32:

$$K_s^{\text{MMB}} = K_s^{\text{ENF}} = \frac{1}{\sum_{i=1}^{12} \frac{\tau_{xz}(z_i)}{\tau_{xz}^{\max}} \frac{h_{\text{rr}}}{G_{\text{rr}}^{\text{ENF}}} + \sum_{j=1}^{12} \frac{\tau_{xz}(z_j)}{\tau_{xz}^{\max}} \frac{h_{\text{rr}}}{G_{\text{rr}}^{\text{ENF}}}}$$

$$= \frac{1}{1.08 \times \frac{0.02286}{1715}} = 69465\,\text{N/mm}^3 \tag{4.58}$$

For the normal penalty stiffness, the stress ratios in Equation 4.11 are identical to those of the DCB model because the MMB and DCB laminates have the same configuration. However, the resin-rich layer in the MMB model has a different elastic modulus. The normal penalty stiffness cannot be directly adopted from the DCB model and must be re-calculated. The corresponding expression is given by:

$$K_n^{\text{MMB}} = \frac{1}{\sum_{i=1}^{12} \frac{\sigma_z(z_i)}{\sigma_z^{\max}} \frac{h_{\text{rr}}}{E_{\text{rr}}^{\text{ENF}}} + \sum_{j=1}^{12} \frac{\sigma_z(z_j)}{\sigma_{\max}} \frac{h_{\text{rr}}}{E_{\text{rr}}^{\text{ENF}}}}$$

$$= \frac{1}{13 \times \frac{0.02286}{4700}} = 15815\,\text{N/mm}^3 \tag{4.59}$$

LOAD-DISPLACEMENT CURVES

The load-displacement curves obtained using the proposed normal and shear penalty stiffness are shown in Figure 4.18b. For comparison, the corresponding results obtained using the conventional penalty stiffness are presented in Figure 4.18a.

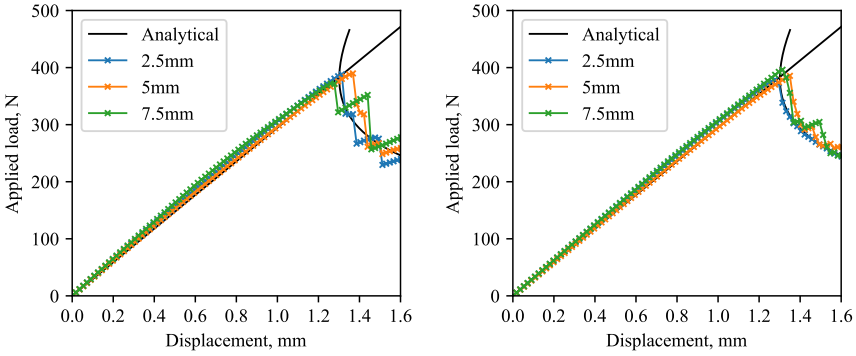

(a) Conventional penalty stiffness

(b) Proposed penalty stiffness

Figure 4.18: Comparison of the load-displacement curves obtained from the MMB simulations using the conventional and proposed penalty stiffness formulations at different mesh densities

A comparison of Figures 4.18b and 4.18a shows that the proposed penalty stiffness formulations produce smoother load-displacement curves than the conventional formulation. After the peak load, the predicted curves remain in excellent agreement with the analytical solution for all mesh sizes considered.

To further quantify the improvement, the MMB specimen is evaluated using the same normalized L_2 error adopted for the DCB specimen. Figure 4.19 compares the normalized L_2 error obtained using the conventional and proposed penalty stiffness formulations at different mesh sizes. As the mesh is refined from 7.5 mm to 2.5 mm, the error decreases for both formulations. Nevertheless, the proposed penalty stiffness consistently produces a lower normalized L_2 error than the conventional penalty stiffness. The improvement becomes more pronounced as the mesh is refined. In summary, the proposed penalty stiffness formulations reduce the prediction error and achieve closer agreement with the analytical solution for the MMB specimen.

4.3.4. THREE-DIMENSIONAL DELAMINATION BENCHMARK: REINFORCED DOUBLE CANTILEVER BEAM (R-DCB)

DESCRIPTION OF THE R-DCB SPECIMEN

THE R-DCB benchmark considered in this study is based on the experimental specimen proposed by Carreras et al. [29]. The specimen consists of a standard DCB laminate fabricated from 16 unidirectional plies oriented at $0°$. Two reinforcement laminates, each composed of eight unidirectional plies with the same stacking sequence, are bonded to the upper and lower surfaces of the DCB laminate. The ply material properties are presented in Table 4.7. The resin-rich layer is modelled by Araldite 2015, whose material properties

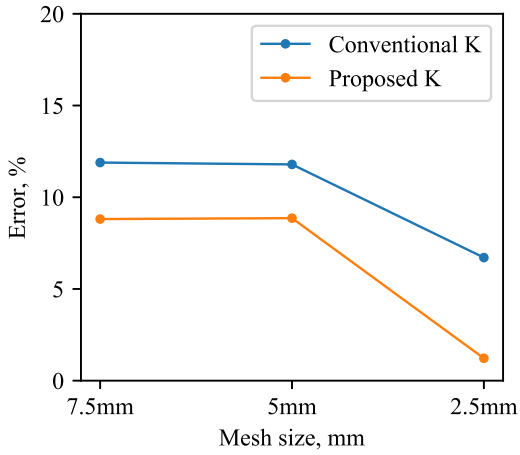

Figure 4.19: Normalized L_2 error of the MMB benchmark versus mesh size for different penalty stiffness formulations

are obtained from Campilho et al. [30]. The corresponding resin-rich layer properties are summarized in Table 4.8. The geometry of the R-DCB specimen is shown in Figure 4.20.

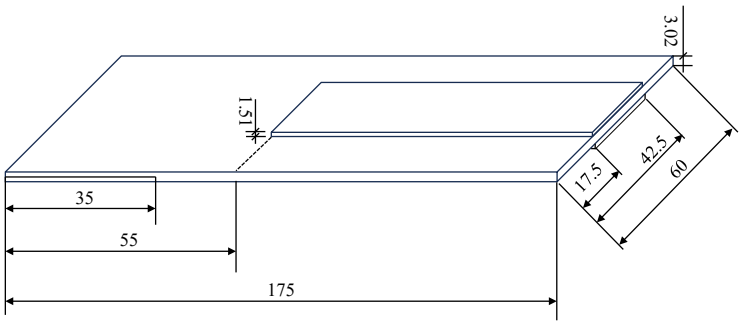

Figure 4.20: Geometry of the R-DCB specimen (units in mm) [29]

Compared with the previously validated benchmark models, the R-DCB model has a larger geometric size and a higher number of finite elements. To improve computational efficiency, symmetry boundary conditions are employed, as illustrated in Figure 4.21. The right end of the model is fixed, while a prescribed displacement is applied at the left end.

PENALTY STIFFNESS OF THE UNREINFORCED REGION IN THE R-DCB SPECIMEN

As shown in Figure 4.22, the R-DCB specimen can be divided into four regions: the pre-crack region, the unreinforced region, the reinforced region, and the undamaged region. Excluding the pre-crack region, structural cohesive elements are inserted along the mid-plane between the top and bottom laminate arms in both the unreinforced and reinforced

Table 4.7: Material properties for the R-DCB specimen[31]

Unidirectional carbon fiber/epoxy prepreg		
E_{11}= 154 GPa	E_{22}= 8.5 GPa	E_{33} = 8.5 GPa
ν_{12} = 0.35	ν_{13} = 0.35	ν_{23} = 0.4
G_{12} = 4.2 GPa	G_{13} = 4.2 GPa	G_{23} = 3.04 GPa
Fracture toughness data		
$G_{\mathrm{Ic}} = 0.305\,\mathrm{kJ/m^2}$	$G_{\mathrm{IIc}} = 2.77\,\mathrm{kJ/m^2}$	$\eta = 2.05$
Interfacial strength data [8]		
$\tau_{\mathrm{Ic}} = 32.6\,\mathrm{MPa}$	$\tau_{\mathrm{IIc}} = 98\,\mathrm{MPa}$	

Table 4.8: Material parameters of Araldite 2015

$E_{\mathrm{rr}}^{\text{R-DCB}}$ [30] (N/mm^2)	$G_{\mathrm{rr}}^{\text{R-DCB}}$ [30] (N/mm^2)	$\nu_{\mathrm{rr}}^{\text{R-DCB}}$ [30]	h_{rr} [27] (mm)
1850	560	0.33	0.02286

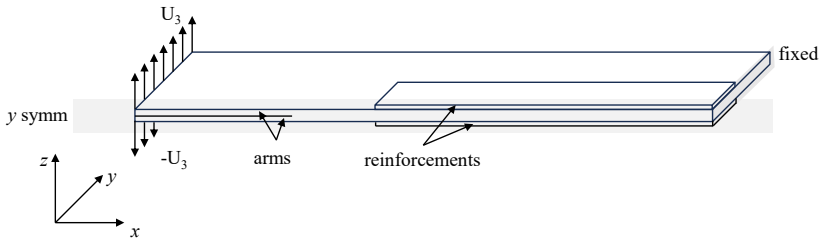

Figure 4.21: Boundary conditions and loading of the finite element model; U_3=7.5 mm

regions to simulate crack initiation and propagation. During loading, these cohesive elements are progressively damaged as the crack propagates. Accordingly, the unreinforced and reinforced regions are collectively referred to as the damaged region, in contrast to the undamaged region, where no damage develops in the cohesive elements located between the laminate arms and the reinforcements. The unreinforced and reinforced regions each consist of a 16-ply laminate, whereas the undamaged region includes two additional 8-ply reinforcement laminates. The derivation of the stress distribution begins with the unreinforced region, as illustrated in Figure 4.23.

Based on the out-of-plane normal stress distribution shown in Figure 4.23, the ratio of the stress in each interface layer relative to the maximum stress value can be derived. The corresponding stress ratio values for each interface layer in the top arm are listed in Table 4.9.

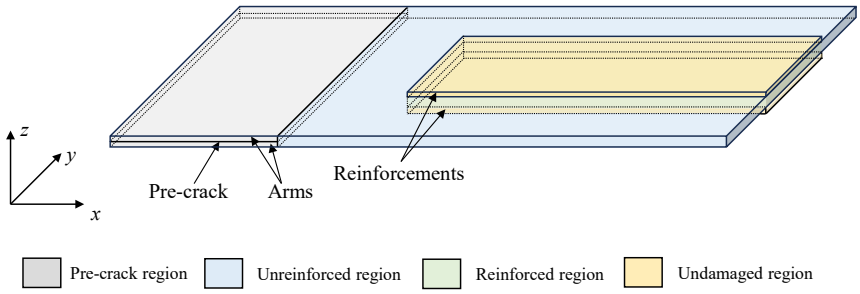

Figure 4.22: Different regions of the R-DCB specimen

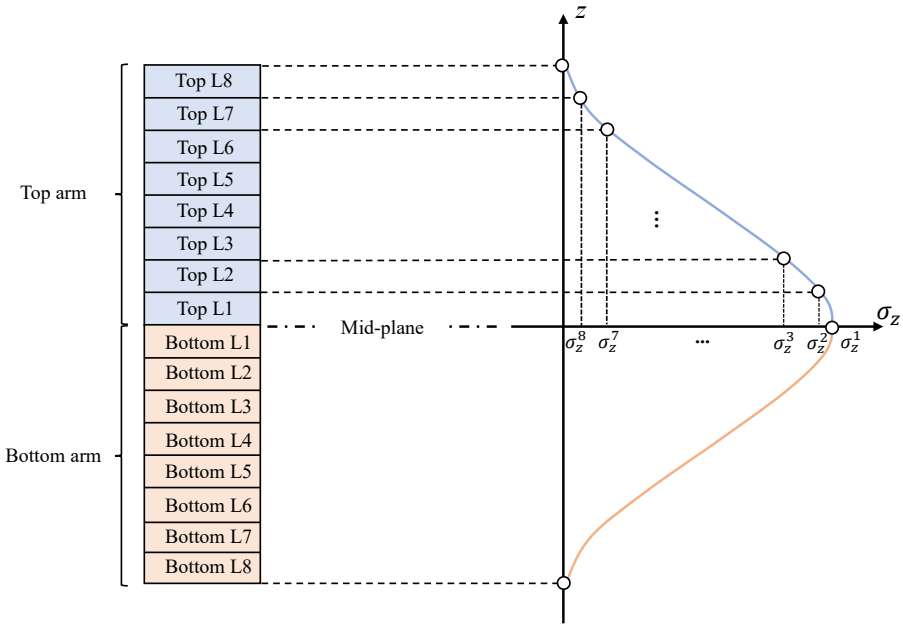

Figure 4.23: Through-thickness distribution of out-of-plane normal stress in the 16-ply unreinforced region of the R-DCB specimen

Table 4.9: Out-of-plane normal stress ratios at the interface layers of the top arm in the 16-ply unreinforced region

$\frac{\sigma_z^1}{\sigma_z^{\max}}$	$\frac{\sigma_z^2}{\sigma_z^{\max}}$	$\frac{\sigma_z^3}{\sigma_z^{\max}}$	$\frac{\sigma_z^4}{\sigma_z^{\max}}$	$\frac{\sigma_z^5}{\sigma_z^{\max}}$	$\frac{\sigma_z^6}{\sigma_z^{\max}}$	$\frac{\sigma_z^7}{\sigma_z^{\max}}$	$\frac{\sigma_z^8}{\sigma_z^{\max}}$
1.00	0.96	0.84	0.68	0.50	0.32	0.16	0.04

Therefore, the sum of the out-of-plane stress ratios for the top arm in the unreinforced

region can be calculated as:

$$\sum_{i=1}^{n_{\text{top}}^{\text{Unreinforced}}} \frac{\sigma_z(z_i)}{\sigma_z^{\max}} = \frac{\sigma_z^1 + \sigma_z^2 + \cdots + \sigma_z^8}{\sigma_z^{\max}} = 4.5 \tag{4.60}$$

where $n_{\text{top}}^{\text{Unreinforced}}$ is the number of plies in the top arm of the unreinforced region of the R-DCB specimen.

Due to the symmetric layup of the 16-layer unreinforced region, the sum of the ratios in Equation 4.11 can be derived as follows:

$$\begin{aligned}\sum_{i=1}^{n_{\text{top}}^{\text{Unreinforced}}} \frac{\sigma_z(z_i)}{\sigma_z^{\max}} + \sum_{j=1}^{n_{\text{bot}}^{\text{Unreinforced}}} \frac{\sigma_z(z_j)}{\sigma_z^{\max}} &= 2\sum_{i=1}^{8} \frac{\sigma_z(z_i)}{\sigma_z^{\max}} \\ &= 2 \times 4.5 = 9\end{aligned} \tag{4.61}$$

where $n_{\text{bot}}^{\text{Unreinforced}}$ is the number of plies in the bottom arm of the unreinforced region of the R-DCB specimen.

Based on Equation 4.11, the normal penalty stiffness for the unreinforced region in the R-DCB model can be calculated as follows:

$$\begin{aligned}K_n^{\text{Unreinforced}} &= \frac{1}{\sum_{i=1}^{8} \frac{\sigma_z(z_i)}{\sigma_z^{\max}} \frac{h_{\text{rr}}}{E_{\text{rr}}^{\text{R-DCB}}} + \sum_{j=1}^{8} \frac{\sigma_z(z_j)}{\sigma_z^{\max}} \frac{h_{\text{rr}}}{E_{\text{rr}}^{\text{R-DCB}}}} \\ &= \frac{1}{9 \times \frac{0.02286}{1850}} = 8992\,\text{N/mm}^3\end{aligned} \tag{4.62}$$

PENALTY STIFFNESS OF THE REINFORCED REGION IN THE R-DCB SPECIMEN

For the 16-ply reinforced region, the through-thickness distribution of the out-of-plane normal stress is shown in Figure 4.24. Based on this distribution, interface stress ratios can be determined. The corresponding values for the interface layers in the top arm are listed in Table 4.10.

Table 4.10: Out-of-plane normal stress ratios at the interface layers of the top arm in the 16-ply reinforced region

$\frac{\sigma_z^1}{\sigma_z^{\max}}$	$\frac{\sigma_z^2}{\sigma_z^{\max}}$	$\frac{\sigma_z^3}{\sigma_z^{\max}}$	$\frac{\sigma_z^4}{\sigma_z^{\max}}$	$\frac{\sigma_z^5}{\sigma_z^{\max}}$	$\frac{\sigma_z^6}{\sigma_z^{\max}}$	$\frac{\sigma_z^7}{\sigma_z^{\max}}$	$\frac{\sigma_z^8}{\sigma_z^{\max}}$
1.00	0.99	0.96	0.91	0.84	0.77	0.68	0.59

The sum of the out-of-plane normal stress ratios for the top arm in the reinforced region can be expressed as follows:

$$\sum_{i=1}^{n_{\text{top}}^{\text{Reinforced}}} \frac{\sigma_z(z_i)}{\sigma_z^{\max}} = \frac{\sigma_z^1 + \sigma_z^2 + \cdots + \sigma_z^8}{\sigma_z^{\max}} = 6.74 \tag{4.63}$$

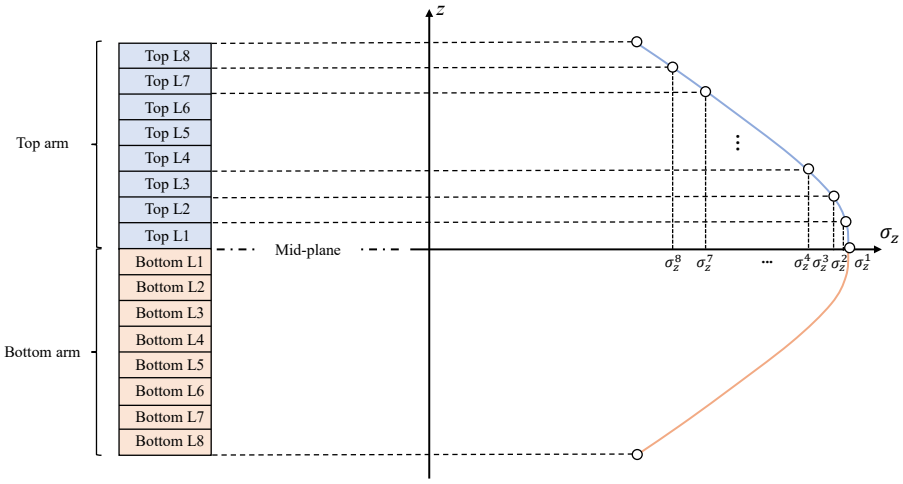

Figure 4.24: Through-thickness distribution of out-of-plane normal stress in the 16-ply reinforced region of the R-DCB specimen

where $n_{\text{top}}^{\text{Reinforced}}$ is the number of plies in the top arm of the reinforced region of the R-DCB specimen.

Because the 16-ply reinforced region is symmetric about the laminate mid-plane, the sum of the out-of-plane normal stress ratios can be written as:

$$\sum_{i=1}^{n_{\text{top}}^{\text{Reinforced}}} \frac{\sigma_z(z_i)}{\sigma_z^{\max}} + \sum_{j=1}^{n_{\text{bot}}^{\text{Reinforced}}} \frac{\sigma_z(z_j)}{\sigma_z^{\max}} = 2\sum_{i=1}^{8} \frac{\sigma_z(z_i)}{\sigma_z^{\max}}$$
$$= 2 \times 6.74 = 13.48 \tag{4.64}$$

where $n_{\text{bot}}^{\text{Reinforced}}$ is the number of plies in the bottom arm of the reinforced region of the R-DCB specimen.

The normal penalty stiffness for the reinforced region in the R-DCB specimen is given by:

$$K_n^{\text{Reinforced}} = \frac{1}{\sum_{i=1}^{8} \frac{\sigma_z(z_i)}{\sigma_z^{\max}} \frac{h_{\text{rr}}}{E_{\text{rr}}^{\text{R-DCB}}} + \sum_{j=1}^{8} \frac{\sigma_z(z_j)}{\sigma_z^{\max}} \frac{h_{\text{rr}}}{E_{\text{rr}}^{\text{R-DCB}}}}$$
$$= \frac{1}{13.48 \times \frac{0.02286}{1850}} = 6004\,\text{N/mm}^3 \tag{4.65}$$

The R-DCB model is similar to the DCB model and exhibits Mode I fracture behavior. Therefore, the effect of the shear penalty stiffness of the damaged region is negligible and is not considered further in the analyses of either the unreinforced or reinforced region.

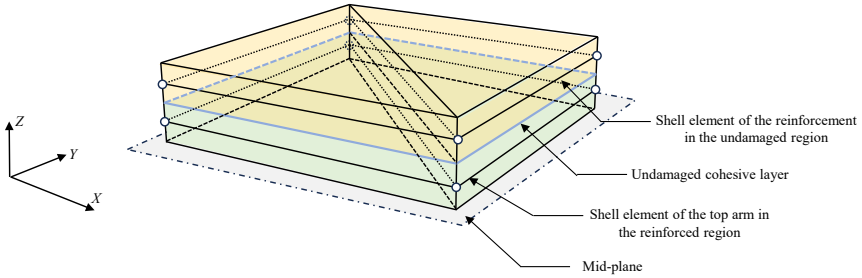

Figure 4.25: Finite element model of the undamaged region in the R-DCB specimen

PENALTY STIFFNESS OF THE UNDAMAGED REGION IN THE R-DCB SPECIMEN

Figure 4.25 illustrates the undamaged region of the R-DCB specimen. The top arm and the reinforcement are modelled by triangular higher-order shell elements, while an undamaged structural cohesive layer is inserted between them to represent the bonding interface. Although no damage develops in this region throughout the loading process, the structural cohesive elements are retained to ensure displacement continuity and to transfer interlaminar tractions. Unlike the DCB benchmark, the shear penalty stiffness can no longer be neglected and must be determined from the through-thickness transverse shear stress distribution. The derivation of the corresponding normal and shear penalty stiffnesses is presented below.

As shown in Figure 4.25, only the through-thickness stress distribution in the reinforcement is required to derive the penalty stiffness for the undamaged region. Because the R-DCB specimen is symmetric about the mid-plane, the penalty stiffnesses of the undamaged regions in the top and bottom reinforcements are identical. Therefore, the following derivation is presented for the top arm only. The corresponding distributions of the out-of-plane normal stress and transverse shear stress are shown in Figure 4.26 and 4.27, respectively.

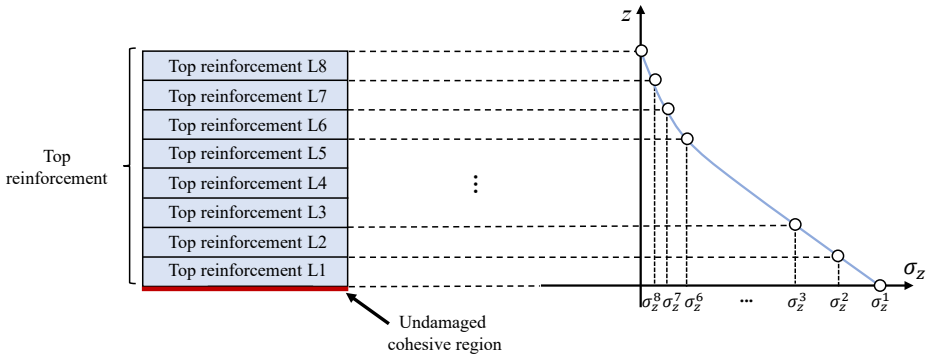

Figure 4.26: Through-thickness distribution of out-of-plane normal stress in the 8-ply undamaged region of the R-DCB specimen

Based on the through-thickness distributions of the out-of-plane normal and transverse shear stresses shown in Figures 4.26 and 4.27, the interface stress ratios relative to the

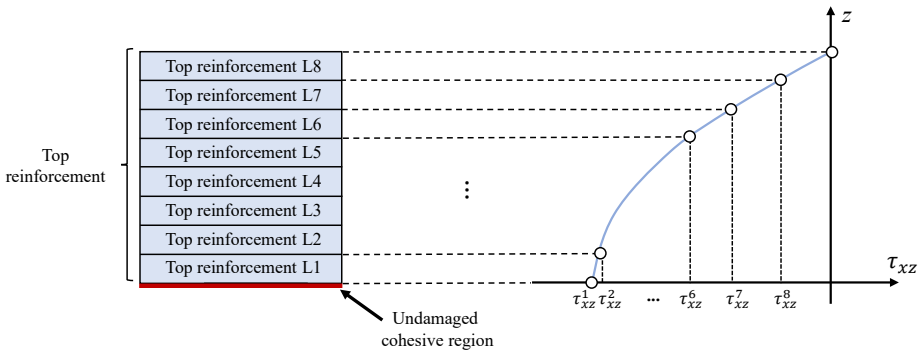

Figure 4.27: Through-thickness distribution of transverse shear stress in the 8-ply undamaged region of the R-DCB specimen

corresponding maximum values are determined. The resulting normal and shear stress ratios for each interface layer are presented in Tables 4.11 and 4.12, respectively.

Table 4.11: Out-of-plane normal stress ratios at the interface layers of the 8-ply undamaged region

$\frac{\sigma_z^1}{\sigma_z^{\max}}$	$\frac{\sigma_z^2}{\sigma_z^{\max}}$	$\frac{\sigma_z^3}{\sigma_z^{\max}}$	$\frac{\sigma_z^4}{\sigma_z^{\max}}$	$\frac{\sigma_z^5}{\sigma_z^{\max}}$	$\frac{\sigma_z^6}{\sigma_z^{\max}}$	$\frac{\sigma_z^7}{\sigma_z^{\max}}$	$\frac{\sigma_z^8}{\sigma_z^{\max}}$
1.00	0.81	0.63	0.46	0.31	0.18	0.09	0.02

Table 4.12: Transverse shear stress ratios at the interface layers of the 8-ply undamaged region

$\frac{\tau_{xz}^1}{\tau_{xz}^{\max}}$	$\frac{\tau_{xz}^2}{\tau_{xz}^{\max}}$	$\frac{\tau_{xz}^3}{\tau_{xz}^{\max}}$	$\frac{\tau_{xz}^4}{\tau_{xz}^{\max}}$	$\frac{\tau_{xz}^5}{\tau_{xz}^{\max}}$	$\frac{\tau_{xz}^6}{\tau_{xz}^{\max}}$	$\frac{\tau_{xz}^7}{\tau_{xz}^{\max}}$	$\frac{\tau_{xz}^8}{\tau_{xz}^{\max}}$
1.00	0.98	0.94	0.86	0.75	0.61	0.44	0.23

The sums of the out-of-plane normal stress ratios and transverse shear stress ratios in the undamaged region are given by:

$$\sum_{i=1}^{n^{\text{Undamaged}}} \frac{\sigma_z(z_i)}{\sigma_z^{\max}} = \frac{\sigma_z^1 + \sigma_z^2 + \cdots + \sigma_z^8}{\sigma_z^{\max}} = 3.5 \tag{4.66}$$

and

$$\sum_{i=1}^{n^{\text{Undamaged}}} \frac{\tau_{xz}(z_i)}{\tau_{xz}^{\max}} = \frac{\tau_{xz}^1 + \tau_{xz}^2 + \cdots + \tau_{xz}^8}{\tau_{xz}^{\max}} = 5.81 \tag{4.67}$$

where $n^{\text{Undamaged}}$ is the number of plies in the undamaged region of the R-DCB specimen.

Substituting these stress ratios into Equations 4.11 and 4.32 yields the normal and shear penalty stiffnesses for the undamaged region of the R-DCB specimen, respectively, as follows:

$$K_n^{\text{Undamaged}} = \frac{1}{\sum_{i=1}^{16} \frac{\sigma_z(z_i)}{\sigma_z^{\max}} \frac{h_{\text{rr}}}{E_{\text{rr}}^{\text{R-DCB}}}}$$

$$= \frac{1}{3.5 \times \frac{0.02286}{1850}} = 23122\,\text{N/mm}^3 \tag{4.68}$$

$$K_s^{\text{Undamaged}} = \frac{1}{\sum_{i=1}^{16} \frac{\tau_{xz}(z_i)}{\tau_{xz}^{\max}} \frac{h_{\text{rr}}}{G_{\text{rr}}^{\text{R-DCB}}}}$$

$$= \frac{1}{5.81 \times \frac{0.02286}{560}} = 4216\,\text{N/mm}^3 \tag{4.69}$$

LOAD-DISPLACEMENT CURVES

The load-displacement curves obtained from the R-DCB simulations are shown in Figure 4.28. The left panel (Figure 4.28a) shows the results obtained by the conventional penalty stiffness, whereas the right panel (Figure 4.28b) presents the results obtained by the proposed penalty stiffness.

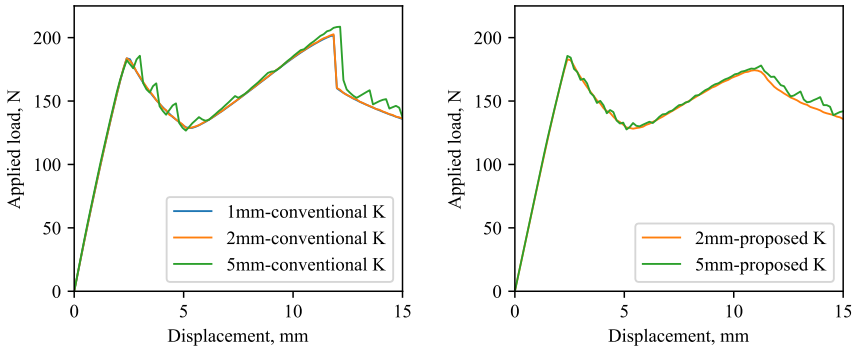

(a) Conventional penalty stiffness

(b) Proposed penalty stiffness

Figure 4.28: Comparison of the load-displacement curves obtained from the R-DCB simulations using the conventional and proposed penalty stiffness formulations at different mesh densities

A comparison of the results in Figures 4.28a and 4.28b shows a clear difference in mesh convergence. When the conventional penalty stiffness is adopted, the load-displacement curve obtained with a 5 mm mesh differs noticeably from those obtained with the 2 mm and 1 mm meshes. In particular, the second peak occurs at a larger displacement and reaches a higher load, and the descending segment exhibits obvious oscillations. By contrast, the results obtained with the 2 mm and 1 mm meshes are in close agreement. When the proposed

penalty stiffness is adopted, the results obtained with a 5 mm mesh closely matches that of the 2 mm mesh, and the oscillations are significantly reduced. These results demonstrate that the proposed penalty stiffness improves the mesh convergence.

In addition to the improved mesh convergence, a further difference can be observed in the response around the second load peak. As shown in Figure 4.28a, the load drops abruptly after reaching the second peak with the conventional penalty stiffness. By contrast, the proposed penalty stiffness (Figure 4.28b) produces a more gradual softening process, which results in a second peak load 14% lower than that predicted with the conventional penalty stiffness.

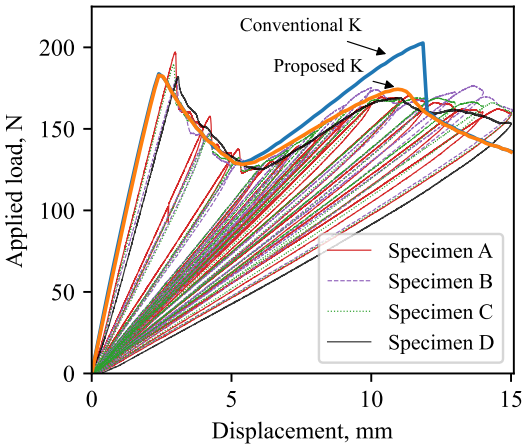

Figure 4.29: Comparison of numerical and experimental results of the load-displacement curves [29]

To assess the accuracy of the two penalty stiffness formulations, the load-displacement curves obtained using a 2 mm mesh are compared with the experimental data, as shown in Figure 4.29. The results show that the curve obtained using the proposed penalty stiffness agrees more closely with the experimental results. In particular, the second loading segment exhibits a lower stiffness than that predicted using the conventional penalty stiffness. Consequently, the predicted second peak load is in much better agreement with the experimental results. This improvement can be attributed to the proposed penalty stiffness formulation, which incorporates the transverse shear compliance. As a result, the proposed method avoids an excessively stiff response when the reinforced region is loaded.

In summary, for complex composite structures with reinforcements or stiffeners, the proposed penalty stiffness provides improved mesh convergence and higher predictive accuracy. Consequently, it enables the use of coarser meshes without losing accuracy, thereby improving the computational efficiency of delamination simulations.

CRACK FRONT EVOLUTION

Figure 4.30 compares the crack front positions obtained from the experiments and numerical simulations at different opening displacements. Regardless of whether the conventional or proposed penalty stiffness is adopted, the predicted crack fronts are in good agreement

with the experimental results. At opening displacements below 6 mm, the crack front remains approximately straight across the specimen width. As the opening displacement exceeds 6 mm, it gradually evolves into a curved profile. At an opening displacement of 10 mm, the central portion of the crack front begins to lag behind the free edges, which indicates a lower crack propagation rate in the central region. As the opening displacement increases further, the crack front continues to evolve. The propagation rate in the central region eventually exceeds that at the free edges, resulting in a convex crack front in the direction of crack propagation.

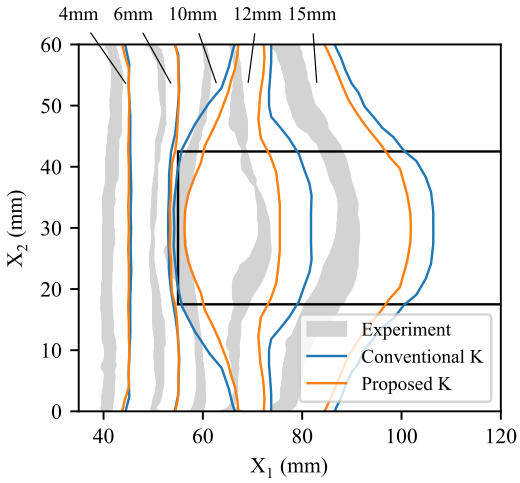

Figure 4.30: Comparison of numerical and experimental [29] delamination front positions

Overall, the crack front evolution predicted by the two penalty stiffness formulations is generally similar. Before the crack reaches the reinforced region (i.e., at opening displacements of 6 mm or less), both predictions agree well with the experimental observations. Once the crack propagates into the reinforced region, obvious differences become evident. At an opening displacement of 10 mm, the crack front predicted using the proposed penalty stiffness extends further into the reinforced region than that predicted using the conventional penalty stiffness. As the opening displacement increases beyond 10 mm, the crack propagation trend reverses. The crack propagation rate predicted using the proposed penalty stiffness becomes lower than that predicted using the conventional penalty stiffness. This prediction shows better agreement with the experimental results. Consequently, the predicted crack length is approximately 14% shorter and agrees more closely with the experimental results.

Both numerical models slightly overpredict crack propagation because the compliance of the testing machine is not included in the numerical model. Nevertheless, the proposed penalty stiffness provides a closer match to the experimental observations throughout the crack propagation process. These results indicate that the proposed formulation improves the accuracy of crack propagation predictions.

4.4. SUMMARY AND CONCLUSIONS

THIS work aims at (a) deriving distributions of the out-of-plane normal and transverse shear stresses, and (b) establishing an accurate penalty stiffness formulation directly from the material properties and the thickness of the resin-rich layer by incorporating these stress distributions. In the previous formulation, the penalty stiffness is determined solely from the resin-rich layer thickness without considering stress distributions. Consequently, it requires a layer-by-layer representation of the laminate and cannot be directly applied to equivalent single-layer models. As a result, the computational efficiency is significantly reduced. The proposed method is based on beam theory and derives analytical expressions for the out-of-plane normal and transverse shear stress distributions through the laminate thickness. The opening displacement is then determined from the ratio of the stress at each interface layer to the maximum stress. The corresponding penalty stiffness is then calculated from the opening displacement. For mixed-mode fracture problems, a mode-dependent cohesive law is employed to accurately predict damage evolution.

The proposed method has been implemented in three-dimensional structural element [8] models and validated using DCB, ENF, MMB, and R-DCB unidirectional laminate benchmarks. By overcoming limitations of the structural cohesive element implementations in equivalent single-layer models, the proposed approach significantly improves computational efficiency. Comparisons with the conventional penalty stiffness show that the proposed penalty stiffness substantially improves mesh convergence and prediction accuracy. Consequently, it allows cohesive elements to be discretized with coarser meshes, thereby reducing computational time. An analysis of the crack-tip stress distribution in the DCB model shows that the proposed method eliminates the mesh dependency observed in previous high-order structural elements with respect to compressive stress distribution ahead of the crack tip. In addition, it reduces the discrepancy between structural-element and solid-element predictions. For fully three-dimensional delamination problems with highly curved crack fronts, the proposed method also provides better agreement with experimental results than existing approaches.

The proposed method enables accurate prediction of out-of-plane delamination and the corresponding out-of-plane stress distributions in three-dimensional composite laminate models based on the equivalent single-layer method. The methods in this chapter also have limitations. In the present study, these assumptions are introduced to derive the penalty stiffness expressions for the specific loading configurations. Therefore, the penalty stiffness expressions derived under the current DCB and ENF assumptions cannot be directly interpreted as universally applicable to arbitrary loading conditions. However, the proposed derivation is not restricted to DCB and ENF configurations. If the through-thickness stress distribution is known for another loading condition, the corresponding stress distribution can also be incorporated into the derivation to determine the penalty stiffness for that case. We have added these limitations in the revised manuscript and included them in the discussion of the limitations and future work. In addition, the comparisons involve different element formulations, which makes it difficult to distinguish the effects of the element type from those of the penalty stiffness. To isolate the influence of element type, the element formulation should be kept consistent across the comparisons. A systematic investigation using the same structural CE with varying penalty stiffness values should be considered in future work.

REFERENCES

1. Baker, A. A. *Composite materials for aircraft structures* (AIAA, 2004).
2. Kassapoglou, C. *Design and analysis of composite structures: with applications to aerospace structures* (Wiley Online Library, 2010).
3. Chen, B., Tay, T., Baiz, P. & Pinho, S. Numerical analysis of size effects on open-hole tensile composite laminates. *Composites Part A: Applied Science and Manufacturing* **47,** 52–62 (2013).
4. Ratcliffe, J. G., Czabaj, M. W. & O'Brien, T. K. *A test for characterizing delamination migration in carbon/epoxy tape laminates* tech. rep. (2013).
5. Chen, B., Tay, T., Pinho, S. & Tan, V. Modelling delamination migration in angle-ply laminates. *Composites Science and Technology* **142,** 145–155 (2017).
6. Dugdale, D. S. Yielding of steel sheets containing slits. *Journal of the Mechanics and Physics of Solids* **8,** 100–104 (1960).
7. Barenblatt, G. I. The mathematical theory of equilibrium cracks in brittle fracture. *Advances in applied mechanics* **7,** 55–129 (1962).
8. Ai, X., Chen, B. & Kassapoglou, C. Structural cohesive element for the modelling of delamination in composite laminates without the cohesive zone limit. *Engineering Fracture Mechanics,* 111586 (2025).
9. Turon, A., Camanho, P. P., Costa, J. & Dávila, C. A damage model for the simulation of delamination in advanced composites under variable-mode loading. *Mechanics of materials* **38,** 1072–1089 (2006).
10. Turon, A., Davila, C. G., Camanho, P. P. & Costa, J. An engineering solution for mesh size effects in the simulation of delamination using cohesive zone models. *Engineering fracture mechanics* **74,** 1665–1682 (2007).
11. Turon, A., Camanho, P., Costa, J. & Renart, J. Accurate simulation of delamination growth under mixed-mode loading using cohesive elements: Definition of interlaminar strengths and elastic stiffness. *Composite structures* **92,** 1857–1864 (2010).
12. Lu, X., Ridha, M., Chen, B., Tan, V. & Tay, T. On cohesive element parameters and delamination modelling. *Engineering Fracture Mechanics* **206,** 278–296 (2019).
13. Dávila, C. G., Camanho, P. M. P. R. d. C. & Turon Travesa, A. Cohesive elements for shells. © *NASA TP Technical Reports, 2007, núm. 214869* (2007).
14. Dávila, C. G., Camanho, P. P. & Turon, A. Effective simulation of delamination in aeronautical structures using shells and cohesive elements. *Journal of Aircraft* **45,** 663–672 (2008).
15. Balducci, G. T. & Chen, B. Overcoming the cohesive zone limit in the modelling of composites delamination with TUBA cohesive elements. *Composites Part A: Applied Science and Manufacturing* **185,** 108356 (2024).
16. Russo, R. & Chen, B. Overcoming the cohesive zone limit in composites delamination: modeling with slender structural elements and higher-order adaptive integration. *International Journal for Numerical Methods in Engineering* **121,** 5511–5545 (2020).

17. Polla, A., Piana, P., Cestino, E., Frulla, G., *et al. Delamination and fracture modeling techniques for shell composite structures in LS-DYNA* in *Proc. 13th European LS-DYNA Conference 2021* (2021).

18. Bazilevs, Y., Pigazzini, M., Ellison, A. & Kim, H. A new multi-layer approach for progressive damage simulation in composite laminates based on isogeometric analysis and Kirchhoff–Love shells. Part I: basic theory and modeling of delamination and transverse shear. *Computational Mechanics* **62,** 563–585 (2018).

19. Ai, X., Kassapoglou, C. & Chen, B. *A new approach for the determination of through-thickness and free-edge stresses in composite laminates based on structural elements* 2026.

20. Borg, R., Nilsson, L. & Simonsson, K. Simulating DCB, ENF and MMB experiments using shell elements and a cohesive zone model. *Composites Science and Technology* **64,** 269–278 (2004).

21. Li, B., Li, Y. & Su, J. A combined interface element to simulate interfacial fracture of laminated shell structures. *Composites Part B: Engineering* **58,** 217–227 (2014).

22. Williams, J. The fracture mechanics of delamination tests. *The Journal of strain analysis for engineering design* **24,** 207–214 (1989).

23. *ASTM D5528/D5528M-21: Standard Test Method for Mode I Interlaminar Fracture Toughness of Unidirectional Fiber-Reinforced Polymer Matrix Composites* ASTM International (West Conshohocken, PA, 2021).

24. *ASTM D6671/D6671M-22, Standard test method for mixed mode I/mode II interlaminar fracture toughness of unidirectional fiber reinforced polymer matrix composites* (ASTM-International, West Conshohocken, PA, 2022).

25. Krueger, R. A summary of benchmark examples to assess the performance of quasi-static delamination propagation prediction capabilities in finite element codes. *Journal of Composite Materials* **49,** 3297–3316 (2015).

26. Crews, J. H., Shivakumar, K. & Raju, I. *A fiber-resin micromechanics analysis of the delamination front in a DCB specimen* tech. rep. (1988).

27. Grande, D. H., Ilcewicz, L. B., Avery, W. B. & Bascom, W. D. *Effects of intra-and inter-laminar resin content on the mechanical properties of toughened composite materials* in *NASA. Langley Research Center, First NASA Advanced Composites Technology Conference, Part 2* (1991).

28. Krueger, R. & Minguet, P. J. *Analysis of composite panel-stiffener debonding using a shell/3D modeling technique* tech. rep. (2006).

29. Carreras, L., Renart, J., Turon, A., Costa, J., Bak, B. L. V., Lindgaard, E., de la Escalera, F. M. & Essa, Y. A benchmark test for validating 3D simulation methods for delamination growth under quasi-static and fatigue loading. *Composite Structures* **210,** 932–941 (2019).

30. Campilho, R. D., Banea, M. D., Neto, J. & da Silva, L. F. Modelling adhesive joints with cohesive zone models: effect of the cohesive law shape of the adhesive layer. *International journal of adhesion and adhesives* **44,** 48–56 (2013).

31. Carreras, L., Turon, A., Bak, B. L., Lindgaard, E., Renart, J., de la Escalera, F. M. & Essa, Y. A simulation method for fatigue-driven delamination in layered structures involving non-negligible fracture process zones and arbitrarily shaped crack fronts. *Composites Part A: Applied Science and Manufacturing* **122,** 107–119 (2019).

5

CONCLUSION AND RECOMMENDATIONS

5.1. MAIN CONCLUSIONS

THIS thesis has developed a higher-order structural cohesive element based on the Kirchhoff–Love theory that can overcome the cohesive zone limitation (Chapter 2). However, Kirchhoff–Love shell elements cannot directly recover the out-of-plane stress components required for three-dimensional composite failure criteria. To address this challenge, this thesis has developed a physically based formulation for the cohesive penalty stiffness (Chapter 3). The proposed formulation is derived from the material properties and thickness of the resin-rich layer, providing a physically meaningful definition of the cohesive penalty stiffness. The interlaminar stress components can be accurately recovered from the interface tractions of the structural cohesive elements. However, this method requires layer-wise laminate modeling, which limits its computational efficiency for large-scale composite laminates with many plies. To overcome this limitation, this thesis has extended the resin-rich layer based formulation for the cohesive penalty stiffness by incorporating the stress distributions through the thickness (Chapter 4). The proposed formulation accurately predicts the cohesive traction distribution and significantly improves the accuracy and convergence of three-dimensional delamination benchmarks. Sections 5.1.1, 5.1.2, and 5.1.3 summarize the main contributions of this thesis.

5.1.1. A HIGHER-ORDER STRUCTURAL COHESIVE FORMULATION FOR EFFICIENT DELAMINATION MODELLING

THE first contribution of this thesis is the development of a higher-order structural cohesive element that can overcome the cohesive zone limitation. The proposed element can use a coarser mesh than traditional solid cohesive elements while maintaining accurate predictions of composite delamination. Therefore, it can significantly improve the computational efficiency of simulating composite delamination. The main highlights of this contribution are listed as follows:

- The cubic plate formulation has been extended from isotropic materials to anisotropic composite laminates with arbitrary ply orientations. To achieve this, the stiffness matrix (including the B, T, and H matrices) formulation has been re-derived. In addition, a compatible higher-order triangular shell element is established by combining the cubic plate and constant-strain membrane element formulations. A corresponding structural cohesive element is then developed based on the shell kinematics for both Mode I and Mode II deformation and combined with a mixed-mode cohesive law.

- The proposed structural element has demonstrated that accurate delamination predictions do not require the fine meshes imposed by conventional cohesive-zone modelling. Validations using the standard benchmark simulation for pure Mode I (DCB), pure Mode II (ENF), and mixed-mode (MMB) delamination have shown good agreement with analytical solutions and solid cohesive element results. The results indicate that the proposed element allows a significantly larger cohesive element size while maintaining high accuracy. The computational time is reduced by more than 90% for all three benchmark problems.

- Further validations using the R-DCB and SLB models have demonstrated that the structural element remains applicable to fully three-dimensional delamination prop-

agation and laminates with different stacking sequences. These results establish the higher-order structural cohesive formulation as an efficient alternative to conventional solid cohesive-element models for composite delamination analysis.

5.1.2. A PHYSICALLY BASED COHESIVE PENALTY STIFFNESS FOR THREE-DIMENSIONAL STRESS RECOVERY

THE second contribution of this thesis is the development of a physically based penalty stiffness formulation for the structural cohesive element. The penalty stiffness has been derived from the material properties and the thickness of the resin-rich layer in the composite laminate. Therefore, it is referred to as a physically based penalty stiffness. Through the proposed penalty stiffness, the interlaminar stresses can be directly recovered from the traction values of the cohesive elements. The main highlights of this contribution are listed as follows:

- The proposed formulation is consistent with the Kirchhoff-Love shell assumption by assuming the resin-rich layer as the region through which the interlaminar stresses are transferred, while the shell elements remain governed by their in-plane kinematics. The normal and shear penalty stiffnesses have been derived independently from the elastic and shear moduli of the resin-rich layer, respectively. This establishes a physically consistent distinction between the two penalty stiffness components and enables their values to be determined directly from the resin-rich layer properties.

- An important outcome of the proposed formulation is the ability to recover the interlaminar normal and shear stresses from the tractions of the structural cohesive elements. Combined with the in-plane stress components obtained from the shell elements, these recovered stresses provide the complete three-dimensional stress state required for the application of three-dimensional composite failure criteria. Sensitivity analyses further show that the predicted interlaminar stress distributions are relatively insensitive to variations in the resin-rich layer thickness, elastic modulus, and Poisson's ratio within the investigated ranges. This indicates that accurate stress predictions can be obtained without requiring highly precise characterization of the resin-rich layer.

- The proposed formulation has been validated for cross-ply, angle-ply, quasi-isotropic, and general laminate configurations through comparisons with analytical solutions and solid-element models. Good agreement is obtained for both through-thickness interlaminar stress distributions and free-edge stress singularities. This contribution bridges the gap between the computational efficiency of Kirchhoff-Love shell models and the three-dimensional stress information required for composite failure analysis.

5.1.3. EXTENSION OF THE PHYSICALLY BASED PENALTY STIFFNESS TO EQUIVALENT SINGLE-LAYER MODELS

THE third contribution of this thesis is to extend the proposed penalty stiffness formulation in Chapter 3 to equivalent single-layer models. This method still relies on the material properties and thickness of the resin-rich layer. Combining this with the model's

stress distribution, a new penalty stiffness equation is derived. This method applies to damage simulation of composite materials modeled using the equivalent single-layer method. The main highlights of this contribution are listed as follows:

- Analytical approximate expressions for the through-thickness distributions of the out-of-plane normal and transverse shear stresses have been derived based on beam deformation theory. These stress distributions are then combined with the material properties and thickness of the resin-rich layer to establish new formulations for the normal and shear penalty stiffnesses. The resulting formulation provides an effective and physically based penalty stiffness for equivalent single-layer models while accounting for the three-dimensional stress behaviour through the laminate thickness.
- The proposed formulation improves both mesh convergence and prediction accuracy. For the DCB model, the proposed normal penalty stiffness achieves converged results with a mesh size of 7.5 mm and significantly reduces the normalized L_2 error, particularly for coarse meshes. It also improves the prediction of the traction distribution ahead of the crack tip and eliminates the non-convergent compressive stress behavior observed in the previous structural-element formulation. For the ENF and MMB models, the proposed shear and mixed-mode penalty stiffnesses improve the predicted response and resolve the small initial stiffness associated with the previous shear penalty stiffness formulation.
- The applicability of the formulation to fully three-dimensional delamination has been further demonstrated using the R-DCB model. The proposed penalty stiffness improves both mesh convergence and agreement with the experimental load-displacement response and delamination front. In particular, it eliminates the overshoot of the second peak load observed with the previous formulation. Overall, this contribution extends the physically based resin-rich-layer concept to equivalent single-layer models and provides a more general and computationally efficient approach for three-dimensional delamination analysis of composite laminates.

5.2. RECOMMENDATIONS FOR FUTURE WORK

THE present thesis develops a higher-order structural cohesive element that improves the computational efficiency of delamination simulations by overcoming the cohesive zone limitation. However, damage in composite laminates includes not only delamination but also intralaminar damage, such as fiber and matrix cracking. Future work will focus on extending the proposed framework to intralaminar damage and coupled intralaminar and interlaminar failure. The main recommendations regarding future work are presented as follows:

- **How can the proposed method be applied to an asymmetric model?**
  In this study, all models used for verification feature symmetric layups. To further demonstrate the general applicability of the proposed approach, its performance on asymmetric laminate configurations will be investigated in future work. To address this issue, each layer is modelled separately. It allows the simulation of asymmetric layups. This approach can accommodate asymmetric laminate configurations by treating each shell element as having an individually defined symmetric layup.

- **How can it be demonstrated that the reconstructed transverse stress field satisfies the local balance of linear momentum within each individual composite layer?**
  In the present work, we have verified that the reconstructed out-of-plane stresses are consistent with the corresponding analytical solutions. However, the in-plane stresses have not yet been calculated. Furthermore, it remains necessary to combine the in-plane and out-of-plane stress components to verify whether the reconstructed transverse stress field satisfies the local balance of linear momentum within each individual composite layer.

  In particular, the stress recovery method presented by Främby et al. [1] can be adopted as a benchmark for comparison. The method proposed in this paper incorporates the three-dimensional stress equilibrium equations into the stress recovery method. By comparing the stress distributions obtained using the proposed method with those from the reference method, the consistency of both the in-plane and out-of-plane stress components can be examined. In our method, the recovered stress distributions can be expressed as functions and substituted into the three-dimensional local equilibrium equations. The corresponding equilibrium residuals are then evaluated to quantify whether the stress field satisfies local equilibrium.

- **How to select an appropriate three-dimensional failure criterion?**
  A key challenge of simulating intralaminar failure is the selection of an appropriate three-dimensional failure criterion. Simple criteria such as the maximum stress and Hashin criteria can be selected because of their relatively low computational cost and straightforward implementation. However, simplified formulations may limit their ability to capture complex failure mechanisms, particularly those associated with fiber compression, such as fiber microbuckling and kink-band formation. More physically based criteria, such as the Pinho criterion [2], adopt physically based failure models for different failure mechanisms, with particular emphasis on fiber kinking under compression.

- **How to calculate the stresses which are used in three-dimensional failure criterion?**
  The stress recovery method proposed in this paper provides an important foundation for overcoming the limitations of structural elements in solving out-of-plane stresses. The recovered out-of-plane normal and shear stresses can be combined with the in-plane stresses obtained from the cubic shell elements to provide the complete three-dimensional stress state at each ply. This information can be incorporated into a physically based three-dimensional failure criterion that distinguishes between matrix cracking and fiber failure under tensile and compressive loading. The detailed procedures for determining the out-of-plane and in-plane stresses are presented below:

  The out-of-plane stress distributions along the thickness have been obtained using the stress recovery method presented in Chapter 3 (shown in Figure 5.1). The out-of-plane stress at any location through the thickness is then determined from the reconstructed stress distribution. Since the stress distribution is generally non-uniform within an individual ply, nine integration points are uniformly distributed through the

thickness of each ply for the application of the three-dimensional damage criterion, as illustrated in Figure 5.2.

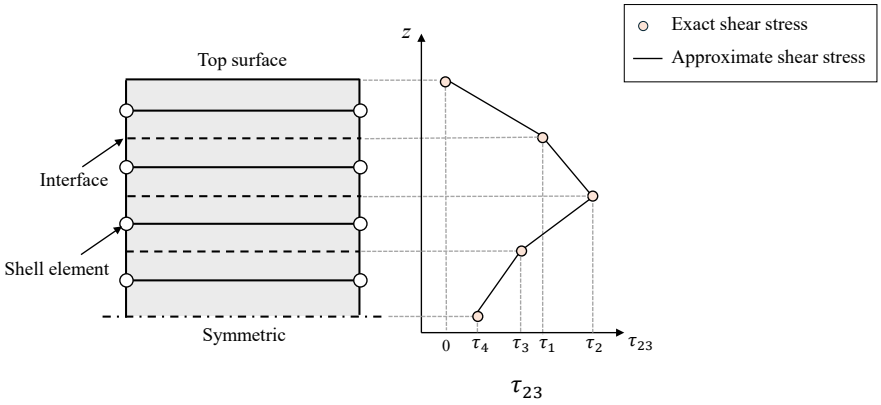

Figure 5.1: Transverse shear stress prediction along the thickness direction

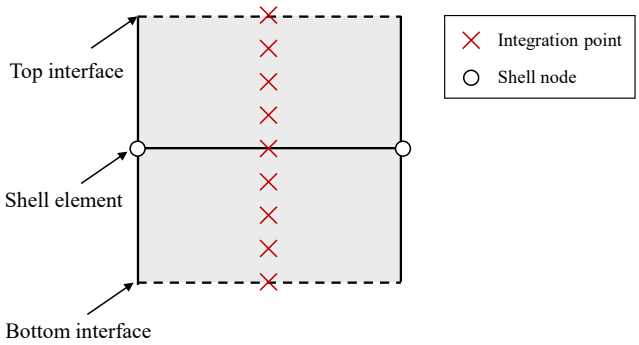

Figure 5.2: Integration points along the thickness direction

The in-plane stresses at each integration point are directly determined from classical laminate theory and the element formulations presented in Chapter 2.

- **How to combine the intralaminar failure and delamination?**
  In practical applications, composite laminates are rarely unidirectional, and fracture often involves multiple interacting failure mechanisms, including intralaminar failure and delamination. The intralaminar failure can be reproduced by inserting in-plane cohesive elements between cubic shell elements within the same ply. The in-plane cohesive element adopts a shell-like architecture while incorporating full three-dimensional deformation characteristics, as shown in Figure 5.3. The element

is defined by eight virtual nodes $(1'', 2'', \ldots, 8'')$, with their nodal displacements extrapolated from the four internal nodes $(1'-4')$ located on the mid-plane according to the Kirchhoff–Love theory. These internal mid-plane nodes provide the connection between the two adjacent subdomain shell elements throughout the cohesive fracture process. It should be noted that the cohesive element shown in the right figure also employs the triangular higher-order structural element proposed in this thesis to enable the simulation of large-scale shell elements.

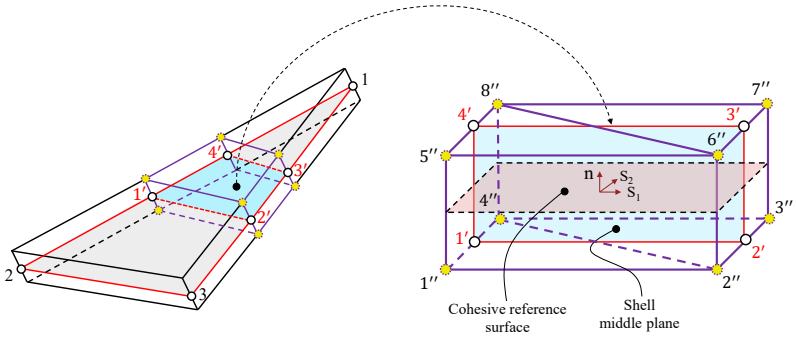

Figure 5.3: Integration points along the thickness direction

Since the proposed structural elements generally adopt a relatively coarse mesh, the use of a smeared fracture model may result in inaccurate prediction of the crack location. It may lead to significant discrepancies between the predicted and experimental maximum loads. In addition, unless the crack path is known a priori, predicting complex crack networks would require cohesive elements to be inserted at all interfaces between the shell elements. This will increase the computational cost.

One possible approach is to enrich the degrees of freedom of structural elements using a discrete fracture model, such as the extended finite element method (XFEM) [3], the phantom node method (PNM) [4], and the floating node method (FNM) [5], to enable the simulation of complex crack networks. Compared with XFEM and PNM, the FNM offers the additional advantage of not requiring numerical integration on the parts of the domain intersected by the crack path. Within this framework, the internal nodes shown in Figure 5.3 can be converted into floating nodes, as defined in the FNM.

- **How can the proposed formulations be extended to curved composite structures?**
  An important direction for future research is to extend the proposed formulations to curved composite structures. In the present work, the numerical investigations have primarily focused on flat composite configurations, and the applicability of the proposed stress recovery and penalty stiffness formulations to general curved geometries has not yet been systematically investigated.

Such an extension requires careful consideration of the geometrical characteristics of curved structures. In particular, the formulation should account for the spatially varying local coordinate systems and curvature-related contributions to the governing equations. These effects may introduce additional coupling between the in-plane and transverse stress components, which needs to be incorporated into the stress reconstruction procedure to ensure consistency with the three-dimensional equilibrium equations.

Future work will focus on extending the proposed framework to curved composite structures, with attention to the incorporation of curvature effects into the kinematic description and the reconstruction of the transverse stress components. The accuracy, numerical robustness, and computational efficiency of the extended formulations will be verified through appropriate benchmark problems involving curved composite models.

REFERENCES

1. Främby, J., Fagerström, M. & Brouzoulis, J. Adaptive modelling of delamination initiation and propagation using an equivalent single-layer shell approach. *International Journal for Numerical Methods in Engineering* **112,** 882–908 (2017).
2. Pinho, S. T., Iannucci, L. & Robinson, P. Physically-based failure models and criteria for laminated fibre-reinforced composites with emphasis on fibre kinking: Part I: Development. *Composites Part A: Applied Science and Manufacturing* **37,** 63–73 (2006).
3. Moës, N. & Belytschko, T. Extended finite element method for cohesive crack growth. *Engineering fracture mechanics* **69,** 813–833 (2002).
4. Hansbo, A. & Hansbo, P. A finite element method for the simulation of strong and weak discontinuities in solid mechanics. *Computer methods in applied mechanics and engineering* **193,** 3523–3540 (2004).
5. Chen, B., Pinho, S., De Carvalho, N., Baiz, P. & Tay, T. A floating node method for the modelling of discontinuities in composites. *Engineering Fracture Mechanics* **127,** 104–134 (2014).

APPENDIX

A. H MATRIX

Before we calculate U_0 in Equation 2.3, we need to calculate six parts. The first part is:

$$\frac{D_{11}}{2}\left(\frac{\partial^2 w}{\partial x^2}\right)^2 = D_{11}\Big(2\alpha_1^2 + 12x\alpha_1\alpha_4 + 4y\alpha_1\alpha_5 + 18x^2\alpha_4^2 + 12xy\alpha_4\alpha_5 + 2y^2\alpha_5^2\Big) \tag{A.1}$$

Based on Equation 2.16, we can obtain:

$$\iint_A \frac{D_{11}}{2}\left(\frac{\partial^2 w}{\partial x^2}\right)^2 \mathrm{d}x\mathrm{d}y = \frac{1}{2}\boldsymbol{\alpha}^{\mathrm{T}}\,\mathbf{H}_1\,\boldsymbol{\alpha} \tag{A.2}$$

where $\mathbf{H}_1$ is:

$$\mathbf{H}_1 = \iint_A D_{11}\begin{bmatrix} 4 & 0 & 0 & 12x & 4y & 0 & 0 \\ & 0 & 0 & 0 & 0 & 0 & 0 \\ & & 0 & 0 & 0 & 0 & 0 \\ & & & 36x^2 & 12xy & 0 & 0 \\ & \text{Symmetric} & & & 4y^2 & 0 & 0 \\ & & & & & 0 & 0 \\ & & & & & & 0 \end{bmatrix}\mathrm{d}x\mathrm{d}y \tag{A.3}$$

The second part is:

$$\frac{D_{22}}{2}\left(\frac{\partial^2 w}{\partial y^2}\right)^2 = D_{22}\Big(2\alpha_3^2 + 4x\alpha_3\alpha_6 + 12y\alpha_3\alpha_7 + 2x^2\alpha_6^2 + 12xy\alpha_6\alpha_7 + 18y^2\alpha_7^2\Big) \tag{A.4}$$

Then, an equation which is similar as Equation A.2 in terms of $\mathbf{H}_2$ can be obtained:

$$\iint_A \frac{D_{22}}{2}\left(\frac{\partial^2 w}{\partial x^2}\right)^2 \mathrm{d}x\mathrm{d}y = \frac{1}{2}\boldsymbol{\alpha}^{\mathrm{T}}\,\mathbf{H}_2\,\boldsymbol{\alpha} \tag{A.5}$$

where $\mathbf{H}_2$ is:

$$\mathbf{H}_2 = \iint_A D_{22} \begin{bmatrix} 0 & 0 & 0 & 0 & 0 & 0 & 0 \\ & 0 & 0 & 0 & 0 & 0 & 0 \\ & & 4 & 0 & 0 & 4x & 12y \\ & & & 0 & 0 & 0 & 0 \\ & \text{Symmetric} & & & 0 & 0 & 0 \\ & & & & & 4x^2 & 12xy \\ & & & & & 0 & 36y^2 \end{bmatrix} \mathrm{d}x\mathrm{d}y \tag{A.6}$$

The third part is:

$$D_{12}\frac{\partial^2 w}{\partial x^2}\frac{\partial^2 w}{\partial y^2} = D_{12}\Big(4\alpha_1\alpha_3 + 4x\alpha_1\alpha_6 + 12x\alpha_3\alpha_4 + 12y\alpha_1\alpha_7 + 4y\alpha_3\alpha_5 + 12x^2\alpha_4\alpha_6 + 12y^2\alpha_5\alpha_7 + 36xy\alpha_4\alpha_7 + 4xy\alpha_5\alpha_6\Big) \tag{A.7}$$

and $\mathbf{H}_3$ can be obtained by using the same method:

$$\mathbf{H}_3 = \iint_A D_{12} \begin{bmatrix} 0 & 0 & 4 & 0 & 0 & 4x & 12y \\ & 0 & 0 & 0 & 0 & 0 & 0 \\ & & 0 & 12x & 4y & 0 & 0 \\ & & & 0 & 0 & 12x^2 & 36xy \\ & \text{Symmetric} & & & 0 & 4xy & 12y^2 \\ & & & & & 0 & 0 \\ & & & & & & 0 \end{bmatrix} \mathrm{d}x\mathrm{d}y \tag{A.8}$$

Therefore, the $\mathbf{H}$ matrix of 4th, 5th and 6th part are expressed by the following expressions:

$$\mathbf{H}_4 = \iint_A D_{16} \begin{bmatrix} 0 & 4 & 0 & 0 & 8x & 8y & 0 \\ & 0 & 0 & 12x & 4y & 0 & 0 \\ & & 0 & 0 & 0 & 0 & 0 \\ & & & 0 & 24x^2 & 24xy & 0 \\ & \text{Symmetric} & & & 16xy & 8y^2 & 0 \\ & & & & & 0 & 0 \\ & & & & & & 0 \end{bmatrix} \mathrm{d}x\mathrm{d}y \tag{A.9}$$

$$\mathbf{H}_5 = \iint_A D_{26} \begin{bmatrix} 0 & 0 & 0 & 0 & 0 & 0 & 0 \\ & 0 & 4 & 0 & 0 & 4x & 12y \\ & & 0 & 0 & 8x & 8y & 0 \\ & & & 0 & 0 & 0 & 0 \\ & \text{Symmetric} & & & 0 & 8x^2 & 24xy \\ & & & & & 16xy & 24y^2 \\ & & & & & & 0 \end{bmatrix} \mathrm{d}x\mathrm{d}y \tag{A.10}$$

and

$$\mathbf{H}_6 = \iint_A D_{66} \begin{bmatrix} 0 & 0 & 0 & 0 & 0 & 0 & 0 \\ & 4 & 0 & 0 & 8x & 8y & 0 \\ & & 0 & 0 & 0 & 0 & 0 \\ & & & 0 & 0 & 0 & 0 \\ & \text{Symmetric} & & & 16x^2 & 16xy & 0 \\ & & & & & 16y^2 & 0 \\ & & & & & & 0 \end{bmatrix} \mathrm{d}x\mathrm{d}y \tag{A.11}$$

The $\mathbf{H}$ matrix can be written as the sum of $\mathbf{H}_i$ $(i = 1, 2, ..., 6)$:

$$\mathbf{H} = \mathbf{H}_1 + \mathbf{H}_2 + \mathbf{H}_3 + \mathbf{H}_4 + \mathbf{H}_5 + \mathbf{H}_6 \tag{A.12}$$

where the integral for each item of the $\mathbf{H}$ matrix can be calculated by using the formulas given in Reference [1].

B. B MATRIX

Plugging the expression of w (Equation 2.13) into Equation 2.2, we can express the moment resultants as:

$$\begin{aligned} M_x = & -2D_{11}\alpha_1 - 2D_{16}\alpha_2 - 2D_{12}\alpha_3 - 6xD_{11}\alpha_4 \\ & - (2yD_{11} + 4xD_{16})\alpha_5 - (2xD_{12} + 4yD_{16})\alpha_6 - 6yD_{12}\alpha_7 \end{aligned} \tag{B.13}$$

which in matrix form is:

$$M_x = \mathbf{B}_{M_x}^{\mathrm{T}}\, \boldsymbol{\alpha} \tag{B.14}$$

where $\mathbf{B}_{M_x}^{\mathrm{T}}$ is:

$$\begin{aligned} \mathbf{B}_{M_x}^{\mathrm{T}} = \big[& -2D_{11},\ -2D_{16},\ -2D_{12},\ -6xD_{11}, \\ & -(2yD_{11} + 4xD_{16}),\ -(2xD_{12} + 4yD_{16}),\ -6yD_{12}\big] \end{aligned} \tag{B.15}$$

Similarly, for M_y, we have:

$$M_y = \mathbf{B}_{M_y}^{\mathrm{T}} \boldsymbol{\alpha} \tag{B.16}$$

where $\mathbf{B}_{M_y}^{\mathrm{T}}$ is:

$$\begin{aligned}\mathbf{B}_{M_y}^{\mathrm{T}} = \big[&-2D_{12},\ -2D_{26},\ -2D_{22},\ -6xD_{12},\\ &-(2yD_{12}+4xD_{26}),\ -(2xD_{22}+4yD_{26}),\ -6yD_{22}\big]\end{aligned} \tag{B.17}$$

For M_{xy}, we can obtain:

$$\begin{aligned}\mathbf{B}_{M_{xy}}^{\mathrm{T}} = \big[&-2D_{16},\ -2D_{66},\ -2D_{26},\ -6xD_{16},\\ &-(4xD_{66}+2yD_{16}),\ -(4yD_{66}+2xD_{26}),\ -6yD_{26}\big]\end{aligned} \tag{B.18}$$

From Equation 2.2, we can calculate the derivative of the moment:

$$\begin{aligned}
\frac{\partial M_x}{\partial x} &= -D_{11}\frac{\partial^3 w}{\partial x^3} - D_{12}\frac{\partial^3 w}{\partial x \partial y^2} - 2D_{16}\frac{\partial^3 w}{\partial x^2 \partial y}\\
\frac{\partial M_x}{\partial y} &= -D_{11}\frac{\partial^3 w}{\partial x^2 \partial y} - D_{12}\frac{\partial^3 w}{\partial y^3} - 2D_{16}\frac{\partial^3 w}{\partial x \partial y^2}\\
\frac{\partial M_y}{\partial x} &= -D_{12}\frac{\partial^3 w}{\partial x^3} - D_{22}\frac{\partial^3 w}{\partial x \partial y^2} - 2D_{26}\frac{\partial^3 w}{\partial x^2 \partial y}\\
\frac{\partial M_y}{\partial y} &= -D_{12}\frac{\partial^3 w}{\partial x^2 \partial y} - D_{22}\frac{\partial^3 w}{\partial y^3} - 2D_{26}\frac{\partial^3 w}{\partial x \partial y^2}\\
\frac{\partial M_{xy}}{\partial x} &= -D_{16}\frac{\partial^3 w}{\partial x^3} - D_{26}\frac{\partial^3 w}{\partial x \partial y^2} - 2D_{66}\frac{\partial^3 w}{\partial x^2 \partial y}\\
\frac{\partial M_{xy}}{\partial y} &= -D_{16}\frac{\partial^3 w}{\partial x^2 \partial y} - D_{26}\frac{\partial^3 w}{\partial y^3} - 2D_{66}\frac{\partial^3 w}{\partial x \partial y^2}
\end{aligned} \tag{B.19}$$

Using Equation 2.4, we calculate M_n for node 1 and node 2 on the side 1-2 as:

$$M_n^{12} = \cos^2\gamma_{12}\mathbf{B}_{M_x^1}^{\mathrm{T}}\boldsymbol{\alpha} + \sin^2\gamma_{12}\mathbf{B}_{M_y^1}^{\mathrm{T}}\boldsymbol{\alpha} + \sin 2\gamma_{12}\mathbf{B}_{M_{xy}^1}^{\mathrm{T}}\boldsymbol{\alpha} \tag{B.20}$$

$$M_n^{21} = \cos^2\gamma_{12}\mathbf{B}_{M_x^2}^{\mathrm{T}}\boldsymbol{\alpha} + \sin^2\gamma_{12}\mathbf{B}_{M_y^2}^{\mathrm{T}}\boldsymbol{\alpha} + \sin 2\gamma_{12}\mathbf{B}_{M_{xy}^2}^{\mathrm{T}}\boldsymbol{\alpha} \tag{B.21}$$

where $\mathbf{B}_{M_x^j}^{\mathrm{T}}$ means Equation B.15 evaluated at the coordinates of node j and $\mathbf{B}_{M_y^j}^{\mathrm{T}}$ means Equation B.17 evaluated at the coordinates of node j, respectively. And the corresponding $\mathbf{B}$ matrix is:

$$\mathbf{B}_{M_n^{12}}^{\mathrm{T}} = \cos^2\gamma_{12}\mathbf{B}_{M_x^1}^{\mathrm{T}} + \sin^2\gamma_{12}\mathbf{B}_{M_y^1}^{\mathrm{T}} + \sin 2\gamma_{12}\mathbf{B}_{M_{xy}^1}^{\mathrm{T}} \tag{B.22}$$

$$\mathbf{B}_{M_n^{21}}^{\mathrm{T}} = \cos^2\gamma_{12}\mathbf{B}_{M_x^2}^{\mathrm{T}} + \sin^2\gamma_{12}\mathbf{B}_{M_y^2}^{\mathrm{T}} + \sin 2\gamma_{12}\mathbf{B}_{M_{xy}^2}^{\mathrm{T}} \tag{B.23}$$

Similarly, M_n for the side 2-3 is:

$$M_n^{23} = \cos^2\gamma_{23}\mathbf{B}_{M_x^2}^{\mathrm{T}}\boldsymbol{\alpha} + \sin^2\gamma_{23}\mathbf{B}_{M_y^2}^{\mathrm{T}}\boldsymbol{\alpha} + \sin 2\gamma_{23}\mathbf{B}_{M_{xy}^2}^{\mathrm{T}}\boldsymbol{\alpha} \tag{B.24}$$

$$M_n^{32} = \cos^2\gamma_{23}\mathbf{B}_{M_x^3}^{\mathrm{T}}\boldsymbol{\alpha} + \sin^2\gamma_{23}\mathbf{B}_{M_y^3}^{\mathrm{T}}\boldsymbol{\alpha} + \sin 2\gamma_{23}\mathbf{B}_{M_{xy}^3}^{\mathrm{T}}\boldsymbol{\alpha} \tag{B.25}$$

And the corresponding $\mathbf{B}$ matrix is:

$$\mathbf{B}_{M_n^{23}}^{\mathrm{T}} = \cos^2\gamma_{23}\mathbf{B}_{M_x^2}^{\mathrm{T}} + \sin^2\gamma_{23}\mathbf{B}_{M_y^2}^{\mathrm{T}} + \sin 2\gamma_{23}\mathbf{B}_{M_{xy}^2}^{\mathrm{T}} \tag{B.26}$$

$$\mathbf{B}_{M_n^{32}}^{\mathrm{T}} = \cos^2\gamma_{23}\mathbf{B}_{M_x^3}^{\mathrm{T}} + \sin^2\gamma_{23}\mathbf{B}_{M_y^3}^{\mathrm{T}} + \sin 2\gamma_{23}\mathbf{B}_{M_{xy}^3}^{\mathrm{T}} \tag{B.27}$$

Finally, M_n for the side 3-1 is:

$$M_n^{31} = \cos^2\gamma_{31}\mathbf{B}_{M_x^3}^{\mathrm{T}}\boldsymbol{\alpha} + \sin^2\gamma_{31}\mathbf{B}_{M_y^3}^{\mathrm{T}}\boldsymbol{\alpha} + \sin 2\gamma_{31}\mathbf{B}_{M_{xy}^3}^{\mathrm{T}}\boldsymbol{\alpha} \tag{B.28}$$

$$M_n^{13} = \cos^2\gamma_{31}\mathbf{B}_{M_x^1}^{\mathrm{T}}\boldsymbol{\alpha} + \sin^2\gamma_{31}\mathbf{B}_{M_y^1}^{\mathrm{T}}\boldsymbol{\alpha} + \sin 2\gamma_{31}\mathbf{B}_{M_{xy}^1}^{\mathrm{T}}\boldsymbol{\alpha} \tag{B.29}$$

And the corresponding $\mathbf{B}$ matrix is:

$$\mathbf{B}_{M_n^{31}}^{\mathrm{T}} = \cos^2\gamma_{31}\mathbf{B}_{M_x^3}^{\mathrm{T}} + \sin^2\gamma_{31}\mathbf{B}_{M_y^3}^{\mathrm{T}} + \sin 2\gamma_{31}\mathbf{B}_{M_{xy}^3}^{\mathrm{T}} \tag{B.30}$$

$$\mathbf{B}_{M_n^{13}}^{\mathrm{T}} = \cos^2\gamma_{31}\mathbf{B}_{M_x^1}^{\mathrm{T}} + \sin^2\gamma_{31}\mathbf{B}_{M_y^1}^{\mathrm{T}} + \sin 2\gamma_{31}\mathbf{B}_{M_{xy}^1}^{\mathrm{T}} \tag{B.31}$$

Before calculating R_N, we need to calculate M_{ns} at first as shown in Equation 2.11. For node 1:

$$M_{ns}^{12} = \left[\frac{1}{2}\left(\mathbf{B}_{M_y^1}^{\mathrm{T}} - \mathbf{B}_{M_x^1}^{\mathrm{T}}\right)\sin 2\gamma_{12} + \mathbf{B}_{M_{xy}^1}^{\mathrm{T}}\cos 2\gamma_{12}\right]\boldsymbol{\alpha} \tag{B.32}$$

$$M_{ns}^{13} = \left[\frac{1}{2}\left(\mathbf{B}_{M_y^1}^{\mathrm{T}} - \mathbf{B}_{M_x^1}^{\mathrm{T}}\right)\sin 2\gamma_{31} + \mathbf{B}_{M_{xy}^1}^{\mathrm{T}}\cos 2\gamma_{31}\right]\boldsymbol{\alpha} \tag{B.33}$$

Thus, plugging the above two terms into Equation 2.11, R_1 is:

$$\begin{aligned} R_1 &= \left[\frac{1}{2}(\sin 2\gamma_{12} - \sin 2\gamma_{31})\left(\mathbf{B}_{M_y^1}^{\mathrm{T}} - \mathbf{B}_{M_x^1}^{\mathrm{T}}\right)\right. \\ &\qquad \left. + (\cos 2\gamma_{12} - \cos 2\gamma_{31})\,\mathbf{B}_{M_{xy}^1}^{\mathrm{T}}\right]\boldsymbol{\alpha} \\ &= \mathbf{B}_{R_1}\boldsymbol{\alpha} \end{aligned} \tag{B.34}$$

where the matrix $\mathbf{B}_{R_1}$ is:

$$\begin{aligned} \mathbf{B}_{R_1}^{\mathrm{T}} &= \frac{1}{2}(\sin 2\gamma_{12} - \sin 2\gamma_{31})\left(\mathbf{B}_{M_y^1}^{\mathrm{T}} - \mathbf{B}_{M_x^1}^{\mathrm{T}}\right) \\ &\quad + (\cos 2\gamma_{12} - \cos 2\gamma_{31})\mathbf{B}_{M_{xy}^1}^{\mathrm{T}} \end{aligned} \tag{B.35}$$

Similarly, the matrix $\mathbf{B}_{R_2}$ related to the node 2:

$$\mathbf{B}_{R_2}^{\mathrm{T}} = \frac{1}{2}\left(\sin 2\gamma_{23} - \sin 2\gamma_{12}\right)\left(\mathbf{B}_{M_y^2}^{\mathrm{T}} - \mathbf{B}_{M_x^2}^{\mathrm{T}}\right) + \left(\cos 2\gamma_{23} - \cos 2\gamma_{12}\right)\mathbf{B}_{M_{xy}^2}^{\mathrm{T}} \tag{B.36}$$

At last, the matrix $\mathbf{B}_{R_3}$:

$$\mathbf{B}_{R_3}^{\mathrm{T}} = \frac{1}{2}\left(\sin 2\gamma_{31} - \sin 2\gamma_{23}\right)\left(\mathbf{B}_{M_y^3}^{\mathrm{T}} - \mathbf{B}_{M_x^3}^{\mathrm{T}}\right) + \left(\cos 2\gamma_{31} - \cos 2\gamma_{23}\right)\mathbf{B}_{M_{xy}^3}^{\mathrm{T}} \tag{B.37}$$

In order to simplify the writing of the above formula, we define the following notations:

$$\begin{aligned} \overline{S}_1 &= \sin 2\gamma_{12} - \sin 2\gamma_{31}, \quad \overline{C}_1 = \cos 2\gamma_{12} - \cos 2\gamma_{31} \\ \overline{S}_2 &= \sin 2\gamma_{23} - \sin 2\gamma_{12}, \quad \overline{C}_2 = \cos 2\gamma_{23} - \cos 2\gamma_{12} \\ \overline{S}_3 &= \sin 2\gamma_{31} - \sin 2\gamma_{23}, \quad \overline{C}_3 = \cos 2\gamma_{31} - \cos 2\gamma_{23} \end{aligned} \tag{B.38}$$

The matrix $\mathbf{B}_R^{\mathrm{T}}$ in Equation B.35, B.36 and B.37 can be rewritten as:

$$\begin{aligned} \mathbf{B}_{R_1}^{\mathrm{T}} &= \frac{1}{2}\overline{S}_1\left(\mathbf{B}_{M_y^1}^{\mathrm{T}} - \mathbf{B}_{M_x^1}^{\mathrm{T}}\right) + \overline{C}_1\mathbf{B}_{M_{xy}^1}^{\mathrm{T}} \\ \mathbf{B}_{R_2}^{\mathrm{T}} &= \frac{1}{2}\overline{S}_2\left(\mathbf{B}_{M_y^2}^{\mathrm{T}} - \mathbf{B}_{M_x^2}^{\mathrm{T}}\right) + \overline{C}_2\mathbf{B}_{M_{xy}^2}^{\mathrm{T}} \\ \mathbf{B}_{R_3}^{\mathrm{T}} &= \frac{1}{2}\overline{S}_3\left(\mathbf{B}_{M_y^3}^{\mathrm{T}} - \mathbf{B}_{M_x^3}^{\mathrm{T}}\right) + \overline{C}_3\mathbf{B}_{M_{xy}^3}^{\mathrm{T}} \end{aligned} \tag{B.39}$$

Next, we calculate V_n according to equations 2.5 to 2.8. Plugging equations 2.7 and 2.8 into 2.5, we get:

$$V_n = \frac{\partial M_n}{\partial n} + 2\frac{\partial M_{ns}}{\partial s} \tag{B.40}$$

Plugging Equation 2.12 into Equation B.40, we get:

$$V_n = \cos\gamma\frac{\partial M_n}{\partial x} + \sin\gamma\frac{\partial M_n}{\partial y} - 2\sin\gamma\frac{\partial M_{ns}}{\partial x} + 2\cos\gamma\frac{\partial M_{ns}}{\partial y} \tag{B.41}$$

The terms on the RHS above require eventually the evaluation of $\frac{\partial M_n}{\partial x}$, $\frac{\partial M_n}{\partial y}$, $\frac{\partial M_{ns}}{\partial x}$, and $\frac{\partial M_{ns}}{\partial y}$.

For V_n^{12} item, the derivation from Equation B.20 is:

$$\frac{\partial M_n^{12}}{\partial x} = \cos^2\gamma_{12}\frac{\partial \mathbf{B}_{M_x^1}^{\mathrm{T}}}{\partial x}\boldsymbol{\alpha} + \sin^2\gamma_{12}\frac{\partial \mathbf{B}_{M_y^1}^{\mathrm{T}}}{\partial x}\boldsymbol{\alpha} + \sin 2\gamma_{12}\frac{\partial \mathbf{B}_{M_{xy}^1}^{\mathrm{T}}}{\partial x}\boldsymbol{\alpha} \tag{B.42}$$

$$\frac{\partial M_n^{12}}{\partial y} = \cos^2\gamma_{12}\frac{\partial \mathbf{B}_{M_x^1}^{\mathrm{T}}}{\partial y}\boldsymbol{\alpha} + \sin^2\gamma_{12}\frac{\partial \mathbf{B}_{M_y^1}^{\mathrm{T}}}{\partial y}\boldsymbol{\alpha} + \sin 2\gamma_{12}\frac{\partial \mathbf{B}_{M_{xy}^1}^{\mathrm{T}}}{\partial y}\boldsymbol{\alpha} \tag{B.43}$$

where

$$\frac{\partial \mathbf{B}^{\mathrm{T}}_{M^1_x}}{\partial x} = \left[0,\ 0,\ 0,\ -6D_{11},\ -4D_{16},\ -2D_{12},\ 0\right] \tag{B.44}$$

$$\frac{\partial \mathbf{B}^{\mathrm{T}}_{M^1_y}}{\partial x} = \left[0,\ 0,\ 0,\ -6D_{12},\ -4D_{26},\ -2D_{22},\ 0\right] \tag{B.45}$$

$$\frac{\partial \mathbf{B}^{\mathrm{T}}_{M^1_{xy}}}{\partial x} = \left[0,\ 0,\ 0,\ -6D_{16},\ -4D_{66},\ -2D_{26},\ 0\right] \tag{B.46}$$

And

$$\frac{\partial \mathbf{B}^{\mathrm{T}}_{M^1_x}}{\partial y} = \left[0,\ 0,\ 0,\ 0,\ -2D_{11},\ -4D_{16},\ -6D_{12}\right] \tag{B.47}$$

$$\frac{\partial \mathbf{B}^{\mathrm{T}}_{M^1_y}}{\partial y} = \left[0,\ 0,\ 0,\ 0,\ -2D_{12},\ -4D_{26},\ -6D_{22}\right] \tag{B.48}$$

$$\frac{\partial \mathbf{B}^{\mathrm{T}}_{M^1_{xy}}}{\partial y} = \left[0,\ 0,\ 0,\ 0,\ -2D_{16},\ -4D_{66},\ -6D_{26}\right] \tag{B.49}$$

Thus, the matrix $\mathbf{B}^{\mathrm{T}}_{M^{12}_{n,x}}$ and $\mathbf{B}^{\mathrm{T}}_{M^{12}_{n,y}}$ are:

$$\mathbf{B}^{\mathrm{T}}_{M^{12}_{n,x}} = \cos^2\gamma_{12}\frac{\partial \mathbf{B}^{\mathrm{T}}_{M^1_x}}{\partial x} + \sin^2\gamma_{12}\frac{\partial \mathbf{B}^{\mathrm{T}}_{M^1_y}}{\partial x} + \sin 2\gamma_{12}\frac{\partial \mathbf{B}^{\mathrm{T}}_{M^1_{xy}}}{\partial x} \tag{B.50}$$

$$\mathbf{B}^{\mathrm{T}}_{M^{12}_{n,y}} = \cos^2\gamma_{12}\frac{\partial \mathbf{B}^{\mathrm{T}}_{M^1_x}}{\partial y} + \sin^2\gamma_{12}\frac{\partial \mathbf{B}^{\mathrm{T}}_{M^1_y}}{\partial y} + \sin 2\gamma_{12}\frac{\partial \mathbf{B}^{\mathrm{T}}_{M^1_{xy}}}{\partial y} \tag{B.51}$$

Using Equation 2.7, the derivative of moment M_{ns} on side 1-2 is:

$$\frac{\partial M^{12}_{ns}}{\partial x} = \left[\frac{1}{2}\left(\frac{\partial \mathbf{B}^{\mathrm{T}}_{M^1_y}}{\partial x} - \frac{\partial \mathbf{B}^{\mathrm{T}}_{M^1_x}}{\partial x}\right)\sin 2\gamma_{12} + \frac{\partial \mathbf{B}^{\mathrm{T}}_{M^1_{xy}}}{\partial x}\cos 2\gamma_{12}\right]\boldsymbol{\alpha} \tag{B.52}$$

$$\frac{\partial M^{12}_{ns}}{\partial y} = \left[\frac{1}{2}\left(\frac{\partial \mathbf{B}^{\mathrm{T}}_{M^1_y}}{\partial y} - \frac{\partial \mathbf{B}^{\mathrm{T}}_{M^1_x}}{\partial y}\right)\sin 2\gamma_{12} + \frac{\partial \mathbf{B}^{\mathrm{T}}_{M^1_{xy}}}{\partial y}\cos 2\gamma_{12}\right]\boldsymbol{\alpha} \tag{B.53}$$

Thus, the matrices $\mathbf{B}^{\mathrm{T}}_{M^{12}_{ns,x}}$ and $\mathbf{B}^{\mathrm{T}}_{M^{12}_{ns,y}}$ are:

$$\mathbf{B}^{\mathrm{T}}_{M^{12}_{ns,x}} = \frac{1}{2}\sin 2\gamma_{12}\left(\frac{\partial \mathbf{B}^{\mathrm{T}}_{M^1_y}}{\partial x} - \frac{\partial \mathbf{B}^{\mathrm{T}}_{M^1_x}}{\partial x}\right) + \cos 2\gamma_{12}\frac{\partial \mathbf{B}^{\mathrm{T}}_{M^1_{xy}}}{\partial x} \tag{B.54}$$

$$\mathbf{B}^{\mathrm{T}}_{M^{12}_{ns,y}} = \frac{1}{2}\sin 2\gamma_{12}\left(\frac{\partial \mathbf{B}^{\mathrm{T}}_{M^1_y}}{\partial y} - \frac{\partial \mathbf{B}^{\mathrm{T}}_{M^1_x}}{\partial y}\right) + \cos 2\gamma_{12}\frac{\partial \mathbf{B}^{\mathrm{T}}_{M^1_{xy}}}{\partial y} \tag{B.55}$$

Finally, using Equation B.41, $\mathbf{B}$ matrix for the Kirchhoff shear force V_n on side 1-2 is:

$$\mathbf{B}^{\mathrm{T}}_{V_n^{12}} = \cos\gamma_{12}\mathbf{B}^{\mathrm{T}}_{M^{12}_{n,x}} + \sin\gamma_{12}\mathbf{B}^{\mathrm{T}}_{M^{12}_{n,y}} - 2\sin\gamma_{12}\mathbf{B}^{\mathrm{T}}_{M^{12}_{ns,x}} + 2\cos\gamma_{12}\mathbf{B}^{\mathrm{T}}_{M^{12}_{ns,y}} \tag{B.56}$$

Similarly, $\mathbf{B}_{V_n}$ matrix on side 2-3 is:

$$\mathbf{B}^{\mathrm{T}}_{M^{23}_{n,x}} = \cos^2\gamma_{23}\frac{\partial\mathbf{B}^{\mathrm{T}}_{M^2_x}}{\partial x} + \sin^2\gamma_{23}\frac{\partial\mathbf{B}^{\mathrm{T}}_{M^2_y}}{\partial x} + \sin 2\gamma_{23}\frac{\partial\mathbf{B}^{\mathrm{T}}_{M^1_{xy}}}{\partial x} \tag{B.57}$$

$$\mathbf{B}^{\mathrm{T}}_{M^{23}_{n,y}} = \cos^2\gamma_{23}\frac{\partial\mathbf{B}^{\mathrm{T}}_{M^2_x}}{\partial y} + \sin^2\gamma_{23}\frac{\partial\mathbf{B}^{\mathrm{T}}_{M^2_y}}{\partial y} + \sin 2\gamma_{23}\frac{\partial\mathbf{B}^{\mathrm{T}}_{M^2_{xy}}}{\partial y} \tag{B.58}$$

and

$$\mathbf{B}^{\mathrm{T}}_{M^{23}_{ns,x}} = \frac{1}{2}\sin 2\gamma_{23}\left(\frac{\partial\mathbf{B}^{\mathrm{T}}_{M^2_y}}{\partial x} - \frac{\partial\mathbf{B}^{\mathrm{T}}_{M^2_x}}{\partial x}\right) + \cos 2\gamma_{23}\frac{\partial\mathbf{B}^{\mathrm{T}}_{M^2_{xy}}}{\partial x} \tag{B.59}$$

$$\mathbf{B}^{\mathrm{T}}_{M^{23}_{ns,y}} = \frac{1}{2}\sin 2\gamma_{23}\left(\frac{\partial\mathbf{B}^{\mathrm{T}}_{M^2_y}}{\partial y} - \frac{\partial\mathbf{B}^{\mathrm{T}}_{M^2_x}}{\partial y}\right) + \cos 2\gamma_{23}\frac{\partial\mathbf{B}^{\mathrm{T}}_{M^2_{xy}}}{\partial y} \tag{B.60}$$

The $\mathbf{B}$ matrix for V_n^{23} is:

$$\mathbf{B}^{\mathrm{T}}_{V_n^{23}} = \cos\gamma_{23}\mathbf{B}^{\mathrm{T}}_{M^{23}_{n,x}} + \sin\gamma_{23}\mathbf{B}^{\mathrm{T}}_{M^{23}_{n,y}} - 2\sin\gamma_{23}\mathbf{B}^{\mathrm{T}}_{M^{23}_{ns,x}} + 2\cos\gamma_{23}\mathbf{B}^{\mathrm{T}}_{M^{23}_{ns,y}} \tag{B.61}$$

On side 3-1:

$$\mathbf{B}^{\mathrm{T}}_{M^{31}_{n,x}} = \cos^2\gamma_{31}\frac{\partial\mathbf{B}^{\mathrm{T}}_{M^3_x}}{\partial x} + \sin^2\gamma_{31}\frac{\partial\mathbf{B}^{\mathrm{T}}_{M^3_y}}{\partial x} + \sin 2\gamma_{31}\frac{\partial\mathbf{B}^{\mathrm{T}}_{M^3_{xy}}}{\partial x} \tag{B.62}$$

$$\mathbf{B}^{\mathrm{T}}_{M^{31}_{n,y}} = \cos^2\gamma_{31}\frac{\partial\mathbf{B}^{\mathrm{T}}_{M^3_x}}{\partial y} + \sin^2\gamma_{31}\frac{\partial\mathbf{B}^{\mathrm{T}}_{M^3_y}}{\partial y} + \sin 2\gamma_{31}\frac{\partial\mathbf{B}^{\mathrm{T}}_{M^3_{xy}}}{\partial y} \tag{B.63}$$

and

$$\mathbf{B}^{\mathrm{T}}_{M^{31}_{ns,x}} = \frac{1}{2}\sin 2\gamma_{31}\left(\frac{\partial\mathbf{B}^{\mathrm{T}}_{M^3_y}}{\partial x} - \frac{\partial\mathbf{B}^{\mathrm{T}}_{M^3_x}}{\partial x}\right) + \cos 2\gamma_{31}\frac{\partial\mathbf{B}^{\mathrm{T}}_{M^3_{xy}}}{\partial x} \tag{B.64}$$

$$\mathbf{B}^{\mathrm{T}}_{M^{31}_{ns,y}} = \frac{1}{2}\sin 2\gamma_{31}\left(\frac{\partial\mathbf{B}^{\mathrm{T}}_{M^3_y}}{\partial y} - \frac{\partial\mathbf{B}^{\mathrm{T}}_{M^3_x}}{\partial y}\right) + \cos 2\gamma_{31}\frac{\partial\mathbf{B}^{\mathrm{T}}_{M^3_{xy}}}{\partial y} \tag{B.65}$$

The $\mathbf{B}$ matrix for V_n^{31} is:

$$\begin{aligned}\mathbf{B}^{\mathrm{T}}_{V_n^{31}} = {} & \cos\gamma_{31}\,\mathbf{B}^{\mathrm{T}}_{M^{31}_{n,x}} + \sin\gamma_{23}\,\mathbf{B}^{\mathrm{T}}_{M^{31}_{n,y}} \\ & - 2\sin\gamma_{23}\,\mathbf{B}^{\mathrm{T}}_{M^{31}_{ns,x}} + 2\cos\gamma_{23}\,\mathbf{B}^{\mathrm{T}}_{M^{31}_{ns,y}}\end{aligned} \tag{B.66}$$

Therefore, the calculations of $\mathbf{B}$ matrices for V_n on sides 23 and 31 can be simplified through the use of the pre-calculated matrices for side 12.

Now, all the components of the $\mathbf{B}$ matrix have been derived. The assembled (7 x 12) matrix $\mathbf{B}$ is:

$$\mathbf{B} = \left[\mathbf{B}_{R_1}, \mathbf{B}_{R_2}, \mathbf{B}_{R_3}, \mathbf{B}_{V_n^{12}}, \mathbf{B}_{V_n^{23}}, \mathbf{B}_{V_n^{31}}, \right.$$
$$\left. \mathbf{B}_{M_n^{12}}, \mathbf{B}_{M_n^{21}}, \mathbf{B}_{M_n^{23}}, \mathbf{B}_{M_n^{32}}, \mathbf{B}_{M_n^{31}}, \mathbf{B}_{M_n^{13}}\right] \tag{B.67}$$

C. CLOSED-FORM SOLUTIONS OF THE DCB, MMB AND ENF LOAD DISPLACEMENT RELATIONSHIPS

C.1. DCB TEST

The relation between the applied load and the opening displacement can be obtained using LEFM. The applied load in a DCB test for crack propagation is obtained as:

$$F = \sqrt{\frac{G_{\mathrm{Ic}} b^2 h^3 E_{11}}{12 a^2}} \tag{C.68}$$

where b and h are the width and the height of the arm, respectively. a is the crack length. The corresponding opening displacement is:

$$u = F \frac{8a^3}{bh^3 E_{11}} \tag{C.69}$$

C.2. ENF TEST

For the ENF test, the applied load reads:

$$F = \sqrt{\frac{G_{\mathrm{IIc}} 16 b^2 h^3 E_{11}}{9 a^2}} \tag{C.70}$$

The corresponding opening displacement is:

$$u = F \frac{3a^3 + 2L^3}{8bh^3 E_{11}} \tag{C.71}$$

where L is the length of the model.

C.3. MMB TEST

For the MMB test, the applied load reads:

$$F = \sqrt{\frac{G_{\mathrm{c}}}{\frac{4(3c-L)^2(a+\xi h)^2 + 3(c+L)^2(a+0.42\xi h)^2}{64 b L^2 \frac{E_{11} b h^3}{12}}}} \tag{C.72}$$

where ξ is:

$$\xi = \sqrt{\frac{E_{11}[3 - 2(\frac{g}{1+g})^2]}{11G_{13}}} \tag{C.73}$$

where g is:

$$g = 1.18\frac{\sqrt{E_{11}E_{22}}}{G_{13}} \tag{C.74}$$

The corresponding lever displacement is:

$$u = F\,\frac{4(3c - L)^2(a + \xi h)^2 + (c + L)^2[3(a + 0.42\xi h)^2 + 2L^3]}{96L^2\frac{E_{11}bh^3}{12}} \tag{C.75}$$

D. Analytical solution of SLB benchmark

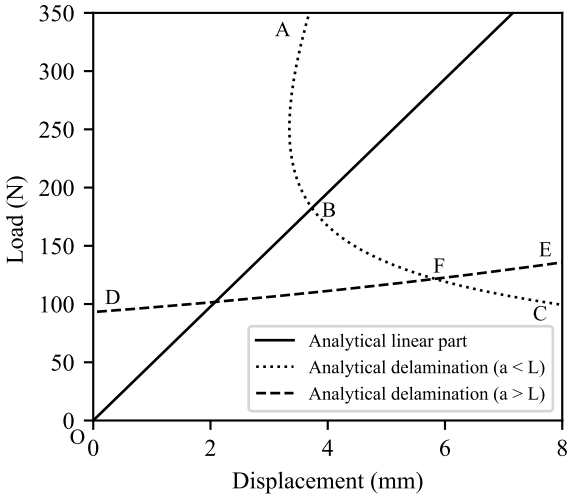

Figure D.1: Analytical solution of SLB model

Referring to Figure D.1, the analytical load-displacement curve consists of three parts. The first part, OB, is the linear elastic stage with the initial crack length a_0. The second part comes from the curve ABC which represents the load-displacement response during delamination propagation when $a < L$ (the half length of the SLB model). When $a > L$, we can obtain the last curve DFE. The full analytical curve would then be OBFE. The derivation process of each curve is shown one by one in the following content.

When the crack length a is smaller than L, the analytical derivation of the SLB benchmark follows from the work of Davidson et el. [2]. Referring to the SLB model in Figure 2.13, it is evident that the bending stiffness in the cracked region comes entirely from

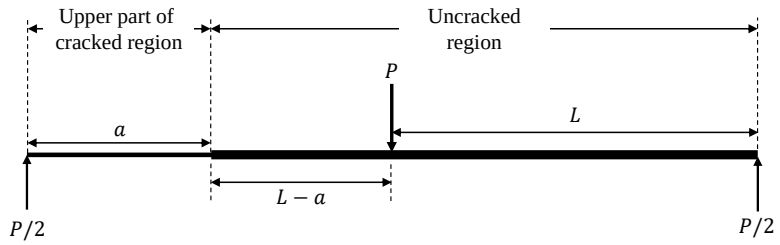

Figure D.2: Beam model of SLB specimen ($a < L$)

the part above the crack, which is midplane symmetrical. The uncracked region is midplane anti-symmetric.

The SLB model ($a < L$) is simplified into a 2D beam model, as shown in Figure D.2. The moment-curvature relationship for the SLB problem can be expressed as:

$$M = -b\,D\,\frac{\mathrm{d}^2 w}{\mathrm{d}x^2} = b\,D\,\kappa_x \tag{D.76}$$

where M is the moment on a face along the x-axis, b is the width of the specimen, w is the deflection along the z direction. And D is the effective bending rigidity per unit width. Because the values of D in the uncracked region and cracked regions are different, D_0 represents the effective bending rigidity of the uncracked region, and D_1 represents the effective bending rigidity of the cracked region to distinguish them.

We assume that the classical laminate theory is applicable to the SLB problem. In matrix form, the constitutive equation can be written as:

$$\begin{bmatrix} N_x \\ N_y \\ N_{xy} \\ -- \\ M_x \\ M_y \\ M_{xy} \end{bmatrix} = \left[\begin{array}{ccc|ccc} A_{11} & A_{12} & A_{16} & B_{11} & B_{12} & B_{16} \\ A_{12} & A_{22} & A_{26} & B_{12} & B_{22} & B_{26} \\ A_{16} & A_{26} & A_{66} & B_{16} & B_{26} & B_{66} \\ -- & -- & -- & -- & -- & -- \\ \hline B_{11} & B_{12} & B_{16} & D_{11} & D_{12} & D_{16} \\ B_{12} & B_{22} & B_{26} & D_{12} & D_{22} & D_{26} \\ B_{16} & B_{26} & B_{66} & D_{16} & D_{26} & D_{66} \end{array}\right] \begin{bmatrix} \varepsilon_x^0 \\ \varepsilon_y^0 \\ \gamma_{xy}^0 \\ -- \\ \kappa_x \\ \kappa_y \\ \kappa_{xy} \end{bmatrix} \tag{D.77}$$

where ε_x^0, ε_y^0, γ_{xy}^0 are the membrane strains of the neutral plane, and κ_x, κ_y, κ_{xy} are the curvatures, derived from the out-of-plane displacement w:

$$\kappa_x = -\frac{\partial^2 w}{\partial x^2}, \quad \kappa_y = -\frac{\partial^2 w}{\partial y^2}, \quad \kappa_{xy} = -\frac{\partial^2 w}{\partial x \partial y} \tag{D.78}$$

The inverted form of the constitutive relationship is:

$$\begin{bmatrix} \varepsilon_x^0 \\ \varepsilon_y^0 \\ \gamma_{xy}^0 \\ -- \\ \kappa_x \\ \kappa_y \\ \kappa_{xy} \end{bmatrix} = \left[\begin{array}{ccc|ccc} \alpha_{11} & \alpha_{12} & \alpha_{16} & \beta_{11} & \beta_{12} & \beta_{16} \\ \alpha_{12} & \alpha_{22} & \alpha_{26} & \beta_{12} & \beta_{22} & \beta_{26} \\ \alpha_{16} & \alpha_{26} & \alpha_{66} & \beta_{16} & \beta_{26} & \beta_{66} \\ -- & -- & -- & -- & -- & -- \\ \beta_{11} & \beta_{12} & \beta_{16} & \delta_{11} & \delta_{12} & \delta_{16} \\ \beta_{12} & \beta_{22} & \beta_{26} & \delta_{12} & \delta_{22} & \delta_{26} \\ \beta_{16} & \beta_{26} & \beta_{66} & \delta_{16} & \delta_{26} & \delta_{66} \end{array}\right] \begin{bmatrix} N_x \\ N_y \\ N_{xy} \\ -- \\ M_x \\ M_y \\ M_{xy} \end{bmatrix} \tag{D.79}$$

If the plate constraint condition is “generalized plane stress", N_y, N_{xy}, M_y, and M_{xy} are zero. When considering $N_x = 0$, Equation D.79 gives:

$$D = \frac{1}{\delta_{11}} \tag{D.80}$$

For the plane strain condition ($\epsilon_y^0 = \gamma_{xy}^0 = \kappa_y = \kappa_{xy} = 0$), Equation D.77 gives:

$$D = D_{11} \tag{D.81}$$

The expression of strain energy is:

$$U = \int_0^{2L} \frac{M^2 \mathrm{d}x}{2bD} \tag{D.82}$$

From Figure D.2, the boundary conditions of the SLB model can be considered similar to three-point bending. So we can get the moment along the beam as:

$$M = \begin{cases} -\dfrac{Px}{2}, & 0 \le x \le L \\ \dfrac{Px}{2} - PL, & L \le x \le 2L \end{cases} \tag{D.83}$$

Since the cross-section of the upper part of the cracked region $(0 \le x \le a)$ is different from that of the uncracked region, the moment M is further divided, and the expression for strain energy is the sum of three parts:

$$U|_{(a<L)} = \int_0^a \frac{M^2 \mathrm{d}x}{2bD_1} + \int_a^{L-a} \frac{M^2 \mathrm{d}x}{2bD_0} + \int_L^{2L} \frac{M^2 \mathrm{d}x}{2bD_0} \tag{D.84}$$

Substituting Equation D.83 into Equation D.84, we can get:

$$U|_{(a<L)} = \int_0^a \frac{\left(-\frac{Px}{2}\right)^2 \mathrm{d}x}{2bD_1} + \int_a^L \frac{\left(-\frac{Px}{2}\right)^2 \mathrm{d}x}{2bD_0} + \int_L^{2L} \frac{\left(\frac{Px}{2} - PL\right)^2 \mathrm{d}x}{2bD_0} \tag{D.85}$$

Based on the expression of strain energy, the displacement δ can be calculated by Castigliano's second theorem:

$$\delta|_{(a<L)} = \frac{\partial U|_{(a<L)}}{\partial P} = \int_0^a \frac{Px^2 \mathrm{d}x}{4bD_1} + \int_a^L \frac{Px^2 \mathrm{d}x}{4bD_0} + \int_L^{2L} \frac{\left(Px^2 - 4PLx + 4PL^2\right) \mathrm{d}x}{4bD_0}$$
$$= \frac{Pa^3}{12bD_1} + \frac{2PL^3 - Pa^3}{12bD_0} \tag{D.86}$$

The above equation can be used to plot the $P - \delta$ curve for a certain crack length a, which for the case of $a = a_0$ gives the first part of the analytical curve, i.e., OB. The compliance C during the elastic region is defined as the center deflection δ divided by the center load P:

$$C|_{(a<L)} = \frac{\delta|_{(a<L)}}{P} = \frac{2L^3 + a^3(R-1)}{12bD_0} \tag{D.87}$$

where R is the ratio of the bending rigidity of the uncracked region to that of the cracked region:

$$R = D_0/D_1 \tag{D.88}$$

The relationship between the critical energy release rate G_c and the derivative of compliance C with respect to the crack length a is:

$$G_c = \frac{P^2}{2b}\frac{\partial C}{\partial a} \tag{D.89}$$

Substituting Equation D.87 into Equation D.89, we can obtain:

$$G_c = \frac{P^2 a^2 (R-1)}{8b^2 D_0} \tag{D.90}$$

Substituting Equation D.87 into Equation D.90, the critical energy release rate G_c can also be obtained by the critical load and deflection:

$$G_c = \frac{3Pa^2\ \delta|_{(a<L)}}{2b} \frac{(R-1)}{[2L^3 + a^3(R-1)]} \tag{D.91}$$

The critical energy release rate G_c in Equation D.91 is the value in mixed mode. It can be calculated by:

$$G_c = G_{\mathrm{Ic}} + (G_{\mathrm{IIc}} - G_{\mathrm{Ic}})B^\eta \tag{D.92}$$

where G_{Ic} and G_{IIc} are the critical energy release rates in pure mode I and mode II, respectively. The mixed mode ratio B in the SLB model is 0.4 [3]. Equation D.90 can be used to calculate the critical load P at a certain crack length a. It can also be used to express a in terms of P for a fixed G_c, which can be plugged into Equation D.91 to obtain the relationship between δ and P for a fixed G_c for the case of $a < L$, hence giving the curve ABC.

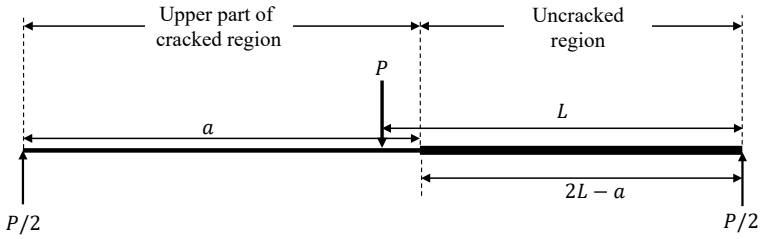

Figure D.3: Beam model of SLB specimen ($a \geq L$)

When the crack length a is greater than or equal to L, the analytical derivation of the SLB benchmark can follow the same derivation process as above. The SLB model ($a \geq L$) is simplified in Figure D.3. Based on Figure D.3, the expression for strain energy is rewritten as:

$$U|_{(a\geq L)} = \int_0^L \frac{M^2 \mathrm{d}x}{2bD_1} + \int_L^a \frac{M^2 \mathrm{d}x}{2bD_1} + \int_a^{2L} \frac{M^2 \mathrm{d}x}{2bD_0} \tag{D.93}$$

Since the boundary conditions have not changed, the expression of the moment is consistent with Equation D.83. Substituting Equation D.83 into Equation D.93, we can obtain:

$$\begin{aligned} U|_{(a\geq L)} = &\int_0^L \frac{P^2x^2 \mathrm{d}x}{8bD_1} + \int_L^a \frac{\left(P^2x^2 - 4P^2Lx + 4P^2L^2\right)\mathrm{d}x}{8bD_1} \\ &+ \int_a^{2L} \frac{\left(P^2x^2 - 4P^2Lx + 4P^2L^2\right)\mathrm{d}x}{8bD_0} \end{aligned} \tag{D.94}$$

The displacement δ at the middle can also be found by Castigliano's second theorem:

$$\begin{aligned} \delta|_{(a\geq L)} = &-\frac{PL^3}{2bD_1} + \frac{Pa^3 - 6PLa^2 + 12PL^2a}{12bD_1} \\ &+ \frac{8PL^3}{12bD_0} - \frac{Pa^3 - 6PLa^2 + 12PL^2a}{12bD_0} \end{aligned} \tag{D.95}$$

Introducing ratio R in Equation D.88, the above equation can be rewritten as:

$$\delta|_{(a\geq L)} = -\frac{(6R-8)PL^3}{12bD_0} + \frac{(R-1)(Pa^3 - 6PLa^2 + 12PL^2a)}{12bD_0} \tag{D.96}$$

The expression of compliance C under the condition $a \geq L$ is:

$$C|_{(a\geq L)} = \frac{\delta|_{(a\geq L)}}{P} = -\frac{(6R-8)L^3}{12bD_0} + \frac{(R-1)(a^3 - 6La^2 + 12L^2a)}{12bD_0} \tag{D.97}$$

Substituting Equation D.97 into Equation D.89, we have:

$$G_c = \frac{P^2(R-1)(3a^2 - 12aL + 12L^2)}{24b^2D_0} \tag{D.98}$$

where G_c is the critical energy release rate given by Equation D.92. Using equations D.96 and D.98, one can then vary a to plot the third part of the analytical curve DE.

E. TUBA3 ELEMENT EXTENSION

E.1. TUBA3 PLATE ELEMENT

The traditional linear triangular plate element exhibits C^0 continuity. It means that displacements are continuous across element boundaries, while rotations are discontinuous. It leads to relatively low computational accuracy. Thus, it is usually used for simple stress analysis. If C^0-continuous plate elements are combined with cohesive elements to simulate delamination, problems related to the limitations of the cohesive zone will arise.

One remarkable method that can solve the cohesive zone limitation is to increase the element size by employing a C^1-continuous higher-order structural element, including a C^1 ply element and compatible cohesive elements (CEs) [**russo**]. Therefore, a suitable plate element satisfying C^1 continuity is required to replace traditional C^0 plate elements. Tosti Balducci et al. [4] choose a C^1 triangular thin plate element which is based on the Kirchhoff-Love assumption and compatible CE to simulate a 3D delamination problem. The triangular thin plate element chosen for this work is the three-noded TUBA3, also known as Bell's triangle. The TUBA3 element is shown in Figure E.4. This method was used to validate the classic benchmark case for mode-I delamination, achieving high accuracy while significantly reducing the computing time. An attempt was made to simulate the pure Mode II ENF specimen using TUBA3 and TUBA3-CE. The results showed that the onset of damage and the limit load were reached erroneously at the first increment. According to the author's suggestion, the problem can be solved by expanding in two aspects: the shell element and geometric nonlinearity. Therefore, this appendix derives the relevant equations and presents the verification of the expansions in these two aspects.

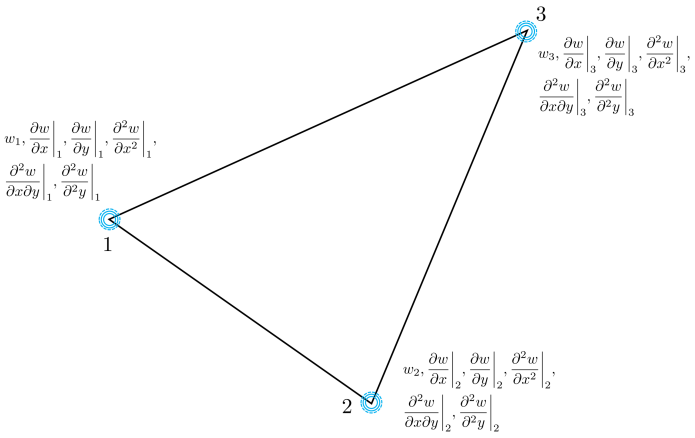

Figure E.4: Bell triangle (TUBA3) [1]

E.2. GENERAL FRAMEWORK

In this work, the derivation of geometric nonlinearity adopts the Total Lagrangian (TL) formulation. The general framework is presented as follows:

Weak form

The weak form (or principle of virtual work) for the Total Lagrangian (TL) formulation, expressed in Voigt notation, is given by:

$$\int_{\Omega_0} \delta \mathbf{E}^{\mathrm{T}}\, \mathbf{S}\, \mathrm{d}V_0 = \int_{\Omega_0} \delta \mathbf{u}^{\mathrm{T}}\, \mathbf{b}_0\, \mathrm{d}V_0 + \int_{\Gamma_0} \delta \mathbf{u}^{\mathrm{T}}\, \mathbf{t}_0\, \mathrm{d}A_0 \tag{E.99}$$

where Ω_0 and Γ_0 are the initial domain and its boundary, respectively. $\mathbf{E}$ is the Green-Lagrange strain vector, $\mathbf{S}$ is the second Piola-Kirchhoff stress vector, $\mathbf{u}$ is the displacement vector, and $\mathbf{b}_0$ and $\mathbf{t}_0$ are the body force density and surface traction in the initial configuration, respectively.

Finite element discretization

To implement the finite element discretization, we introduce the following formulation:

$$\mathbf{u} = \mathbf{N}\,\mathbf{a} \quad \delta\mathbf{u} = \mathbf{N}\,\delta\mathbf{a} \quad \delta\mathbf{E} = \mathbf{B}\,\delta\mathbf{a} \tag{E.100}$$

where $\mathbf{N}$ is the shape function matrix, $\mathbf{B}$ is the strain-displacement matrix and $\mathbf{a}$ is the nodal DOF vector. Substituting Equation E.100 into Equation E.99, we obtain the finite element method (FEM) equilibrium equation as follows:

$$\underbrace{\int_{\Omega_0} \mathbf{B}^{\mathrm{T}}\, \mathbf{S}\, \mathrm{d}V_0}_{\mathbf{f}_{\mathrm{int}}} = \underbrace{\int_{\Omega_0} \mathbf{N}^{\mathrm{T}}\, \mathbf{b}_0\, \mathrm{d}V_0 + \int_{\Gamma_0} \mathbf{N}^{\mathrm{T}}\, \mathbf{t}_0\, \mathrm{d}A_0}_{\mathbf{f}_{\mathrm{ext}}} \tag{E.101}$$

where the left-hand side (LHS) corresponds to the internal force vector $\mathbf{f}_{\mathrm{int}}$.

Within the linear elastic regime, the second Piola-Kirchhoff stress tensor can be calculated from the Green-Lagrange strain tensor via the constitutive stiffness tensor $\mathbb{C}$ as follows:

$$\mathbf{S} = \mathbb{C}\,\mathbf{E} \tag{E.102}$$

where the Green-Lagrange strain vector $\mathbf{E}$ can be expressed in terms of the gradient of displacement:

$$\begin{aligned} \mathbf{E} &= \frac{1}{2}\left(\mathbf{F}^{\mathrm{T}}\,\mathbf{F} - \mathbf{I}\right) \\ &= \frac{1}{2}\left[\left(\frac{\partial \mathbf{u}}{\partial \mathbf{X}}\right) + \left(\frac{\partial \mathbf{u}}{\partial \mathbf{X}}\right)^{\mathrm{T}} + \left(\frac{\partial \mathbf{u}}{\partial \mathbf{X}}\right)^{\mathrm{T}}\left(\frac{\partial \mathbf{u}}{\partial \mathbf{X}}\right)\right] \end{aligned} \tag{E.103}$$

where $\mathbf{F}$ is the deformation gradient:

$$\mathbf{F} = \frac{\partial \mathbf{x}}{\partial \mathbf{X}} = \mathbf{I} + \frac{\partial \mathbf{u}}{\partial \mathbf{X}} \tag{E.104}$$

Taking the derivative of the internal force vector with respect to the DoF vector, we obtain the tangent stiffness matrix expression as a sum of $\mathbf{K}_{\mathrm{mat}}$ and $\mathbf{K}_{\mathrm{geo}}$:

By taking the derivative of the internal force vector with respect to the degree-of-freedom (DoF) vector, we obtain the tangent stiffness matrix, which can be expressed as the sum of the elastic stiffness matrix $\mathbf{K}_{\mathrm{mat}}$ and the geometric stiffness matrix $\mathbf{K}_{\mathrm{geo}}$:

$$\mathbf{K} = \frac{\partial \mathbf{f}_{\mathrm{int}}}{\partial \mathbf{a}} = \underbrace{\int_{\Omega_0} \frac{\partial \mathbf{B}^{\mathrm{T}}}{\partial \mathbf{a}} \mathbf{S} \, \mathrm{d}V_0}_{\mathbf{K}_{\mathrm{geo}}} + \underbrace{\int_{\Omega_0} \mathbf{B}^{\mathrm{T}} \mathbb{C} \mathbf{B} \, \mathrm{d}V_0}_{\mathbf{K}_{\mathrm{mat}}} \tag{E.105}$$

The TUBA3 shell element introduced in this section comprises two primary components: (a) the membrane part and (b) the plate part. For this reason, the aforementioned theories are divided into these two components for analysis. Further details regarding the derivation process are provided in subsequent sections.

SOME BASIC RELATIONS IN AREA CO-ORDINATE

TUBA3 is a three-noded triangular element. It uses area co-ordinates for a triangle element. A typical element is shown in Figure E.5. The co-ordinates L_i within the element are defined by

$$L_i = A_i / A \quad (i = 1, 2, 3) \tag{E.106}$$

where A is the area of the element. The basic relations between area co-ordinates and co-ordinates are given by

$$\begin{aligned} x &= L_1 \, x_1 + L_2 \, x_2 + L_3 \, x_3 \\ y &= L_1 \, y_1 + L_2 \, y_2 + L_3 \, y_3 \\ 1 &= L_1 + L_2 + L_3 \\ L_i &= (a_i + b_i \, x + c_i \, y) \, / 2A \quad (i = 1, 2, 3) \end{aligned} \tag{E.107}$$

where

$$A = \frac{1}{2} \left[(x_2 \, y_3 - x_3 \, y_2) + (x_3 \, y_1 - x_1 \, y_3) + (x_1 \, y_2 - x_2 \, y_1) \right] \tag{E.108}$$

and

$$\begin{aligned} a_i &= x_j \, y_k - x_k \, y_j \\ b_i &= y_j - y_k \\ c_i &= x_k - x_j \end{aligned} \tag{E.109}$$

where i, j, k are cyclic permutations of 1,2 and 3.

The differentiation with respect to Cartesian coordinates may be obtained from

$$\frac{\partial}{\partial x} = \frac{1}{2A} \left(b_1 \frac{\partial}{\partial L_1} + b_2 \frac{\partial}{\partial L_2} + b_3 \frac{\partial}{\partial L_3} \right) \tag{E.110}$$

$$\frac{\partial}{\partial y} = \frac{1}{2A} \left(c_1 \frac{\partial}{\partial L_1} + c_2 \frac{\partial}{\partial L_2} + c_3 \frac{\partial}{\partial L_3} \right) \tag{E.111}$$

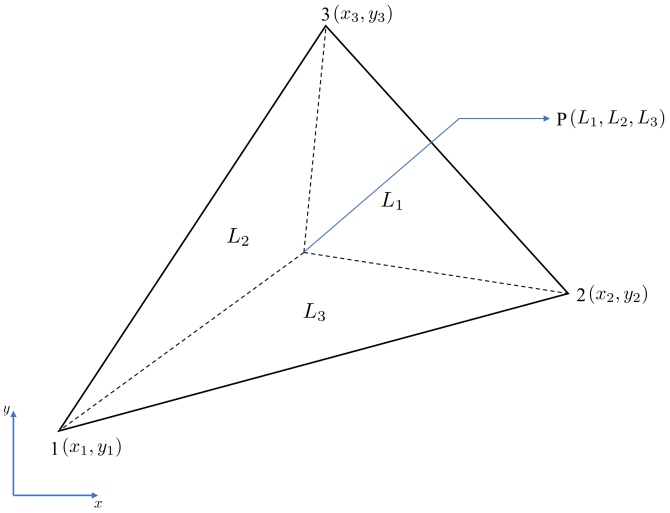

Figure E.5: Area coordinates of a point in the generic triangle

E.3. Degrees of Freedom and Shape Functions

Membrane Part

Based on the classical membrane element, the vector $\mathbf{u}^0$ represents the membrane displacement in this work, where 0 means the membrane part.

Using the finite element discretization (Equation E.100), the relationship between the displacement, including its variation, and DOFs or its variation can be expressed using the shape function $\mathbf{N}^0$ as

$$\mathbf{u}^0 = \mathbf{N}^0 \mathbf{u} \quad \delta\mathbf{u}^0 = \mathbf{N}^0 \delta\mathbf{u} \tag{E.112}$$

where $\mathbf{N}^0$ is the shape function matrix. The shape functions are:

$$N_1^0 = L_1 \tag{E.113}$$

$$N_2^0 = L_2 \tag{E.114}$$

$$N_3^0 = L_3 \tag{E.115}$$

where L_i is the area co-ordinates defined in the former section. The displacement vector $\mathbf{u}^0$ and DOFs vector $\mathbf{u}$ can be built as

$$\mathbf{u}^0 = \left[u^0,\, v^0\right]^{\mathrm{T}} \tag{E.116}$$

$$\mathbf{u} = \left[u_1,\, v_1,\, u_2,\, v_2,\, u_3,\, v_3\right]^{\mathrm{T}} \tag{E.117}$$

BENDING PART

Different from the membrane part, the bending part only has one displacement component, w. Equation E.100 can be rewritten by using w:

$$w = \mathbf{N}\,\mathbf{a} \quad \delta w = \mathbf{N}\,\delta\mathbf{a} \quad \delta\mathbf{E}^{\mathrm{b}} = \mathbf{B}^{\mathrm{b}}\,\delta\mathbf{a} \tag{E.118}$$

where $\mathbf{N}$ are the TUBA3 plate shape functions. Details are shown in Appendix G.

Bending element with transverse displacement w, the DOF vector at each node i is taken as

$$\mathbf{a}_i = \left[w_i, \left(\frac{\partial w}{\partial x}\right)_i, \left(\frac{\partial w}{\partial y}\right)_i, \left(\frac{\partial^2 w}{\partial x^2}\right)_i, \left(\frac{\partial^2 w}{\partial x \partial y}\right)_i, \left(\frac{\partial^2 w}{\partial^2 y}\right)_i\right]^{\mathrm{T}} \tag{E.119}$$

Then, the total plate degree-of-freedom (DoF) vector corresponding to nodes 1, 2, and 3 is expressed as:

$$\mathbf{a} = [\,\mathbf{a}_1 \quad \mathbf{a}_2 \quad \mathbf{a}_3\,]^{\mathrm{T}} \tag{E.120}$$

Combining membrane part and bending part, the DOF of the total TUBA3 shell element can be easily obtained. In this work, the total DOFs vector is named as $\mathbf{q}$:

$$\mathbf{q} = [\,\mathbf{u},\,\mathbf{a}\,]^{\mathrm{T}}_{24\times 1} \tag{E.121}$$

E.4. GREEN-LAGRANGE STRAIN

The Green-Lagrange strain tensor is defined by Equation E.103. Evidently, it is necessary to calculate the displacement gradient $\partial\mathbf{u}/\partial\mathbf{X}$. This term and its transpose are expressed as follows:

$$\frac{\partial \mathbf{u}}{\partial \mathbf{X}} = \begin{bmatrix} \frac{\partial u}{\partial X} & \frac{\partial u}{\partial Y} & \frac{\partial u}{\partial Z} \\ \frac{\partial v}{\partial X} & \frac{\partial v}{\partial Y} & \frac{\partial v}{\partial Z} \\ \frac{\partial w}{\partial X} & \frac{\partial w}{\partial Y} & \frac{\partial w}{\partial Z} \end{bmatrix} \quad \left(\frac{\partial \mathbf{u}}{\partial \mathbf{X}}\right)^{\mathrm{T}} = \begin{bmatrix} \frac{\partial u}{\partial X} & \frac{\partial v}{\partial X} & \frac{\partial w}{\partial X} \\ \frac{\partial u}{\partial Y} & \frac{\partial v}{\partial Y} & \frac{\partial w}{\partial Y} \\ \frac{\partial u}{\partial Z} & \frac{\partial v}{\partial Z} & \frac{\partial w}{\partial Z} \end{bmatrix} \tag{E.122}$$

where u, v, w are the displacements (in the x-, y-, and z-directions, respectively). Among these, u and v are further decomposed into two components.

$$\begin{aligned} u &= u^0 + u^{\mathrm{b}} \\ v &= v^0 + v^{\mathrm{b}} \\ w &= w \end{aligned} \tag{E.123}$$

where u^0 and v^0 represent the membrane displacement, while u^{b} and v^{b} represent the bending-induced in-plane displacement. For the latter u^{b} and v^{b}, the Kirchhoff kinematic assumption is adopted. It means that these bending-induced in-plane displacements can be derived from the out-of-plane displacement w.

$$u^{\mathrm{b}} = -Z\,\frac{\partial w}{\partial X} \tag{E.124}$$

$$v^{\mathrm{b}} = -Z\,\frac{\partial w}{\partial Y} \tag{E.125}$$

By combing the Equations E.122, E.123, E.124 and E.125, the deformation gradient $\partial \mathbf{u}/\partial \mathbf{x}$ can be expressed in terms of displacement. In continuum mechanics analysis, three fundamental strains are considered: E_{11}, E_{22}, and E_{12}.

$$
\begin{aligned}
E_{11} &= \underbrace{\frac{\partial u^0}{\partial X} + \frac{1}{2}\left[\left(\frac{\partial u^0}{\partial X}\right)^2 + \left(\frac{\partial v^0}{\partial X}\right)^2\right]}_{E_{11}^0} - Z\underbrace{\frac{\partial^2 w}{\partial X^2}}_{E_{11}^{\mathrm{bL}}} + \underbrace{\frac{1}{2}\left(\frac{\partial w}{\partial X}\right)^2}_{E_{11}^{\mathrm{bN}}} \\
E_{22} &= \underbrace{\frac{\partial v^0}{\partial Y} + \frac{1}{2}\left[\left(\frac{\partial u^0}{\partial Y}\right)^2 + \left(\frac{\partial v^0}{\partial Y}\right)^2\right]}_{E_{22}^0} - Z\underbrace{\frac{\partial^2 w}{\partial Y^2}}_{E_{22}^{\mathrm{bL}}} + \underbrace{\frac{1}{2}\left(\frac{\partial w}{\partial Y}\right)^2}_{E_{22}^{\mathrm{bN}}} \\
E_{12} &= \underbrace{\frac{1}{2}\left[\frac{\partial u^0}{\partial Y} + \frac{\partial v^0}{\partial X} + \frac{\partial u^0}{\partial X}\frac{\partial u^0}{\partial Y} + \frac{\partial v^0}{\partial X}\frac{\partial v^0}{\partial Y}\right]}_{E_{12}^0} - Z\underbrace{\frac{\partial^2 w}{\partial X \partial Y}}_{E_{12}^{\mathrm{bL}}} + \underbrace{\frac{1}{2}\left(\frac{\partial w}{\partial X}\right)\left(\frac{\partial w}{\partial Y}\right)}_{E_{12}^{\mathrm{bN}}}
\end{aligned}
\tag{E.126}
$$

The superscripts bL and bN in Equation E.126 represent the bending linear part and bending nonlinear part, respectively. For the bending component, the total Green-Lagrange strain $\mathbf{E}^{\mathrm{b}}$ can be expressed as

$$
\mathbf{E}^{\mathrm{b}} = -Z\,\mathbf{E}^{\mathrm{bL}} + \mathbf{E}^{\mathrm{bN}} \tag{E.127}
$$

In conclusion, the Green-Lagrange strain $\mathbf{E}$ of the shell element is the sum of the membrane strain $\mathbf{E}^0$ and the bending strain $\mathbf{E}^{\mathrm{b}}$. It should be noted that E is not used to calculate other terms in the present work.

$$
\begin{aligned}
\mathbf{E} &= \mathbf{E}^0 + \mathbf{E}^{\mathrm{b}} \\
&= \mathbf{E}^0 + \left(-Z\mathbf{E}^{\mathrm{bL}} + \mathbf{E}^{\mathrm{bN}}\right)
\end{aligned}
\tag{E.128}
$$

Expressed in matrix form, this equation becomes:

$$
\mathbf{E} = \begin{bmatrix} E_{11} \\ E_{22} \\ E_{12} \end{bmatrix} = \begin{bmatrix} E_{11}^0 \\ E_{22}^0 \\ E_{12}^0 \end{bmatrix} - Z \begin{bmatrix} E_{11}^{\mathrm{bL}} \\ E_{22}^{\mathrm{bL}} \\ E_{12}^{\mathrm{bL}} \end{bmatrix} + \begin{bmatrix} E_{11}^{\mathrm{bN}} \\ E_{22}^{\mathrm{bN}} \\ E_{12}^{\mathrm{bN}} \end{bmatrix} \tag{E.129}
$$

E.5. $\mathbb{C}$ MATRIX

In the case of an isotropic material under plane stress conditions, the stiffness matrix can be written in terms of the Young's modulus E and Poisson's ratios ν. For clarity, the general form of the plane stress stiffness matrix for an isotropic material is:

$$
\mathbb{C} = \frac{E}{1-\nu^2}\begin{bmatrix} 1 & \nu & 0 \\ \nu & 1 & 0 \\ 0 & 0 & 1-\nu \end{bmatrix} \tag{E.130}
$$

Since E and ν are material-defined parameters, the stiffness tensor $\mathbb{C}$ is a constant matrix in the present work

E.6. SECOND PIOLA-KIRCHHOFF STRESS

The Second Piola-Kirchhoff stress is defined by Equation E.102. With Green-Lagrange strain $\mathbf{E}$ and stiffness tensor$\mathbb{C}$ derived in preceding sections, the Second Piola-Kirchhoff stress tensor $\mathbf{S}$ can be directly computed by substituting Equation E.128 into the constitutive relation:

$$\begin{aligned}\mathbf{S} &= \mathbb{C}\left(\mathbf{E}^0 + \mathbf{E}^{\mathrm{b}}\right) \\ &= \mathbb{C}\,\mathbf{E}^0 + \mathbb{C}\,\mathbf{E}^{\mathrm{b}}\end{aligned} \tag{E.131}$$

Introducing the symbols $\mathbf{S}^0$ (membrane Second Piola-Kirchhoff stress) and $\mathbf{S}^{\mathrm{b}}$ (bending Second Piola-Kirchhoff stress) to distinguish the two components, Equation E.131 can be rewritten as:

$$\mathbf{S} = \mathbf{S}^0 + \mathbf{S}^{\mathrm{b}} \tag{E.132}$$

$$\mathbf{S}^0 = \mathbb{C}\,\mathbf{E}^0 \tag{E.133}$$

$$\mathbf{S}^{\mathrm{b}} = \mathbb{C}\,\mathbf{E}^{\mathrm{b}} \tag{E.134}$$

Expressed in matrix form, consistent with the Green-Lagrange strain vector notation in Section E.4, the Second Piola-Kirchhoff stress vector becomes:

$$[\,\mathbf{S}\,]_{3\times 1} = \begin{bmatrix} S_{11} \\ S_{22} \\ S_{12} \end{bmatrix} = \begin{bmatrix} S^0_{11} \\ S^0_{22} \\ S^0_{12} \end{bmatrix} - Z \begin{bmatrix} S^{\mathrm{bL}}_{11} \\ S^{\mathrm{bL}}_{22} \\ S^{\mathrm{bL}}_{12} \end{bmatrix} + \begin{bmatrix} S^{\mathrm{bN}}_{11} \\ S^{\mathrm{bN}}_{22} \\ S^{\mathrm{bN}}_{12} \end{bmatrix} \tag{E.135}$$

E.7. B MATRIX

MEMBRANE PART OF B MATRIX

By taking the variation of the Green-Lagrange (GL) strain for the membrane component derived above, the following equations are obtained:

$$\begin{aligned}
\delta E^0_{11} &= \underbrace{\left[\frac{\partial N_i}{\partial X} + \frac{\partial u}{\partial X}\frac{\partial N_i}{\partial X},\quad \frac{\partial v}{\partial X}\frac{\partial N_i}{\partial X}\right]}_{{}^{i}\mathbf{B}^0_X}\begin{bmatrix}\delta u_i \\ \delta v_i\end{bmatrix} \\
\delta E^0_{22} &= \underbrace{\left[\frac{\partial u}{\partial Y}\frac{\partial N_i}{\partial Y},\quad \frac{\partial N_i}{\partial Y} + \frac{\partial v}{\partial Y}\frac{\partial N_i}{\partial Y}\right]}_{{}^{i}\mathbf{B}^0_Y}\begin{bmatrix}\delta u_i \\ \delta v_i\end{bmatrix} \\
\delta E^0_{12} &= \underbrace{\frac{1}{2}\left[\frac{\partial N_i}{\partial Y} + \frac{\partial u}{\partial X}\frac{\partial N_i}{\partial Y} + \frac{\partial u}{\partial Y}\frac{\partial N_i}{\partial X},\quad \frac{\partial N_i}{\partial X} + \frac{\partial v}{\partial X}\frac{\partial N_i}{\partial Y} + \frac{\partial v}{\partial Y}\frac{\partial N_i}{\partial X}\right]}_{{}^{i}\mathbf{B}^0_{XY}}\begin{bmatrix}\delta u_i \\ \delta v_i\end{bmatrix}
\end{aligned} \tag{E.136}$$

Therefore, the final $\mathbf{B}^0$ matrix is simply to be assembled as:

$$\mathbf{B}^0 = \begin{bmatrix} {}^1\mathbf{B}^0_X & {}^2\mathbf{B}^0_X & {}^3\mathbf{B}^0_X \\ {}^1\mathbf{B}^0_Y & {}^2\mathbf{B}^0_Y & {}^3\mathbf{B}^0_Y \\ {}^1\mathbf{B}^0_{XY} & {}^2\mathbf{B}^0_{XY} & {}^3\mathbf{B}^0_{XY} \end{bmatrix}_{3\times 6} \tag{E.137}$$

Bending part of B matrix

Similar to the method in the membrane part, taking variations of the bending GL strains, the equations are shown as follows

$$\delta E^{\mathrm{b}}_{11} = \left[-Z \underbrace{\frac{\partial^2 \mathbf{N}}{\partial X^2}}_{\mathbf{B}^{\mathrm{bL}}_X} + \underbrace{\frac{\partial w}{\partial X}\frac{\partial \mathbf{N}}{\partial X}}_{\mathbf{B}^{\mathrm{bN}}_X} \right] \delta\mathbf{a} = \mathbf{B}^{\mathrm{b}}_X \, \delta\mathbf{a} \tag{E.138}$$

$$\delta E^{\mathrm{b}}_{22} = \left[-Z \underbrace{\frac{\partial^2 \mathbf{N}}{\partial Y^2}}_{\mathbf{B}^{\mathrm{bL}}_Y} + \underbrace{\frac{\partial w}{\partial Y}\frac{\partial \mathbf{N}}{\partial Y}}_{\mathbf{B}^{\mathrm{bN}}_Y} \right] \delta\mathbf{a} = \mathbf{B}^{\mathrm{b}}_Y \, \delta\mathbf{a} \tag{E.139}$$

$$\delta E^{\mathrm{b}}_{12} = \left[-Z \underbrace{\frac{\partial^2 \mathbf{N}}{\partial X \partial Y}}_{\mathbf{B}^{\mathrm{bL}}_{XY}} + \underbrace{\frac{1}{2}\frac{\partial w}{\partial Y}\frac{\partial \mathbf{N}}{\partial X} + \frac{1}{2}\frac{\partial w}{\partial X}\frac{\partial \mathbf{N}}{\partial Y}}_{\mathbf{B}^{\mathrm{bN}}_{XY}} \right] \delta\mathbf{a} = \mathbf{B}^{\mathrm{b}}_{XY} \, \delta\mathbf{a} \tag{E.140}$$

Expanding $\mathbf{B}^{\mathrm{b}}$ matrix to each term:

$${}^i B^{\mathrm{b}}_X = -Z\frac{\partial^2 N_i}{\partial X^2} + \frac{\partial w}{\partial X}\frac{\partial N_i}{\partial X} = -Z\frac{\partial^2 N_i}{\partial X^2} + \frac{\partial N_i}{\partial X}\frac{\partial N_j}{\partial X}\, a_j \tag{E.141}$$

$${}^i B^{\mathrm{b}}_Y = -Z\frac{\partial^2 N_i}{\partial Y^2} + \frac{\partial w}{\partial Y}\frac{\partial N_i}{\partial Y} = -Z\frac{\partial^2 N_i}{\partial Y^2} + \frac{\partial N_i}{\partial Y}\frac{\partial N_j}{\partial Y}\, a_j$$

$$\begin{aligned} {}^i B^{\mathrm{b}}_{XY} &= -Z\frac{\partial^2 N_i}{\partial X \partial Y} + \frac{1}{2}\frac{\partial w}{\partial Y}\frac{\partial N_i}{\partial X} + \frac{1}{2}\frac{\partial w}{\partial X}\frac{\partial N_i}{\partial Y} \\ &= -Z\frac{\partial^2 N_i}{\partial X \partial Y} + \frac{1}{2}\left(\frac{\partial N_i}{\partial X}\frac{\partial N_j}{\partial Y} + \frac{\partial N_i}{\partial Y}\frac{\partial N_j}{\partial X}\right) a_j \end{aligned}$$

In Equation E.141, $i, j = (1, 2, 3, \cdots, 16, 17, 18)$. Although the same letter i is used to represent the component of the $\mathbf{B}^0$ matrix, its value is 1 to 3, different from Equation E.141. Combining $\mathbf{B}^0$ and $\mathbf{B}^{\mathrm{b}}$ together, the total $\mathbf{B}$ matrix can be built as:

$$\mathbf{B} = \left[\mathbf{B}^0, \mathbf{B}^{\mathrm{b}}\right]_{3\times 24} \tag{E.142}$$

Written in matrix form:

$$\mathbf{B} = \begin{bmatrix} \mathbf{B}_X \\ \mathbf{B}_Y \\ \mathbf{B}_{XY} \end{bmatrix} = \left[\begin{array}{c|c} \mathbf{B}_X^0 & \mathbf{B}_X^b \\ \mathbf{B}_Y^0 & \mathbf{B}_Y^b \\ \mathbf{B}_{XY}^0 & \mathbf{B}_{XY}^b \end{array}\right]_{3\times 24} \tag{E.143}$$

E.8. $\mathbf{K}_{\text{mat}}$ MATRIX

Back to the original expression of the $\mathbf{K}_{\text{mat}}$ matrix, it is necessary to deal with the volume integral at first in order to use Gauss quadrature. The method in this work is to split the integral into a line integral and an area integral:

$$\begin{aligned} \mathbf{K}_{\text{mat}} &= \int_{\Omega_0} \mathbf{B}^{\mathrm{T}}\, \mathbb{C}\, \mathbf{B}\, \mathrm{d}V_0 \\ &= \int_{A_0} \int_{h_0} \mathbf{B}^{\mathrm{T}}\, \mathbb{C}\, \mathbf{B}\, \mathrm{d}h_0 \mathrm{d}A_0 \end{aligned} \tag{E.144}$$

Substituting Equation E.143 into the integrand in the above equation:

$$\begin{aligned} \mathbf{B}^{\mathrm{T}}\, \mathbb{C}\, \mathbf{B} &= \begin{bmatrix} \left(\mathbf{B}^0\right)^{\mathrm{T}} \\ \left(\mathbf{B}^b\right)^{\mathrm{T}} \end{bmatrix} \mathbb{C} \left[\mathbf{B}^0, \mathbf{B}^b\right] \\ &= \begin{bmatrix} \left(\mathbf{B}^0\right)^{\mathrm{T}}\, \mathbb{C}\, \mathbf{B}^0 & \left(\mathbf{B}^0\right)^{\mathrm{T}}\, \mathbb{C}\, \mathbf{B}^{\mathrm{b}} \\ \left(\mathbf{B}^{\mathrm{b}}\right)^{\mathrm{T}}\, \mathbb{C}\, \mathbf{B}^0 & \left(\mathbf{B}^{\mathrm{b}}\right)^{\mathrm{T}}\, \mathbb{C}\, \mathbf{B}^{\mathrm{b}} \end{bmatrix} \end{aligned} \tag{E.145}$$

Therefore, only consider the line integral of the integrand; the following matrix can be obtained:

$$\int_{h_0} \mathbf{B}^{\mathrm{T}}\, \mathbb{C}\, \mathbf{B}\, \mathrm{d}h_0 = \begin{bmatrix} (\mathbf{B}^0)^{\mathrm{T}} h_0 \mathbb{C} \mathbf{B}^0 & (\mathbf{B}^0)^{\mathrm{T}} h_0 \mathbb{C} \mathbf{B}^{\mathrm{bN}} \\ (\mathbf{B}^{\mathrm{bN}})^{\mathrm{T}} h_0 \mathbb{C} \mathbf{B}^0 & (\mathbf{B}^{\mathrm{bL}})^{\mathrm{T}} \frac{h_0^3}{12} \mathbb{C} \mathbf{B}^{\mathrm{bL}} \\ & + (\mathbf{B}^{\mathrm{bN}})^{\mathrm{T}} h_0 \mathbb{C} \mathbf{B}^{\mathrm{bN}} \end{bmatrix} \tag{E.146}$$

E.9. INTERNAL FORCE VECTOR $\mathbf{f}_{\text{int}}$

Applying the same method used to derive the internal force vector $\mathbf{f}_{\text{int}}$ as the $\mathbf{K}_{\text{mat}}$ matrix, the expression of $\mathbf{f}_{\text{int}}$ can be rewritten as:

$$\begin{aligned} \mathbf{f}_{\text{int}} &= \int_{\Omega_0} \mathbf{B}^{\mathrm{T}}\, \mathbf{S}\, \mathrm{d}V_0 \\ &= \int_{A_0} \int_{h_0} \mathbf{B}^{\mathrm{T}}\, \mathbf{S}\, \mathrm{d}h_0 \mathrm{d}A_0 \end{aligned} \tag{E.147}$$

By extracting the line integral from Equation E.147 and dividing it into two parts based on the Second Piola-Kirchhoff stress tensor $\mathbf{S}$:

$$\begin{aligned}\int_{h_0} \mathbf{B}^{\mathrm{T}}\,\mathbf{S}\,\mathrm{d}h_0 &= \int_{h_0} \mathbf{B}^{\mathrm{T}}\left(\mathbf{S}^{0}+\mathbf{S}^{\mathrm{b}}\right)\mathrm{d}h_0 \\ &= \int_{h_0} \mathbf{B}^{\mathrm{T}}\,\mathbf{S}^{0}\,\mathrm{d}h_0 + \int_{h_0} \mathbf{B}^{\mathrm{T}}\,\mathbf{S}^{\mathrm{b}}\,\mathrm{d}h_0 \end{aligned} \tag{E.148}$$

The first part is:

$$\begin{aligned}\int_{h_0} \mathbf{B}^{\mathrm{T}}\,\mathbf{S}^{0}\,\mathrm{d}h_0 &= \int_{h_0} \left(\mathbf{B}^{0}\right)^{\mathrm{T}}\mathbf{S}^{0} + \left(\mathbf{B}^{\mathrm{b}}\right)^{\mathrm{T}}\mathbf{S}^{0}\,\mathrm{d}h_0 \\ &= \int_{h_0} \left(\mathbf{B}^{0}\right)^{\mathrm{T}}\mathbf{S}^{0} + \left(-Z\left(\mathbf{B}^{bL}\right)^{\mathrm{T}} + \left(\mathbf{B}^{\mathrm{bN}}\right)^{\mathrm{T}}\right)\mathbf{S}^{0}\,\mathrm{d}h_0 \\ &= \int_{h_0} \left(\mathbf{B}^{0}\right)^{\mathrm{T}}\mathbf{S}^{0} - Z\left(\mathbf{B}^{bL}\right)^{\mathrm{T}}\mathbf{S}^{0} + \left(\mathbf{B}^{\mathrm{bN}}\right)^{\mathrm{T}}\mathbf{S}^{0}\,\mathrm{d}h_0 \\ &= h_0\left(\mathbf{B}^{0}\right)^{\mathrm{T}}\mathbf{S}^{0} + h_0\left(\mathbf{B}^{\mathrm{bN}}\right)^{\mathrm{T}}\mathbf{S}^{0}\end{aligned} \tag{E.149}$$

And the second part is:

$$\begin{aligned}\int_{h_0} \mathbf{B}^{\mathrm{T}}\,\mathbf{S}^{\mathrm{b}}\,\mathrm{d}h_0 &= \int_{h_0} \left(\mathbf{B}^{0}\right)^{\mathrm{T}}\mathbf{S}^{\mathrm{b}} + \left(\mathbf{B}^{\mathrm{b}}\right)^{\mathrm{T}}\mathbf{S}^{\mathrm{b}}\,\mathrm{d}h_0 \\ &= \int_{h_0} \left(\mathbf{B}^{0}\right)^{\mathrm{T}}\left(-Z\mathbf{S}^{\mathrm{bL}}+\mathbf{S}^{\mathrm{bN}}\right) + \left(-Z\mathbf{B}^{\mathrm{bL}}+\mathbf{B}^{\mathrm{bN}}\right)^{\mathrm{T}}\left(-Z\mathbf{S}^{\mathrm{bL}}+\mathbf{S}^{\mathrm{bN}}\right)\,\mathrm{d}h_0 \\ &= h_0\left(\mathbf{B}^{0}\right)^{\mathrm{T}}\mathbf{S}^{\mathrm{bN}} + \frac{h_0^3}{12}\left(\mathbf{B}^{\mathrm{bL}}\right)^{\mathrm{T}}\mathbf{S}^{\mathrm{bL}} + h_0\left(\mathbf{B}^{\mathrm{bN}}\right)^{\mathrm{T}}\mathbf{S}^{\mathrm{bN}}\end{aligned} \tag{E.150}$$

Combining two parts and substituting them into the area integral, the final form of $\mathbf{f}_{\mathrm{int}}$ can be built:

$$\begin{aligned}\mathbf{f}_{\mathrm{int}} = \int_{A_0} & h_0\left(\mathbf{B}^{0}\right)^{\mathrm{T}}\mathbf{S}^{0} + h_0\left(\mathbf{B}^{\mathrm{bN}}\right)^{\mathrm{T}}\mathbf{S}^{0} + h_0\left(\mathbf{B}^{0}\right)^{\mathrm{T}}\mathbf{S}^{\mathrm{bN}} \\ & + \frac{h_0^3}{12}\left(\mathbf{B}^{\mathrm{bL}}\right)^{\mathrm{T}}\mathbf{S}^{\mathrm{bL}} + h_0\left(\mathbf{B}^{\mathrm{bN}}\right)^{\mathrm{T}}\mathbf{S}^{\mathrm{bN}}\,\mathrm{d}A_0\end{aligned} \tag{E.151}$$

In order to simplify the process of Gauss quadrature, the first and fourth terms in the Equation E.151 can be extracted from the integral symbol:

$$\mathbf{f}^{0}_{\mathrm{int}} = \int_{A_0} h_0\left(\mathbf{B}^{0}\right)^{\mathrm{T}}\mathbf{S}^{0}\,\mathrm{d}A_0 = h_0\left(\mathbf{B}^{0}\right)^{\mathrm{T}}\mathbf{S}^{0}\,A_0 \tag{E.152}$$

$$\mathbf{f}^{\mathrm{bL}}_{\mathrm{int}} = \int_{A_0} \frac{h_0^3}{12}\left(\mathbf{B}^{\mathrm{bL}}\right)^{\mathrm{T}}\mathbf{S}^{\mathrm{bL}}\mathrm{d}A_0 = \mathbf{K}^{\mathrm{bL}}_{\mathrm{mat}}\,\mathbf{a} \tag{E.153}$$

E.10. $\mathbf{K}_{\text{geo}}$ MATRIX

To obtain $\mathbf{K}_{\text{geo}}$, the term $^{\partial \mathbf{B}^{\mathrm{T}}}/_{\partial \mathbf{q}}$ need to be defined firstly. Similarly, it is also divided into two parts. For membrane part, expanding term $^{\partial \mathbf{B}^{\mathrm{T}}}/_{\partial \mathbf{u}}$ for the odd rows:

$$\begin{aligned}
\frac{\partial B^0_{Xi^*}}{\partial u_j} &= \left(\frac{\partial N^0_j}{\partial X}\right)\left(\frac{\partial N^0_i}{\partial X}\right), \quad \frac{\partial B^0_{Xi^*}}{\partial v_j} = 0, \quad i,j \in [1,2,3], \quad i^* = 2\,i-1 \\
\frac{\partial B^0_{Yi*}}{\partial u_j} &= \left(\frac{\partial N^0_j}{\partial Y}\right)\left(\frac{\partial N_i}{\partial Y}\right), \quad \frac{\partial B^0_{Yi^*}}{\partial v_j} = 0 \\
\frac{\partial B^0_{XYi^*}}{\partial u_j} &= \frac{1}{2}\left[\left(\frac{\partial N^0_j}{\partial X}\right)\left(\frac{\partial N^0_i}{\partial Y}\right) + \left(\frac{\partial N^0_j}{\partial Y}\right)\left(\frac{\partial N^0_i}{\partial X}\right)\right], \quad \frac{\partial B^0_{XYi^*}}{\partial v_j} = 0
\end{aligned} \tag{E.154}$$

and for the even rows:

$$\begin{aligned}
\frac{\partial B_{Xi^*}}{\partial u_j} &= 0,, \quad \frac{\partial B_{Xi^*}}{\partial v_j} = \left(\frac{\partial N^0_j}{\partial X}\right)\left(\frac{\partial N^0_i}{\partial X}\right), \quad i,j \in [1,2,3], \quad i^* = 2\,i \\
\frac{\partial B_{Yi^*}}{\partial u_j} &= 0, \quad \frac{\partial B_{Yi*}}{\partial v_j} = \left(\frac{\partial N^0_j}{\partial Y}\right)\left(\frac{\partial N^0_i}{\partial Y}\right), \\
\frac{\partial B_{XYi^*}}{\partial u_j} &= 0, \quad \frac{\partial B_{XYi^*}}{\partial v_j} = \frac{1}{2}\left[\left(\frac{\partial N^0_j}{\partial X}\right)\left(\frac{\partial N^0_i}{\partial Y}\right) + \left(\frac{\partial N^0_j}{\partial Y}\right)\left(\frac{\partial N^0_i}{\partial X}\right)\right]
\end{aligned} \tag{E.155}$$

For bending part, expanding the term $^{\partial \mathbf{B}^{\mathrm{T}}}/_{\partial \mathbf{a}}$ similarly:

$$\frac{\partial B_{Xi}}{\partial a_j} = \frac{\partial N_i}{\partial X}\frac{\partial N_j}{\partial X} \tag{E.156}$$

$$\frac{\partial B_{Yi}}{\partial a_j} = \frac{\partial N_i}{\partial Y}\frac{\partial N_j}{\partial Y} \tag{E.157}$$

$$\frac{\partial B_{XYi}}{\partial a_j} = \frac{1}{2}\left(\frac{\partial N_i}{\partial X}\frac{\partial N_j}{\partial Y} + \frac{\partial N_i}{\partial Y}\frac{\partial N_j}{\partial X}\right) \tag{E.158}$$

Finally, the term of total shell element $^{\partial \mathbf{B}^{\mathrm{T}}}/_{\partial \mathbf{q}}$ can be assembling membrane part and

bending part together:

$$\frac{\partial \mathbf{B}_X}{\partial \mathbf{q}} = \left[\begin{array}{c|c} \frac{\partial \mathbf{B}_X^0}{\partial \mathbf{u}} & 0 \\ \hline 0 & \frac{\partial \mathbf{B}_X}{\partial \mathbf{a}} \end{array}\right]_{24\times 24} \tag{E.159}$$

$$\frac{\partial \mathbf{B}_Y}{\partial \mathbf{q}} = \left[\begin{array}{c|c} \frac{\partial \mathbf{B}_Y^0}{\partial \mathbf{u}} & 0 \\ \hline 0 & \frac{\partial \mathbf{B}_Y}{\partial \mathbf{a}} \end{array}\right]_{24\times 24} \tag{E.160}$$

$$\frac{\partial \mathbf{B}_{XY}}{\partial \mathbf{q}} = \left[\begin{array}{c|c} \frac{\partial \mathbf{B}_{XY}^0}{\partial \mathbf{u}} & 0 \\ \hline 0 & \frac{\partial \mathbf{B}_{XY}}{\partial \mathbf{a}} \end{array}\right]_{24\times 24} \tag{E.161}$$

Back to the original expression of the $\mathbf{K}_{\text{geo}}$ matrix, the same expanding method is used for numerical calculation:

$$\begin{aligned} \mathbf{K}_{\text{geo}} &= \int_{\Omega_0} \frac{\partial \mathbf{B}^{\mathrm{T}}}{\partial \mathbf{q}} \mathbf{S}\, \mathrm{d}V_0 \\ &= \int_{A_0}\int_{h_0} \frac{\partial \mathbf{B}^{\mathrm{T}}}{\partial \mathbf{q}} \mathbf{S}\, \mathrm{d}h_0 \mathrm{d}A_0 \end{aligned} \tag{E.162}$$

Integrating the stresses along the plate's thickness allows finding the axial forces ($\mathcal{N}_X \; and \; \mathcal{N}_Y$) and shear force ($\mathcal{N}_{XY}$) per unit length as

$$\mathcal{N}_X = \int_{h_0} S_{11}\, \mathrm{d}h_0 \tag{E.163}$$

$$\mathcal{N}_Y = \int_{h_0} S_{22}\, \mathrm{d}h_0 \tag{E.164}$$

$$\mathcal{N}_{XY} = \int_{h_0} S_{12}\, \mathrm{d}h_0 \tag{E.165}$$

where

$$\begin{aligned}\mathcal{N}_X &= \mathcal{N}_X^0 + \mathcal{N}_X^b \\ &= h_0 \left(S_{22}^0 + S_{22}^{\text{bN}}\right) \qquad \text{(E.166)} \\ \mathcal{N}_Y &= \mathcal{N}_Y^0 + \mathcal{N}_Y^b \\ &= h_0 \left(S_{22}^0 + S_{22}^{\text{bN}}\right) \qquad \text{(E.167)} \\ \mathcal{N}_{XY} &= \mathcal{N}_{XY}^0 + \mathcal{N}_{XY}^b \\ &= h_0 \left(S_{12}^0 + S_{12}^{\text{bN}}\right) \qquad \text{(E.168)}\end{aligned}$$

Then the component of the $\mathbf{K}_{\text{geo}}$ matrix can be defined by using all the above terms:

$$\begin{aligned}K_{ij}^{\text{Geo}} = &\int_{A_0} \mathcal{N}_X \frac{\partial B_{Xi}}{\partial q_j}\, \mathrm{d}A_0 + \\ &\int_{A_0} \mathcal{N}_Y \frac{\partial B_{Yi}}{\partial q_j}\, \mathrm{d}A_0 + \\ &\int_{A_0} \mathcal{N}_{XY} \frac{\partial B_{XYi}}{\partial q_j}\, \mathrm{d}A_0 \qquad \text{(E.169)}\end{aligned}$$

where $i, j \in [1, 2, \ldots, 23, 24]$

The formulation presented above has been implemented as a user element (UEL). The following sections present the verification and validation of the proposed shell element.

F. TUBA3 SHELL ELEMENT VERIFICATION

This section presents the verification of the proposed TUBA3 shell element. The membrane and plate elements described in Appendix B are first verified separately. These two components are then combined to form the TUBA3 shell element, which is subsequently verified through a benchmark problem. The corresponding verification procedures and numerical results are presented in the following subsections.

F.1. MEMBRANE ELEMENT VERIFICATION

The membrane element is first evaluated using the standard patch test to verify its ability to exactly reproduce a constant strain field. As shown in Figure F.6, a square plate with dimensions of $20\ \text{mm} \times 20\ \text{mm}$ is discretized using an irregular mesh of distorted triangular elements. These meshes are adopted to ensure that the test is independent of element shape and mesh distortion. The geometric dimensions, prescribed displacement, and material properties are summarized in Figure F.6.

As shown in Figure F.6, the boundary conditions are defined as follows: (1) the bottom edge is constrained in the vertical direction, (2) the lower-left corner is additionally constrained in the horizontal direction to prevent rigid-body motion, (3) A prescribed vertical displacement of $U_2 = 1\ \text{mm}$ is uniformly applied along the top edge.

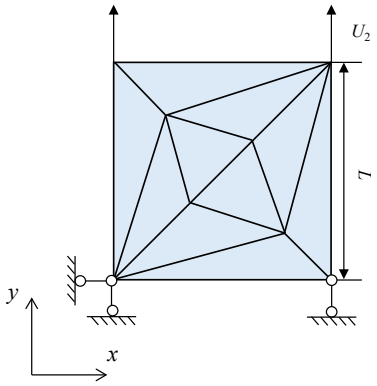

Geometric and material properties for patch test model

Length L (mm)	Displacement U_2 (mm)	Elastic modulus E (MPa)	Poisson's ratio ν
20	1	210000	0.3

Figure F.6: Patch test of the membrane element

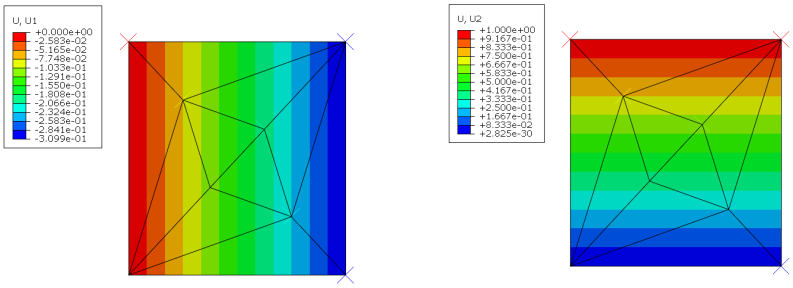

(a) Displacement U_1 (b) Displacement U_2

Figure F.7: Patch test results

Figure F.7 presents the displacement contours obtained from the membrane patch test. As expected, the horizontal displacement (U_1) varies linearly along the x-direction, while the vertical displacement (U_2) varies linearly along the y-direction. The displacement contours remain smooth and continuous across all distorted triangular elements, with no discontinuities at element boundaries. In conclusion, these results demonstrate that the membrane element successfully passes the patch test.

F.2. PLATE ELEMENT VERIFICATION

This subsection evaluates the accuracy and robustness of the proposed TUBA3 plate element using two benchmark problems: (1) a simply supported plate subjected to a concentrated load at its center and (2) a cantilever plate. For each benchmark, both geometrically linear and geometrically nonlinear analyses are conducted, and the numerical results are compared with reference solutions.

SIMPLY SUPPORTED PLATE WITH CENTER LOAD

The simply supported plate considered in this benchmark is illustrated in Figure F.8. The plate has a side length of L and a thickness of h and is assumed to be made of an isotropic linear elastic material. The geometric dimensions and material properties are summarized in Table F.1. All four edges are simply supported, and a concentrated load P is applied at the plate center.

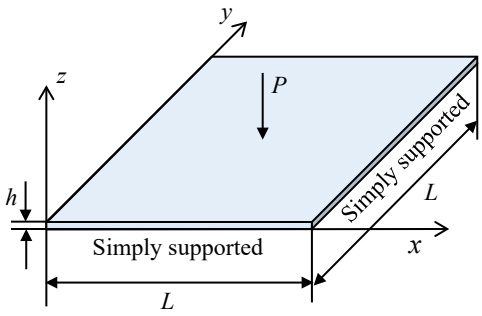

Figure F.8: Simply supported plate with center load model

Table F.1: Parameters of the simply supported plate

Elastic modulus E (N/mm^2)	Poisson's ratio ν	Length L (mm)	Thickness h (mm)
7170	0.3	150	10

For a given applied load P, the analytical displacement at the plate center is calculated using Equation F.170, as given by Timoshenko [5].

$$w\left(\frac{L}{2},\frac{L}{2}\right)=\alpha\frac{PL^3}{D} \tag{F.170}$$

where α is 0.0116 for a square plate and P = -30 kN is the applied concentrated load. For a homogeneous isotropic plate, the flexural rigidity is:

$$D=\frac{Eh^3}{12(1-\nu^2)} \tag{F.171}$$

The model is discretized using two mesh configurations, as shown in Figure F.9, both using uniform elements. Mesh 1 consists of three nodes along each edge, whereas Mesh 2 consists of four nodes along each edge. For a simply supported plate, the bending moment normal to each supported edge must vanish. For an isotropic plate, the bending moments in

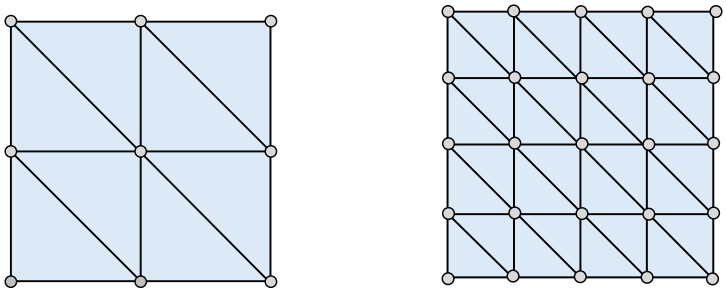

(a) Mesh 1 (b) Mesh 2

Figure F.9: Coarse and fine finite element meshes for the simply supported plate

the x- and y-directions are given by

$$M_x = \frac{Eh^3}{12(1-\nu^2)}\left(\frac{\partial^2 w}{\partial x^2} + \nu\frac{\partial^2 w}{\partial y^2}\right) \tag{F.172}$$

$$M_y = \frac{Eh^3}{12(1-\nu^2)}\left(\nu\frac{\partial^2 w}{\partial x^2} + \frac{\partial^2 w}{\partial y^2}\right) \tag{F.173}$$

The detailed boundary conditions of the benchmark model are illustrated in Figure F.10.

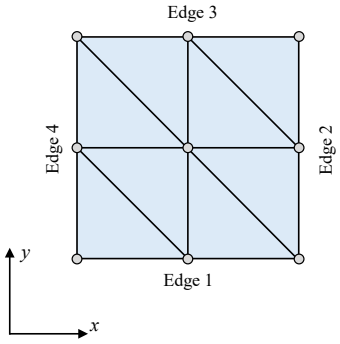

Edge	Type	Boundary conditions
1	Simply supported	$w = 0, \theta_y = 0, M_y = 0$
2	Simply supported	$w = 0, \theta_y = 0, M_y = 0$
3	Simply supported	$w = 0, \theta_y = 0, M_y = 0$
4	Simply supported	$w = 0, \theta_y = 0, M_y = 0$

Figure F.10: Boundary conditions of the simply supported plate

Table F.2 presents the convergence study for the center deflection of the simply supported plate subjected to a concentrated center load. The results compare two mesh configurations under both geometrically linear and geometrically nonlinear analyses with the analytical solution obtained from Equation F.170.

The results show excellent mesh convergence for both the geometrically linear and geometrically nonlinear analyses. For each analysis, the difference between the two mesh

Table F.2: Center deflection of the simply supported isotropic plate subjected to a concentrated center load

Mesh	Displacement w (mm)	Error (%)
1-Linear	-1.22656	2.85
2-Linear	-1.22334	2.58
1-Nonlinear	-1.20462	1.01
2-Nonlinear	-1.20155	0.76
Analytical	-1.19252	—

configurations is negligible. Moreover, the geometrically nonlinear results show better agreement with the analytical solution, with relative errors below 1.1% for both mesh configurations.

CANTILEVER PLATE

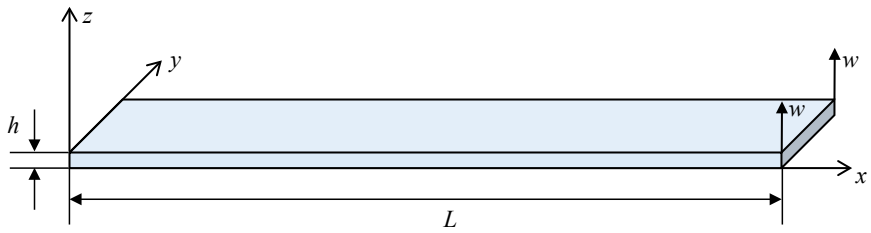

Figure F.11: Cantilever plate model

The cantilever plate model is as shown in Figure F.11, while the geometric and material parameters are presented in Table F.3. The analytical solution formula is as follows:

$$F = \frac{3EI}{L^3} w \tag{F.174}$$

where I is the second moment of area of the cross section, which is defined as:

$$I = \frac{bh^3}{12} \tag{F.175}$$

The model is discretized using three mesh configurations, as shown in Figure F.12. Mesh 1 consists of 4 elements, Mesh 2 consists of 8 elements, and Mesh 3 consists of 32 elements. For a cantilever plate, the detailed boundary condition is shown in Figure F.13.

Figure F.14 compares the load-displacement curves of the cantilever plate obtained using three different mesh configurations with the analytical solution under both geometrically linear and geometrically nonlinear analyses.

Table F.3: Parameters of the cantilever plate

Elastic modulus E (N/mm^2)	Poisson's ratio ν	Length L (mm)	Width b (mm)	Thickness h (mm)
139400	0	150	10	3

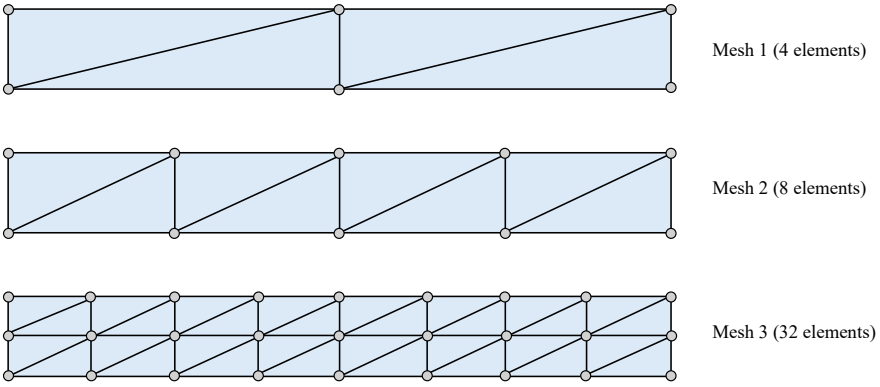

Figure F.12: Finite element meshes for the cantilever plate

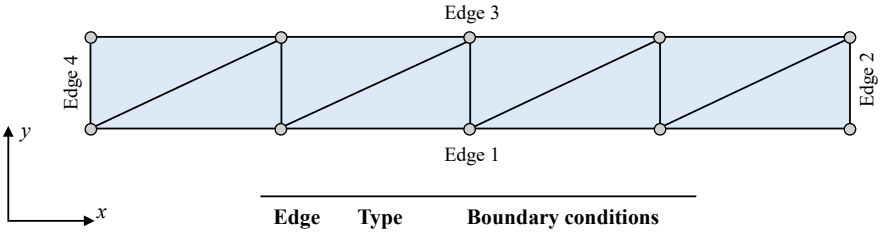

Edge	Type	Boundary conditions
1	Free	$M_y = 0$
2	Free	$M_x = 0$
3	Free	$M_y = 0$
4	Clamped	$w = 0, \theta_x = 0, \theta_y = 0$

Figure F.13: Boundary condition of the cantilever plate

As shown in Figure F.14a, all three mesh configurations produce identical results for the geometrically linear analysis. The numerical predictions coincide with the analytical solution throughout the loading process, demonstrating excellent accuracy and mesh convergence of the proposed TUBA3 shell element. In contrast, as shown in Figure F.14b, the response becomes highly nonlinear as the applied load increases.

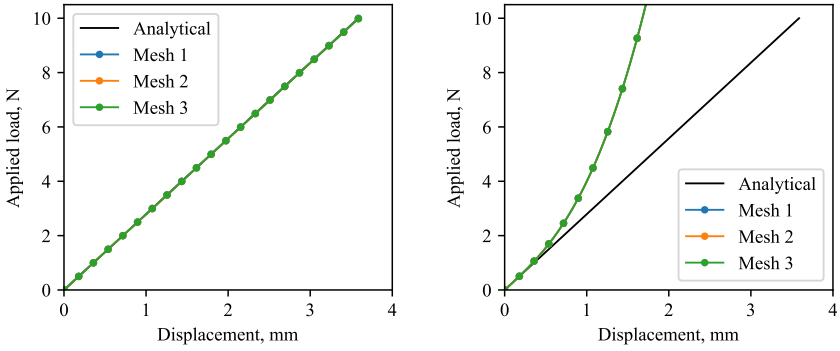

(a) Geometrical linearity

(b) Geometrical nonlinearity

Figure F.14: Results for the cantilever plate

G. TUBA3 SHAPE FUNCTIONS

The first six shape functions of the TUBA3 triangle, as reported in [6], are given by:

$$\begin{aligned} N_1 =& L_1^5 + 5L_1^4L_2 + 5L_1^4L_3 + 10L_1^3L_2^2 + 10L_1^3L_3^2 \\ &+ 20L_1^3L_2L_3 + 30r_{21}L_1^2L_2L_3^2 + 30r_{31}L_1^2L_3L_2^2 \end{aligned} \tag{G.176}$$

$$\begin{aligned} N_2 =& c_3L_1^4L_2 - c_2L_1^4L_3 + 4c_3L_1^3L_2^2 + 4c_2L_1^3L_3^2 \\ &+ 4\left(c_3 - c_2\right)L_1^3L_2L_3 - \left(3c_1 + 15r_{21}c_2\right)L_1^2L_2L_3^2 \\ &+ \left(3c_1 + 15r_{31}c_3\right)L_1^2L_3L_2^2 \end{aligned} \tag{G.177}$$

$$\begin{aligned} N_3 =& - b_3L_1^4L_2 + b_2L_1^4L_3 + 4b_3L_1^3L_2^2 + 4b_2L_1^3L_3^2 \\ &+ 4\left(b_2 - b_3\right)L_1^3L_2L_3 + \left(3b_1 + 15r_{21}b_2\right)L_1^2L_2L_3^2 \\ &+ \left(3b_1 + 15r_{31}b_3\right)L_1^2L_3L_2^2 \end{aligned} \tag{G.178}$$

$$\begin{aligned} N_4 =& \frac{c_3^2}{2}L_1^3L_2^2 + \frac{c_2^2}{2}L_1^3L_3^2 - c_2c_3L_1^3L_2L_3 \\ &+ \left(c_1c_2 + \frac{5}{2}r_{21}c_2^2\right)L_2L_3^2L_1^2 + \left(c_1c_3 + \frac{5}{2}r_{31}c_3^2\right)L_3L_2^2L_1^2 \end{aligned} \tag{G.179}$$

$$\begin{aligned} N_5 =& - b_3c_3L_1^3L_2^2 - b_2c_2L_1^3L_3^2 + \left(b_2c_3 + b_3c_2\right)L_1^3L_2L_3 \\ &- \left(b_1c_2 + b_2c_1 + 5r_{21}b_2c_2\right)L_2L_3^2L_1^2 \\ &- \left(b_1c_3 + b_3c_1 + 5r_{31}b_3c_3\right)L_3L_2^2L_1^2 \end{aligned} \tag{G.180}$$

$$
\begin{aligned}
N_6 = & \frac{b_3^2}{2} L_1^3 L_2^2 + \frac{b_2^2}{2} L_1^3 L_3^2 - b_2 b_3 L_1^3 L_2 L_3 \\
& + \left(b_1 b_2 + \frac{5}{2} r_{21} b_2^2 \right) L_2 L_3^2 L_1^2 \\
& + \left(b_1 b_3 + \frac{5}{2} r_{31} b_3^2 \right) L_3 L_2^2 L_1^2
\end{aligned} \tag{G.181}
$$

where L_1, L_2 and L_3 are the triangle's area coordinates. And

$$
\begin{cases}
a_i = x_j y_k - x_k y_j \\
b_i = y_j - y_k \\
c_i = x_k - x_j
\end{cases} \tag{G.182}
$$

$$
r_{ij} = -\frac{b_i b_j + c_i c_j}{b_i^2 + c_i^2} \tag{G.183}
$$

where i, j, k are cyclic permutations of 1, 2, 3. For the TUBA3 element, the nodal coordinates are given by (x_1, y_1), (x_2, y_2), and (x_3, y_3). The remaining shape functions (N_7 to N_{18}) are defined in groups of six, obtained by cyclically permuting the indices 1, 2, and 3.

Appendix References

1. Bell, K. A refined triangular plate bending finite element. *International journal for numerical methods in engineering* **1,** 101–122 (1969).
2. Davidson, B., Krüger, R. & König, M. Three-dimensional analysis of center-delaminated unidirectional and multidirectional single-leg bending specimens. *Composites Science and Technology* **54,** 385–394 (1995).
3. Krueger, R. A summary of benchmark examples to assess the performance of quasi-static delamination propagation prediction capabilities in finite element codes. *Journal of Composite Materials* **49,** 3297–3316 (2015).
4. Balducci, G. T. & Chen, B. Overcoming the cohesive zone limit in the modelling of composites delamination with TUBA cohesive elements. *Composites Part A: Applied Science and Manufacturing* **185,** 108356 (2024).
5. Timoshenko, S. & Woinowsky-Krieger, S. *Theory of plates and shells* (McGraw-Hill, 1959).
6. Dasgupta, S. & Sengupta, D. A higher-order triangular plate bending element revisited. *International Journal for Numerical Methods in Engineering* **30,** 419–430 (1990).

ACKNOWLEDGEMENTS

Time flies, and my doctoral journey is finally approaching its end. Looking back on these years, from the excitement of starting my PhD to the challenges, uncertainties, and achievements along the way, I am filled with gratitude. This journey has been an important period of both academic and personal growth. I would like to take this opportunity to thank everyone who has supported, guided, and accompanied me throughout these years.

First and foremost, I would like to express my sincere gratitude to my supervisors, Professor Christos Kassapoglou and Professor Boyang Chen, for their guidance and support throughout my PhD. I am especially grateful to Christos for his guidance on my research, from defining the research direction to conducting the work and writing papers. Your advice and encouragement helped me persevere through the most challenging periods of my PhD, and I truly appreciate the freedom you gave me to explore and develop as a researcher. My sincere thanks also go to Boyang for your valuable guidance, understanding, and continuous support. Since my arrival in the Netherlands, you have supported me not only academically but also in many aspects of my personal life. I especially appreciate your encouragement and help during the early stages of the COVID-19 pandemic, which made a difficult period much easier to overcome. I have greatly benefited from the different perspectives and expertise of both supervisors, and it has been a privilege to complete my PhD under your supervision.

I would also like to thank our group secretaries, Laura and Gemma, as well as our department chair, Roeland, for their help with administrative matters and various arrangements throughout my PhD. Your patience, efficiency, and kindness made many things much easier and contributed greatly to my daily working life.

Special thanks go to my groupmate Giorgio. My research involved extensive mathematical derivations and programming, and I am particularly grateful for your generous help and patient guidance during the early stages of my PhD. Your advice on research ideas, mathematical derivations, and code implementation helped me quickly adapt to my research topic and the PhD environment, providing a solid foundation for my subsequent work.

I would also like to thank my other groupmates, Zhe, Mohamad, Arne, Swapan, Georgios, Sergio, and Karthikayen. Thank you for your friendship, help, and companionship. I will always remember the lunches we shared, our academic discussions, and the conversations during coffee breaks. These simple moments brought much joy to our busy research lives and became some of my fondest memories of my PhD.

I am also grateful to my office colleagues, Zhi, Panos, Kubair, Christopher, and Eva, for their companionship and support. My thanks also go to the academic staff in the department, Dimitrios, Sergio, Saullo, Xuerui, and Nan, as well as other colleagues and fellow students, including John-Alan, Bianca, Morteza, Julien, Jimmy, Clemens, René, Hammad, Ehshan, Arne, and Luc. I would also like to thank Dario and Friso from the University of Twente. Thank you all for the discussions, advice, and pleasant moments we shared. Your

presence made my working environment more enjoyable and my PhD experience more memorable.

I would like to express my special thanks to my Chinese colleagues and friends, Shichen, Ruipeng, Wenjie, Zhiyuan, Lubin, Nan, Ran, Xiang, Yuqian, Xi, Hongwei, Yuzhe, and Xiaodong. Living far away from home, it was a great pleasure to meet people who share similar cultural backgrounds and experiences. Thank you for your friendship, support, and the many moments we shared, both in research and in daily life. Your companionship brought warmth and a sense of familiarity to my life in the Netherlands, making these years abroad much more meaningful.

Beyond my academic life, I would also like to thank my friends Shuainan, Min, Benjamin, Wencan, Kai, Jingyi, Yu, Yifei, Yifu, Patrick, and Yanwei. Thank you for bringing so much joy to my life outside research. Whether spending weekends together, travelling, or simply sharing everyday conversations, these moments allowed me to take a break from academic pressures and enjoy life. I will always cherish the memories and friendships we have built over the years.

My deepest gratitude goes to my parents for their unconditional love, understanding, and support throughout my life. Thank you for respecting my decisions and supporting my choice to pursue my studies abroad. Despite the distance and the years we have spent apart, you have always been my strongest source of support and encouragement. I am forever grateful for your love and sacrifices. I hope to spend more time with you in the years ahead, and wish you good health, happiness, and peace.

Last but certainly not least, I would like to thank my wife, Zihan Ding, for her unwavering love, patience, and support. During these years of living apart, you have always stood by my side. Thank you for understanding the demands of my research, sharing my worries, encouraging me through difficult times, and being my greatest source of comfort. Completing this PhD would not have been possible without your love and support. Thank you for making this long journey less lonely. I look forward to continuing our journey together, supporting one another, and building a beautiful future side by side.

Finally, I would like to thank everyone who has been part of this journey. Although my PhD is coming to an end, the experiences, friendships, and memories I have gained will remain with me forever. With a grateful heart, I look forward to the next chapter of life.

CURRICULUM VITÆ

Xiaopeng AI



17-06-1993 Born in Tai'an, China.

EDUCATION

2012–2016 **BSc**, School of Aeronautics
Northwestern Polytechnical University, Xi'an, China

2016–2019 **Msc**, School of Aeronautics
Northwestern Polytechnical University, Xi'an, China

2019-2026 **Ph.D**, Faculty of Aerospace Engineering
Delft University of Technology, Delft, the Netherlands

List of Publications

3. **Xiaopeng Ai**, Christos Kassapoglou, Boyang Chen, *Accurate simulation of delamination with a resin-rich layer-dependent penalty stiffness based on structural cohesive elements*, arXiv:2608.05881, Under review.

2. **Xiaopeng Ai**, Christos Kassapoglou, Boyang Chen, *A new approach for the determination of through-thickness and free-edge stresses in composite laminates based on structural elements*, arXiv:2607.27559, Under review.

1. **Xiaopeng Ai**, Boyang Chen, Christos Kassapoglou, *Structural cohesive element for the modelling of delamination in composite laminates without the cohesive zone limit*, Engineering Fracture Mechanics **345**, 111586 (2025)